frontiers | Research Topics

Advanced green and sustainable chemical and physical technologies for resources recycling of solid wastes

Edited by
Xiangning Bu, Ilhwan Park and Ugur Ulusoy

Published in
Frontiers in Chemistry

FRONTIERS EBOOK COPYRIGHT STATEMENT

The copyright in the text of individual articles in this ebook is the property of their respective authors or their respective institutions or funders. The copyright in graphics and images within each article may be subject to copyright of other parties. In both cases this is subject to a license granted to Frontiers.

The compilation of articles constituting this ebook is the property of Frontiers.

Each article within this ebook, and the ebook itself, are published under the most recent version of the Creative Commons CC-BY licence. The version current at the date of publication of this ebook is CC-BY 4.0. If the CC-BY licence is updated, the licence granted by Frontiers is automatically updated to the new version.

When exercising any right under the CC-BY licence, Frontiers must be attributed as the original publisher of the article or ebook, as applicable.

Authors have the responsibility of ensuring that any graphics or other materials which are the property of others may be included in the CC-BY licence, but this should be checked before relying on the CC-BY licence to reproduce those materials. Any copyright notices relating to those materials must be complied with.

Copyright and source acknowledgement notices may not be removed and must be displayed in any copy, derivative work or partial copy which includes the elements in question.

All copyright, and all rights therein, are protected by national and international copyright laws. The above represents a summary only. For further information please read Frontiers' Conditions for Website Use and Copyright Statement, and the applicable CC-BY licence.

ISSN 1664-8714
ISBN 978-2-83251-625-6
DOI 10.3389/978-2-83251-625-6

About Frontiers

Frontiers is more than just an open access publisher of scholarly articles: it is a pioneering approach to the world of academia, radically improving the way scholarly research is managed. The grand vision of Frontiers is a world where all people have an equal opportunity to seek, share and generate knowledge. Frontiers provides immediate and permanent online open access to all its publications, but this alone is not enough to realize our grand goals.

Frontiers journal series

The Frontiers journal series is a multi-tier and interdisciplinary set of open-access, online journals, promising a paradigm shift from the current review, selection and dissemination processes in academic publishing. All Frontiers journals are driven by researchers for researchers; therefore, they constitute a service to the scholarly community. At the same time, the *Frontiers journal series* operates on a revolutionary invention, the tiered publishing system, initially addressing specific communities of scholars, and gradually climbing up to broader public understanding, thus serving the interests of the lay society, too.

Dedication to quality

Each Frontiers article is a landmark of the highest quality, thanks to genuinely collaborative interactions between authors and review editors, who include some of the world's best academicians. Research must be certified by peers before entering a stream of knowledge that may eventually reach the public - and shape society; therefore, Frontiers only applies the most rigorous and unbiased reviews. Frontiers revolutionizes research publishing by freely delivering the most outstanding research, evaluated with no bias from both the academic and social point of view. By applying the most advanced information technologies, Frontiers is catapulting scholarly publishing into a new generation.

What are Frontiers Research Topics?

Frontiers Research Topics are very popular trademarks of the *Frontiers journals series*: they are collections of at least ten articles, all centered on a particular subject. With their unique mix of varied contributions from Original Research to Review Articles, Frontiers Research Topics unify the most influential researchers, the latest key findings and historical advances in a hot research area.

Find out more on how to host your own Frontiers Research Topic or contribute to one as an author by contacting the Frontiers editorial office: frontiersin.org/about/contact

Advanced green and sustainable chemical and physical technologies for resources recycling of solid wastes

Topic editors

Xiangning Bu — China University of Mining and Technology, China

Ilhwan Park — Hokkaido University, Japan

Ugur Ulusoy — Cumhuriyet University, Türkiye

Citation

Bu, X., Park, I., Ulusoy, U., eds. (2023). *Advanced green and sustainable chemical and physical technologies for resources recycling of solid wastes*.

Lausanne: Frontiers Media SA. doi: 10.3389/978-2-83251-625-6

Table of contents

frontiers | Frontiers in Chemistry

TYPE Editorial
PUBLISHED 24 January 2023
DOI 10.3389/fchem.2023.1146404

Check for updates

OPEN ACCESS

EDITED AND REVIEWED BY
James Clark,
University of York, United Kingdom

*CORRESPONDENCE
Xiangning Bu,
xiangning.bu@foxmail.com
Ilhwan Park,
i-park@eng.hokudai.ac.jp
Ugur Ulusoy,
uulusoy@cumhuriyet.edu.tr

SPECIALTY SECTION
This article was submitted to Green and Sustainable Chemistry, a section of the journal Frontiers in Chemistry

RECEIVED 17 January 2023
ACCEPTED 19 January 2023
PUBLISHED 24 January 2023

CITATION
Bu X, Park I and Ulusoy U (2023), Editorial: Advanced green and sustainable chemical and physical technologies for resources recycling of solid wastes.
Front. Chem. 11:1146404.
doi: 10.3389/fchem.2023.1146404

COPYRIGHT
© 2023 Bu, Park and Ulusoy. This is an open-access article distributed under the terms of the Creative Commons Attribution License (CC BY). The use, distribution or reproduction in other forums is permitted, provided the original author(s) and the copyright owner(s) are credited and that the original publication in this journal is cited, in accordance with accepted academic practice. No use, distribution or reproduction is permitted which does not comply with these terms.

Editorial: Advanced green and sustainable chemical and physical technologies for resources recycling of solid wastes

Xiangning Bu[1]*, Ilhwan Park[2]* and Ugur Ulusoy[3]*

[1]School of Chemical Engineering and Technology, China University of Mining and Technology, Xuzhou, China, [2]Division of Sustainable Resources Engineering, Faculty of Engineering, Hokkaido University, Sapporo, Japan, [3]Department of Chemical Engineering, Cumhuriyet University, Sivas, Türkiye

KEYWORDS

sustainable mining, e-waste, mineral waste processing, metals recycling, solution purification, zero-waste recycling, acid leaching, metal extraction

Editorial on the Research Topic
Advanced Green and Sustainable Chemical and Physical Technologies for Resources Recycling of Solid Wastes

To prevent CO_2-induced climate change, the world is quickly moving toward a carbon-neutral society by using electric vehicles, renewable energy sources, and other energy sources, which demand more resources than traditional ones in terms of materials, minerals, and metals. In this regard, recycling processes of rare earth elements (REEs), metals, plastic, and glass from secondary sources with a zero-waste strategy have become more important in order to reduce environmental damage and bring them into the economy when primary mineral resources are running out. Therefore, in this Research Topic, studies on effective, non-hazardous, long-term, and ecological recycling processes of solid wastes, including by-products from industrial processes containing metals have been compiled.

This Research Topic, which selects and collects eleven original research papers and one mini-review paper that has conducted studies on this field, sheds fresh light on critical aspects providing crucial scientific knowledge that will benefit future research. The first part of the articles collected is related to the release and migration of heavy metals in solid wastes. Zhang et al. calculated the environmental vulnerability factors affecting the dissolution of heavy metals in fly ash from a thermal power plant. Fly ash has been suggested as a possible soil conditioner and additive that might be used to enhance reclamation soil in coal mining subsidence sites. Zheng et al. analyzed how low molecular weight organic acids such as citric acid and malic acid impacted the migratory characteristics of Pb in polluted soils. Due to its capacity to activate Pb, the use of citric acid has been suggested as a technique that can improve the efficacy of remediating reclaimed soil. Since it has been reported that the smelting technique has the potential for innocuous processing to overcome the waste Research Topic in the electrolytic manganese industry by creating glass ceramics using electrolytic manganese slag as feedstock and solidified heavy metal constituents (Sun et al., 2020), Wang et al. studied the process of heavy metal solidification and stability in glass-ceramics containing electrolytic manganese slag. It has been concluded that the glass-ceramic system's interwoven pattern of glass and crystal phases also contributed to the improved curative influence of heavy metals. In addition, Hao et al. explored the possibility of making glass ceramics from wastes such as coal gasification slag

and petrochemical incineration fly ash (PIFA) by trapping dangerous toxic metals in their crystalline-noncrystalline multistage composition.

The second part of the collected papers are on resource recycling of solid wastes using chemical and physical separation techniques. Phann et al. demonstrated that Alanine is an ecologically friendly option for the preferential leaching of used hydrodesulfurization catalysts containing Mo and Co metals. Huang et al. introduced ultrasonication to enhance the oxidation leaching of chromium from electroplating sludge. In addition to leaching, Li et al. proposed innovative, inexpensive, and hugely beneficial recycling of carbon fiber-reinforced polymer (CFRP) wastes using the swelling agent of dimethylacetamide (DMAC) for diminishing the loss of carbon fiber length and strength. Wang et al. investigated the recovery of discarded carbon anode slag from aluminum electrolysis by flotation. It was found that carbon anode slag demonstrated a higher flotation selectivity under the optimized grinding flotation compared to direct flotation. For advanced physical separation, Phengsaart et al. designed a new technique named as the reverse hybrid jig integrating the methods of jigging and flotation to separate plastics (polypropylene/polyethylene) and suggested a new index using concentration criterion for predicting the effectiveness of the separation.

The rest of the collected papers are related to the preparation of the brazing alloy using recycled E-waste and arsenic removal in gold-smelting wastewater by the modified agricultural mulch film residual. Since the majority of the metals used in circuit boards can serve as parts of the multi-element alloy brazing alloy, Yang et al. have utilized discarded mobile phones for e-waste recycling by investigating the contents, smelting point, form, and characteristics as well as the size, form, and other microstructure development of the second phase of brazing alloy created by smelting the circuit boards. The work of Zhang et al. proposed an innovative and efficient method to purify and remove arsenic from gold-smelting wastewater by utilizing agricultural mulch film residual followed by an iron modification to avoid the harmful effect of arsenic on humans and the environment.

Author contributions

This Editorial was cooperatively prepared by XB, IP, and UU. The authors approved the final submitted version.

Acknowledgments

The reviewers and authors who are specialists in their fields deserve a hearty thank you from the editors for their insightful criticisms, assessments, and remarks. In addition, we would like to express our gratitude and appreciation to the journal's internal responsible editors and publishing staff, who have contributed significantly to the successful completion of the protracted and important peer-review processes by offering significant technical support. Without their constant help and generosity, our Research Topic would not have been as successful.

Conflict of interest

The authors declare that the research was conducted in the absence of any commercial or financial relationships that could be construed as a potential conflict of interest.

Publisher's note

All claims expressed in this article are solely those of the authors and do not necessarily represent those of their affiliated organizations, or those of the publisher, the editors and the reviewers. Any product that may be evaluated in this article, or claim that may be made by its manufacturer, is not guaranteed or endorsed by the publisher.

Reference

Sun, D., Yang, L., Liu, N., Jiang, W., Jiang, X., Li, J., et al. (2020). Sulfur resource recovery based on electrolytic manganese residue calcination and manganese oxide ore desulfurization for the clean production of electrolytic manganese. *Chin. J. Chem. Eng.* 28 (3), 864–870. doi:10.1016/j.cjche.2019.11.013

frontiers | Frontiers in Chemistry

ORIGINAL RESEARCH
published: 14 July 2022
doi: 10.3389/fchem.2022.934949

Effect of Low-Molecular-Weight Organic Acids on Migration Characteristics of Pb in Reclaimed Soil

Yonghong Zheng[1,2,3], Yating Li[1], Zhiguo Zhang[2,4], Yuning Tan[1], Weiqing Cai[1], Chengnan Ma[1], Fangling Chen[1] and Jiangwei Lu[1]*

[1]School of Earth and Environment, Anhui University of Science and Technology, Huainan, China, [2]Anhui Engineering Laboratory for Comprehensive Utilization of Water and Soil Resources and Ecological Protection in Mining Area with High Groundwater Level, Huainan, China, [3]National Engineering Laboratory for Protection of Colliery Eco-environment, Huainan, China, [4]Hefei Comprehensive National Science Center, Institute of Energy, Hefei, China

OPEN ACCESS

Edited by:
Ilhwan Park,
Hokkaido University, Japan

Reviewed by:
Shiwen Zhang,
Anhui University of Science and Technology, China
Chuncai Zhou,
Hefei University of Technology, China
Qingguang Li,
Guizhou University, China
Xuetao Guo,
Northwest A&F University, China
Bao Wang,
Xi'an University of Architecture and Technology, China

***Correspondence:**
Zhiguo Zhang
zzgaust@qq.com

Specialty section:
This article was submitted to Green and Sustainable Chemistry, a section of the journal Frontiers in Chemistry

Received: *03 May 2022*
Accepted: *03 June 2022*
Published: *14 July 2022*

Citation:
Zheng Y, Li Y, Zhang Z, Tan Y, Cai W, Ma C, Chen F and Lu J (2022) Effect of Low-Molecular-Weight Organic Acids on Migration Characteristics of Pb in Reclaimed Soil. Front. Chem. 10:934949. doi: 10.3389/fchem.2022.934949

The effect of low-molecular-weight organic acids (citric acid and malic acid) on the migration characteristics of Pb in contaminated soils was explored in this study. Reclaimed soil was collected from the coal gangue hill area of the Panyi mine in Huainan City (China). The effect of citric acid and malic acid on the form of Pb present in the reclaimed soil was analyzed by spiking soil samples and simulating Pb-contaminated soil. The results indicate the following. 1) With increased concentration of exogenous Pb, the activity of Pb in the reclaimed soil was effectively improved. 2) The addition of citric acid and malic acid both resulted in an increased fraction of exchangeable Pb in the soil, which effectively promoted the active Pb fraction. As the concentrations of citric acid and malic acid increased, the active Pb fraction of the reclaimed soil increased accordingly. The Pb activation effect of citric acid was observed to be greater than that of malic acid. 3) With extended soil aging time, the activation effect of organic acids on Pb weakened, with the loosely bound Pb gradually transforming into strongly bound Pb. Chelating agents can activate heavy metals in soil, mainly through the combination of chelating agents and heavy metal ions in the soil solution to form soluble metal chelates, so as to increase the bioavailability of heavy metals in soil to plant roots. Therefore, adding citric acid can be considered as a strategy to enhance the efficiency of reclaimed soil remediation because of the ability of Pb activation.

Keywords: heavy metal, plumbum, citric acid, malic acid, form, pollution remediation

1 INTRODUCTION

In recent years, the environmental impacts of anthropogenic activities have become increasingly serious because of rapid urbanization and industrial and agricultural development. Lead (Pb) fraction in the soil environment exceeded natural threshold and seriously affected the soil ecology. Pb can be ingested by human through the food chain, thereby negatively affecting health (Zhang et al., 2021). According to the National Soil Pollution Survey Report in 2014, the main contaminants of arable land were heavy metals including cadmium (Cd), nickel (Ni), and Pb. Among them, the ratio of exceedance of Pb in soil reached 1.5%, while the ratio of heavily contaminated points of Pb was

0.1% (Wang et al., 2014). Soil Pb contamination can be caused by Pb mining activities (Zhang et al., 2012; Foulds et al., 2014), Pb-containing wastewater discharged during industrial production (Zheng and Zhang, 2017), excessive use of chemical fertilizers and pesticides (Pichtel et al., 2000), and use of Pb batteries (Picard et al., 2017). Among them, heavy metal-containing exhaust gas deposition, wastewater irrigation emitted by metal mining, and dissolution and diffusion of solid wastes soil are the main ways of heavy metal pollution (Zhou et al., 2014). Mining can result in a large accumulation of heavy metals in the surrounding and downstream rivers and soils. Coal gangue is the largest source of industrial solid waste in China. Moreover, the long-term exposure of coal gangue to sun and rain can increase the soil pollution owing to the release of heavy metal elements (Shang et al., 2021). Some of the reclaimed area soils are affected by coal mining and reclamation filling activities with increased Pb fraction (Zheng et al., 2013).

In the past few years, the soil remediation industry regarding heavy metal has developed rapidly in China, with a significant increase in the number of projects and continuous innovation. As a chemical remediation strategy, organic complexation is relatively mature, low cost, and fast acting; however, secondary pollution of organic complexation has impeded widespread adoption of this technology (Liu GH et al., 2018). Engineering measures, often taken for physical remediation, cost a lot of material and financial resources, and the construction process is prone to cause serious fluctuations in the soil and damage the soil structure (Tomohito et al., 2010). Microbial remediation has limited fixation of heavy metals and poor metabolic capacity (Jin et al., 2018). Compared with other remediation technologies, phytoremediation is a more green and environmentally friendly remediation technology. Phytoremediation is a sustainable *in situ* soil treatment technology (Amanullah et al., 2016) and can be applied in combination with other remediation technologies to significantly improve the performance of heavy metal pollution treatment (Khalid et al., 2016). Phytoremediation is a technical method to remove heavy metals from polluted soil by using the physical and chemical action of plants, which can effectively reduce secondary pollution and improve the physical, chemical, and biological environment of polluted soil. Plant-enhanced remediation technology can obtain higher remediation efficiency by increasing plant biomass or increasing the content of heavy metals in plants. Furthermore, chelating agents can change the growth state, biochemical characteristics, and resistance mechanism of plants and promote the absorption and enrichment of heavy metals in polluted soil. Therefore, plant chelator–combined remediation technology is widely used in the plant extraction and enhancement process of heavy metal-contaminated soil and has broad application prospects (Komarek et al., 2007). Natural chelating agents mainly refer to low-molecular-weight organic acids, such as citric acid, tartaric acid, and oxalic acid. They are biodegradable and environment-friendly and are considered to have strong application potential in the phytoremediation of heavy metal-contaminated soil (Chen et al., 2020). For instance, Huang et al. (2008) studied the removal effect of citric acid, oxalic acid, and acetic acid on heavy metals such as CD and Pb in sludge and analyzed the morphological changes and bioavailability of heavy metals in sludge. Their results showed that the removal rate of heavy metals in sludge increased with the increase of reaction time and acid concentration, and the concentration of exchangeable heavy metals increased in varying degrees. Inge and Hans (2000) investigated the effects of citric acid and arginine on the adsorption of heavy metal nickel in soil at 0.5 and 5 mmol/L. Their results showed that both of citric acid and arginine combined with nickel resulted in the formation of metal complexes. Yang and Liao (2010) used citric acid, oxalic acid, and tartaric acid to leach heavy metals to pollute farmland soil. Results showed that the three acids had good extraction effects on heavy metals such as Cd, Pb, copper, and zinc in soil. The effective components of heavy metals (Li et al., 2017) can react with the substances in the soil, and the reaction products with different form can change the physicochemical properties of soil and subsequently affect plant growth. Therefore, it is crucial to understand the form of the reaction products for the heavy metal remediation of soil (Abhishek et al., 2018). Organic acid is a natural chelating agent that can be electrically adsorbed, complexed, and chelated with heavy metals to improve their bioeffectiveness, which is very helpful in remediation of soil heavy metal pollution (Li et al., 2017; Ye et al., 2018).

In the present study, the Pb soil contamination was simulated using reclaimed soil from the mining area of Huainan City (China). The effect of exogenous heavy metals and endogenous organic acids on the form, morphology, and migration of Pb in reclaimed soil was investigated. The methodology and outcomes of the present study provide insights on the reclamation and management of heavy metal pollution in mining area.

2 MATERIALS AND METHODS

2.1 Sample Collection and Processing

The soil used for analysis was collected from the surface layer (0–20 cm depth) of reclaimed soil in the Panyi mine reclamation area of Huainan City, China. The soil samples were spread evenly in an air-drying tray, and then biological matter, debris, gravel, and other impurities were removed before the soil samples were placed in a well-ventilated place to dry naturally without exposure to direct sunlight. The air-dried soil samples were ground and passed through an 18-mesh sieve and then stored for later use.

2.2 Experimental Procedure

2.2.1 Analytical Methods and Instruments

The basic physical and chemical properties of soil were determined according to the standard methods specified for standardized soil analysis technology method (Zha, 2017). Allosteric Pb in reclaimed soils was determined by triple acid wet digestion (HF-HNO_3-$HClO_4$). A modified version of the Tessier five-step continuous extraction method (Qian et al., 2011) was used to extract the different forms of Pb present in contaminated soil, including the following: exchangeable (F1), carbonate bound (F2), iron and manganese oxide bound (F3),

TABLE 1 | Tessier continuous extraction method.

Heavy metal form	Extractant	Operating conditions
1. Exchangeable	8 ml 1 mol/L $MgCl_2$ (pH = 7.0)	Vibrate for 1 h at room temperature
2. Bound to Carbonate	16 ml 1 mol/L NaAc (pH = 5.0)	Shake at room temperature for 5 h
3. Bound to Iron and Manganese Oxide	16 ml 0.04 mol/L $NH_2OH{\cdot}HCl$ (25% HAc)	(96 ± 3) °C water bath intermittently shake for 6 h
4. Bound to Organic Matter	3 ml 0.01 mol/L HNO_3 5 ml 30%H_2O_2(pH = 2)	(85 ± 2)°C water bath extraction for 5 h, and finally add NH_4Ac to prevent re-adsorption and shake for 30 min
5. Residual	HF-HNO_3-$HClO_4$	Completely dissolve

TABLE 2 | Concentration of organic acids added.

Types of organic acids	Molecular formula	Molecular weight	Add concentration (mmol/L)		
Citric acid	$C_6H_8O_7$	192.14	0	1	10
Malic acid	$C_4H_6O_5$	134.09	0	1	10

organic matter bound (F4), and residual (F5). The extraction process is shown in **Table 1**. The Pb fraction in the test solution was measured via inductively coupled plasma mass spectrometry (ICP-MS; PE NexION 300).

2.2.2 Preparation of Pb-Contaminated Soil

According to the Chinese National Soil Environmental Quality Agricultural Land Soil Pollution Risk Control Standards (GB 15618-2018), five pollution concentration gradients were applied. First, different concentrations of $Pb(NO_3)_2$(GR) aqueous solution were added to the soil samples, resulting in Pb concentrations in the simulated contaminated soil of 0, 100, 200, 400, and 800 mg/kg, with the water-holding capacity maintained at 40–60%. Simulated samples were placed in an artificial climate incubator (RCX-180F) in simulated sunlight and maintained for 7 days at 25°C; then, the final Pb-contaminated soil was air-dried.

2.2.3 Organic Acid Addition Experiment

First, the effect of low-molecular-weight organic acid type and concentration on the Pb form in soil was assessed by adding different concentrations of citric acid and malic acid to the prepared soil samples, as shown in **Table 2**. The samples were collected after 7 days of incubation at 25°C and then air-dried and sieved. All samples were prepared in triplicate.

Second, the effect of low-molecular-weight organic acids on the form of Pb in soil was assessed under different incubation duration conditions. A 400 mg/kg sample of 20 g Pb-contaminated soil was combined with 12 ml of 10 mmol/L citric acid or malic acid, as shown in **Table 2**. Spiked soils were incubated for 30 days at 25°C and then air-dried and sieved before being preserved, with samples collected at intervals of 1, 3, 5, 7, 15, and 30 days. The collected soil samples taken out are air-dried and sieved. All samples were prepared in triplicate.

2.3 Quality Control and Data Processing Methods

The acids used were all of superior purity, and other chemical reagents were all of analytical purity. The heavy metal (Pb) standard stock solution was prepared from plumbum nitrate ($Pb(NO_3)_2$)(GR) (1,000 mg/L).

The relative deviations were between −2.12 and 2.28% for the calibration of all-state Pb fraction in the simulated Pb-contaminated soil, as shown in **Table 3**.

The data obtained from experiments were organized in Excel 2019, and graphs were prepared using Origin2021 software.

3 RESULTS AND ANALYSIS

3.1 Physicochemical Properties of Soils in Coal Mine Reclamation Areas

Analyzing the data in **Table 4** and **Table 5**, and comparing them with the nutrient grading standard of the second national soil census (Guo et al., 2020), it can be seen that the average pH value of the soil in the reclaimed area of Panyi mine is 7.80, which is alkaline. The mean value of soil bulk weight is 1.33 g/cm^3, which is on a too tight level. The average value of organic matter fraction is 4.13 g/kg, which is at the level of 6 (extreme deficiency). The average value of quick-acting potassium fraction was 191.03 mg/kg, suggesting a high level of grade 2. The average value of effective phosphorus fraction was 10.41 mg/kg, which is in the middle to upper level of 3. The average value of alkaline nitrogen fraction is 28.98 mg/kg, which is a very low level of grade 6. The soil in the reclamation area is affected by artificial filling and reclamation activities. Soil in the reclamation area was affected by artificial filling and reclamation activities, which disturbed the original soil sequence, and mechanical rolling caused by engineering construction, resulting in tight surface

TABLE 3 | Fraction and deviation of Pb in the simulated soil.

Measurement objects	Simulation of the predicted concentration of Pb-contaminated soil (mg/kg)	Measured mean all-state Pb fraction (mg/kg)	Relative deviation (%)
A	100	102.03	2.03
B	200	197.70	−1.15
C	400	409.11	2.28
D	800	783.04	−2.12

TABLE 4 | Nutrient classification standard of the second national nutrient census.

Level	Organic matter (g/kg)	Quick-acting potassium (mg/kg)	Available phosphorus (mg/kg)	Hydrolyzable nitrogen (mg/kg)
Level 1	>40	>200	>40	>150
Level 2	30–40	150–200	20–40	120–150
Level 3	20–30	100–150	10–20	90–120
Level 4	10–20	50–100	5–10	60–90
Level 5	6–10	30–50	3–5	30–60
Level 6	<6	<30	<3	<30

TABLE 5 | Physicochemical properties of soils in reclaimed areas.

Capacity (g/cm^3)	pH	Organic matter (g/kg)	Quick-acting potassium (mg/kg)	Available phosphorus (mg/kg)	Hydrolyzable nitrogen (mg/kg)
1.33	7.80	4.13	191.03	10.41	28.98

soil bulk density, and the soil nutrients, except for the high fraction of fast-acting potassium and effective phosphorus, are all at very low levels.

3.2 Pb Form Distribution in Soil Contaminated by Exogenous Pb

The form distribution pattern of Pb in soil contaminated with increasing concentrations of exogenous Pb, is shown in **Figure 1**. It can be seen from **Figure 1** that the main form of Pb in the original soil sample (prior to the addition of exogenous Pb) is the residual-state Pb, accounting for 56.08% of the total Pb concentration. The second most abundant form in the original sample was the organic-combined state, which accounts for 24.88% of the total Pb concentration, with the remaining fraction being in an exchangeable state (0.00%), carbonate-combined state (0.11%), and iron–manganese oxide-combined state (18.93%). With the addition of exogenous Pb, the percent fraction of Pb form in the soil has changed, and the fraction of Pb in the iron–manganese oxide-combined state gradually increased from 18.93% in the original soil to 44.13%, becoming the main form of Pb in the soil. This is because of the fact that exogenous Pb entered the soil and adsorbed to the surface of soil particles, and it gradually transformed to stable forms such as the

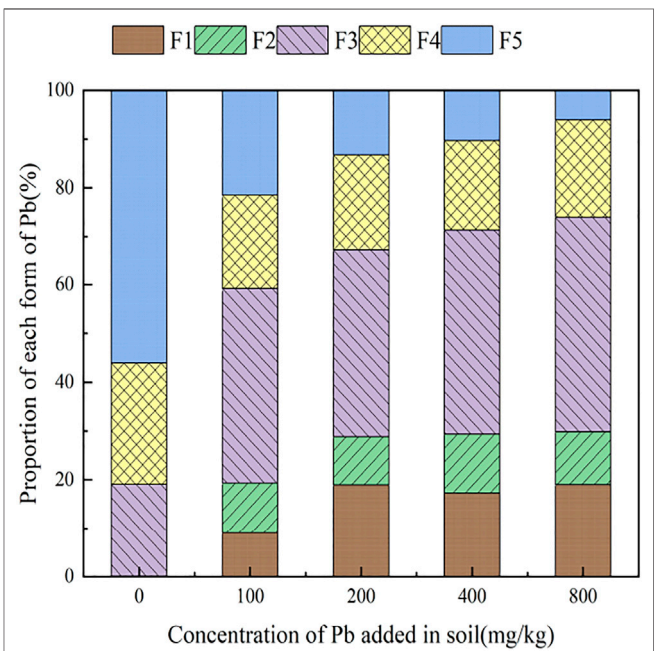

FIGURE 1 | The distribution of Pb form in the soil after adding exogenous Pb.

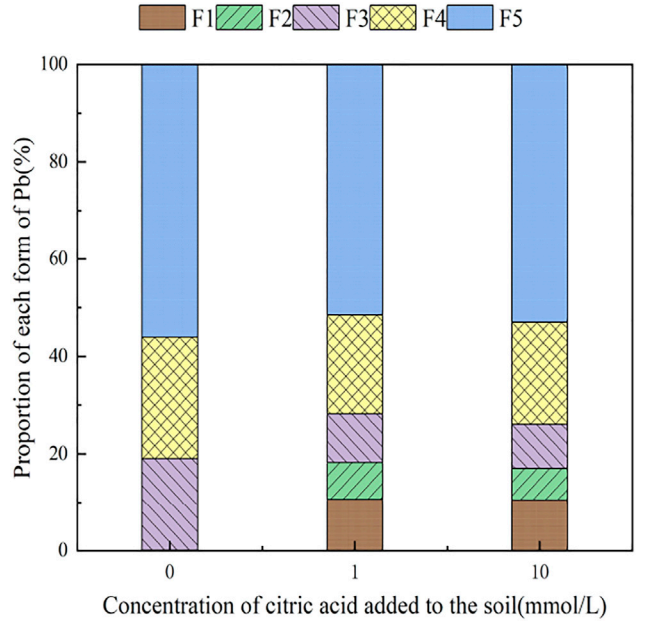

FIGURE 2 | Distribution of Pb in the original soil after adding citric acid.

iron–manganese oxide-combined state as the contact time with soil was prolonged. The exchangeable and carbonate-combined Pb first increased slightly and then remained unchanged, and the fraction of organic-bound Pb remained relatively unchanged. With the increase of exogenous Pb concentration, the residual-state Pb fraction gradually decreased from 56.08 to 6.04% in the original soil. This is because of the fact that the residual-state Pb is chemically stable, its formation process is calculated by geological age, and its mass fraction is not easily affected by external environmental changes, with the percentage of Pb fraction decreasing when the total amount of Pb increases. It can be seen that the addition of different concentrations of exogenous Pb to the soil can significantly change the distribution of each form of Pb in the original soil, which indicates that the form of Pb in the soil is equally affected by the total amount of Pb and the concentration of exogenous Pb.

3.3 The Influence of Organic Acids on the Form of Pb in Soil

3.3.1 The Effect of Citric Acid on the Form of Pb in Soil

With the addition of different concentrations of citric acid, changes were observed in the distribution of Pb in the soil, as shown in **Figure 2**. As the concentration of citric acid increased, the fraction of exchangeable Pb and carbonate-bound Pb gradually increased, with their relative proportion in soil increasing from 0.00 and 0.11% to 0.49 and 6.5%, respectively. The proportion of iron–manganese oxide-combined state and organic-combined state Pb decreased gradually from 18.93 and 24.88% to 9.09 and 20.92%, respectively. The residual state remained largely unchanged owing to its high stability in the environment.

Figures 3–6 illustrated the changes in the form of Pb in contaminated soil with the addition of different concentrations of citric acid. It can be seen that as the concentration of citric acid increased, the exchangeable Pb fraction gradually increased. The effect was especially visible in the 400 mg/kg Pb-contaminated soil, in which the exchangeable Pb fraction increased from 17.22 to 36.57%. The addition of citric acid to the soil was beneficial to increase the solubility and mobility of heavy metals in the soil. The carbonate-bound state Pb fraction did not change significantly and showed a slight increasing trend. The addition of 10 mmol/L citric acid to 400 mg/kg Pb-contaminated soil decreased the iron–manganese oxide-combined Pb fraction from 40.02 to 25.80%, which is because of the fact that the iron–manganese oxide-combined Pb fraction is susceptible to changes in soil pH. pH affects the mobility and biological effectiveness of heavy metals in soil. The addition of organic acids led to a decrease in soil pH, which increased the solubility of Pb and contributed to the conversion of the iron–manganese oxide-bound state to the exchangeable state, increasing its effectiveness (Zhang et al., 2008). The organic-bound Pb and residue Pb fraction did not change significantly because the organic-bound state is generally released only under strong oxidation conditions, while the residual state is generally present in the soil lattice of silicates and primary and secondary minerals, which are chemically stable and not easily affected by the external environment (Zheng et al., 2022).

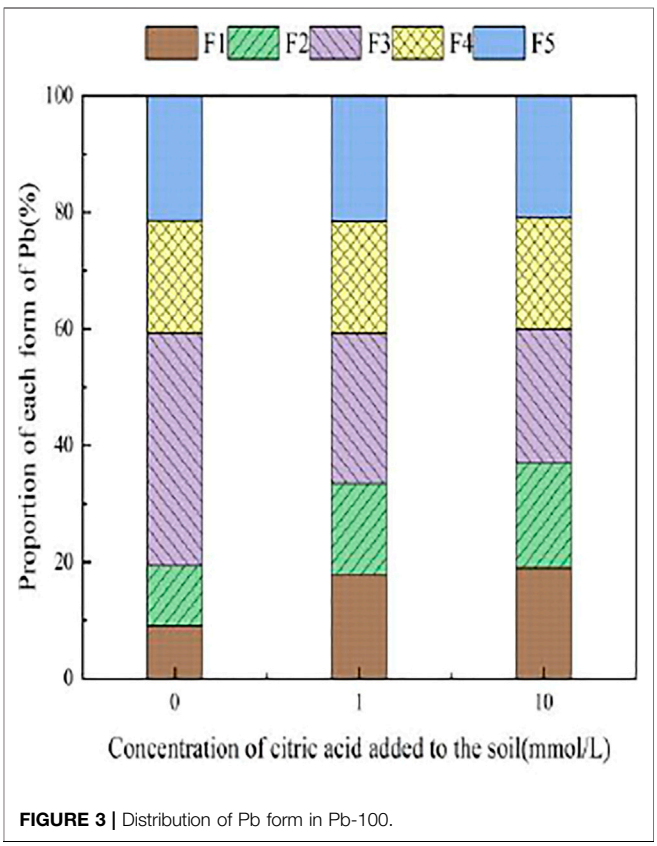

FIGURE 3 | Distribution of Pb form in Pb-100.

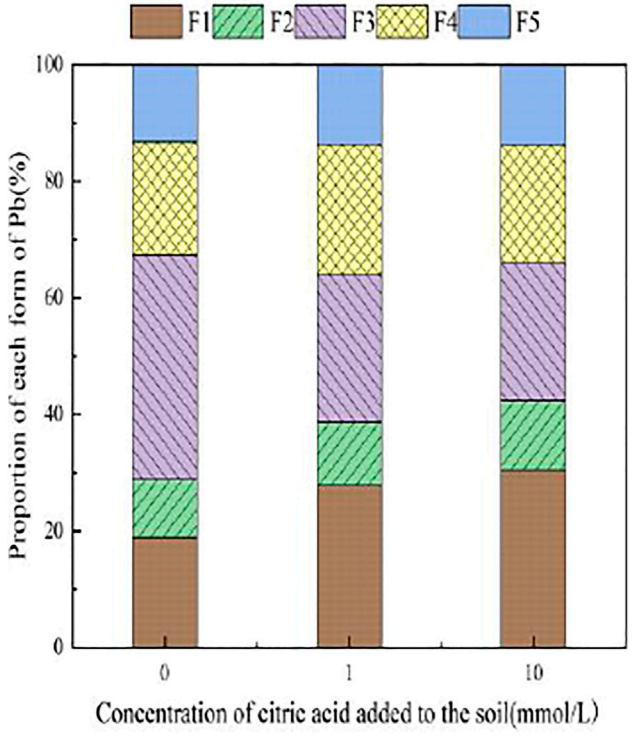

FIGURE 4 | Distribution of Pb form in soil after adding citric acid and Pb-200 soil after adding citric acid.

3.3.2 The Effect of Malic Acid on the Form of Pb in Soil

Figure 7 presents the changes in Pb form with the addition of different concentrations of malic acid to soil. As shown, the addition of malic acid induced a downward trend in the proportion of iron–manganese oxide-bound Pb and organic-bound Pb, from 18.93 and 24.88% to 11.14 and 20.18%, respectively, with the observed change being approximately proportional to that induced by citric acid. The exchangeable Pb and carbonate-bound Pb contents gradually increased with increasing organic acid concentration, from 0.00 and 0.11% to 10.87 and 7.5%, respectively, with relatively similar increases compared to citric acid. The change in the residual-state Pb fraction was not significant.

With the addition of different concentrations of malic acid, the changes in the form of Pb in contaminated soil are shown in **Figures 8–11**. It can be seen that in Pb-contaminated soil, the addition of malic acid plumbum resulted in a sharp increase in exchangeable Pb. For example, in 400 and 800 mg/kg Pb-contaminated soil, the exchangeable Pb fraction increased from 17.22 and 18.96% to 34.66 and 29.12%, exhibiting an increase of 101.28 and 53.59%, respectively. Compared with that because of the addition of citric acid, the increase in exchangeable Pb because of the addition of malic acid was slightly lower, as was the overall activation effect. Carbonate-bound Pb exhibited an increasing trend from 10.34 to 15.99% in soil polluted with 100 mg/kg Pb, which was the largest increase induced by malic acid (54.64%). The growth rate of citric acid under the same conditions was 74.56%. The results of comparison indicate that citric acid activation of Pb was more effective than that of malic acid, which is consistent with the results of Qian et al. (2011). The iron–manganese oxidation state Pb fraction in contaminated soil gradually decreased with increasing malic acid concentrations, exhibiting a reduction from 42.02% in the original soil to 29.21% in the 400 mg/kg Pb sample, which was the maximum observed reduction of 67.82%. Previous research by Zheng and Zhu (2009) demonstrated that the addition of chelating agents such as EDTA, EDDS, and organic acids to soil can reduce the fraction of iron–manganese oxidation state Pb, increase the activity of Pb, and promote its conversion to exchangeable Pb. A study by Liu M.L. et al. (2018) also pointed out that high concentrations of organic acids promoted the desorption of Pb from soil. Except for the 200 mg/kg Pb treatment, the fraction of organically bound Pb increased slightly with the addition of malic acid, while the proportion of other Pb fractions decreased slightly. The residual Pb fraction did not change significantly with the addition of malic acid.

3.4 The Influence of Organic Acids on Dynamic Changes in Pb Form in Soil

During the 30 days of soil incubation experiment, the change in Pb fractions in soils under the influence of the two organic acids is shown in **Figures 12**, **13**. With the addition of citric acid and malic acid, extended incubation time resulted in an increasing trend of exchangeable Pb fraction exhibited, followed by a decrease until equilibrium is reached. With the addition of

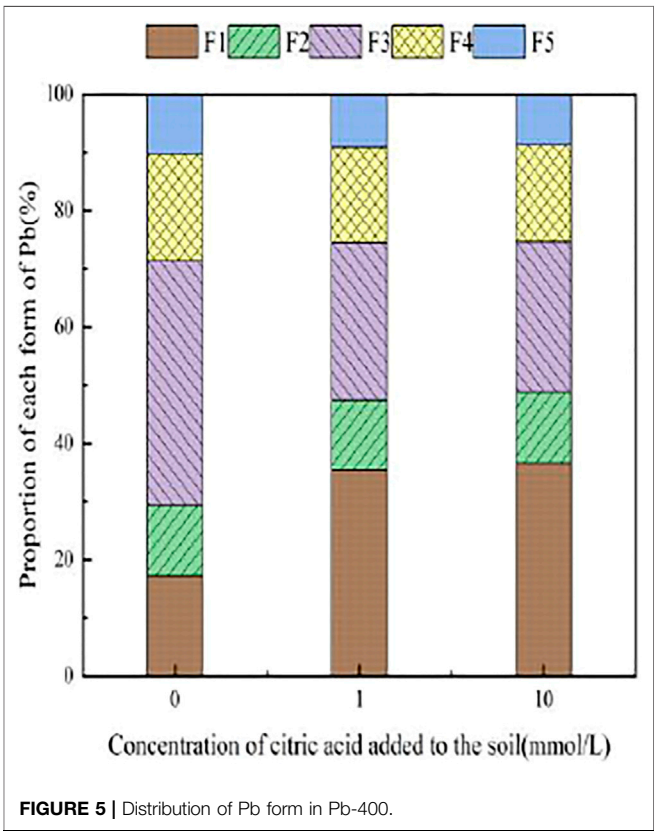

FIGURE 5 | Distribution of Pb form in Pb-400.

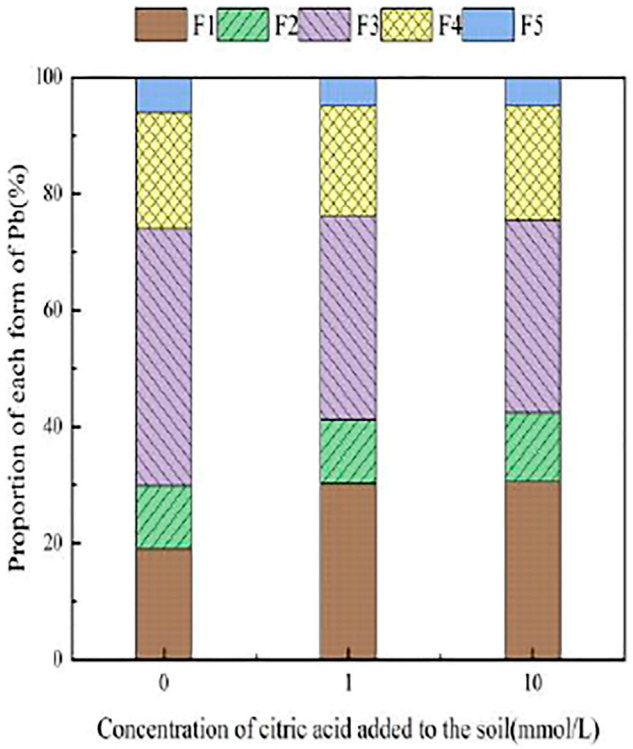

FIGURE 6 | Distribution of Pb form in soil after adding citric acid and Pb-800 soil after adding citric acid.

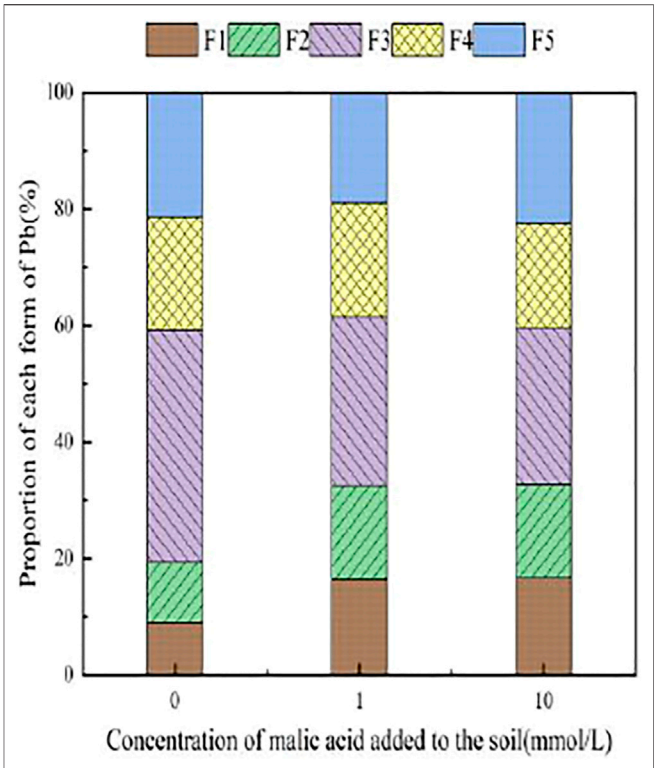

FIGURE 8 | Distribution of Pb form in Pb-100.

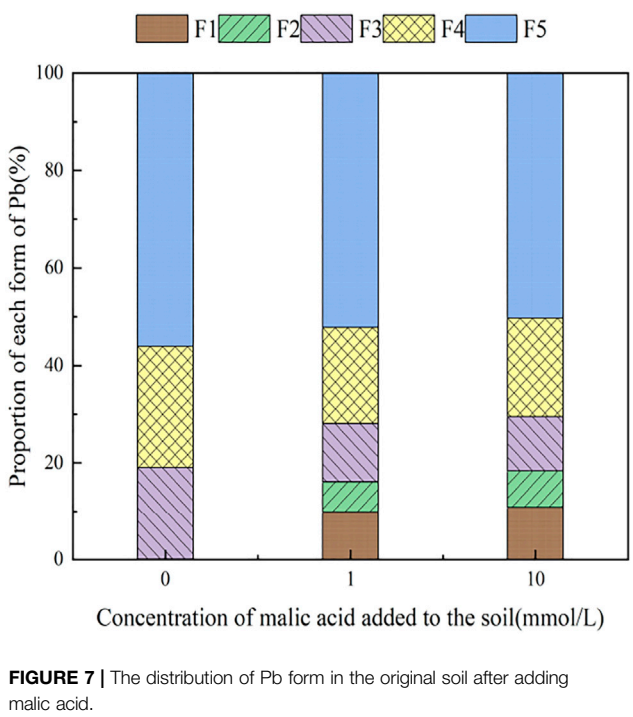

FIGURE 7 | The distribution of Pb form in the original soil after adding malic acid.

citric acid, the fraction of proportion of exchangeable Pb increased from 28.36% on the first day and reached 36.57% on the seventh day and then gradually decreased with time. By the 30th day, the fraction of exchangeable Pb decreased to 34.61%, reaching a balanced state. With the addition of malic acid, the trend in change of exchangeable Pb was similar, with the exception of that on the seventh day, as the fraction of exchangeable Pb was only 34.66%, which is lower than that of the addition of citric acid. The difference of activation effects between citric acid and malic acid occurred because the reaction between organic acids and heavy metals is related to the number and position of carboxyl and phenolic groups in the lower-molecular-weight organic acids (Liu, 2011). Citric acid is a tricarboxylic acid, while malic acid is a dicarboxylic acid, and the stability constants of citric acid and the formation of complexes are greater than those of malic acid. The solubility of organic acids for heavy metals also depends on the solubility constant of the organic acid itself, which is higher for citric acid (7.1×10^{-4}) than for malic acid (3.9×10^{-4}) (Fan et al., 2008), so the activation ability of citric acid for Pb is stronger than that of malic acid, which is basically consistent with the results of Zheng and Zhu (2009).

The change of the carbonate-bound state Pb presented a similar pattern to that of the exchangeable-state Pb, with a trend of increasing and then decreasing percent fraction with

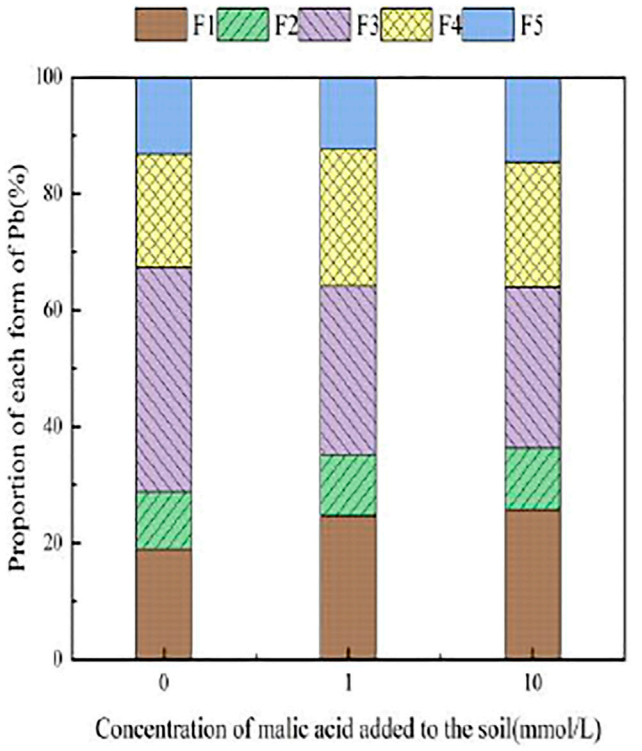

FIGURE 9 | Distribution of Pb form in soil after adding malic acid and Pb-200 soil after adding malic acid.

time. However, the change of the carbonate-bound state Pb and the exchangeable-state Pb was flat, fluctuating up and down approximately 11%, and there was little difference between the effects of citric acid and malic acid. The oxidation state of iron–manganese-bound Pb decreased significantly and reached its lowest point approximately 15 days with 25.39% (citric acid) and 27.55% (malic acid), and increased again to 26.41% (citric acid) and 28.48% (malic acid) by 30 days. The increase of corresponding values was the main contribution to the transformation of active state. The organic bound state of Pb did not change significantly during the first week of soil incubation, but slowly increased from 16.62 and 15.71% to 18.61% (citric acid) and 18.41% (malic acid) from 7 days onward. The residue state did not change significantly with the increase of incubation time. From the above trends of various forms of Pb, it is indicated that after the exogenous heavy metal Pb enters the soil medium in water-soluble form, there is an obvious aging process, i.e., the process of transformation from a more active form to a more stable form, which is basically consistent with the findings of Gleyzes et al. (2022).

4 DISCUSSION

The physicochemical properties of reclaimed areas of reconstituted soils have been significantly changed. The soils were anthropogenically disturbed, mutable, and susceptible to environmental factors (Zhang et al., 2018). The addition of exogenous Pb and different types and concentrations of organic acids to the soil resulted in changes in the fraction, morphology, and biological activity of elemental Pb in the soil. The main form of Pb observed in the original reclaimed soil was residual-state Pb with less toxicity, which is chemically stable and hardly affected by environmental conditions. With the addition of exogenous Pb, the Pb in the soil changes from a residual state to an exchangeable state and a combined state with iron and manganese oxides. This reduced the relative proportion of residual Pb and increased the available fraction of active and mobile Pb in soil, which promoted the overall impact on the environment.

The adsorption–desorption process of heavy metal ions in soil media was affected by the interaction of several factors (soil composition, environmental factors, pollutant composition, etc.) (Zhang et al., 2019). Wang et al. (2017) used soil column simulation to investigate the effect of pH on the adsorption–desorption process of soil media, and the results showed that the adsorption of Pb by soil media fluctuates and increases with increasing pH within a certain range. The addition of organic acids to the soil increased the exchangeable-state Pb fraction and decreased the iron–manganese oxide-combined state in the soil, while other morphological changes were not obvious. The organic ligands dissociated from organic acids are able to interact with heavy metal ions in the soil to form stable complexes, thus altering the migration capacity of heavy metal

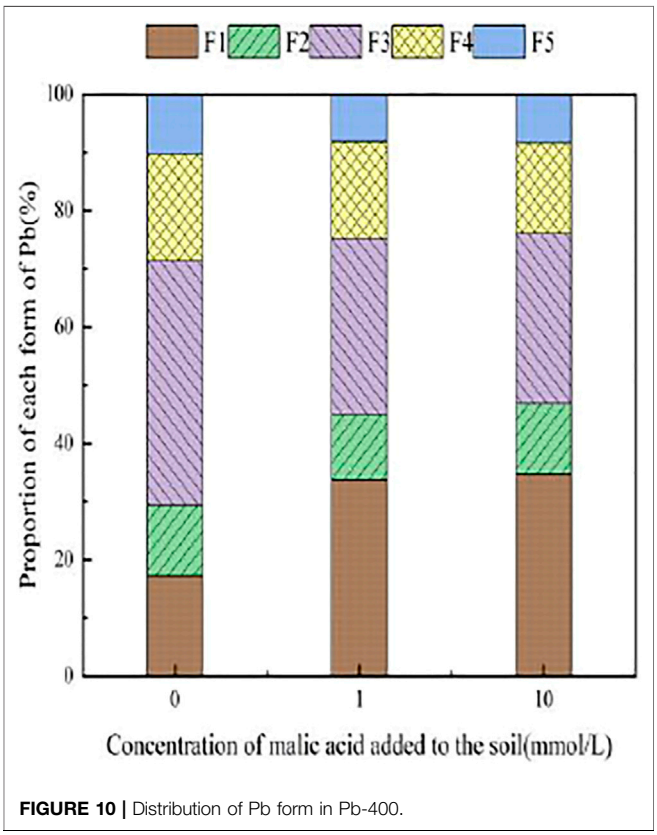

FIGURE 10 | Distribution of Pb form in Pb-400.

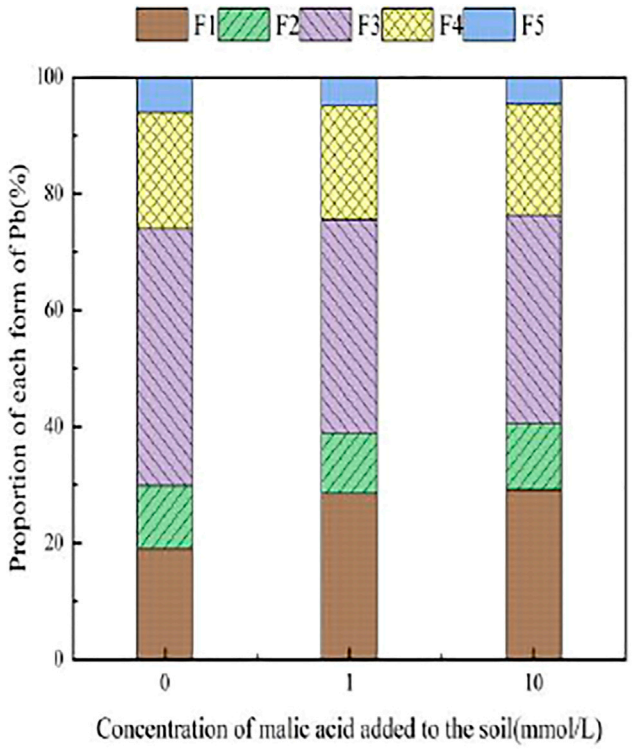

FIGURE 11 | Distribution of Pb form in soil after adding malic acid and Pb-800 soil after adding malic acid.

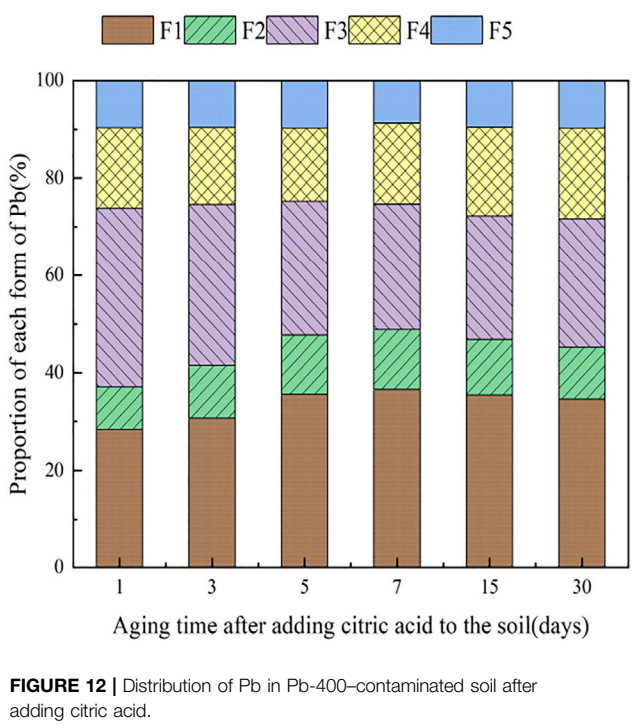

FIGURE 12 | Distribution of Pb in Pb-400–contaminated soil after adding citric acid.

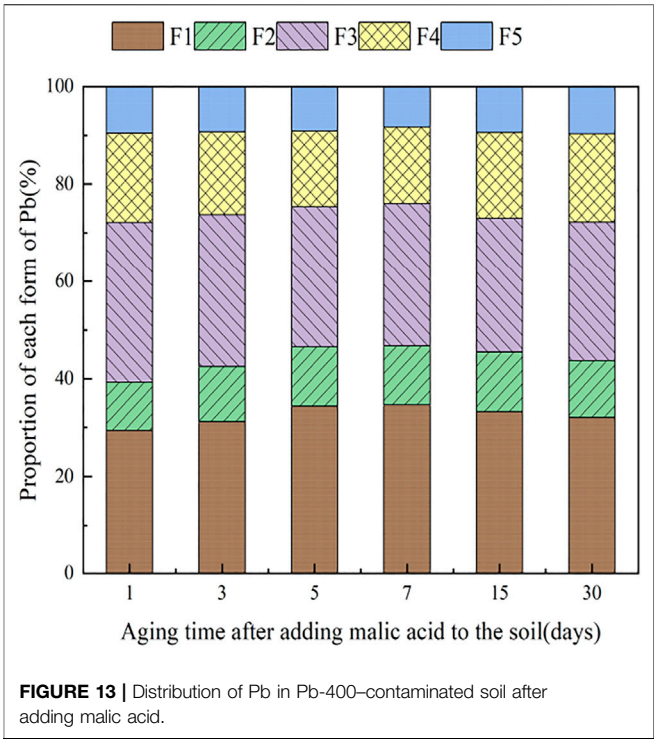

FIGURE 13 | Distribution of Pb in Pb-400–contaminated soil after adding malic acid.

ions (Huang, 2020). Low-molecular-weight organic acids also release more H protons to promote the desorption of heavy metals (Luo, 2016). Citric and malic acids presented similar pattern, whereas the growth rate of exchangeable Pb by adding citric acid was twice as high as that by adding malic acid (in 400 and 800 mg/kg contaminated soils), suggesting that citric acid is more beneficial in activating Pb in soils and increasing its mobility than malic acid. However, the activation effect of a single addition still needs to be improved, so it is very relevant to explore the adoption of a combination of organic acid additions. Liu (2011) added citric acid and malic acid to soil in a combined manner compared to a single addition to activate heavy metal Pb in soil more effectively because, first, the combination of two organic acids can more significantly reduce soil pH and promote the dissolution of solid-phase heavy metals in soil as the H^+ concentration increases; second, the combination of two organic acids added reduces the amount of single organic acids chelating other competitive metal cations, converting the other more stable forms of Pb into the active exchangeable state of Pb, thus more favorable to the uptake of Pb by hyperaccumulating plants.

The topsoil capacity of the reclaimed soil was tight, and the soil nutrients were at very low levels except for quick-acting potassium and available phosphorus. Whereas organic acids are associated with specific physical and biochemical processes, the presence of organic acids changes the physical properties of the soil and may facilitate the uptake of soil nutrients. Related experiments proved (Zhao et al., 2018) that the addition of exogenous low-molecular-weight organic acids to the soil

within a certain concentration range significantly increased the organic matter fraction. Zhang et al. (2019) showed that the addition of low-molecular-weight organic acids in the concentration range of 0–1 mol/L resulted in a significant increase in the available phosphorus fraction of the soil. Therefore, the addition of organic acids to reclaimed soils not only helps enhance the activity of Pb in the soil but also increases the soil organic matter fraction and promotes the uptake of soil nutrients.

5 CONCLUSION

Changes in the form of Pb in soil are affected by the addition of exogenous Pb, with continuous increases in exogenous Pb concentrations resulting in Pb existing in the form of iron–manganese oxide-combined state > organic-combined state > exchangeable state > carbonate-combined state > residual-state species. The relative proportion of residual-state Pb continuously decreased, while the fraction of iron–manganese oxide-combined Pb gradually increased, becoming the dominant form, which is beneficial for enhanced Pb activity in the soil.

The addition of citric acid and malic acid to soil increased the availability of Pb and as the concentration of organic acids increased, the degree of Pb activation increased accordingly. Citric acid gradually increased both exchangeable Pb and carbonate-binding Pb in the soil, reaching a maximum at 10 mmol/L in group C, while both exchangeable Pb and carbonate-binding Pb increased less than citric acid in the contaminated soil under the influence of malic acid under the same conditions. Comparing the two acids, we found that the overall activation effect of citric acid was stronger than that of malic acid. With extended soil aging times in the presence of citric acid and malic acid, the loosely bound Pb in soil is gradually transformed into strongly bound Pb. Therefore, citric acid, presenting a better activation effect, can be considered as a remediation aid to enhance soil remediation efficiency in the remediation of soil Pb pollution.

DATA AVAILABILITY STATEMENT

The original contributions presented in the study are included in the article/Supplementary Material, and further inquiries can be directed to the corresponding author.

AUTHOR CONTRIBUTIONS

YZ: conceptualization, funding acquisition; investigation; data collection, project administration; resources, writing-original draft and editing, YL: investigation; statistical analysis and writing, review and editing the manuscript. ZZ, YT, WC, CM, FC, and JL: reviewing the manuscript. All authors have read and agreed to the published version of the manuscript.

FUNDING

This research was supported by the National Natural Science Foundation of China (No. 51904014), the Postdoctoral Foundation of Anhui Province (No. 2019B337) and the Institute of Energy, Hefei Comprehensive National Science Center (No. 21KZS217).

ACKNOWLEDGMENTS

The authors appreciate the constructive comments from a reviewer.

REFERENCES

Abhishek, R., Rupali, D., and Sarkar, D. (2018). Heavy Metal Pollution and Remediation. *Green Chem.* 3 (10), 359–373. doi:10.1016/B978-0-12-809270-5.00015-7

Amanullah, M., Wang, P., Ali, A., Awasthi, M. K., Lahori, A. H., Wang, Q., et al. (2016). Challenges and Opportunities in the Phytoremediation of Heavy Metals Contaminated Soils: A Review. *Ecotoxicol. Environ. Saf.* 126, 111–121. doi:10.1016/j.ecoenv.2015.12.023

Chen, L., Yang, J. Y., and Wang, D. (2020). Phytoremediation of Uranium and Cadmium Contaminated Soils by Sunflower Enhanced with Biodegradable Chelating Agents. *J. Clean. Prod.* 263, 121491. doi:10.1016/j.jclepro.2020.121491

Fan, H. L., Wang, X., and Zhou, W. (2008). Effect of Malic Acid and Citric Acid Addition on Cd Transformations in Soil and Cd Uptake in Amaranth. *J. Plant Nutr. Fertilizers* 1, 132–138.

Foulds, S. A., Brewer, P. A., Macklin, M. G., Haresign, W., Betson, R. E., and Rassner, S. M. E. (2014). Flood-related Contamination in Catchments Affected by Historical Metal Mining: An Unexpected and Emerging Hazard of Climate Change. *Sci. TOTAL Environ.* 476-477, 165–180. doi:10.1016/j.scitotenv.2013.12.079

Gleyzes, C., Sylvaine, T., and Michel, A. (2022). Fractionation Studies of Trace Elements in Contaminated Soils and Sediments: A Review of Sequential Extraction Procedures. *Trends Anal. Chem.* 21 (6), 451–467. doi:10.1016/S0165-9936(02)00603-9

Guo, C. J., Sun, Y. T., Li, H. F., Fang, H. L., Yu, Y. C., and Liu, Y. X. (2020). Soil Nutrients Assessment of Ecological Restoration Zone of West Open Pit of Fushun Mine. *J. Shenyang Agric. Univ.* 51 (02), 137–145.

Huang, L., Zhou, Q. X., and Zhang, Q. R. (2008). Removal Effects of Citric Acid, Oxalic Acid and Acetic Acid on Cd, Pb, Cu and Zn in Sewage Sludge. *Ying Yong Sheng Tai Xue Bao* 19 (3), 641–646.

Huang, M. (2020). *Effects of Organic Acids on Cd Migration and Accumulation in Soil-Rice Systems*. China: Central South University of Forestry and Technology.

Inge, F. P., and Hans, C. B. H. (2000). Soil Sorption of Nickel in Presence of Citrate of Arginine. *Water,Air,and Soil Pollut.* 120, 249–259. doi:10.1023/A:1005201925212

Jin, Y. Y., Luan, Y. N., Ning, Y. C., and Wang, L. (2018). Effects and Mechanisms of Microbial Remediation of Heavy Metals in Soil: A Critical Review. *Appl. Sci.* 8 (8), 1336. doi:10.3390/app8081336

Komárek, M., Tlustoš, P., Száková, J., Chrastný, V., and Ettler, V. (2007). The Use of Maize and Poplar in Chelant-Enhanced Phytoextraction of Lead from Contaminated Agricultural Soils. *Chemosphere* 67 (4), 640–651. doi:10.1016/j.chemosphere.2006.11.010

Khalid, S., Shahid, M., Niazi, N., Murtaza, B., Bibi, I., and Dumat, C. (2017). A Comparison of Technologies for Remediation of Heavy Metal Contaminated Soils. *J. Geochem. Explor.* 182 (SIB), 247–268. doi:10.1016/j.gexplo.2016.11.021

Li, W. B., Wang, D. Y., Yu, D., and Liu, S. H. (2017). Comparison Between Distribution Characteristics of Pb and its Bio-Available Transform of Spring and Autumn Soil in Central Jilin Province. *J. Maize Sci.* 25 (01), 69–74. doi:10.13597/j.cnki.maize.science.20170112

Liu, G. H., Ren, J., Hu, G., Qin, S., and Fan, C. W. (2018). Effects of Low Molecular Organic Acids on the Removing of Pb, Cd in Calcareous Soils. *Hubei Agric. Sci.* 57 (06), 43–47. doi:10.14088/j.cnki.issn0439-8114.2018.06.010

Liu, M. L., Jiang, M., Li, B., Chen, J., Zu, Y., and Zhan, F. D. (2018). Research Advances on the Immobilization Remediation of Farmland Soil Cadmium Pollution. *J. Yunnan Agric. Univ. Nat. Sci.* 33 (02), 350–359.

Liu, Y. (2011). Effects of Organic Acids on Heavy Metal Speciation in Soil of Qingdao. *Qingdao Univ. Sci. Technol.* 57 (06), 43–47.

Luo, T. (2016). *Effect of Low-Molecular-Weight Organic Acids on the Mobilization of Cadmium in Different Forms*. China: Jinan University.

Picard, F., and Chaouki, J. (2017). NaClO/NaOH Soil Oxidation for the Remediation of Two Real Heavy-Metal and Petroleum Contaminated Soils. *J. Environ. Chem. Eng.* 5 (3), 2691–2698. doi:10.1016/j.jece.2017.05.005

Pichtel, J., Kuroiwa, K., and Sawyerr, H. T. (2000). Distribution of Pb, Cd and Ba in Soils and Plants of Two Contaminated Sites. *Environ. Pollut.* 110 (1), 171–178. doi:10.1016/s0269-7491(99)00272-9

Qian, Y., Liu, Y., and Peng, X. L. (2011). Effects of Low Molecular Weight Organic Acids on Speciation of Pb in Soil. *J. Soil Water Conservation* 51 (02), 137–145. doi:10.13870/j.cnki.stbcxb.2011.04.004

Shang, Y., and Sang, N. (2021). Pollution Characteristics and Phytotoxicity of Heavy Metals in the Soil Around Coal Gangue Accumulation Area. *Environ. Sci.* 1, 12. doi:10.13227/j.hjkx.202106016

Tomohito, A., Ishikawa, S., Murakami, M., Abe, K., Makino, T., and Maejima, Y. (2010). Heavy Metal Contamination of Agricultural Soil and Countermeasures in Japan. *PADDY WATER Environ.* 8 (3), 247–257. doi:10.1007/s10333-010-0205-7

Wang, J., Xiao, G. J., Bi, J. T., Ma, F., and Han, L. (2017). Effect of High pH Value on Heavy Metal Adsorption and Desorption Process in Saline-alkali Land of Ningxia Yellow River Irrigation Region. *Ecol. Environ. Sci.* 26 (10), 1782–1787. doi:10.16258/j.cnki.1674-5906.2017.10.019

Wang, Y. J., Liu, C., Zhou, D. M., and Chen, H. M. (2014). A Critical View on the Status Quo of the Farmland Soil Environmental Quality in China: Discussion and Suggestion of Relevant Issues on Report on the National General Survey of Soil Contamination. *J. Agro-Environment Sci.* 33 (08), 1465–1473.

Yang, H. L., and Liao, B. H. (2010). Extraction Condition for Heavy Metals from Contaminated Soil by Using Low Molecular Organic Acids. *J. Agro-Environment Sci.* 12, 2330–2337.

Ye, C. J., Wu, J. S., Zhong, B., Chen, J., Guo, J., Xu, M., et al. (2018). Effects of EDTA and Organic Acid on Phytoremediation of Heavy Metal Contaminated Soil by Phyllostachys Edulis. *J. Zhejiang A F Univ.* 35 (03), 431–439.

Zha, T. G. (2017). *Soil Physicochemical Analysis[M]*. BeiJing: China Forestry Publishing House.

Zhang, J. (2019). *Investigation of Heavy Metal Pollution and Form Transformation of Lead in Ion-Type Rare Earth Mining Area*. China: Jiangxi University of Science and Technology.

Zhang, N. Y., Yan, S. D., Li, J., Wang, Y. N., Liu, Y., and Bu, Y. S. (2019). Meta-analysis on the Effects of Low Molecular Weight Organic Acids on Increasing Availability of Soil Phosphorus. *J. Plant Nutr. Fertilizers* 25 (12), 2076–2083.

Zhang, S., Liu, H., Luo, M., Zhou, X., Lei, M., Huang, Y., et al. (2018). Digital Mapping and Spatial Characteristics Analyses of Heavy Metal Content in Reclaimed Soil of Industrial and Mining Abandoned Land. *Sci. Rep.* 8 (1), 17150. doi:10.1038/s41598-018-35624-9

Zhang, X. H., Yang, W. T., Wei, C. C., and Lu, Y. Q. (2008). Development of Rhizosphere Microecology in Heavy Metal Hyperaccumulators. *J. Guilin Univ. Technol.* 28 (04), 548–553.

Zhang, X., Yang, L., Li, Y., Li, H., Wang, W., and Ye, B. (2012). Impacts of Lead/zinc Mining and Smelting on the Environment and Human Health in China. *Environ. Monit. Assess.* 184 (4), 2261–2273. doi:10.1007/s10661-011-2115-6

Zhang, Z., Lu, R., Wu, S. Y., Jia, Z. B., and Wang, N. (2021). Heavy Metal Pollution and Health Risk Assessment of Mine Soil in Yangtze River Economic Belt. *Environ. Sci.* 1, 15. doi:10.13227/j.hjkx.202109102

Zhao, P. Z., Chen, X. W., Yang, X. Y., Qi, S. M., and Wang, E. H. (2018). Relationship between Enzyme Activities and Nutrients of Black Soil Subjected to Low Molecular Organic Acid. *J. Nanjing For. Univ. Nat. Sci. Ed.* 42 (01), 105–112.

Zheng, X. L., and Zhu, K. (2009). The Application of Chelating Agents in the Phytoremediation of Heavy Metal Contaminated Soils. *Environ. Sci. Manag.* 34 (08), 106–109.

Zheng, X. M., and Zhang, S. W. (2017). Pollution Characteristics of Wastewater from Nonferrous Metals Industry in China. *China Manganese Ind.* 35 (03), 142–144. doi:10.14101/j.cnki.issn.1002-4336.2017.03.040

Zheng, Y. H., Zhang, Z. G., Chen, Y. C., An, S., Zhang, L., and Chen, F. (2022). Adsorption and Desorption of Cd in Reclaimed Soil under the Influence of Humic Acid: Characteristics and Mechanisms. *Int. J. Coal Sci. Technol.* 9 (1), 7. doi:10.1007/s40789-022-00480-6

Zheng, Y. H., Zhang, Z. G., Yao, D. X., and Chen, X-Y. (2013). Characteristics of Temporal-Spatial Distribution and Enrichment of Heavy Metals in Coal Mine Reclaimed Soil. *J. China Coal Soc.* 38 (08), 1476–1483. doi:10.13225/j.cnki.jccs.2013.08.033

Zhou, J. J., Zhou, J., and Feng, R. G. (2014). Status of China's Heavy Metal Contamination in Soil and its Remediation Strategy. *Bull. Chin. Acad. Sci.* 29 (03), 315–320.

Zhu, L. J., Cheng, H., Ma, J. F., Kong, Y., Qin, Y., and Komarneni, S. (2020). Decolorization of Methyl Orange by MnO2/organic Acid System: The Role of Mn(III). *Mater. Res. Bull.* 122, 110670. doi:10.1016/j.materresbull.2019.110670

Conflict of Interest: The authors declare that the research was conducted in the absence of any commercial or financial relationships that could be construed as a potential conflict of interest.

Publisher's Note: All claims expressed in this article are solely those of the authors and do not necessarily represent those of their affiliated organizations, or those of the publisher, the editors, and the reviewers. Any product that may be evaluated in this article, or claim that may be made by its manufacturer, is not guaranteed or endorsed by the publisher.

Copyright © 2022 Zheng, Li, Zhang, Tan, Cai, Ma, Chen and Lu. This is an open-access article distributed under the terms of the Creative Commons Attribution License (CC BY). The use, distribution or reproduction in other forums is permitted, provided the original author(s) and the copyright owner(s) are credited and that the original publication in this journal is cited, in accordance with accepted academic practice. No use, distribution or reproduction is permitted which does not comply with these terms.

frontiers | Frontiers in Chemistry

ORIGINAL RESEARCH
published: 22 July 2022
doi: 10.3389/fchem.2022.932133

Ecological Risk Assessment and Influencing Factors of Heavy-Metal Leaching From Coal-Based Solid Waste Fly Ash

Zhiguo Zhang[1,2], Weiqing Cai[1], Youbiao Hu[1], Ke Yang[2][,3], Yonghong Zheng[1,2,4], Chao Fang[1], Chengnan Ma[1] and Yuning Tan[1]*

[1]School of Earth and Environment, Anhui University of Science and Technology, Huainan, China, [2]Institute of Energy, Hefei Comprehensive National Science Center, Hefei, China, [3]State Key Laboratory of Mining Response and Disaster Prevention and Control in Deep Coal Mines, Anhui University of Science and Technology, Huainan, China, [4]National Engineering Laboratory for Protection of Colliery Eco-environment, Huainan, China

OPEN ACCESS

Edited by:
Ugur Ulusoy,
Cumhuriyet University, Turkey

Reviewed by:
Rabia Nazir,
Pakistan Council of Scientific & Industrial Research, Pakistan
Alessandra Zanoletti,
Postdoctoral fellow, Italy

***Correspondence:**
Ke Yang
keyang2003@163.com

Specialty section:
This article was submitted to Green and Sustainable Chemistry, a section of the journal Frontiers in Chemistry

Received: 03 May 2022
Accepted: 22 June 2022
Published: 22 July 2022

Citation:
Zhang Z, Cai W, Hu Y, Yang K, Zheng Y, Fang C, Ma C and Tan Y (2022) Ecological Risk Assessment and Influencing Factors of Heavy-Metal Leaching From Coal-Based Solid Waste Fly Ash. Front. Chem. 10:932133. doi: 10.3389/fchem.2022.932133

In order to promote and broaden the utilization of fly ash as a resource, the fly ash from a 2,660-MW coal-fired power plant in Huainan (China) was investigated. The physical and chemical properties of fly ash were characterized by scanning electron microscopy, energy spectrum analysis, and XRD. The content and different forms of the heavy metals Cd, Cr, Cu, Co, and Ni were determined by acid digestion, oscillation leaching, and Tessier five-step extraction. The effect of pH, temperature, and particle size on the leached amount of heavy metals was studied. Finally, the ecological risk index was calculated for each heavy metal *via* the risk assessment coding (RAC) method and Hakanson ecological risk assessment method, allowing the ecological risk of fly ash to be determined under different environmental conditions. Results showed that the average concentrations of Cd, Cr, Co, and Ni were all below the risk screening values reported for environmental pollutants (pH > 7.5). Under varying pH, temperature, and particle size conditions, the leached amounts (oscillation leaching) were below the soil risk screening values for agricultural land in China. An RAC-Cd value of >50% indicates a high ecological risk, while the RAC values of Co and Ni were between 10 and 30%, indicating a medium ecological risk, and the RAC values of Cr and Cu were <10%, indicating a low ecological risk. With increasing pH, the potential ecological risk index (RI) decreased, with a maximum RI of 59.62 observed at pH 2.8. With increasing temperature, the potential ecological RI increased initially to a maximum of 27.69 at 25°C and then decreased thereafter. With increasing particle size, the ecological RI decreased, with the highest RI of 4.06 occurring at <0.075 mm. The Hakanson ecological RI value was below 150, indicating a slight ecological risk. Therefore, fly ash can be considered as a soil additive and conditioner that is suitable for use in the improvement of reclamation soil in coal mining subsidence areas.

Keywords: coal-based solid waste, fly ash, heavy metals, leaching content, risk assessment

1 INTRODUCTION

China is rich in coal resources and is one of the major coal-producing countries worldwide. Coal is currently the main energy source used in China (Bai et al., 2018; Xie et al., 2019), reportedly accounting for 56.8% of the total energy consumption in China in 2020 (National Bureau of Statistics, 2020). The 2020 Annual Report on the Development of China's Coal Industry states that coal production in China increased from 620 million tons in 1978 to 3.41 billion tons in 2016 and 3.90 billion tons in 2020 (China Coal Industry Association, 2020). It has been estimated that before 2050, the proportion of coal in China's energy structure will remain at about 50%, as the coal-dominated energy structure is difficult to change and coal-based energy is an inevitable choice for national development (Teng et al., 2016; Yuan, 2020). In the process of coal utilization, thermal power generation has the most direct and largest environmental impact (Sahu et al., 2014), with fly ash being a major waste product generated by the combustion of coal in thermal power plants (Nayak et al., 2015).

Fly ash is a non-uniform complex of various minerals, dominated by spherical particles which are mainly composed of sodium, potassium, and calcium aluminum silicate compounds, while also being rich in certain essential elements (such as iron, zinc, manganese, boron, and molybdenum) and toxic elements (such as nickel, chromium, lead, aluminum, and silicon) (Mtarfi et al., 2017; Pandey and Bhattacharya, 2019). At present, the disposal of fly ash by most coal-fired power plants is based on the open-air stacking process, in which fly ash is naturally weathered by the surrounding environment. This process results in the formation of atmospheric dust, which causes air pollution and results in fly ash particles being easily inhaled, presenting a major risk to human health (Liu et al., 2015). In addition, during the open-air stacking process, various substances contained in fly ash dissolve and leach into the surrounding soil and water bodies due to the action of natural factors such as rain, affecting the pH and polluting soils and water bodies (Kostova et al., 2016).

Several studies evaluated the risk of heavy metals by the total concentration of heavy metals in fly ash, but the conclusions were usually inconclusive (Feng et al., 2022; Wang et al., 2022). The characterization of total heavy-metal concentrations in fly ash may indicate elemental enrichment but could not be a good predictor of the availability and toxic behavior of heavy metals in the environment (Pan et al., 2013). In addition, the environmental risk of heavy metals was closely related to their chemical forms, with the soluble and exchangeable fractions of heavy metals also being highly mobile and the residual fractions relatively stable under weathering conditions, rather than being closely related to the total concentration of heavy metals in fly ash (Cai et al., 2019; Liu et al., 2021a). The effective state of heavy metals (water-soluble and exchangeable fractions) under natural conditions is the part that could be easily absorbed and utilized by plants, which can effectively respond to the biological and environmental hazards of heavy metals (Zhang et al., 2022). At present, the mineral phase fugitive morphology of heavy metals in fly ash is mainly based on soil heavy-metal morphology research methods, which include the Tessier method, BCR continuous extraction method, and modified BCR continuous extraction method (Liu et al., 2021b). Among them, the Tessier continuous extraction method is widely used to quantify the different chemically bonded morphologies of heavy metals in sediments. The continuous extraction of fly ash is based on the reaction of fly ash with a sequence of extraction reagents, which contributes to the release of metals from the binding sites (Tessier et al., 1979). Meanwhile, the concentration of leaching of trace heavy-metal elements in fly ash was related to external factors such as pH, temperature, and its own particle size. pH has a direct impact on the solubility of elements and compounds in fly ash. Zhang et al. (2016) studied the effects of different pH conditions on the trace element concentrations in solid waste fly ash effluent, finding that most of the measured heavy metals (such as Cu, Mn, Zn, As, Ag, Cr, Cd, and Pb) followed a cationic leaching pattern, with the concentration of trace elements in the effluent decreasing with increasing fly ash pH. Temperature is also an important factor affecting the leaching of trace elements. Yu et al. (2007) showed that under increasing temperature conditions, Cr dissolution from various types of fly ash increased. However, when the temperature was increased to >40°C, the dissolution of Cr from fly ash stabilized, with no further increase in leaching observed. The size of fly ash particles has also been shown to affect the leaching of elements. Zhou et al. (2015a) investigated the content and morphology of heavy metals in fly ash composed of different particle sizes, finding that volatile metals (such as Zn, Pb, Cu, and Cd) tended to be more abundant in finer particles, resulting in a higher risk to human and environmental health. Furthermore, Tang et al. (2021) also found that heavy metals are more concentrated in finer particulate matter, with the potential ecological risk increasing as the particle size of fly ash decreases. Risk assessment is an important way to evaluate the environmental safety of heavy-metal risks. The current evaluation methods of heavy metals include the single factor index method, the Nemero integrated pollution index method, the ground accumulation index method, the Hakanson ecological risk evaluation method, and the risk assessment code method (Li et al., 2021; Wang et al., 2022; Xu et al., 2022). Among them, the Hakanson ecological risk evaluation method and the risk assessment code method were widely used to evaluate the possible hazards of heavy metals to the environment. Qian et al. (2016) used the Nemerow index to evaluate heavy metals in soil. Furthermore, Tang et al. (2021) used the ecological risk index (RI) to evaluate the risk level of heavy-metal pollution.

At present, fly ash is commonly utilized as an additive to improve soil, with researchers having investigated the physical and chemical properties of the soil before and after treatment, as well as the effect on nutrient indices and beneficial trace element concentrations. However, few studies have investigated the influence of heavy-metal species distribution and abundance or the effect of fly ash's physical and chemical properties on heavy-metal leaching and the subsequent human and ecological risk under varying environmental conditions. In this study, the total amount and morphology of different heavy metals in the ash silo of a coal-fired power plant in Huainan, China, were determined using acid digestion and the Tessier extraction method. The ecological risks posed by heavy metals in fly ash were evaluated using the risk assessment coding (RAC) method and the Hakanson ecological risk index. The aim of this study was

TABLE 1 | Composition and content of surface elements of fly ash.

Element	O	Si	Al	C	Fe	K	Ti	Na	Ca
Mass percentage content (Wt)%	40.65	28.96	21.89	3.31	2.46	1.00	0.65	0.60	0.47
Atomic percentage content (At)%	53.16	21.57	16.97	5.77	0.92	0.53	0.28	0.55	0.25

to provide scientific guidance and a theoretical basis for the application of fly ash in the Lianghuai mining area of Anhui Province, China, for the improvement of reclaimed soil quality in a manner that ensures the safety of both human and environmental health.

2 MATERIALS AND METHODS

2.1 Sample Collection and Pretreatment

Fly ash samples were collected from a large thermal generator in Panji District, Huainan City (Anhui Province, China) with an installed capacity of 2,660 MW, and the annual emission of fly ash is 1.8 million tons. The power plant was a typical pit-mouth power station operated using the "coal-to-electricity integration" model, utilizing coal that mainly originates from the Dingji coal mine, which was constructed at the same time as the power plant. The type of coal used for thermal power generation was mainly gas coal and coking coal.

Once the collected samples were returned to the laboratory, they were dried at 105°C for 24 h and filtered through 200 and 60 mesh sieves to isolate fly ash with particle sizes of <0.075 mm and 0.075–0.25 mm. The different particle size fractions were then stored in sealed bags and labeled for later use.

2.2 Fly Ash Physicochemical Analysis

The N, P, K, and organic matter indicators were measured using the Bao (2000). Fly ash morphological observations and compositional analysis were performed using a scanning electron microscope (FlexSEM 1000, Hitachi) and an energy dispersive X-ray fluorescence spectrometer (IXRF 550i, Hitachi), respectively, while the phase composition of fly ash was determined by X-ray diffraction (XRD-6000, Shimadzu). The available heavy metals were extracted from fly ash with DTPA extractant using a method based on the standard protocol, as described previously (HJ 804–2016), while the Cd, Cr, Cu, Co, and Ni concentrations were measured using an inductively coupled plasma mass spectrometer (ICP-MS) (PE NexION 300X, Perkin Elmer). The total content of heavy metals was determined by treating 0.2 g samples with an HNO_3/$HClO_4$/HF acid mixture at 120°C until digestion was complete and the solution was clear. A modified Tessier five-step sequential extraction method (see **Table 1**) was adopted to fractionate heavy metals into an exchangeable fraction (F1), carbonate-bound fraction (F2), iron-manganese (Fe/Mn) oxide-bound fraction (F3), organic matter/sulfide-bound fraction (F4), and residual fraction (F5) (Lu et al., 2019). After each extraction step, fractions were separated by centrifugation at 3,000 rpm for 30 min, with the supernatant filtered through a 0.45 μM membrane. The residual fraction was also digested and analyzed using the same method. Cd, Cr, Cu, Co, and Ni concentrations in the extracts were determined by ICP-MS. Quality assurance and control were performed using reagent blanks, duplicate sample analysis, and comparison to standard reference soil samples. Statistical data analysis was based on one-way ANOVA by SPSS v.26.0, with Origin 2021 used for plotting images.

2.3 Leaching Behavior

2.3.1 Effect of Different pH Conditions

The fly ash fraction containing particle sizes of <0.075 mm was dried and 20 g was placed in a jar, with two parallel samples prepared in triplicate. Superior grade pure nitric acid and ultrapure water were combined to prepare 100 ml of nitric acid solution at pH 2.8, 3.9, 4.9, 5.7, and 6.8. The mixtures were then shaken for 30 min at 25°C and 180 r/min and filtered through a 0.45 μM microporous membrane for heavy-metal analysis.

2.3.2 Effects of Different Temperatures

The fly ash fraction containing particle sizes of <0.075 mm was dried and 20 g was placed in a jar, with two parallel samples prepared in triplicate for each sample. Samples were combined with 100 ml of ultrapure water and shaken for 30 min at 180 r/min at varying temperatures. According to meteorological data for Huainan (China Weather Network, 2021), the average annual temperature in Huainan ranges from 3 to 29°C, and the temperature in summer reaches 33°C. Therefore, using a temperature-controlled oscillator, the treatment temperatures were set to 0, 10, 15, 20, 25, 30, and 35°C, with the temperature being corrected every 10 min during the experimental period to counteract the influence of ambient temperature. After the oscillation period, samples were removed and left to stand, then filtered through a 0.45 μM microporous membrane prior to analysis.

2.3.3 Effects of Different Particle Sizes

Dried fly ash samples were screened to separate fractions containing particle sizes of <0.075 mm and 0.075–0.25 mm, with 20 g of each particle size fraction placed in a jar (two parallel samples prepared in triplicate) and mixed with 100 ml of ultrapure water. The mixtures were then shaken for 30 min at 25°C and 180 r/min and filtered through a 0.45 μM microporous membrane for heavy-metal analysis.

2.4 Evaluation Methods

2.4.1 Risk Assessment Coding Evaluation Method

The risk assessment coding (RAC) method and the bioavailability coefficient were used to assess the environmental risk for each

TABLE 2 | Physicochemical properties of the fly ash.

Parameter	Value
pH	8.60 ± 0.02
Organic matter (g/kg)	15.93 ± 1.94
Available N (mg/kg)	41.68 ± 1.28
Available P (mg/kg)	15.58 ± 0.23
Available K (mg/kg)	107.48 ± 12.78

sample (Wang et al., 2021), using the following calculation formula:

$$K = \frac{E + C}{Q} \times 100\%, \quad (1)$$

where K is the bioavailability coefficient; E is the heavy-metal concentration in the exchangeable state; C is the heavy-metal concentration in the carbonate binding state; and Q is the total sum of heavy-metal concentration. When the overall K value is less than 1%, it is considered risk-free; while K values from 1 to 10% indicate a low risk; 11–30%, a medium risk; 31–50%, a high risk; and >50%, a very high risk.

2.4.2 Hakanson Ecological Risk Assessment Method

The Hakanson ecological hazard index (*RI*) evaluation method is based on the characteristics of heavy metals and their environmental behavior, considering the content of heavy metals and their ecological and environmental effects, among which the potential ecological hazard index method involves a single pollution coefficient, a heavy-metal toxicity response coefficient, and a single coefficient of potential ecological hazard (Hakanson, 1980), described as follows:

$$E_r^i = T_r^i \frac{C_s^i}{C_n^i}, \quad (2)$$

$$RI = \sum E_f^i, \quad (3)$$

where C_f^i is the single pollution coefficient; C_s^i is the measured concentration of the heavy metal in fly ash; C_n^i is the minimum soil risk screening value for agricultural land in China; E_r^i is the single coefficient of potential ecological risk; T_r^i is the toxic response coefficient for a single pollutant; and E_f^i is the potential ecological risk index.

Hakanson found that the potential toxicity of heavy metals was generally inversely correlated with their abundance while being positively correlated with their rarity. Therefore, according to the E_r^i and *RI* values, the assessed heavy metals were divided into different levels of potential ecological hazard (Qian et al., 2016). The canonical treatment rating for the toxic response coefficient of heavy-metal contaminants was Ni = Cu = Co = 5, Cr = 2, and Cd = 30 (Xu et al., 2008). Therefore, the hazard levels were divided into different degrees, and the relationships between E_r^i, *RI*, and the degree of pollution are shown in **Table 2**.

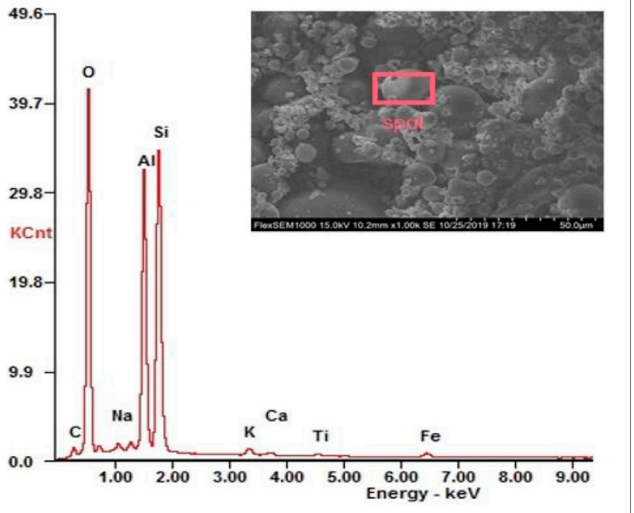

FIGURE 1 | SEM-EDS of fly ash.

3 RESULTS AND ANALYSIS

3.1 Physicochemical Properties of Fly Ash

As shown in **Figure 1**, the fly ash samples consisted of spherical microbeads and porous particles of varying particle sizes, with the surface of spherical beads being relatively smooth compared to the porous particles, which generally had an uneven surface, with some pores and cracks. Furthermore, there were numerous small particles attached to the surface of the spherical microbeads, with small diameter particles aggregating to form large particles. As shown in **Figure 1** and **Table 3**, the surface of fly ash contained 9 elements: O, Si, Al, C, Fe, K, Ti, Na, and Ca, among which the concentrations of O, Si, and Al were relatively high, with the total mass fraction and the total atomic fraction of these three elements accounting for 91.5 and 91.7%, respectively. The EDS results did not show the target heavy-metal elements (Cd, Cr, Cu, Co, and Ni), but these heavy metals could be detected by ICP-MS, which is the same as the results of Zhao et al. (2018) and Fu et al. (2019). This may be due to the fact that EDS is a semi-quantitative analysis, which cannot reflect the overall type and content of heavy metals in the sample. The detection limit of SEM-EDS is generally 0.1–0.5%, which is mainly used for point analysis of the main elements of minerals in geochemical mode, and the detection of heavy metals such as Cd, As, and Pb in the measured objects may not reach the detection limit.

As shown in **Figure 2**, the characteristic peaks of fly ash were mainly derived from the crystalline minerals mullite (M) and quartz (Q), with small amounts of hematite (H), anhydrite (A), and other mineral phases. It was established that the mullite content of fly ash was 67.2% and the quartz content was 8.82%, while hematite accounted for 9.0% and anhydrite for 10.0%. According to the nutrient classification standard of the second soil survey in China (China Soil, 1998), the average organic matter content of the fly ash was 15.93 g/kg (**Table 4**), indicating that the organic matter content was deficient (level

TABLE 3 | Tessier extraction method operation steps.

Steps	Heavy-metal form	Extraction reagents	Extraction conditions
1	Exchangeable fraction (F1)	16 ml 1.0 mol/L $Mgcl_2$	Oscillate at 25°C for 1 h
2	Carbonate-bound fraction (F2)	16 ml 1.0 mol/L NaOAc	Oscillate at 25°C for 5 h
3	Fe/Mn oxide-bound fraction (F3)	40 ml 0.04 mol/L NH_3ClOH	Oscillate at 96°C for 6 h
4	Organic matter/sulfide-bound fraction (F4)	6 ml 0.02 mol/L $HN0_3$	85°C water bath for 2 h
		10 ml 30% H_2O_2	85°C water bath for 3 h
		6 ml 30% H_2O_2	
		10 ml 3.2 mol/L NH_4OAc	Oscillate at 25°C for 0.5 h
5	Residual fraction (F5)	HNO_3 + HF + $HClO_4$	Dissolve to white or yellowish

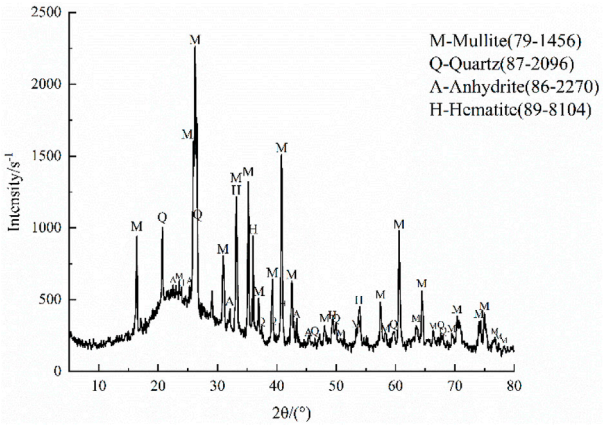

FIGURE 2 | XRD atlas of fly ash.

TABLE 4 | Relationship between E_r^i and *RI* and pollution.

Hazard level	E_r^i	*RI*
Low ecological hazards I	$E_r^i < 40$	$RI < 150$
Medium ecological hazards II	$40 \le E_r^i < 80$	$150 \le RI < 300$
High ecological hazards III	$80 \le E_r^i < 160$	$300 \le RI < 600$
High ecological hazards IV	$160 \le E_r^i < 320$	
Extremely high ecological hazard V	$E_r^i \ge 320$	$RI \ge 600$

four deficiency). The average available nitrogen content was 41.68 mg/kg, corresponding to the maximum deficiency grade of level five. The available phosphorus content was 15.58 mg/kg (medium level), while the average available potassium content of fly ash was high at 107.48 mg/kg (medium level).

3.2 Concentration and Chemical Speciation of Heavy Metals in Fly Ash

A high abundance of heavy metals are attached to the surface of coal during combustion, a large number of which are considered to be toxic and able to be leached from fly ash under atmospheric rainfall or other meteorological conditions, resulting in the pollution of surrounding environments. In this study, the total amount of five harmful heavy-metal elements in different phase fractions was determined, including Cd, Cr, Cu, Co, and Ni.

The heavy-metal content of fly ash is shown in **Table 5**, which was analyzed according to the Chinese soil environmental quality standard (GB15618-2018, 2018), showing that the average content of Cd, Cr, Cu, and Ni was lower than the environmental pollutant risk screening value (pH > 7.5). Both the total amount and the available content of heavy metals in fly ash exceeded the Huainan soil background value, suggesting that fly ash poses a potential risk of heavy-metal contamination.

Figure 3 shows the percentage content of different forms of heavy metals in fly ash, with F1 indicating elements in an exchangeable ionic and water-soluble state, F2 indicating elements in a carbonate-bound state, F3 in an iron-manganese oxide state, F4 in an organically bound state, and F5 in a residual state.

As shown in **Figure 3**, Cd was mainly present in an exchangeable ionic or water-soluble form (43.5%), followed by a carbonate-bound state (30.08%), indicating that a portion of Cd in fly ash migrates easily and presents a high risk of release into the environment. Cr was mainly present in a residual state in fly ash (80.84%), while the content of Cr in the exchangeable state, carbonate-bound state, iron-manganese oxide state, and organic-bound state was 5.63, 3.31, 7.82, and 2.39%, respectively, indicating that Cr is less able to migrate and be converted in the natural environment. Co and Ni were mainly present in fly ash in the residual state, accounting for 68.18 and 67.43%, respectively, followed by the exchangeable state. Therefore, only a small fraction of Co and Ni migrate to the surrounding environment, while Co and Ni in the carbonate-bound state, iron-manganese oxidation state, and organically bound state did not exhibit a significant change, indicating a risk of pollution in the area immediately surrounding the fly ash storage yard. Cu was found to be mainly present in a residual state, an organically bound state, and an iron-manganese oxidation state, with abundances of 79.34, 3.5, and 11.38%, respectively. Cu has a higher boiling point and is entrained in particles with silt during coal combustion, resulting in the Cu mainly existing in a residual state in fly ash. In addition, during the process of weathering, some of the organically bound Cu elements are transferred to the iron-manganese oxide binding state.

Previous research has found that after the addition of fly ash, gangue, and other alkaline substances to the soil, the activity of heavy metals decreases, with their ion-exchange state significantly reduced, while the bound state and residual state of iron and manganese oxides significantly increase, resulting in heavy metals in fly ash being relatively resistant to migration and conversion

TABLE 5 | Comparison of trace heavy-metal content in fly ash and background value of each element (mg/kg).

Metallic elements		Maximum	Minimum	Average	Standard deviation	Coefficient %	Huainan soil (Wei et al., 2017)	GB15618-2018
Cd	Total	0.38	0.24	0.31	0.1	31.93	0.06	0.6
	Available	0.06	0.03	0.04	0.02	38.57		
Cr	Total	129.5	117.6	123.55	8.41	6.81	64.93	250
	Available	2.2	1.5	1.85	0.49	26.76		
Co	Total	31	30.55	30.78	0.32	1.03	10.74	-
	Available	0.45	0.42	0.44	0.02	4.06		
Ni	Total	62.8	60	61.4	1.98	3.22	25.74	190
	Available	0.38	0.35	0.36	0.02	5.47		
Cu	Total	132.6	126	129.3	4.67	3.61	24.16	100
	Available	2.03	1.77	1.9	0.18	9.62		

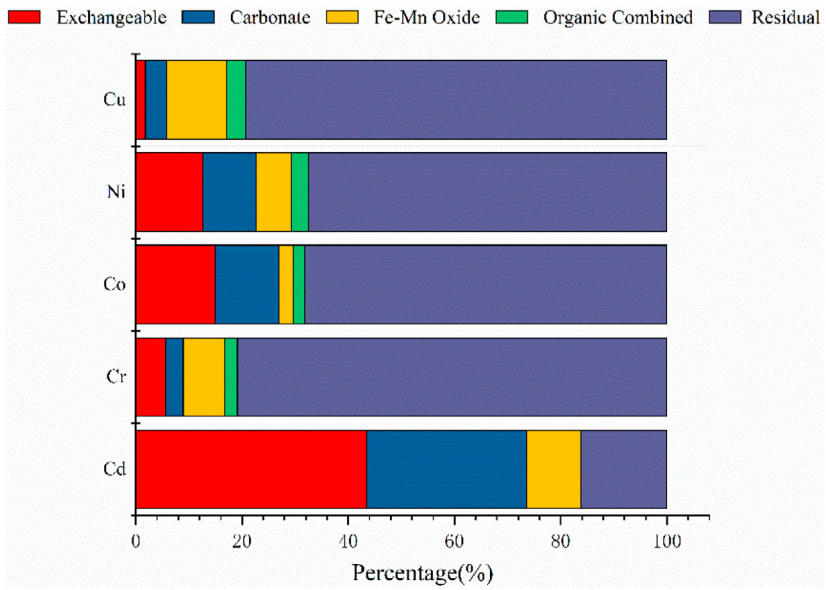

FIGURE 3 | Chemical fractionation of metals in fly ash.

(Garau et al., 2007; Zhou et al., 2015b). The large specific surface area and alkalinity of fly ash contribute to the precipitation of heavy metals (Cho et al., 2005), with higher ratios of fly ash to soil resulting in higher soil pH levels, increasing the immobilization of heavy metals and significantly decreasing the active state content of heavy metals (Cui et al., 2016).

3.3 Main Influencing Factors on Fly Ash Heavy-Metal Leaching

3.3.1 Effect of pH on Fly Ash Heavy-Metal Leaching

Zheng et al. (2022) studies have shown that submersion in different pH level solutions significantly affects the amount of heavy-metal dissolution (Kanokwan et al., 2015; Zheng et al., 2022). **Figure 4A** shows that when the pH was set at 2.8, 4.9, 5.7, or 6.8, Cu leaching was the highest (0.712 mg/kg, 0.411 mg/kg, 0.221 mg/kg, and 0.291 mg/kg, respectively), while at pH 3.9, Ni exhibited the highest level of leaching (0.399 mg/kg). At pH 2.8, the heavy metals Cd, Cr, Cu, Co, and Ni all exhibited significant differences in their leaching behavior. At pH 3.9, Cu, Cr, and Ni did not exhibit significant differences in their leaching behavior, while they were significantly different from Cd and Co. At pH 4.9, 5.7, and 6.8, the leached amount of Cu was significantly different from that of Cd, Cr, Co, and Ni, while at pH 4.9, Ni leaching differed significantly from Cd, Cr, and Co.

As can be seen from **Figure 4B**, the leaching of heavy metals shows a gradual trend of reduced leaching as the pH changes from acidic to neutral, which is consistent with the previous findings of Zhang et al. (2016). Most fly ash contains crystal phases of quartz and mullite, with particle surfaces usually covered with a higher abundance of amorphous silicates and a lower abundance of amorphous aluminates (Luo et al., 2017).

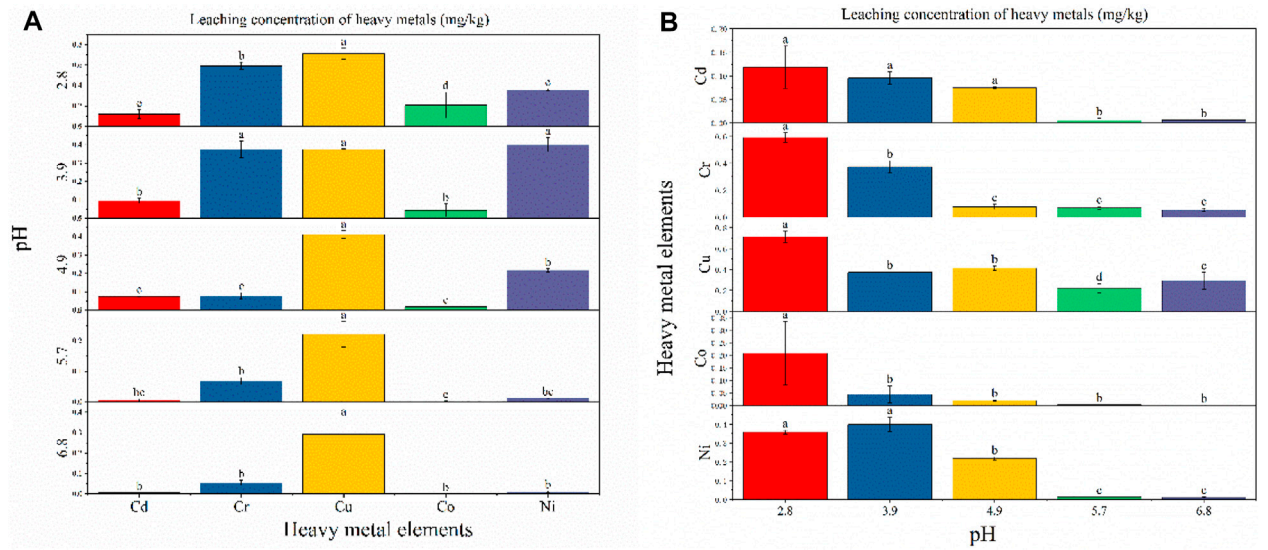

FIGURE 4 | Leaching concentration of heavy metals at different pH conditions: **(A)** difference analysis (Fisher LSD) of different heavy-metal element leaching concentrations under the same pH condition; **(B)** difference analysis of different pH leaching concentrations under the same heavy metal element condition.

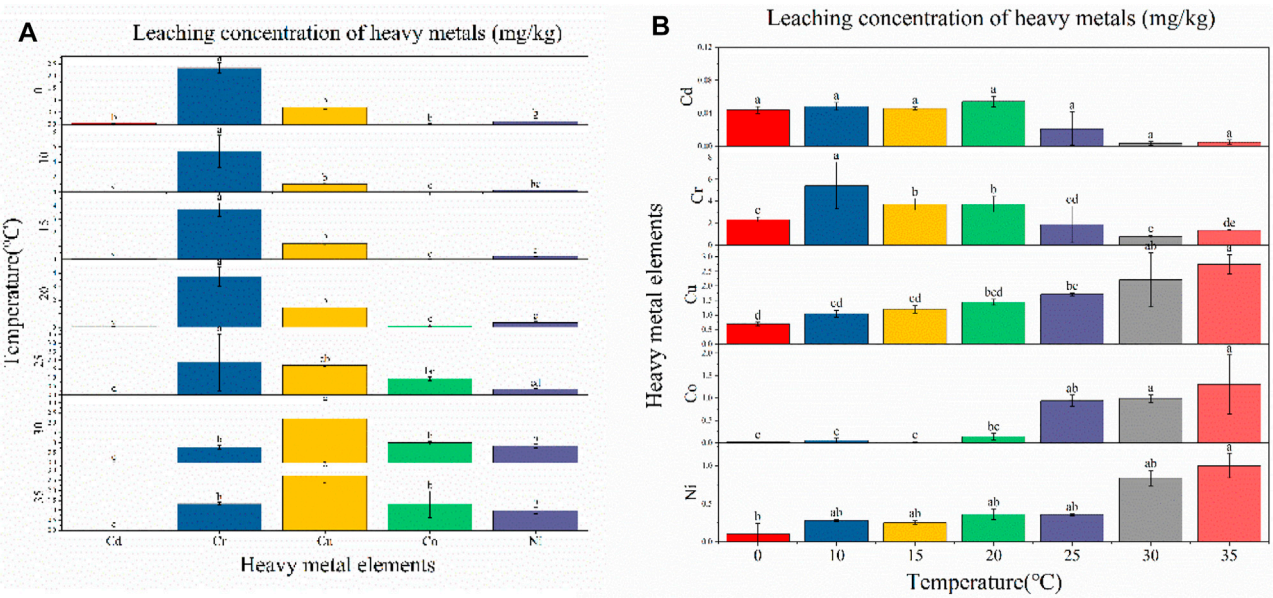

FIGURE 5 | Leaching concentration of heavy metals at different temperature conditions: **(A)** difference analysis of different heavy-metal element leaching concentrations under the same temperature condition; **(B)** difference analysis of different temperature leaching concentrations under the same heavy-metal element condition.

Liu et al. (2020) reported that heavy metals are generally physically adsorbed on the surface of fly ash particles, while some may also be embedded in the amorphous aluminum silicate component. At a low pH, high H^+ concentrations destroy the structure of amorphous aluminum silicate and increase heavy-metal ion leaching. With the change in pH from acidic to neutral, the concentration of H^+ decreased and the amorphous structure gradually stabilized, leading to a decrease in the source of heavy-metal ions and, subsequently, their concentration in the leaching solution. Zhao et al. (2018) found that the leaching solution of fly ash was alkaline, indicating that fly ash leaches alkaline substances and alters the pH of the solution. With the increase in pH, residual alkali components remain in the

leaching solution and the generated OH^- precipitates with heavy metals, resulting in a decrease in the concentration of heavy-metal ions in the leaching solution.

3.3.2 Effect of Temperature on Fly Ash Heavy-Metal Leaching

Experiments showed that the temperature of the leaching solution can have a major influence on the amount of heavy-metal leaching. As shown in **Figure 5A**, at each temperature level, the amount of leaching varied for each heavy metal. At temperatures of 0, 10, 15, 20, and 25°C, Cr exhibited the maximum amount of leaching (2.329 mg/kg, 5.427 mg/kg, 3.708 mg/kg, 3.727 mg/kg, and 1.885 mg/kg, respectively), showing significant differences with Cd, Cu, Co, and Ni at 25°C. At temperatures of 30 and 35°C, Cu leaching was the highest (2.207 mg/kg and 2.739 mg/kg, respectively), exhibiting significant differences compared with Cr, Cd, Co, and Ni.

As shown in **Figure 5B**, different temperatures did not have significantly different effects on the same heavy metal. Cu, Co, and Ni leaching increased with increasing temperature, which was mainly due to higher temperatures promoting the dissolution and diffusion of heavy metals. This conforms to the Einstein–Stokes equation shown in **Eq. 4**, where the diffusion coefficient (D) is proportional to the temperature (T), with higher temperatures increasing diffusion.

$$D = \frac{RT}{6L\pi rn}. \tag{4}$$

However, at temperatures of 0, 10, 15, 20, 25, 30, and 35°C, the leached concentration did not change significantly in the present study, exhibiting a downward trend overall. Pan et al. (2013) show a closer correlation between heavy-metal leaching concentrations and the weakly acid-extracted state (exchangeable and carbonate-bound) fractions. Whereas heavy metals in the weakly acid-extracted state fraction were considered to be weakly bound to fly ash (Kirby and Rimstidt, 1993), which represents a potential bioeffectiveness and leaching capacity. The two fractions of Cd accounted for 74.58% (see **Figure 3**), thus Cd was more easily leached compared to the other four heavy metals, and the total concentration of Cd and the effective concentration of Cd were also less (see **table 5**), leading to no significant change in leaching when the temperature was varied. The leached concentration of Cr showed a significant downward trend over the tested temperature range. To interpret the leaching pattern of Cr in solid fly ash, two factors were taken into account: 1) the ion type in the leaching solution (e.g., metal ions and acid ions) (Yang et al., 2002; Liu et al., 2015); 2) the leaching experiment is a dynamic process of adsorption and desorption (Gupta et al., 1992). Due to the high total concentration and effective concentration of Cr (**Table 5**), the rate of adsorption of the heavy metal Cr by fly ash is lower than the rate of desorption at low temperatures, resulting in Cr being released. At high temperatures, the rate of fly ash adsorption of Cr was higher than the desorption rate, increasing the adsorption of Cr adsorbed on the surface of fly ash and, subsequently, reducing its release. It is also possible that the alkaline substances in fly ash are released slowly with increasing temperature, which increases the concentration of Cr precipitate adsorbed on the surface of fly ash and reduces the concentration of Cr in solution.

3.3.3 Effect of Particle Size on Fly Ash Heavy-Metal Leaching

After continuous weathering of fly ash, particles become looser, and the particle size changes accordingly. As shown in **Figure 6A**, differences were observed in the leaching of heavy metals in each particle size fraction. In the <0.075 mm particle size fraction, the leached concentrations of Cr and Co were 0.317 mg/kg, which were significantly different compared with Cd, Cu, and Ni. The levels of Cd and Ni leaching were minimal and exhibited no significant difference. In the 0.075–0.25 mm particle size fraction, Cr exhibited the largest leaching capacity of 0.299 mg/kg, which was significantly different from the other four metals. Co exhibited the lowest level of leaching at 0.0058 mg/kg, with no significant difference observed compared to Co and Ni, although it was significantly different from Cr and Cu.

As can be seen from **Figure 6B**, the leaching of heavy metals generally showed an upward trend with a decrease in particle size, which is consistent with the results of Zhou et al. (2015a) and Tang et al. (2021). Cd, Cr, Cu, and Ni leaching increased with decreasing particle size, with no significant differences observed among these metals. The leaching of Co increased with decreasing particle size and was significantly different from the other metals. Small-particle fly ash has a large specific surface area and, therefore, allows more heavy metals to adhere to its surface. Conditions with large particle sizes require sufficient diffusion resistance for heavy metals to leach from within, and the concentration of leachable heavy metals is relatively low.

4 ECOLOGICAL RISK ASSESSMENT OF HEAVY METALS IN FLY ASH

4.1 Risk Assessment Coding Evaluation Index

The RAC evaluation index expresses the ecological risks posed by each form of heavy metal to the environment. As can be seen from **Figure 7**, RAC-Cd is greater than 50%, indicating a very high ecological risk impact as Cd will easily migrate and be converted under certain environmental conditions. The RAC values of Co and Ni were between 10 and 30%, indicating a medium risk, while the RAC values of Cr and Cu were less than 10%, which indicates a low risk. This reflects the varying risks posed by these five elements in fly ash, depending on their form and phase, which significantly alter their level of hazard to the environment.

4.2 The Hakanson Potential Ecological Risk Index Evaluation

4.2.1 Hakanson Potential Ecological Risk Index Under Different pH Conditions

In this study, the potential ecological hazard level of fly ash heavy-metal pollution was evaluated using the Hakanson

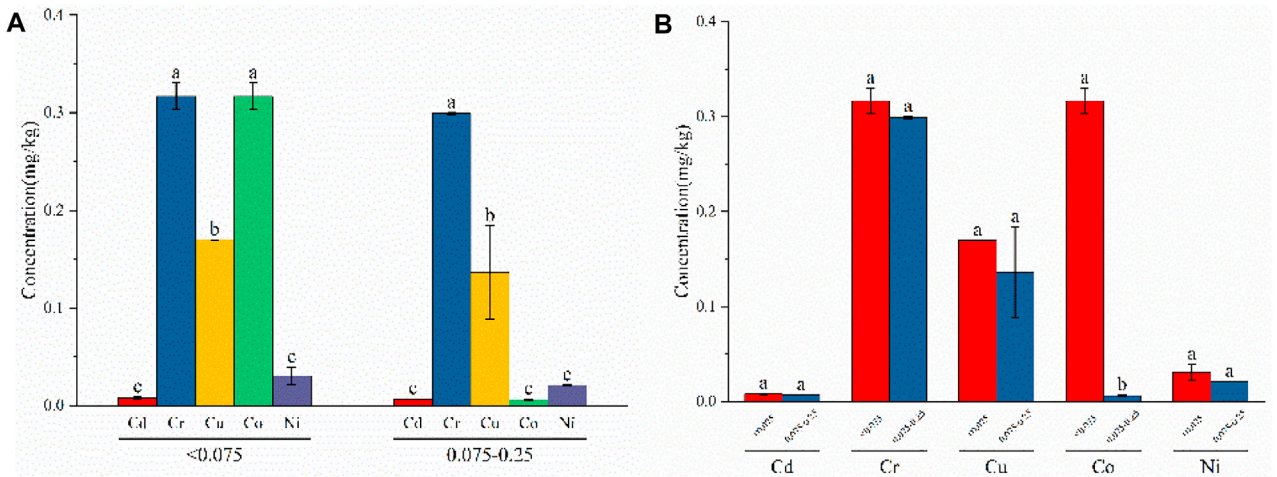

FIGURE 6 | Leaching concentration of heavy metals at different particle sizes conditions: **(A)** difference analysis of different heavy-metal element leaching concentrations under the same particle size conditions; **(B)** difference analysis of different particle size leaching concentrations under the same heavy-metal element condition.

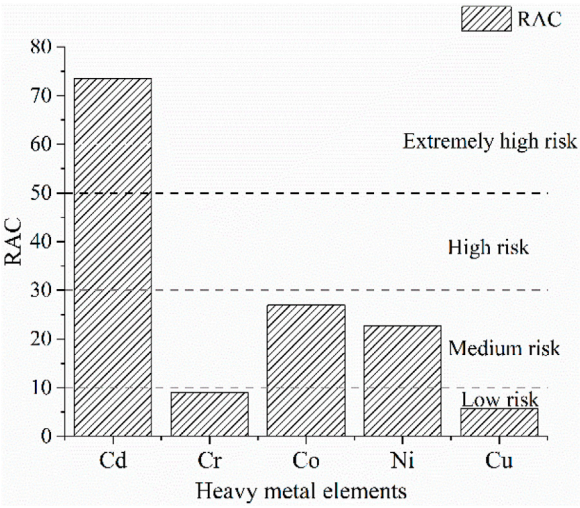

FIGURE 7 | Risk assessment grade of heavy metals.

potential ecological hazard index method, allowing the single potential ecological risk index and potential ecological hazard index to be established for the five heavy-metal elements in fly ash samples under different pH conditions, as shown in **Table 6**. At pH levels of 2.8, 3.9, 4.9, 5.7, and 6.8, the individual potential risk index values for Cr, Cu, Co, and Ni did not exceed 40, indicating that their pollution levels present a low ecological risk. At pH levels of 4.9, 5.7, and 6.8, Cd pollution levels present a low ecological hazard, while at pH 2.8 and 3.9, a moderate ecological hazard is exhibited. This shows that the heavy-metal element Cd presents the greatest potential ecological risk in fly ash. The potential ecological hazard index *RI* values for the five heavy-metal elements at pH levels of 2.8, 3.9, 4.9, 5.7, and 6.8 were

TABLE 6 | Hakanson potential ecological risk index under different pH conditions.

pH	Metals	C_s^i	C_n^i	E_r^i	RI
2.8	Cd	0.1186	0.06	59.28	59.62
	Cr	0.5920	64.93	0.02	
	Cu	0.7117	24.16	0.15	
	Co	0.2071	10.74	0.10	
	Ni	0.3573	25.74	0.07	
3.9	Cd	0.0955	0.06	47.77	47.96
	Cr	0.3737	64.93	0.01	
	Cu	0.3734	24.16	0.08	
	Co	0.0436	10.74	0.02	
	Ni	0.3993	25.74	0.08	
4.9	Cd	0.0752	0.06	37.59	37.73
	Cr	0.0774	64.93	0.00	
	Cu	0.4112	24.16	0.09	
	Co	0.0191	10.74	0.01	
	Ni	0.2175	25.74	0.04	
5.7	Cd	0.0055	0.06	2.76	2.81
	Cr	0.0684	64.93	0.00	
	Cu	0.2211	24.16	0.05	
	Co	0.0029	10.74	0.00	
	Ni	0.0124	25.74	0.00	
6.8	Cd	0.0061	0.06	3.07	3.13
	Cr	0.0539	64.93	0.00	
	Cu	0.2916	24.16	0.06	
	Co	0.0002	10.74	0.00	
	Ni	0.0103	25.74	0.00	

59.62, 47.96, 37.73, 2.81, and 3.13, respectively, none of which exceeded 150, indicating that they present only a slight ecological hazard. As the pH increases, the potential ecological risk index RI decreases accordingly, with the *RI* being largest at pH 2.8 (59.62). Numerous studies have shown that the soil in the Lianghuai mining area is weakly alkaline (Yang et al., 2019; Sandeep et al., 2016), indicating that fly ash can be safely applied for soil reclamation in the Lianghuai mining area.

TABLE 7 | Hakanso potential ecological risk index under different temperature conditions.

Temperature (°C)	Metals	C_s^i	E_r^i	RI
0	Cd	0.0440	22.01	22.25
	Cr	2.3290	0.07	
	Cu	0.6949	0.14	
	Co	0.0237	0.01	
	Ni	0.1030	0.02	
10	Cd	0.0483	24.16	24.62
	Cr	5.4265	0.17	
	Cu	1.0501	0.22	
	Co	0.0527	0.02	
	Ni	0.2813	0.05	
15	Cd	0.0458	22.88	23.30
	Cr	3.7082	0.11	
	Cu	1.1999	0.25	
	Co	0.0121	0.01	
	Ni	0.2531	0.05	
20	Cd	0.0543	27.15	27.69
	Cr	3.7267	0.11	
	Cu	1.4412	0.30	
	Co	0.1385	0.06	
	Ni	0.3623	0.07	
25	Cd	0.0212	10.61	11.54
	Cr	1.8853	0.06	
	Cu	1.7133	0.35	
	Co	0.9635	0.45	
	Ni	0.3572	0.07	
30	Cd	0.0036	1.80	2.90
	Cr	0.7804	0.02	
	Cu	2.2070	0.46	
	Co	0.9969	0.46	
	Ni	0.8382	0.16	
35	Cd	0.0049	2.46	3.90
	Cr	1.3319	0.04	
	Cu	2.7393	0.57	
	Co	1.3781	0.64	
	Ni	0.9995	0.19	

4.2.2 The Hakanson Potential Ecological Risk Index Under Different Temperature Conditions

The potential ecological risk index for the five heavy-metal elements in fly ash samples under different temperature conditions was calculated using the Hakanson formula, as shown in **Table 7**. At temperatures of 0, 10, 15, 20, 25, 30, and 35°C, the individual potential ecological risk index and the potential ecological risk index for the five heavy metals were all less than 40 and 150, respectively, indicating a low ecological hazard. With increasing temperature, the potential ecological risk index *RI* tended to rise initially and then decline, reaching a maximum *RI* at 25°C (27.69). The Lianghuai region is a typical temperate monsoon region with an average annual temperature of about 15°C (Lu et al., 2017; Xie et al., 2020). At this temperature, the risk of fly ash to the environment is low, further supporting its potential for use as a safe soil conditioner.

4.2.3 The Hakanson Potential Ecological Risk Index Under Different Particle Size Conditions

The potential ecological risk index for the five heavy-metal elements in fly ash samples under different particle size conditions was calculated using the Hakanson formula, as shown in **Table 8**.

TABLE 8 | Hakanson potential ecological risk index of fly ash under different particle size conditions.

Particle (mm)	Metals	C_s^i	E_r^i	RI
<0.075	Cd	0.0077	3.86	4.06
	Cr	0.3166	0.01	
	Cu	0.1698	0.04	
	Co	0.3166	0.15	
	Ni	0.0305	0.006	
0.25–0.075	Cd	0.0069	3.43	3.48
	Cr	0.2990	0.009	
	Cu	0.1362	0.03	
	Co	0.0058	0.003	
	Ni	0.0208	0.004	

At particle sizes of <0.075 mm and 0.25–0.075 mm, the E_r^i of Cd, Cr, Cu, Ni, and Co were less than 40, indicating that the degree of contamination was at the cleaning grade level. The potential ecological hazard index *RI* values for the five heavy-metal elements at particle sizes of <0.075 mm and 0.25–0.075 mm were 4.06 and 3.48, respectively, indicating that fly ash presents a slight ecological hazard. With the increase in particle size, the ecological risk index decreased overall.

5 CONCLUSION

The physicochemical properties, heavy-metal content, morphology, and leached content of heavy metals were determined for fly ash under different pH, temperature, and particle size conditions, with their relative risks established by calculating their ecological risk index and RAC index values. Based on these findings, it can be concluded that 1) the active content and the total amount of Cd, Cr, Cu, and Ni elements in fly ash leaching liquid were less than the corresponding minimum soil risk screening value for agricultural land in China, while the heavy metal Co was not specified in the soil pollution risk control standard for agricultural land. Overall, results indicated that fly ash would have little impact on the soil ecological environment under short-term immersion conditions and, therefore, can be ignored under normal circumstances; 2) generally, a low level of harm is likely to be caused by fly ash to the environment under the three different experimental conditions assessed. In the morphological evaluation (RAC) of heavy metals, Cd exhibited a very high ecological risk, indicating that fly ash may cause an ecological risk to the soil. The long-term accumulation of fly ash would allow the accumulation of trace elements in the soil under leaching conditions, which may also present soil ecological and environmental risks, as well as a risk to public health; 3) under different pH, temperature, and particle size conditions, the oscillating leaching amount of fly ash was less than the soil risk screening value for agricultural land in China. With an increase in pH, the potential ecological risk index *RI* value

decreased, with pH 2.8 exhibiting the highest *RI* value of 59.62. Under increasing temperature conditions, the potential ecological risk index RI value tended to rise initially and then decrease, with the highest RI observed at 25°C (27.69). With increasing particle size, the ecological risk index value decreased, exhibiting a maximum *RI* at <0.075 mm of 4.06; 4) fly ash is composed of spherical microbeads and porous particles of different particle sizes, with its microstructure exhibiting good porosity, a high specific surface area, and a strong adsorption capability, with low bulk weight and an abundance of trace elements such as Si, Al, and Fe. Furthermore, the nutrient availability (such as available potassium and available phosphorus) was relatively rich, providing the basic requirements for fly ash as a soil amendment. The results of this study indicate that fly ash can safely be applied to the improvement of reclaimed soil in the Lianghuai mining area, although the potential ecological risks of Cd leaching should be taken into account and monitored. Therefore, the use of environmentally-friendly eluents (chelators and organic acids) should be used to chemically leach fly ash prior to use, reducing the ecological risk of the heavy metal Cd and achieving the safe utilization of fly ash as a sustainable resource.

DATA AVAILABILITY STATEMENT

The original contributions presented in the study are included in the article/Supplementary Material; further inquiries can be directed to the corresponding author.

AUTHOR CONTRIBUTIONS

ZZ: conceptualization, investigation. WC: investigation; statistical analysis and writing, review and editing the manuscript. KY and YZ: funding acquisition, YH, CF, CM, and YT: reviewing the manuscript. All authors have read and agreed to the published version of the manuscript.

FUNDING

This research was supported by the Institute of Energy, Hefei Comprehensive National Science Center (No. 21KZS217), the National Natural Science Foundation of China (No. 51904014), and the Postdoctoral Foundation of Anhui Province (No. 2019B337). The authors appreciate the constructive comments from the reviewer.

REFERENCES

Bai, X., Ding, H., Lian, J., Ma, D., Yang, X., Sun, N., et al. (2018). Coal Production in China: Past, Present, and Future Projections. *Int. Geol. Rev.* 60 (5–6), 535–547. doi:10.1080/00206814.2017.1301226

Bao, S. D. (2000). *Soil and Agricultural Chemistry Analysis [M]*. Beijing: China Agricultural Press.

Cai, S., Zhou, S., Wu, P., and Zhao, J. (2019). Speciation and Bioavailability of Metals in Sediments from a Stream Impacted by Abandoned Mines in Maoshi Town, Southwest of China. *Bull. Environ. Contam. Toxicol.* 103 (2), 302–307. doi:10.1007/s00128-019-02635-9

China Coal Industry Association.2020 Coal Industry Development Annual Report [R]. 2020.

China Soil (1998). *National Soil Survey Office*. Beijing: China Agricultural Press. [M].

China Weather Network (2021).. Historical Weather - Annual Monthly Mean Temperature in Huainan [EB/OL] http://www.weather.com.cn/forecast/history.shtml?areaid=101220401&month=8.

Cho, H., Oh, D., and Kim, K. (2005). A Study on Removal Characteristics of Heavy Metals from Aqueous Solution by Fly Ash. *J. Hazard Mater* 127 (1), 187–195. doi:10.1016/j.jhazmat.2005.07.019

Cui, H. B., Wu, Q. G., and Zhang, X. (2016). Immobilization of Cu and Cd in Contaminated Soil by Coal Fly Ash[J]. *Soil* 48 (5), 971–977. doi:10.13758/j.cnki.tr.2016.05.019

Feng, T., Zheng, L., and Zhang, J. (2022). Risk Assessment of Heavy Metal in the Soil of an Abandoned Pesticide Factory and its Remediation Effect by Calcination[J]. *Environ. Eng.* 40 (02), 132–138. doi:10.13205/j.hjgc.202202021

Fu, B., Liu, G., Mian, M. M., Sun, M., and Wu, D. (2019). Characteristics and Speciation of Heavy Metals in Fly Ash and FGD Gypsum from Chinese Coal-Fired Power Plants. *Fuel* 251, 593–602. doi:10.1016/j.fuel.2019.04.055

Garau, G., Castaldi, P., Santonal, L., Deiana, P., and Melis, P. (2007). Influence of Red Mud, Zeolite and Lime on Heavy Metal Immobilization, Culturable Heterotrophic Microbial Populations and Enzyme Activities in a Contaminated Soil[J]. *Geoderma* 142 (1), 47–57. doi:10.1016/j.geoderma.2007.07.011

GB15618-2018, (2018) Soil Environmental Quality Agricultural Soil Pollution Risk Control Standards (Trial) [S].

Gupta, G. S., Prasad, G., and Singh, V. N. (1992). Study on Removal of Chromium Dye from Aqueous Solution by Fly Ash and Coal Mixed Adsorbent[J]. *Environ. Prot. Sci.* 4, 76–81+62.

Hakanson, L. (1980). An Ecological Risk Index for Aquatic Pollution control.a Sedimentological Approach. *Water Res.* 14, 975–1001. doi:10.1016/0043-1354(80)90143-8

Kanokwan, K., Bora, C., Ahmet, H. A., Benson, C. H., and Edil, T. B. (2015). Effects of pH on the Leaching Mechanisms of Elements from Fly Ash Mixed Soils[J]. *Fuel* 140, 788–802. doi:10.1016/j.fuel.2014.09.068

Kirby, C. S., and Rimstidt, J. D. (1993). Mineralogy and Surface Properties of Municipal Solid Waste Ash. *Environ. Sci. Technol.* 27, 652–660. doi:10.1021/es00041a008

Kostova, I., Vassileva, C., Dai, S., and Hower, J. C. (2016). Mineralogy, Geochemistry and Mercury Content Characterization of Fly Ashes from the Maritza 3 and Varna Thermoelectric Power Plants, Bulgaria. *Fuel* 186, 674–684. doi:10.1016/j.fuel.2016.09.015

Li, H., Chao, J., Yao, W., Zhao, L., Zhang, C., and Liu, G. (2021). Characteristics of Heavy Metal Content in Wheat Grains and Human Health Risk Assessment-A County in Northern Henan Province[J]. *Environ. Chem.* 41 (04), 1158–1167. doi:10.7524/j.issn.0254-6108.2021092306

Liu, B., Luo, J., Jiang, S., Wang, Y., Li, Y., Zhang, X., et al. (2021b). Geochemical Fractionation, Bioavailability, and Potential Risk of Heavy Metals in Sediments of the Largest Influent River into Chaohu Lake, China[J]. *Environ. Pollut.* 290, 118018. doi:10.1016/j.envpol.2021.118018

Liu, B., Yao, T., and Ma, S. (2021a). Occurrence and Dissolution of Heavy Metals in Fly Ash-Based Soil Conditioner[J]. *Environ. Sci. Technol.* 44 (S2), 292–298. doi:10.19672/j.cnki.1003-6504.0216.21.338

Liu, F., Ma, S., Ren, K., and Wang, X. (2020). Mineralogical Phase Separation and Leaching Characteristics of Typical Toxic Elements in Chinese Lignite Fly Ash. *Sci. Total Environ.* 708, 135095. doi:10.1016/j.scitotenv.2019.135095

Liu, K., Yang, C., and Li, S. (2015). Characteristics of Distribution and Enrichment of Heavy Metal Elements in Fly Ash from Coal-Burning Electric Power Plant[J]. *Environ. Sci. Technol.* 38 (12), 145–150.

Lu, C., Hu, X., and Cai, J. (2019). Analysis and Comparison of Heavy Metals Extracted from Feather and Down by Tessier Five Step Continuous Method and

BCR Four Step Continuous Method[J]. *Light Text. Industry Technol.* 48 (4), 20–22+25. (in chinese).

Lu, L. (2017). *Environmental Biogeochemistry of Trace Elements in the Supergene Environment of Huainan and Huaibei Mining areas[D]*. Anhui: University of Science and Technology of China.

Luo, Y., Ma, S., Liu, C., Zhao, Z., Zheng, S., and Wang, X. (2017). Effect of Particle Size and Alkali Activation on Coal Fly Ash and Their Role in Sintered Ceramic Tiles. *J. Eur. Ceram. Soc.* 37, 1847–1856. doi:10.1016/j.jeurceramsoc.2016.11.032

Mtarfi, N. H., Rais, Z., Taleb, M., and Kada, K. M. (2017). Effect of Fly Ash and Grading Agent on the Properties of Mortar Using Response Surface Methodology. *J. Build. Eng.* 9, 109–116. doi:10.1016/j.jobe.2016.12.004

National Bureau of Statistics (2020). Statistical Bulletin of National Economic and Social Development of the People ' S Republic of China in 2020 [EB/OL]. Avaialable at: http://www.stats.gov.cn/tjsj/zxfb/202102/t20210227_1814154.html.

Nayak, A. K., Raja, R., Rao, K. S., Shukla, A. K., Mohanty, S., Shahid, M., et al. (2015). Effect of Fly Ash Application on Soil Microbial Response and Heavy Metal Accumulation in Soil and Rice Plant. *Ecotoxicol. Environ. Saf.* 114, 257–262. doi:10.1016/j.ecoenv.2014.03.033

Pan, Y., Wu, Z., Zhou, J., Zhao, J., Ruan, X., Liu, J., et al. (2013). Chemical Characteristics and Risk Assessment of Typical Municipal Solid Waste Incineration (MSWI) Fly Ash in China. *J. Hazard. Mater.* 261, 269–276. doi:10.1016/j.jhazmat.2013.07.038

Pandey, S. K., and Bhattacharya, T. (2019). Mobility, Ecological Risk and Change in Surface Morphology during Sequential Chemical Extraction of Heavy Metals in Fly Ash: A Case Study. *Environ. Technol. Innovation* 13, 373–382. doi:10.1016/j.eti.2016.10.004

Qian, Q., Fang, S., and Qiao, Y. (2016). Comparison of Soil Heavy Metals Pollution Assessment Result of Yancheng Coastal Zone[J]. *Environ. Pollut. Control* 38 (12), 43–48.

Sahu, S. K., Tiwari, M., Bhangare, R. C., and Pandit, G. G. (2014). Enrichment and Particle Size Dependence of Polonium and Other Naturally Occurring Radionuclides in Coal Ash. *J. Environ. Radioact.* 138, 421–426. doi:10.1016/j.jenvrad.2014.04.010

Sandeep, P., Sahu, S. K., Kothai, P., and Pandit, G. G. (2016). Leaching Behavior of Selected Trace and Toxic Metals in Coal Fly Ash Samples Collected from Two Thermal Power Plants, India. *Bull. Environ. Contam. Toxicol.* 97, 425–431. doi:10.1007/s00128-016-1864-x

Tang, Y., Pan, J., Li, B., Zhao, S., and Zhang, L. (2021). Residual and Ecological Risk Assessment of Heavy Metals in Fly Ash from Co-combustion of Excess Sludge and Coal. *Sci. Rep.* 11, 2499. doi:10.1038/s41598-021-81812-5

Teng, J., Qiao, Y., and Song, P. (2016). Analysis of Exploration, Potential Reserves and High Efficient Utilization of Coal in China. *Chin. J. Geophys.* 59 (12), 4633–4653.

Tessier, A., Campbell, P. G. C., and Bisson, M. (1979). Sequential Extraction Procedure for the Speciation of Particulate Trace Metals. *Anal. Chem.* 51 (7), 844–851. doi:10.1021/ac50043a017

Wang, R., Chen, N., and Zhang, E. (2022). Ecological and Health Risk Assessments Based on the Total Amount and Speciation of Heavy Metals in SoilsAround Mining Areas[J]. *Environ. Sci.* 43 (03), 1546–1557. doi:10.13227/j.hjkx.202106109

Wang, Y., Li, X., Li, J., Li, W., Zhang, M., Zhao, C., et al. (2021). Heavy Metal Pollution Characteristics and Risk Evaluation of Soil Around Coal Gangue Stockpile Area[J]. *Bull. Chin. Ceram. Soc.* 40 (10), 3464–3471. doi:10.16552/j.cnki.issn1001-1625.20210827.001

Wei, Y., Zhou, C., and Wang, J. (2017). Distribution and Ecological Risk Assessment of 6 Typical Trace Elements in Minning Soils in Huainan Coalfield[J]. *J. Univ. Sci. Technol. China* 47 (5), 413–420.

Xie, H., Huang, W., An, S., Jiang, C., and Tang, Z. (2020). Study on Difference of Water Chemical Characteristics of Main Aquifers in Huainan and Huaibei Mining Area[J]. *Coal Technol.* 39 (03), 92–95. doi:10.13301/j.cnki.ct.2020.03.027

Xie, H., Wu, L., and Zheng, D. (2019). Prediction on the Energy Consumption and Coal Demand of China in 2025[J]. *J. China Coal Soc.* 44 (7), 1949–1960. doi:10.13225/j.cnki.jccs.2019.0585

Xu, C., Lu, X., and He, X. (2022). Pollution and Human Health Risk Assessment of Paddy Soil Heavy Metals in Typical Black Shale Areas in the West of Zhejiang Province[J]. *Environ. Ecol.* 4 (04), 11–20.

Xu, R., Ni, S., and Tuo, X. (2008). Progress in Nanoparticles Characterization: Sizing and Zeta Potential Measurement. *Particuology* 6, 112–115. doi:10.1016/j.partic.2007.12.002

Yang, J., Li, L., and Hou, T. (2002). The Study of the Solubility of Anion in Combustion Residue of Municipal Solid Waste[J]. *Environ. Monit. China* 06, 48–50. doi:10.19316/j.issn.1002-6002.2002.06.014

Yang, Y. (2019). *Quality Evaluation of Reclaimed Soil in Subsidence Area of Huainan and Huaibei Mining area[D]*. Anhui: AnHui University of Science and Technology.

Yu, Q., Bai, R., Zeng, X., Wei, J., and Zhou, C. (2007). Leaching Test Conditions for Cr(VI) in Cement, Fly Ash and Cement Solidified Fly Ash and Their Influencing Factors[J]. *J. Chin. Ceram. Soc.* 35 (8).

Yuan, L. (2020). Challenges and Countermeasures for High Quality Development of China's Coal Industry[J]. *China coal.*. 46 (1), 6–12. doi:10.19880/j.cnki.ccm.2020.01.001

Zhang, F., Chen, X., and Ma, H. (2022). Discuss on Scientific Construction of Ecological Risk Assessment Methods in the High Background Areas of Soil heavyMetals[J]. *J. Zhejiang Univ.* 48 (01), 57–67.

Zhang, Y., Cetin, B., Likos, W. J., and Edil, T. B. (2016). Impacts of pH on Leaching Potential of Elements from MSW Incineration Fly Ash. *Fuel* 184, 815–825. doi:10.1016/j.fuel.2016.07.089

Zhao, S., Duan, Y., Lu, J., Gupta, R., Pudasainee, D., Liu, S., et al. (2018). Chemical Speciation and Leaching Characteristics of Hazardous Trace Elements in Coal and Fly Ash from Coal-Fired Power Plants. *Fuel* 232, 463–469. doi:10.1016/j.fuel.2018.05.135

Zheng, Y., Zhang, Z., Chen, Y., An, S., Zhang, L., Chen, F., et al. (2022). Adsorption and Desorption of Cd in Reclaimed Soil under the Influence of Humic Acid: Characteristics and Mechanisms. *Int. J. Coal Sci. Technol.* 9 (1), 7. doi:10.1007/s40789-022-00480-6

Zhou, J., Cui, H., and Liang, J. (2015b). Remediation Technologies and Current Problems of Heavy Metal Contaminated Sites with "Demonstration Project of Soil Remediation on the Periphery of Guixi Smelter" as Example[J]. *Soil* 47 (2), 283–288. doi:10.13758/j.cnki.tr.2015.02.014

Zhou, J., Wu, S., Pan, Y., Zhang, L., Cao, Z., Zhang, X., et al. (2015a). Enrichment of Heavy Metals in Fine Particles of Municipal Solid Waste Incinerator (MSWI) Fly Ash and Associated Health Risk. *Waste Manag.* 43, 239–246. doi:10.1016/j.wasman.2015.06.026

Conflict of Interest: The authors declare that the research was conducted in the absence of any commercial or financial relationships that could be construed as a potential conflict of interest.

Publisher's Note: All claims expressed in this article are solely those of the authors and do not necessarily represent those of their affiliated organizations, or those of the publisher, the editors, and the reviewers. Any product that may be evaluated in this article, or claim that may be made by its manufacturer, is not guaranteed or endorsed by the publisher.

Copyright © 2022 Zhang, Cai, Hu, Yang, Zheng, Fang, Ma and Tan. This is an open-access article distributed under the terms of the Creative Commons Attribution License (CC BY). The use, distribution or reproduction in other forums is permitted, provided the original author(s) and the copyright owner(s) are credited and that the original publication in this journal is cited, in accordance with accepted academic practice. No use, distribution or reproduction is permitted which does not comply with these terms.

frontiers | Frontiers in Chemistry

TYPE Original Research
PUBLISHED 25 August 2022
DOI 10.3389/fchem.2022.958773

Check for updates

OPEN ACCESS

EDITED BY
Ilhwan Park,
Hokkaido University, Japan

REVIEWED BY
Hossein Aghajani,
Iran University of Science and Technology, Iran
Marthias Silwamba,
University of Zambia, Zambia

*CORRESPONDENCE
Jianwei Du,
dujianwei@scies.org
Xiaoying Hu,
huxiaoying@scies.org

SPECIALTY SECTION
This article was submitted to Green and Sustainable Chemistry, a section of the journal Frontiers in Chemistry

RECEIVED 01 June 2022
ACCEPTED 01 August 2022
PUBLISHED 25 August 2022

CITATION
Huang K, Wang L, Wen Y, He K, Zhang M, Du J and Hu X (2022), Oxidation leaching of chromium from electroplating sludge: Ultrasonic enhancement and its mechanism. *Front. Chem.* 10:958773. doi: 10.3389/fchem.2022.958773

COPYRIGHT
© 2022 Huang, Wang, Wen, He, Zhang, Du and Hu. This is an open-access article distributed under the terms of the Creative Commons Attribution License (CC BY). The use, distribution or reproduction in other forums is permitted, provided the original author(s) and the copyright owner(s) are credited and that the original publication in this journal is cited, in accordance with accepted academic practice. No use, distribution or reproduction is permitted which does not comply with these terms.

Oxidation leaching of chromium from electroplating sludge: Ultrasonic enhancement and its mechanism

Kaihua Huang[1], Lizhangzheng Wang[1,2], Yong Wen[1], Kuang He[1], Mingyang Zhang[1], Jianwei Du[1]* and Xiaoying Hu[1]*

[1]South China Institute of Environmental Sciences, Ministry of Ecology and Environment, Guangzhou, China, [2]School of Resources and Environmental Engineering, Wuhan University of Technology, Wuhan, China

The oxidation leaching of chromium from electroplating sludge was investigated, and ultrasonication was introduced for the enhancement of the leaching process. Two different types of Cr-bearing electroplating sludge were selected for the study, and the effects of the reagent dosage, temperature, and ultrasonic pulse ratio on the leaching efficiency were tested through oxidation leaching experiments. The experimental results show that hydrogen peroxide and sodium hypochlorite exhibit different leaching effects on different types of electroplating sludge. The control of reagent dosage is crucial for the oxidation leaching of Cr, while the effect of temperature turns out to be small. Hydrogen peroxide turns out to be a more effective oxidizer for chromium sludge, and the leaching efficiency of Cr could be promoted from 77.52% to 87.08% using ultrasonic enhancement under optimum conditions. Interestingly, sodium hypochlorite exhibited better leaching efficiency than hydrogen peroxide for the mixed sludge since the organic matter in the mixed sludge will lead to the rapid decomposition and consumption of hydrogen peroxide. The leaching efficiency of Cr from the mixed sludge could also be promoted from 56.82% to 67.10% using ultrasonic enhancement under optimum conditions. According to the scanning electron microscope imaging, ultrasonic enhancement can create voids and cracks on the surface of the sludge particles, hence promoting the contact between electroplating sludge and leaching agents, and promoting the oxidation leaching efficiency. In addition, ultrasound seems to be able to remove the coverings on the surface of the mixed sludge particles, which may facilitate the oxidation reaction.

KEYWORDS

chromium, oxidation leaching, ultrasonic enhancement, electroplating sludge (EPS), mechanism

1 Introduction

Electroplating sludge (EPS) is the heavy metal-containing sludge produced after the treatment of wastewater in the operation of electroplating industry. Generally, electroplating sludge can be divided into two categories, including separated sludge and mixed sludge. Separated sludge contains single heavy metal element, such as copper sludge, nickel sludge, and chromium sludge. Mixed sludge contains two or more heavy metal elements and is usually mixed with organic sludge such as oily sludge and biochemical sludge. Since the heavy metals in EPS pose great risks to environment and human health, EPS has been listed as hazardous waste in many countries and regions, including China and the European Union (Magalhaes et al., 2005). What's more, with the development of machinery manufacturing industry and advances in technology like composite coating (Mahmoudi et al., 2021; Shakiba et al., 2022), the amount of chromium coating and demand for chromium resources are increasing, which makes the resource utilization of chromium-bearing wastes become even more important. Thus, how to deal with electroplating sludge reasonably and effectively has attracted the attention of many research workers.

At present, the main treatment methods for EPS include harmless treatment and resource utilization. Harmless treatment methods mainly include stabilization (Chen et al., 2020) and incineration (Zhou et al., 2018). However, with the increasing requirements for environmental protection and carbon emissions, resource utilization has become a more preferred method than harmless treatment, especially for the treatment of wastes with a high utilization value such as EPS. The resource utilization methods for electroplating sludge mainly include pyrometallurgy (Huang et al., 2013), hydrometallurgy (Wu et al., 2020), and preparation of functional materials like construction materials, catalysts, and pigments (Carneiro et al., 2018; Zhang et al., 2018; Dai et al., 2019). Although the preparation of functional materials from EPS is more value-added, the application of the product is usually restricted, which limits the applicability of the technology. Therefore, pyrometallurgy and hydrometallurgy methods are now more widely used in the industry.

The pyrometallurgy method is more suitable for the treatment of separated sludge with high content of Cu or Ni, while Cr cannot be effectively recovered since the melting point of Cr is much higher. Commonly, acid leaching is employed for extracting heavy metals from mixed EPS due to its simplicity and convenience (Yan et al., 2019). Nevertheless, the acid leaching method is nonselective for mixed heavy metal sludge, resulting in multi-metal solutions, which require further separation operations (Li et al., 2010). Solvent extraction is usually applied for the separation of mixed heavy metals from the acid leachate, but its procedure is relatively complicated (Kul and Oskay, 2015). Currently, the electrowinning method has been developed to selectively recover high-purity Cu from the acid leaching solution of electroplating sludge containing Cu and Ni (Veglio et al., 2003; Wang et al., 2018), while Cr plays a negative role in the process which will hinder the utilization of the multi-heavy metal solutions. Therefore, the selective recovery of Cr from electroplating sludge is necessary, but research in this area is scarce (Yue et al., 2019; Zheng et al., 2020). Existing research shows that Cr can be selectively recovered by Cr (III) oxidation under high temperature roasting and the subsequent Cr (VI) leaching; the leaching rate of Cr (IV) can reach higher than 90% (Ding et al., 2008; Verbinnen et al., 2013). However, the high temperature roasting process is accompanied by high energy consumption and smoke pollution. Thus, the oxidation of Cr (III) under low temperature is a promising idea for the selective recovery of Cr from EPS, which could avoid high energy consumption and smoke pollution. Research workers have studied the oxidation leaching of molybdenum from molybdenite concentration with different oxidizing agents under lower temperature, and 89.3% of the Mo-leaching rate was achieved under optimum conditions, which provides a good guide for our research (Arbat et al., 2020).

In this study, the oxidation leaching of chromium from chromium sludge and mixed sludge was investigated and compared, which would provide a more comprehensive perspective for the resource utilization of electroplating sludge. The difference between the two kinds of sludge was analyzed, including physical, chemical, and reaction properties. The effects of different reaction conditions on the leaching results were investigated and ultrasonication was introduced to enhance the oxidation leaching process. Finally, the surface morphology change of EPS was investigated by a scanning electron microscope to explain the influence mechanism of the leaching process. This study provides a novel thought for the selective extraction of chromium from Cr-bearing EPS; the findings of this study may give significant guidance for the resource utilization of Cr-bearing EPS.

2 Materials and methods

2.1 Material

Two different types of Cr-bearing electroplating sludge were collected for the study, including the chromium sludge and the mixed sludge.

The chromium sludge (EPS1) used in this study was collected from a chromium plating company in Guangzhou city (China), where chromium-containing wastewater is precipitated by sodium hydroxide after reduction with a reducing agent and then filtered by a pressure filter separately. Thus, EPS1 mainly consists of $Cr(OH)_3$ and inorganic matters.

The mixed sludge (EPS2) was collected from the wastewater treatment plant of an electroplating park in Jiangmen city

TABLE 1 Main composition of the electroplating sludge.

Sample	Organic content (%)	Ca (mg/kg)	Cr (mg/kg)	Fe (mg/kg)	Ni (mg/kg)	Cu (mg/kg)	Zn (mg/kg)
EPS1	4.19	3,313.4	359,621.3	846.2	9,298.5	5,575.9	28.2
EPS2	16.12	90,320.4	21,589.9	27,725.6	35,224.3	56,928.9	16,218.6

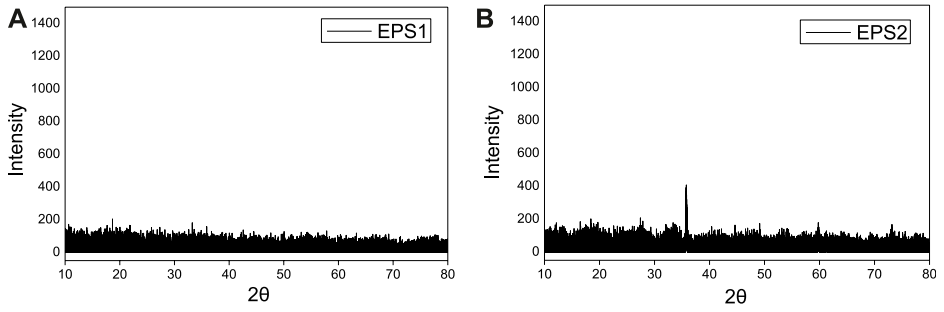

FIGURE 1
XRD pattern of **(A)** EPS1 and **(B)** EPS2.

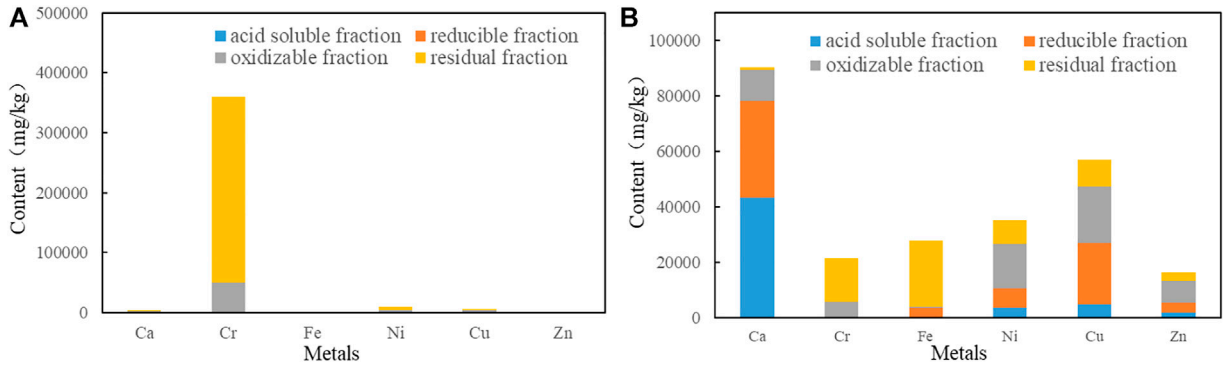

FIGURE 2
Fractions of Ca, Fe, Cu, Ni, Zn, and Cr by BCR analysis in **(A)** EPS1 and **(B)** EPS2.

(China), where different types of sludges were mixed and filtered, including chromium sludge, copper sludge, nickel sludge, and oily sludge. Thus, EPS2 mainly consists of different types of heavy metal hydroxides and organic matters.

Prior to use, the sludge was dried at 105°C to constant weight. The sample was all ground by milling and sieved with a particle size of ≤150 μm to get the prepared sludge power. The prepared sludge powder was then used in the following oxidation leaching experiments.

Other chemicals used in this study were purchased from commercial suppliers with analytical-grade purity. All experiments were carried out with distilled water.

2.2 Oxidation leaching

The oxidation leaching experiments were carried out in water bath under stirred condition. One gram of the prepared EPS sample was weighed and added into a 50-ml beaker. A certain volume of 2 mol/L sodium hydroxide solution was then added, followed by a certain amount of oxidizer, and finally, an appropriate amount of pure water was added to control the liquid–solid ratio of about 20:1 for the reaction. The water bath temperature was set to a desired value, and the reaction lasted for 2 h. After the reaction, the leachate was filtered and separated; the metal content in the leachate was determined by an inductively

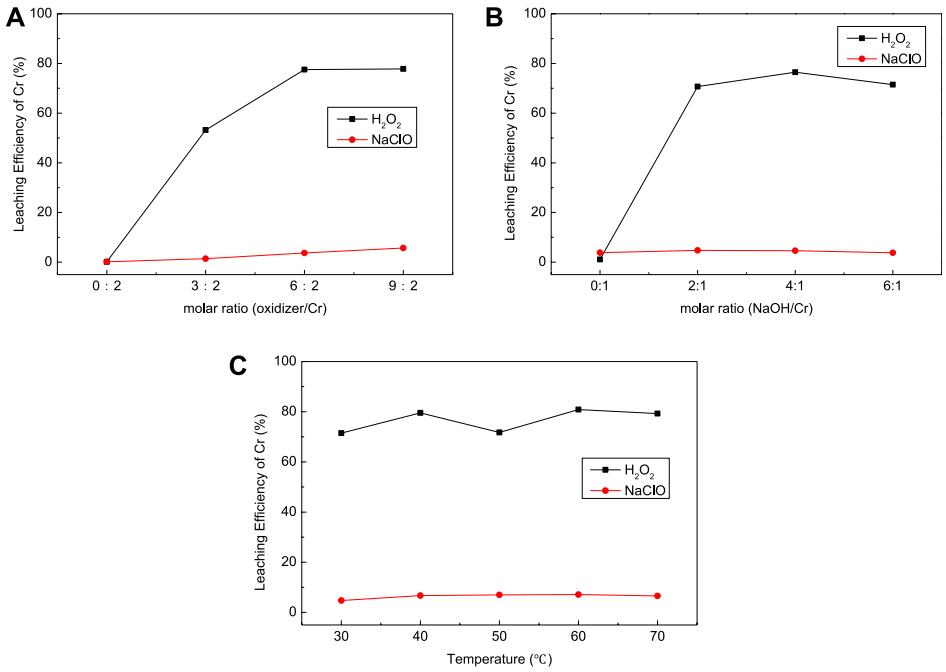

FIGURE 3
Effect of **(A)** oxidizer dosage, **(B)** NaOH dosage, and **(C)** temperature on the leaching results for chromium sludge (EPS1).

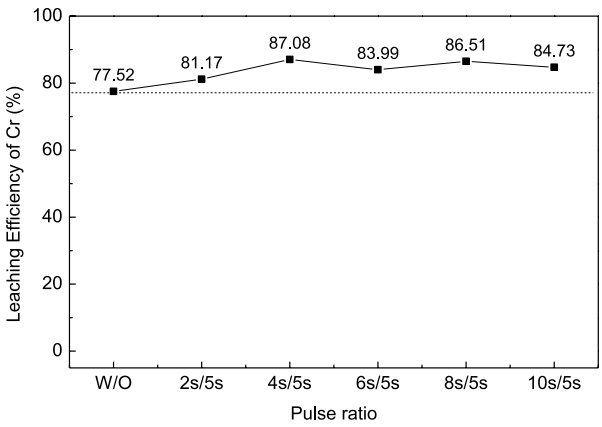

FIGURE 4
Effect of ultrasonic pulse ratio on the leaching efficiency of Cr for chromium sludge (EPS1).

coupled plasma mass spectrometer (ICP-MS, 7800 ICP-MS system, Agilent Technologies Co., Ltd., United States) or an atomic absorption spectrometer (AAS, PinAAcle 900T, PerkinElmer, United States), and the residue was weighed after drying.

The ultrasonic-enhanced leaching experiment was carried out in the ultrasonic cell crusher (SM-900A, Shunmatech, Nanjing). The reactants were mixed in the beaker as described earlier, then the ultrasonic horn was placed in the beaker below the liquid level, and the ultrasonic action time, frequency, power, and pulse ratio were adjusted to the desired value before the reaction began. After the reaction, the metal content in the leachate was determined by the same method.

2.3 Characterization

The organic content of the EPS was tested by the gravimetric method as described in the relevant industry standard (CJ/T 221-2005). The crystal mineralogical composition of the prepared sludge powder was analyzed by X-ray diffraction (XRD, X'pert Pro MRD, PANalytical BV, the Netherlands). The chemical composition of the sludge powder was determined using ICP-MS after digestion using an HF-HNO_3-HCl mixed solution. The surface micro-topography of the sludge powders before and after oxidation leaching were characterized by a field emission scanning electron microscope (SEM, GeminiSEM300, ZEISS, Germany) and an electron probe micro-analysis (JXA-8100, JEOL, Japan).

Fraction analysis of heavy metals present in the sludge was carried out by a modified Community Bureau of Reference (BCR) three-stage sequential extraction procedure; the details of the extraction steps are as described by Rauret et al. (1999). According to the method, metal forms in the sludge were categorized into four fractions: acid soluble fraction, reducible fraction, oxidizable fraction, and non-mobile residual fraction.

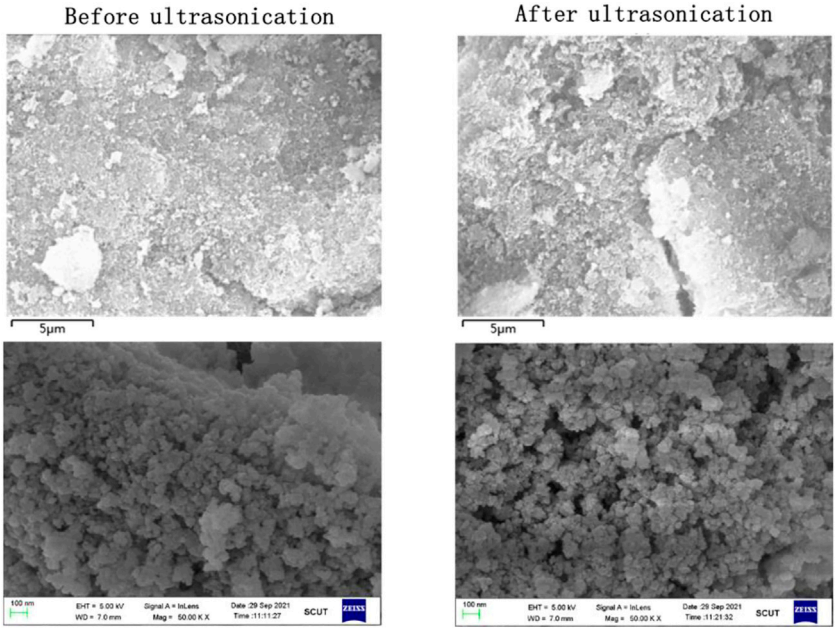

FIGURE 5
Topography change of chromium sludge (EPS1) before and after ultrasonic treatment.

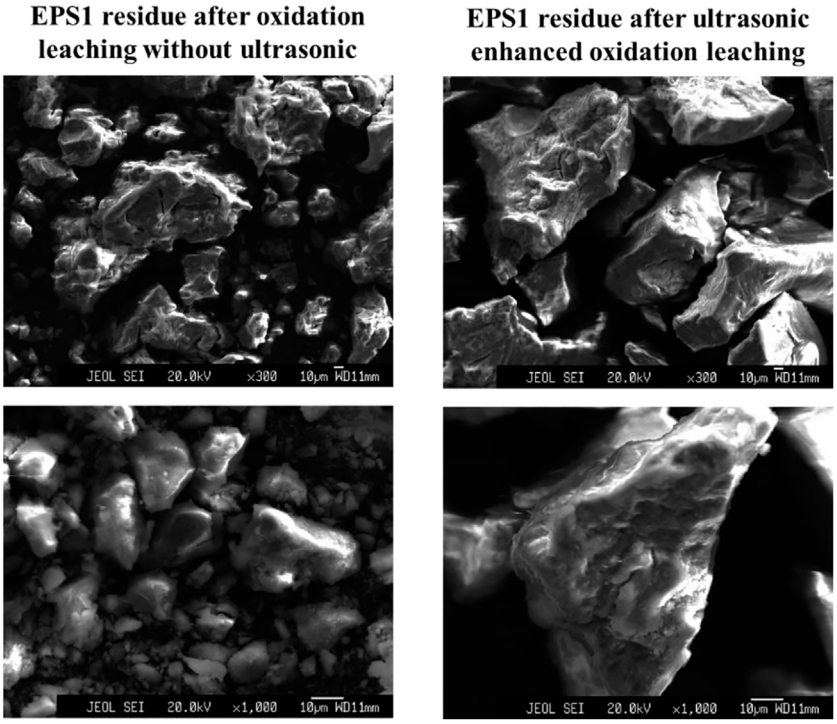

FIGURE 6
Particle morphology of chromium sludge (EPS1) after oxidation leaching with and without ultrasonic treatment.

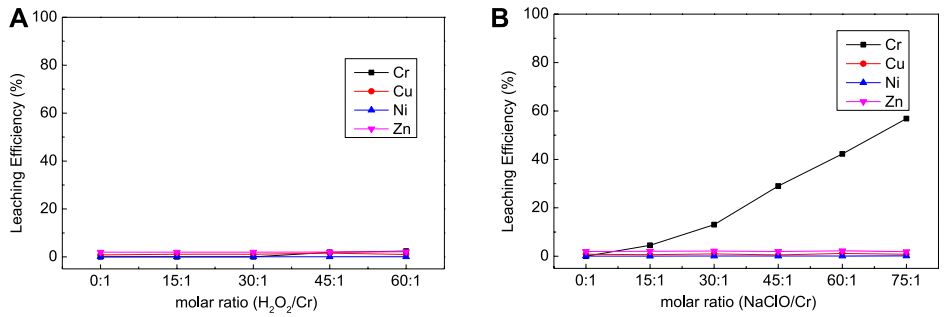

FIGURE 7
Effect of oxidizer dosage on the leaching results [**(A)** with H_2O_2; **(B)** with NaClO] for complex sludge (EPS2).

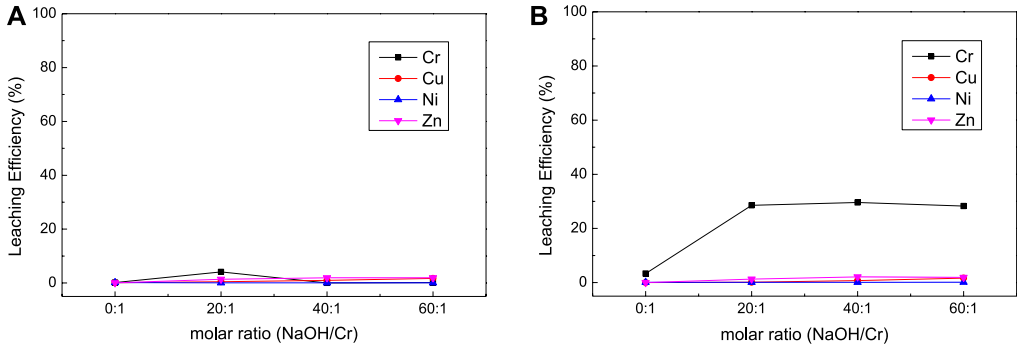

FIGURE 8
Effect of NaOH dosage on the leaching results [**(A)** with H_2O_2; **(B)** with NaClO] for complex sludge (EPS2).

3 Results and discussion

3.1 Characterization of electroplating sludge

The content of organic matter and main metal elements in chromium sludge (EPS1) and mixed sludge (EPS2) is shown in Table 1. The results show that the composition of EPS1 is relatively simpler than that of EPS2. EPS1 has very high content of Cr of 35.96% and relatively low content of organic matter and other heavy metals. In comparison, the organic content of EPS2 is much higher than that of EPS1, and EPS2 contains multiple heavy metal elements of contents ranging from 1% to 6%.

The XRD patterns of the two sludge powders are shown in Figure 1, which indicated that the heavy metal compounds in the sludge did not form crystalline matters for both samples. The amorphous state of the EPS samples may result from the formation conditions of electroplating sludge by rapid neutralization or precipitation under room temperature and atmospheric pressure (Yang et al., 2015).

Data obtained by BCR analysis (Figure 2) revealed that the dominant existence form of Cr were the oxidizable and residual fractions for EPS1 and EPS2, accounting for >99.0%. For mixed sludge (EPS2), Cu, Ni, and Zn were distributed in all four fractions. Typically, metals in the acid soluble fraction (consisting of adsorbed ions on ion-exchangeable phases) and reducible fraction (iron and manganese oxyhydroxides) are considered to be more mobile and dangerous than those in other forms, whereas metals in the oxidizable (sulfides and organic matter-bound fraction) and residual (associated with stable minerals such as silicates and crystallized oxides) fractions are considered to have lower mobility (Nguyen et al., 2015). Therefore, the high proportion of Cr in the oxidizable and residual fractions showed that Cr in sludge was more stable than Cu, Ni, and Zn (Zhang et al., 2020). The proportion of Cu, Ni, and Zn in the oxidizable fraction mainly exists in organic matter-bound form and will be released under the oxidizing

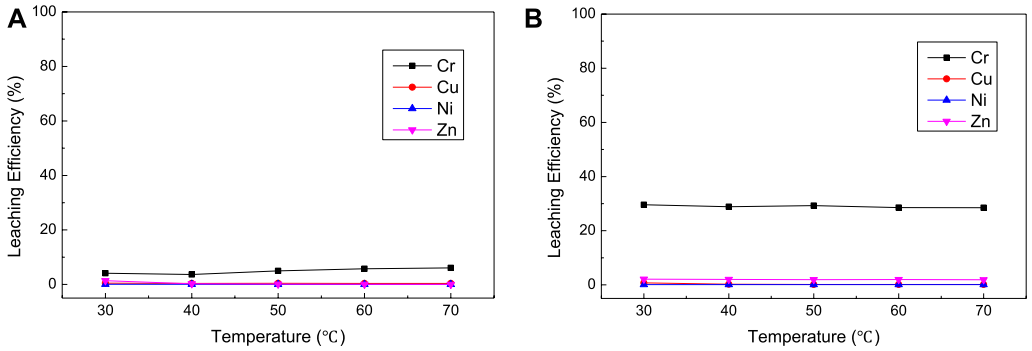

FIGURE 9
Effect of temperature on the leaching results [**(A)** with H_2O_2; **(B)** with NaClO] for complex sludge (EPS2).

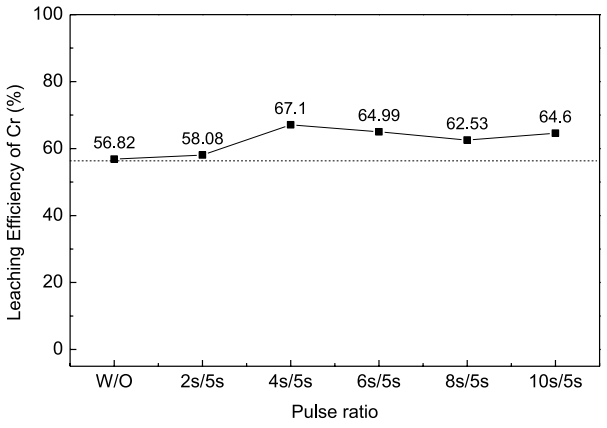

FIGURE 10
Effect of the ultrasonic pulse ratio on the leaching efficiency of Cr for complex sludge (EPS2).

condition; thus, proper alkaline condition is required for the sediment of the released ions to ensure the selective extraction of Cr.

3.2 Oxidation leaching of chromium sludge

Hydrogen peroxide (H_2O_2) and sodium hypochlorite (NaClO) are used as oxidants for the oxidation leaching of electroplating sludge under alkaline conditions. The reaction equations are shown in Eqs 1,2:

$$2Cr(OH)_3 + 4NaOH + 3H_2O_2 \longrightarrow 2Na_2CrO_4 + 8H_2O \quad (1)$$

$$2Cr(OH)_3 + 4NaOH + 3NaClO \longrightarrow 2Na_2CrO_4 + 3NaCl + 5H_2O \quad (2)$$

The effects of oxidizer dosage, NaOH dosage, and temperature on the leaching results were investigated by condition experiments.

As shown in Figure 3A, the type of oxidizer has a great impact on the leaching efficiency of Cr for EPS1; H_2O_2 exhibited stronger leaching ability than NaClO for the oxidation leaching of Cr from EPS1. The reason is that H_2O_2 has higher oxidation potential than NaClO, so it possesses stronger oxidation capacity and reactivity (Behin et al., 2017). The dosage of H_2O_2 was about twice the reaction ratio (6:2) when the reaction reached equilibrium with Cr leaching efficiency of 77.79%; the extra consumption of H_2O_2 may be due to its tendency to break down during the reaction.

The effect of NaOH dosage and temperature on the leaching efficiency of Cr was also studied as shown in Figures 3B,C, respectively. As indicated by Eqs 1,2, the oxidation leaching process requires consumption of NaOH. Thus, Cr cannot be oxidized and leached without the addition of NaOH, and the increase of NaOH would increase the extraction of Cr. However, when the dosage of NaOH exceeds the molar ratio of the reaction (2:1), further increase of NaOH dosage can hardly improve the leaching efficiency. Temperature has little effect on the leaching results, which indicates that the leaching process can be operated under room temperature.

The experimental results above indicated that the oxidation leaching of Cr from EPS must be conducted under alkaline condition, whereas the BCR analysis was conducted under acidic condition. Hence, the oxidizable fraction of Cr by BCR analysis was much lower than the proportion of Cr that can be extracted by oxidation leaching. In other words, the residual fraction of Cr can also be extracted by oxidation leaching under alkaline condition.

In order to improve the leaching efficiency of Cr, the ultrasonic-enhanced oxidation leaching experiment was carried out under optimal conditions. The ultrasonic power was set at 450W, and the frequency was 20–25kHz; the

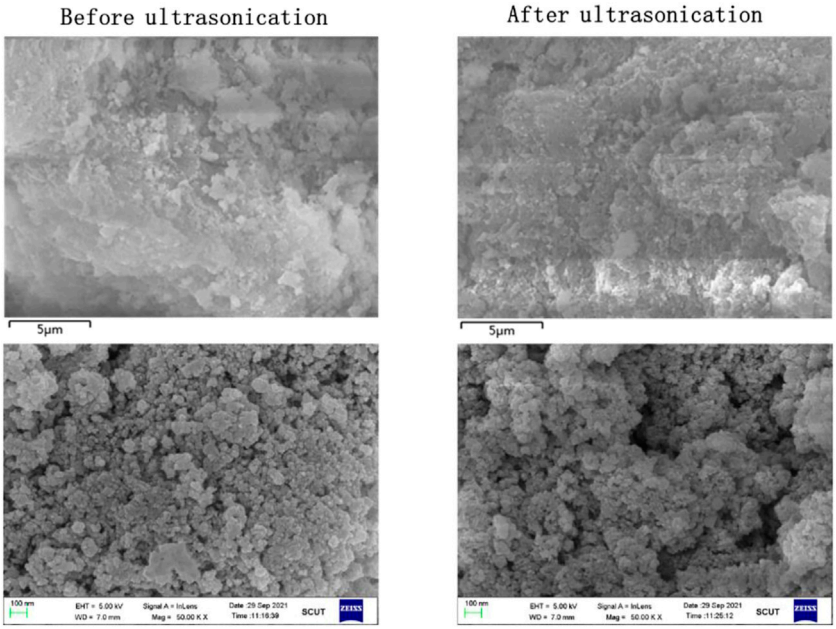

FIGURE 11
Topography change of complex sludge (EPS2) before and after ultrasonic treatment.

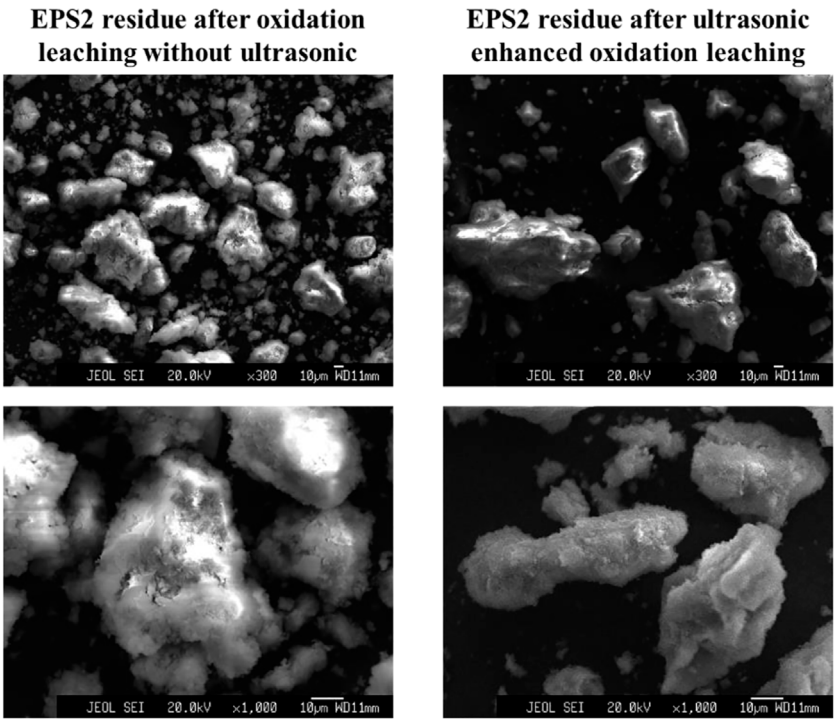

FIGURE 12
Particle morphology of complex sludge (EPS2) after oxidation leaching with and without ultrasonic treatment.

reaction time was controled at 10 min to avoid overheating. The effect of ultrasonic pulse ratio on the leaching efficiency of Cr was studied as shown in Figure 4 (pulse ration W/O means without ultrasonic enhancement; pulse ration 2s/5s means ultrasonic enhancement intervals—on for 2s and off for 5s). The results show that the introduction of ultrasonication can improve the leaching efficiency of Cr from chromium sludge and reduce the reaction time. A pulse ratio of 4s/5s was found to be appropriate for the ultrasonication since further increase of the pulse ratio has an adverse effect on the leaching efficiency.

Figure 5 shows the surface morphology changes of sludge particles before and after ultrasonic treatment at 50,000 times magnification. It can be found that there are more cracks and pores on the surface of the particles after ultrasonic treatment, thus improving the surface area of the particles. As a result, the sludge particles can react with the leaching agent more fully to improve the leaching efficiency (Zhang et al., 2017). Figure 6 shows the particle morphology of EPS1 after oxidation leaching with and without ultrasonic treatment at smaller magnification (3,000 times). The results indicated that the overall particle size of sludge particles increased after ultrasonic-enhanced leaching, which means the ultrasonication may cause particle agglomeration (Spengler and Jekel, 2000). Therefore, it is deduced that the influence of ultrasonic enhancement on the leaching process was a result of the combined effect of particle surface destruction and particle agglomeration. The extraction of Cr was substantially enhanced when ultrasonication was introduced since the effect of particle surface destruction plays a more critical role. However, when the ultrasonic pulse ratio exceeds a certain value, the effect of particle agglomeration will become stronger, leading to the decrease of leaching efficiency, which is consistent with the experimental results shown in Figure 4.

3.3 Oxidation leaching of complex sludge

The effects of oxidizer dosage, NaOH dosage, and temperature on the leaching efficiency of Cr, Ni, Cu, and Zn from mixed suldge (EPS2) were investigated as shown in Figures 7,8,9. It is interesting that NaClO exhibited stronger leaching ability than H_2O_2 for the oxidation leaching of Cr from EPS2, which is contrary to the leaching charateristic of EPS1. The reason might be that H_2O_2 can react more easily with the organic matter in the mixed sludge and cause severe decomposition, while NaClO is more stable (Li et al., 2020). The organic matters in the mixed sludge mainly come from the biochemical sludge and oil removal sludge produced during the wastewater treatment stage, and the test results proved that the organic matter content of EPS2 was much higher than that of EPS1, as shown in Table 1. This explanation can also be supported by the experimental phenomena that the reaction is violent and a large amount of bubbles formed when H_2O_2 was added to the mixed sludge, indicating that hydrogen peroxide was decomposed quickly.

On the contrary, NaClO exihibited better leaching ability for Cr and good selectivity against Cu, Ni, and Zn. The experimental results show that the oxidation leaching process can effectively extract chromium from EPS, including a significant portion of the residual fraction, while the more mobile heavy metal elements (Cu, Ni, and Zn) stay in the insoluble form. Hence, the oxidation leaching process can achieve the selective extraction of chromium, which is difficult to achieve through traditional acid leaching or pyrometallurgical process. However, this requires a large consumption of NaClO; the leaching efficiency of Cr reached 56.82% when the molar ratio of NaClO/Cr reached about 75:1. It was indicated that NaClO was also consumed by the organic matters in the mixed sludge, while the reaction was less violent than H_2O_2 and it can still react with Cr and leach it out.

The results of NaOH dosage and temperature condition experiment (Figure 8 and Figure 9) were similar to the experimental results of EPS1, which indicate that proper amount of NaOH is required to ensure the oxidation leaching of Cr and temperature has little effect on the leaching results.

The oxidation leaching of Cr from EPS2 can also be enhanced by ultrasonication, as shown in Figure 10. Similar trends were observed when the ultrasonic pulse ratio increased as the leaching results of EPS1 (Figure 4). The introduction of ultrasonication can enhance the leaching of Cr from the mixed sludge and reduce the reaction time, and 4s/5s is an appropriate ultrasonic pulse ratio for the optimal leaching result.

The electron microscope results of EPS2 (Figures 11, 12) were also similar to those of EPS1. Under the combined effect of particle surface destruction and particle agglomeration, the leaching efficiency of Cr was improved by ultrasonication to a certain extent. Another interesting phenomenon is that the coverings on the surface of the mixed sludge particles seem to be removed after ultrasonicaction, which may facilitate the oxidation reaction on the surface of the sludge particles.

4 Conclusion

The oxidation leaching of two different types of Cr-bearing sludge was studied; the experimental results showed that the two kinds of sludge exhibited different leaching characteristics to different oxidizers. H_2O_2 exhibited stronger oxidation leaching ability for chromium sludge due to its stronger oxidation capacity and reactivity, whereas it is more susceptible to the influence of organic matter in the mixed sludge. NaClO showed higher leaching efficiency of Cr and good selectivity against other heavy metals in the mixed sludge, while a large consumption of dosage was required. The introduction of ultrasonication can strengthen the oxidation leaching for both kinds of sludges as a result of the combined effect of particle surface damage and particle agglomeration. In addition, ultrasound can also remove the coverings on the surface of the mixed sludge particles, which may facilitate the oxidation reaction.

Data availability statement

The original contributions presented in the study are included in the article/Supplementary Material; further inquiries can be directed to the corresponding authors.

Author contributions

KH: conceptualization, methodology, investigation, and writing—original draft; LW: investigation; Yong Wen: resources and supervision; KH: investigation; MZ: investigation; JD: resources, supervision, and writing—review and editing; XH: investigation, supervision, and writing—review and editing.

Funding

The authors express their appreciation for the support of the Fundamental Program of the Special Scientific Research Fund of Central Public Welfare Scientific Research Institutes (PM-zx703-202104-045), the Youth Innovation Fund of Eco environment Remediation Research Center, SCIES (hx_202109_002) and the Guangzhou Science and Technology Planning Project (202201011174).

Conflict of interest

The authors declare that the research was conducted in the absence of any commercial or financial relationships that could be construed as a potential conflict of interest.

Publisher's note

All claims expressed in this article are solely those of the authors and do not necessarily represent those of their affiliated organizations, or those of the publisher, the editors, and the reviewers. Any product that may be evaluated in this article, or claim that may be made by its manufacturer, is not guaranteed or endorsed by the publisher.

References

Arbat, A. G., Fesaghandis, E. A., Tabrizi, A. T., and Aghajani, H. (2020). Comparison of the effect of $NaClO_3$ and H_2O_2 on the molybdenum leaching from molybdenite concentrate[J]. *Trans. Indian Inst. Metals* 73 (9), 2355–2360. doi:10.1007/s12666-020-02036-1

Behin, J., Akbari, A., Mahmoudi, M., and Khajeh, M. (2017). Sodium hypochlorite as an alternative to hydrogen peroxide in fenton process for industrial scale. *Water Res.* 121, 120–128. doi:10.1016/j.watres.2017.05.015

Carneiro, J., Tobaldi, D. M., Capela, M. N., Novais, R., Seabra, M., and Labrincha, J. (2018). Synthesis of ceramic pigments from industrial wastes: red mud and electroplating sludge. *Waste Manag.* 80, 371–378. doi:10.1016/j.wasman.2018.09.032

Chen, H. X., Yuan, H. H., Mao, L. Q., Hashmi, M. Z., Xu, F., and Tang, X. (2020). Stabilization/solidification of chromium-bearing electroplating sludge with alkali-activated slag binders. *Chemosphere* 240, 124885. doi:10.1016/j.chemosphere.2019.124885

Dai, Z. Q., Zhou, H., Zhang, W. Y., Hu, L., Huang, Q., and Mao, L. (2019). The improvement in properties and environmental safety of fired clay bricks containing hazardous waste electroplating sludge: the role of Na_2SiO_3. *J. Clean. Prod.* 228, 1455–1463. doi:10.1016/j.jclepro.2019.04.274

Ding, L., Du, J., and Zhao, Y. (2008). Recovery of chromium from sludge by alkaline oxidizing roasting process[J]. *Environ. Prot. Chem. Industry* 28 (1), 66–69. doi:10.3969/j.issn.1006-1878.2008.01.016

Huang, R., Huang, K. L., Lin, Z. Y., Wang, J. W., Lin, C., and Kuo, Y. M. (2013). Recovery of valuable metals from electroplating sludge with reducing additives via vitrification. *J. Environ. Manag.* 129, 586–592. doi:10.1016/j.jenvman.2013.08.019

Kul, M., and Oskay, K. O. (2015). Separation and recovery of valuable metals from real mix electroplating wastewater by solvent extraction. *Hydrometallurgy* 155, 153–160. doi:10.1016/j.hydromet.2015.04.021

Li, C., Xie, F., Ma, Y., Cai, T., Li, H., Huang, Z., et al. (2010). Multiple heavy metals extraction and recovery from hazardous electroplating sludge waste via ultrasonically enhanced two-stage acid leaching. *J. Hazard. Mater.* 178 (1-3), 823–833. doi:10.1016/j.jhazmat.2010.02.013

Li, Y., Yang, S., Liu, D., Yang, C., Yang, Z., Li, H., et al. (2020). Experimental study of shale-fluids interaction during oxidative dissolution with hydrogen peroxide, sodium hypochlorite and sodium persulfate. *Appl. Geochem.* 113, 104503. doi:10.1016/j.apgeochem.2019.104503

Magalhaes, J., Silva, J., Castro, F., and Labrincha, J. A. (2005). Physical and chemical characterisation of metal finishing industrial wastes. *J. Environ. Manag.* 75 (2), 157–166. doi:10.1016/j.jenvman.2004.09.011

Mahmoudi, D., Tabrizi, A. T., and Aghajani, H. (2021). Study the variation of surface topography & corrosion resistance of Cr-GO nanocomposite coatings by addition of GO nanoparticles. *Surf. Topogr.* 9 (1), 015025. doi:10.1088/2051-672x/abe6f3

Nguyen, V. K., Lee, M. H., Park, H. J., and Lee, J. U. (2015). Bioleaching of arsenic and heavy metals from mine tailings by pure and mixed cultures of Acidithiobacillus spp. *J. Ind. Eng. Chem.* 21, 451–458. doi:10.1016/j.jiec.2014.03.004

Rauret, G., Lopez-Sanchez, J., Sahuquillo, A., Rubio, R., Davidson, C., Ure, A., et al. (1999). Improvement of the BCR three step sequential extraction procedure prior to the certification of new sediment and soil reference materials. *J. Environ. Monit.* 1 (1), 57–61. doi:10.1039/a807854h

Shakiba, S., Khabbazi, N. S., Tabrizi, A. T., et al. (2022). Enhancing the electroplated chromium coating for corrosion protection of aluminum by adding graphene oxide[J]. *Surf. Eng. Appl. Electrochem.* 58 (2), 202–209.

Spengler, J., and Jekel, M. (2000). Ultrasound conditioning of suspensions – studies of streaming influence on particle aggregation on a lab- and pilot-plant scale. *Ultrasonics* 38 (1-8), 624–628. doi:10.1016/s0041-624x(99)00145-6

Veglio, F., Quaresima, R., Fornari, P., and Ubaldini, S. (2003). Recovery of valuable metals from electronic and galvanic industrial wastes by leaching and electrowinning. *Waste Manag.* 23 (3), 245–252. doi:10.1016/s0956-053x(02)00157-5

Verbinnen, B., Billen, P., Coninckxloo, M. V., and Vandecasteele, C. (2013). Heating temperature dependence of Cr(III) oxidation in the presence of alkali and alkaline earth salts and subsequent Cr(VI) leaching behavior. *Environ. Sci. Technol.* 47 (11), 5858–5863. doi:10.1021/es4001455

Wang, M., Gong, X., and Wang, Z. (2018). Sustainable electrochemical recovery of high-purity Cu powders from multi-metal acid solution by a centrifuge electrode. *J. Clean. Prod.* 204 (PT.1-1178), 41–49. doi:10.1016/j.jclepro.2018.09.020

Wu, P., Zhang, L. J., Lina, C. B., Xie, X. x., Yong, X. y., Wu, X. y., et al. (2020). Extracting heavy metals from electroplating sludge by acid and bioelectrical leaching using Acidithiobacillus ferrooxidans. *Hydrometallurgy* 191, 105225. doi:10.1016/j.hydromet.2019.105225

Yan, K., Liu, Z., Li, Z., Yue, R., Guo, F., and Xu, Z. (2019). Selective separation of chromium from sulphuric acid leaching solutions of mixed electroplating sludge

using phosphate precipitation. *Hydrometallurgy* 186, 42–49. doi:10.1016/j.hydromet.2019.03.013

Yang, Y., Liu, X., Wang, J., Huang, Q., Xin, Y., and Xin, B. (2015). Screening bioleaching systems and operational conditions for optimal Ni recovery from dry electroplating sludge and exploration of the leaching mechanisms involved. *Geomicrobiol. J.* 33 (3–4), 179–184. doi:10.1080/01490451.2015.1068888

Yue, T., Niu, Z., Hu, Y., Han, H., Lyu, D., and Sun, W. (2019). Cr(III) and Fe(II) recovery from the polymetallic leach solution of electroplating sludge by Cr(III)-Fe(III) coprecipitation on maghemite[J]. *Hydrometallurgy* 184, 132–139. doi:10.1016/j.hydromet.2018.11.013

Zhang, C., Song, J., Zhang, J., Xing, J., Hu, D., et al. (2018). Understanding and application of an electroplating sludge-derived catalyst with an active texture for improved NO reduction. *Sci. Total Environ.* 631/632, 308–316. doi:10.1016/j.scitotenv.2018.02.290

Zhang, D., Li, M., Gao, K., et al. (2017). Physical and chemical mechanism underlying ultrasonically enhanced hydrochloric acid leaching of non-oxidative roasting of bastnaesite[J]. *Ultrasonics Sonochemistry*, 774–781. doi:10.1016/j.ultsonch.2017.05.020

Zhang, L., Zhou, W., Liu, Y., Jia, H., Zhou, J., Wei, P., et al. (2020). Bioleaching of dewatered electroplating sludge for the extraction of base metals using an adapted microbial consortium: Process optimization and kinetics[J]. *Hydrometallurgy* 191, 105227. doi:10.1016/j.hydromet.2019.105227

Zheng, J., Lv, J., Liu, W., Dai, Z., Liao, H., Deng, H., et al. (2020). Selective recovery of Cr from electroplating nanosludge *via* crystal modification and dilute acid leaching. *Environ. Sci. Nano* 7, 1593–1601. doi:10.1039/d0en00196a

Zhou, C. L., Ge, S. F., Yu, H., Zhang, T., Cheng, H., Sun, Q., et al. (2018). Environmental risk assessment of pyrometallurgical residues derived from electroplating and pickling sludges. *J. Clean. Prod.* 177, 699–707. doi:10.1016/j.jclepro.2017.12.285

frontiers | Frontiers in Chemistry

TYPE Original Research
PUBLISHED 21 September 2022
DOI 10.3389/fchem.2022.989087

Check for updates

OPEN ACCESS

EDITED BY
Xiangning Bu,
China University of Mining and Technology, China

REVIEWED BY
Guojun Ma,
Wuhan University of Science and Technology, China
Yujin Sun,
Taiyuan University of Technology, China
Huaizhi Shao,
Shandong University of Technology, China

*CORRESPONDENCE
Fenglan Han,
2002074@nmu.edu.cn

SPECIALTY SECTION
This article was submitted to Green and Sustainable Chemistry, a section of the journal Frontiers in Chemistry

RECEIVED 08 July 2022
ACCEPTED 09 September 2022
PUBLISHED 21 September 2022

CITATION
Wang J, Han F, Yang B, Xing Z and Liu T (2022), A study of the solidification and stability mechanisms of heavy metals in electrolytic manganese slag-based glass-ceramics.
Front. Chem. 10:989087.
doi: 10.3389/fchem.2022.989087

COPYRIGHT
© 2022 Wang, Han, Yang, Xing and Liu. This is an open-access article distributed under the terms of the Creative Commons Attribution License (CC BY). The use, distribution or reproduction in other forums is permitted, provided the original author(s) and the copyright owner(s) are credited and that the original publication in this journal is cited, in accordance with accepted academic practice. No use, distribution or reproduction is permitted which does not comply with these terms.

A study of the solidification and stability mechanisms of heavy metals in electrolytic manganese slag-based glass-ceramics

Jiaqi Wang[1], Fenglan Han[1,2]*, Baoguo Yang[3,4], Zhibing Xing[1] and Tengteng Liu[1]

[1]School of Material Science and Engineering, North Minzu University, Yinchuan, China, [2]International Scientific & Technological Cooperation Base of Industrial Waste Recycling and Advanced Materials, Yinchuan, China, [3]Ningxia Institute of Geophysical and Geochemical Survey, Yinchuan, China, [4]Hubei Key Laboratory of Yangtze River Basin Environmental Aquatic Science, School of Environmental Studies, China University of Geosciences, Wuhan, China

To better solve the waste pollution problem generated by the electrolytic manganese industry, electrolytic manganese slag as the main raw material, chromium iron slag, and pure chemical reagents containing heavy metal elements mixed with electrolytic manganese slag doping. A parent glass was formed by melting the slag mixture at 1,250°C, which was, thereafter, heat-treated at 900°C to obtain the glass-ceramic. The results from characterizations showed that the heavy metal elements in the glass-ceramic system were well solidified and isolated, with a leakage concentration at a relatively low level. After crystallization, the curing rates of harmful heavy metals all exceed 99.9%. The mechanisms of heavy metal migration, transformation, and solidification/isolation in glass-ceramic curing bodies were investigated by using characterization methods such as chemical elemental morphological analysis, transmission electron microscopy, and electron microprobe. The most toxic Cr and Mn elements were found to be mainly kept in their residual state in the glass-ceramic system. It was concluded that the curing mechanism of the heavy metals in a glass-ceramic can either be explained by the chemical curing induced by bonding (or interaction) during phase formation, or by physical encapsulation. Characterization by using both Transmission electron microscopy and EPMA confirmed that Cr and Mn were mainly present in the newly formed spinel phase, while the diopside phase contained a small amount of Mn. Zn, Cd, and Pb are not found to be concentrated and uniformly dispersed in the system, which is speculated to be physical coating and curing.

KEYWORDS

glass-ceramic, heavy metal contamination, curing/stabilization, electrolytic manganese slag, solid-waste management

1 Introduction

With the continuous expansion of the production of electrolytic manganese metals (EMMs), the waste residues, which are also produced in the process, are also increasing. The electrolytic manganese slag (EMS) comes predominantly from the following three processes in the electrolytic production of metal manganese: sulfuric acid leaking, oxidation iron removal, and pressure filtration removal of impurities (He et al., 2021; Zhou, 2021). With the existing EMMs production technology, every ton of produced manganese metal generates 10–12 tons of EMS (Ning et al., 2010). After decades of development, China alone has an inventory of over 100 million tons of EMS that, in the year 2020, has not been properly taken care of. And, with the continuous reduction of manganese ore resources in nature, the rate of new EMS production will exceed 10 million tons per year (He et al., 2021). Most of these manganese-containing waste residues are stored in dams and have not undergone any harmless form of treatment. Thus, they will not only occupy a large area of land resources but do also constitute a severe problem in terms of environmental safety. In the years 2010–2012, serious manganese slag dam failures and leaks did occur in Hunan, Sichuan, and Guizhou, which caused significant economic losses as well as environmental pollution. If the landfill of manganese slag is not in place to prevent seepage and major leakages, the manganese will seep into the soil and groundwater. This will cause serious problems in especially rainy areas. Coupled with the perennial weathering, the fine manganese slag particles will enter the atmosphere, becoming a great threat to environmental safety and human health (Röllin and Nogueira, 2011; Miah et al., 2020). The realization of harmless treatments and resource utilization of EMS is, therefore, a key step toward the sustainable development of the EMMs industry.

Many research groups around the world have performed a vast number of experimental studies in this direction. Shu et al. (2019) et al. compared the removal effects of hydroxide precipitation, sulfide precipitation, and carbonate precipitation on manganese and ammonia nitrogen in EMS. They found that the carbonate precipitation method is more efficient than the other two methods. For a C/Mn molar ratio of 1.1:1, and a pH value of 9.5 Mn was found to be excluded in the form of $MnCO_3$, with a removal rate up to 99.9%. Furthermore, for a P/N molar ratio of 1.1:1, and a pH value of 9.5, ammonia nitrogen could be removed in the form of magnesium ammonium phosphate, with a removal rate as high as 97.4%. Xu et al. (2019) used a combination of EMS, blast furnace slag, and cement clinker to prepare cementitious materials. A mixture containing 15% EMS was shown to give the best material performance, with a flexural strength of 6.8 MPa, compressive strength of 32.9 MPa, and a 28 days strength of up to 52.5 MPa. And the heavy metals contained in the EMS in the system can be solidified well, and the levels of manganese and other heavy metals, as well as ammonia nitrogen, have reached the emission level of the national standard. However, the current methods cannot completely and effectively realize the harmless and resourceful treatment of EMS. This is mainly due to the disadvantages with a complex treatment process, excessive cost, low consumption of industrial waste residues, and unstable treatment of harmful elements.

In addition to electrolytic manganese slag, the production of solid waste chromium slag in the growing chromium salt industry causes serious pollution problems. The chromium slag composition is relatively complex. It is often composed of a variety of oxides, and accompanied by calcium chromate, magnesium chromate, and other carcinogenic substances. The chromium slag in addition to chromium, iron, magnesium and aluminum and other metal elements, but also contains highly toxic Cr (VI). The Cr (VI) ion in the chromium slag is characterized by a high content and high mobility. It can pollute soil, surface water, and groundwater, thus posing a threat to human beings and the surrounding ecological environment (Liu et al., 2020). A treatment of the chromium slag is, therefore, necessary to protect the environment and human health.

At present, the harmless treatment of chromium slag includes two categories; dry and wet methods (Zhang et al., 2013). However, wet detoxification of water and salt detoxification cannot effectively remove the acid-soluble hexavalent chromium ions. Furthermore, acid detoxification can be complete, but the acid dosage is large and there are high operating costs. There is also a problem with the outlet for the treated slag. Poor environmental safety stability of chromium slag after detoxification using alkaline methods. In addition, the wet detoxification method requires the addition of chemicals, and one must pay attention to not introduce new pollutants. The dry detoxification methods mainly use detoxification in the processes of cement making and iron sintering, as well as detoxification using a rotary kiln equipment. The detoxification in the process of cement making does mainly use a vertical kiln method, and this method is listed as a priority by the national industry restructuring. The usage has been reduced year by year, so this method is not a long-term alternative. The detoxification in the process of iron sintering is a complete method, and has a high potential for resource utilization. However, it is required that the treated chromium slag has a large quantity and a relatively stable composition. At the same time, there must also be available sintering iron-making equipment around the enterprise, otherwise there is a greater environmental risk problem in the process of long-distance transfer of chrome slag. In summary, the current harmless treatment of chrome slag has problems with an incomplete detoxification, high operating costs, and high environmental risks. In recent years, glass-ceramics have attracted more and more attention due to their excellent curing performance and good corrosion resistance, and are widely used in building materials, medical, industrial, and other fields (Zhao et al., 2021b). Chen et al. (2020) successfully synthesized high-

TABLE 1 Chemical composition of electrolytic manganese slag and chromite slag (wt%).

Material	SiO_2	Al_2O_3	CaO	MgO	Fe_2O_3	Cr	Mn	S	Other
Ferrochrome slag	27.70	15.70	2.80	32.10	2.90	2.06	0.15	—	16.58
Electrolytic manganese slag	51.28	10.74	18.87	3.94	3.57	0.01	2.57	0.82	8.20

calcium glass-ceramics by using ferromanganese-manganese slag as the main raw material and improving its crystallization by adjusting the content of Al_2O_3. The mass fraction of ferromanganese slag is 72.4%–88.7%. When the Al_2O_3 content is 11%, the flexural strength of the sample is 67 MPa and water absorption is 1.8%. Considering that there are a lot of SiO_2, CaO, Al_2O_3, and MgO in the slag, the composition is like that of glass-ceramics. Slag containing MnO_2, Fe_2O_3, and Cr_2O_3 can be used as an excellent nucleating agent. The large amount of energy consumed in the process of sulfur removal by high-temperature calcination of electrolytic manganese slag can be used as the condition of the melting stage. Based on the above analysis, the smelting process can be considered to prepare glass ceramics with electrolytic manganese slag as raw material and solidified heavy metal elements to achieve harmless treatment (Shu et al., 2020; Sun et al., 2020).

The harmless treatment of heavy metal elements in slags is not only depending on the presence and type of heavy metals in the system, but also their form, migration behavior, and solidification efficiency. The CMAS (CaO-MgO-Al_2O_3-SiO_2) series of glass-ceramics have in the present study been successfully prepared from EMS. Furthermore, the degree of leakage, distribution of solidification, migration, and transformation of harmful heavy metal elements in glass-ceramics, have been studied and discussed. A comprehensive toxicity index model (STIM) was also established by calculating the potential toxicity of the various elements. It has generally been used to illustrate the ecological threat severity of heavy metals (Liu et al., 2008). In addition, the solidification mechanism of heavy metals has also been described in the present study. In addition, except for the pure chemical reagents used to simulate the composite heavy metal slag system, 100% of the slag is used as raw material, which saves cost and is in line with the concept of "treating waste with waste". The finished glass ceramics have excellent performance, can meet the industrial use standard, and the leaching level of harmful heavy metals is also within the safe range. It can provide an effective way and choice for dealing with heavy metal pollution of solid waste.

2 Experimental

2.1 Sample preparations

The electrolytic manganese slag and ferrochrome slag that was used in the experiments in the present study were collected from an electrolytic manganese enterprise in China. The compositions of the two slag materials are presented in Table 1. The electrolytic manganese slag was subject to high-temperature calcination and de-sulfurization treatment, but the ferrochromium slag was not pre-treated. After both slags were retrieved from the enterprise, it was dried at 105°C for 1 h. It was, thereafter, crushed and ground into powder (after cooling) and passed through a 200-mesh sieve (with a particle size ≤75 μm). In addition to ferrochrome slag as well as electrolytic manganese slag, the chemicals used in the experiment include cadmium nitrate ($CdN_2O_6.4H_2O$), lead oxide (PbO), hydrofluoric acid (HF), concentrated sulfuric acid (H_2SO_4), and concentrated nitric acid (HNO_3) (Shanghai Hushi Laboratorial Equipment, China, CP), as well as zinc oxide (ZnO) and sodium hydroxide (NaOH) (Tianjin Kemiou Chemical Reagent, China, CP).

2.2 The preparation of glass-ceramics

Based on the results of XRF analysis, there were, with one exception, low concentrations of heavy metal elements in the electrolytic manganese slag. The ferrochrome slag was, therefore, selected for the preparation of glass-ceramics in the present study, in addition to pure chemicals containing Pb, Cd, and Zn. The latter ones were added to simulate a slag system containing a variety of heavy metals and blended with electrolytic manganese slag. The resulting material systems were used in the investigation of the effect of the glass-ceramic curing process on the curing of heavy metals in composite systems.

In the raw material systems, the ratio of electrolytic manganese slag to ferrochromium slag was 9:1, and the total mass of the mixed slag is regarded as 100%. The additional pure chemical added is calculated by the heavy metal monomeric elements contained therein and the corresponding mass of the chemical is weighed. The raw materials, with a total weight of about 50 g, were then mixed and stirred in a pot mill for 2 h.

Since the mass ratios of Cr and Mn were constant in the different samples, the addition of the three heavy metal elements (Pb, Cd, and Zn) could be used as experimental variables. The raw material samples are presented in Table 2.

The raw material was, thereafter, placed in a corundum crucible and heated to above 1,250°C in a muffle furnace (KSL-1400X-A3, China). It was then kept for 150 min after which the material had melted into a glass liquid. The sample was, thereafter, immediately transferred to a preheated mold and

TABLE 2 Amount of heavy metal elements added to each group of samples (wt%).

	Pb	Cd	Zn	Total
GC-1	1.0	1.0	1.0	3.0
GC-2	1.0	1.0	1.5	3.5
GC-3	1.0	1.5	1.0	3.5
GC-4	1.0	1.5	1.5	4.0
GC-5	1.5	1.0	1.0	3.5
GC-6	1.5	1.0	1.5	4.0
GC-7	1.5	1.5	1.0	4.0
GC-8	1.5	1.5	1.5	4.5

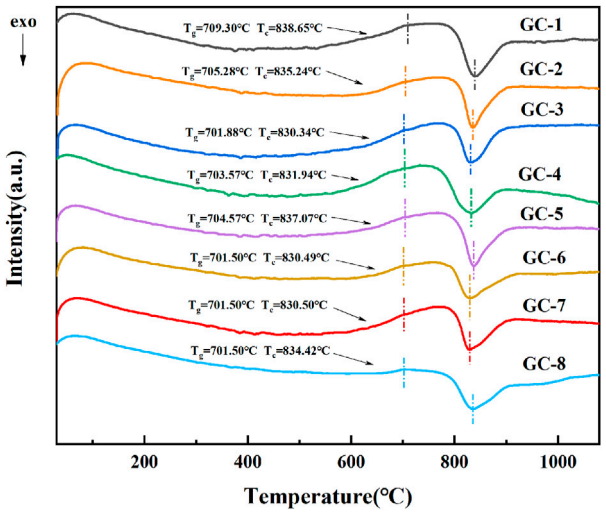

FIGURE 1
DSC spectra of different types of parent glass. (Exo: exothermic direction; T_g: glass transition temperature; T_c: crystallization temperatures; GC-1-8: Sample number).

kept in a muffle furnace for further annealing treatments. A parent glass was formed at the end of these annealing treatments (at specific holding times) and after cooling at room temperature.

A part of the parent glass was taken for grinding treatments, and the thereby formed glass powder was analyzed by using differential scanning calorimetry (DSC, STA 449 F3, Germany). When the raw material system reaches the transition temperatures (T_g), it softens and absorbs heat, resulting in a slope in the endothermic direction on the curve. When the temperature reaches the crystallization temperatures (T_c), crystals are precipitated in the system, and the arrangement of molecules changes from irregular to order. This process gives off heat and a clear exothermic peak appears on the curve. The heat treatment system could, based on these results, then be determined. The DSC results are shown in Figure 1.

The position of the crystallization peak in the DSC curve is about 830°C, and the heat treatment temperature is generally set at 50°C higher than the crystallization temperature. Therefore, the basic glass was held at 900°C for 150 min to complete the nucleation process, and the sample was cut and polished to obtain glass ceramics.

2.3 Sample characterization

X-ray diffraction (XRD; Shimadzu XRD 6000, Japan) was used to qualitatively analyze the phases in the samples. The following experimental parameters were used: working voltage = 40 k; working current = 30 mA; Cu-Kα ray; scanning rate = 2 / min: step size = 0.02°: 2θ Range = 10–80°. The chemical composition of the slag in the raw material was detected by using X-ray fluorescence spectroscopy (XRF, ZSX Primus II, Japan). A flat and regular glass-ceramic block was selected for the measurements. It was immersed in a 5% volume fraction of HF for more than 30 s and, thereafter, ultrasonically cleaned and dried. The morphology of the cleaned sample was analyzed by using an electron scanning microscope (SEM; Zeiss SIGMA 500, Germany). Moreover, the distribution of heavy metals in the glass-ceramic sample was investigated by using an electron probe microanalyzer (EPMA; Shimadzu EPMA-1720H, Japan) under the following experimental conditions: acceleration voltage = 15 kV; current = 50 nA; beam spot diameter = Min; step diameter = 0.1 μm; test time = 5 ms/point. The finely ground sample powder that should be analyzed was dispersed in ethanol, and the upper layer of the liquid (with the powder) was transferred to the sample holder and dried. Furthermore, a block sample was prepared by using FIB-SEM (Focused Ion Beam Scanning Electron Microscopy) by which it is possible to form a very thin test sample. Field emission transmission microscopy (TEM, JEM-2100, Japan) was, thereafter, used for the characterization of the microstructure of these very thin samples. An acceleration voltage of 200 kV, and a linear resolution less than, or equal to 0.14 nm were used for these measurements. Moreover, the binding energies of the electrons in the samples were characterized by using X-ray photoelectron spectroscopy (XPS; ESCALAB Xi+, United States). In this analysis, the pass energy was 20 eV, the number of scans was 5, and the energy step size was 0.05 eV (since the adsorption of carbon introduces some errors in the measurements). Also, the XPS curve was fitted by using the binding energy of C1s (284.8 eV). With reference to the HJ/T 299-2007 Chinese environmental protection standard (HJ/T 299-2007, solid waste—extraction procedure for leaching toxicity—sulphuric acid and nitric acid method), the heavy metals in the glass-ceramics were extracted. In this extracted solution, the concentration of Cr(VI) was determined according to the Chinese national standard GB/T 15,555.4-1995 (GB/T 15,555.4-1995 Solid waste-Determination of chromium (VI)-

TABLE 3 STIM toxicity parameters and values.

Model parameters	Parameter value				
E_j	E1 = 0.65	E2 = 0.4	E3 = 0.2		E4 = 0
Heavy metal	Zn	Pb	Cd	Mn	Cr
T_i	1	5	30	1	2
Ci N (mg/kg)	58.8	20.6	0.11	524	60.6

1,5-Diphenylcarbohydrazide spectrophotometric method), and the concentrations of the other elements were measured by using ICP-MS(Inductively Coupled Plasma-Mass spectrometry). The heavy metal leaking rate, η, is expressed by Eq. 1 as a demonstration of the curing effect of the glass-ceramics.

$$\eta = C_T / C_{T0} \tag{1}$$

where C_{T0} is the total concentration of heavy metals in the system, and C_T is the concentration of heavy metals that have leaked from the sample.

The Synthesis Toxicity Index Model (STIM) can be used to evaluate the toxicity of the different heavy metals in the glass-ceramic curing systems. By using this model, the pH of the leakage in the BCR test has here been used to determine the values of bioavailability. The resulting values of bioavailability in the acid leaking state, reduction state, and oxidation state became 0.65, 0.4, and 0.2, respectively. A good environmental stability is needed for the residue state, and it is less likely to migrate than the states. Hence, bioavailability value for the residue state has been set to 0. See Table 3 for other specific parameter settings.

The mathematical expression of the STIM is:

$$STIM = \sum_{i=1}^{n} \left[T_i \left(\sum_{j=1}^{m} E_j Q_i^j / C_n^i \right) \right] \tag{2}$$

where n is the number of heavy metal species, m is the number of the formed chemical species (m = 4), T_i is the toxicity response coefficient of the *i*th heavy metal (Hakanson, 1980; Xu et al., 2008), E_j is the chemical form j of the *i*th heavy metal bioavailability, Qj i is the content of the *i*th heavy metal chemical form j, and Ci N is the background value of the *i*th heavy metal in the natural environment. The background value of the local soil element in Ningxia has been used in this study (State Environmental Protection and China Environmental Monitoring, 1990).

The hardness of the glass-ceramic samples was tested by using a force of 5,000 g and a micro-Vickers hardness tester (432SVD, China). Furthermore, the flexural strength of glass-ceramic sample strips (of size 4 mm × 4 mm × 40 mm) was tested by using a universal testing machine (CMT5305, China). Measurements and calculation of the density, and water absorption of glass-ceramic samples are tested by Archimedes drainage. The acid and alkali resistance of the glass-ceramic samples was also evaluated by calculating the mass loss of the samples before and after immersion in 1% (v/v) H_2SO_4 and 1% (m/m) NaOH for 650 h, respectively. These tests were performed in triplicate to ensure the accuracy and reliability of the results. Calculated average values were used as the final data.

3 Results and discussion

3.1 Physical and chemical properties of glass-ceramics

After the final micro-crystallization of the parent glass, the stability of the cured bodies of harmful heavy metal elements has become closely related to the performance of the final glass-ceramic material. In the process of this crystallization, the generated crystalline phase has become intersected with the glass, forming a dense structure that can seal and isolate heavy metals and, thereby, play an encapsulating role. A higher density of the glass-ceramic system is correlated with improved cladding and improved stability of the heavy metal elements in the system. In addition, sintering occurs between the raw material powder particles during the preparation of the glass-ceramic, which makes the structure of the curing body denser and the surface flatter. The water absorption of the glass-ceramic can thus be kept at a low level. The reduction of water absorption will prevent harmful elements from leaking into the interior of the curing body, and make it difficult for corrosive liquids (such as acids and bases) to attack the system. This will, together with the excellent physical and mechanical properties of the curing system, ensure that the curing body material can still maintain its integrity when subjected to external forces. New exposure of surfaces, to the environment, can thereby be avoided, i.e., the interaction of heavy metals with the environment will be inhibited. In short, the better the physical and chemical properties of the curing system, the better its curing effect. The performance test results of each group of prepared samples are shown in Figure 2. However, the difference in performances, for each component, is not obvious. However, GC-6 show the best performance, with a density of 3.05 g/cm^3, a water absorption rate of 0.04%, a flexural strength of 107.35 MPa, a Vickers hardness of 6.67 GPa, an acid resistance of 99.38%, and an alkali resistance of 99.86%. In fact, the overall performance of each glass-ceramic sample meets, and even exceeds, the requirements of China building materials industry standard (JC/T 2097-2011, glass - ceramics plate for industrial application).

3.2 Analysis of the glass-ceramic curing ability

3.2.1 Analysis of toxicity leakage

The content of each element in the materials has been analyzed by using XRF. The experimental content of the two

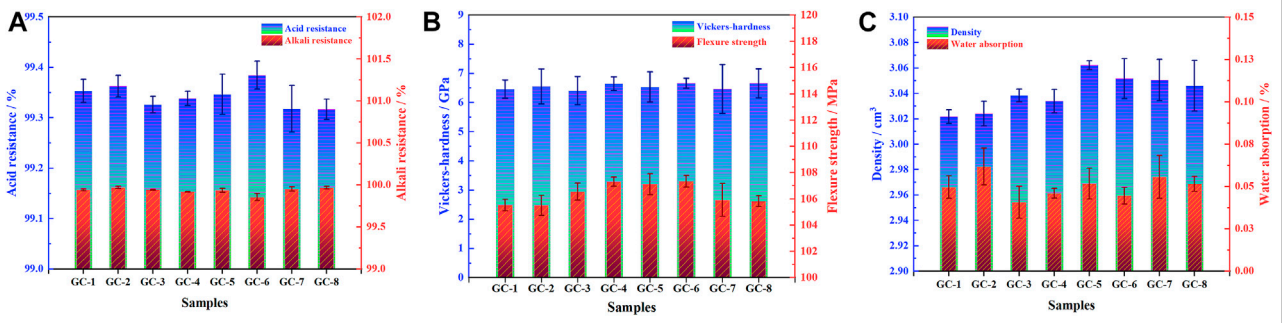

FIGURE 2
Physical and chemical properties of glass-ceramic solidified bodies. **(A)** Acid resistance and alkali resistance; **(B)** flexural strength and Vickers hardness; **(C)** density and water absorption rate.

TABLE 4 The leakage concentration of heavy metals in the toxicity leakage experiment (mg/L).

Samples	Cr (VI)	Cr	Pb	Cd	Zn	Mn
Ferrochrome slag	66.79	73.74	≤0.01	≤0.005	≤0.001	6.74
Electrolytic manganese slag	0.51	1.72	≤0.01	≤0.005	≤0.001	870.06
GC-1	≤0.01	0.01	0.96	0.88	0.45	1.64
GC-2	0.01	0.02	1.14	0.79	0.60	1.85
GC-3	0.01	0.02	0.68	0.57	0.83	1.20
GC-4	0.01	0.02	0.79	0.60	0.42	1.52
GC-5	≤0.01	0.01	0.79	0.93	0.59	1.55
GC-6	≤0.01	≤0.01	1.16	0.54	0.25	1.10
GC-7	0.01	0.02	1.05	0.60	0.74	1.60
GC-8	0.01	0.02	1.02	0.49	0.46	1.37
Toxicity threshold	5[a]	15[a]	5[a]	1[a]	100[a]	2[b]

[a]GB 5085.3-2007 Hazardous Waste Identification Standard Leaking Toxicity Identification.
[b]GB 8978-1996 Integrated Wastewater Discharge Standard.

heavy metal elements, Cr and Mn, was found to be identical with the contents in the two kinds of slag materials: ferrochrome slag and electrolytic manganese slag. In addition, the content of Cd, Pb, and Zn in the original slag materials were negligible, so the addition of these elements in the glass-ceramic samples could be directly selected as the experimental content (as presented in Table 2).

The environmental damage caused by electrolytic manganese slag and ferrochromium slag can basically be attributed to the excessive content of Mn and Cr. The mass percentage of Mn in the electrolytic manganese slag was about 2.57%, and the mass percentage of Cr in the ferrochromium slag was 2.06%. The form of Cr that most easily diffuses into the environment is Cr (VI), which is carcinogenic. The content of Cr (VI) in the ferrochrome slag has, thus, severe toxicological effects on the environment. Therefore, the leaching and diffusion behavior of Cr (VI) has in the present study been given great attention in the toxicological leaching tests. However, the content of Cu, Co., Ni, Hg, and As in the mixed slag system was lower than the detection limit of ICP, so the present study did not consider the hazardous risks with these elements.

The toxicity leakage experiment was designed with reference to the HJT 299-2007 Chinese environmental protection standard, and Table 4 shows the concentration of heavy metals involved in the leakage experiment. The Cr (VI) element in the ferrochromium slag, and the Mn element in the electrolytic manganese slag, were 13 times and 430 times higher than the safe discharge standards, respectively. There were, thus, immense potential risks with these slags. After nucleation crystallization treatment, the leakage concentration level became much lower than the total elemental content in the feedstock system. The experimental results were compared with the allowed emission standard values (GB 5085.3-2007, Identification standards for hazardous wastes identification for extraction toxicity; GB 8978-1996, Integrated wastewater discharge standard). The results showed that the levels of all heavy metals were below the

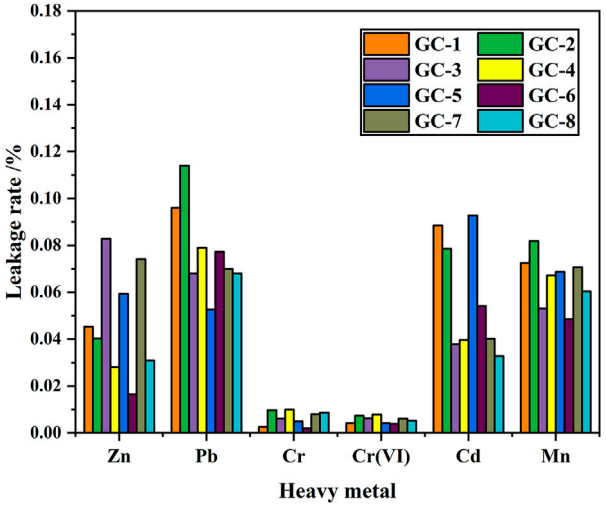

FIGURE 3
Leakage rate of heavy metals in glass-ceramic samples.

safety regulatory limits. This was especially the situation for the Mn and Cr (VI) levels, which were initially remarkably high in the original slag materials. This shows that by preparing a mixture of electrolytic manganese slag and ferrochrome slag, and transfer it into a glass-ceramic, the environmental toxicity of the heavy metals will be reduced very effectively.

By comparing the leaching rates of several heavy metals, we have found that when the contents of the heavy metal elements are similar, the order of the solidification effect becomes: Cr (VI) > Mn > Zn > Cd > Pb, with solidification rates that all exceed 99.9%. Moreover, the curing efficiency of Cr (VI) was found to be the best, with the efficiency of larger than 99.99%. The leakage rate for each heavy metal element, in each curing system, is shown in Figure 3. It has been shown that the solidification in the glass-ceramics will effectively reduce the released amount of heavy metal elements. This is especially the situation for the environmentally most hazardous Mn and Cr (VI) elements. However, it should be noted that although the content of the other three heavy metal elements is lower than those of Cr and Mn, the level of solidification efficiency of Mn and Cr is higher. The reason is that both Mn and Cr act as nucleating agents during the preparation of the glass-ceramic samples. When the temperature is higher than the glass transition temperature, the Cr ions will attract the surrounding Fe, Mn, and Mg ions to form the spinel phase. Furthermore, when the temperature is increased to the crystallization temperature, the existence of the spinel phase can act as a heterogeneous nucleation core. It makes it easier to achieve the conditions required to produce a diopside phase, which precipitates and grows on the surface of the spinel phase. Thus, both Mn and Cr will more easily end up in the interior of the crystalline lattice and to become solidified and sealed (which also improves the microcrystalline structure to a certain extent). As a matter of fact, the crystallinity of the glass-ceramic will improve the solidification degree of also other heavy metal elements, as compared with the situation where only a single heavy metal element exists.

3.2.2 Chemical analysis of heavy metal elements

The curing stability of the heavy metals contained in the glass-ceramics and parent glass was found to be mainly related to the state of the heavy metal elements in the curing system and the curing bonding method. The experimental samples in groups 1 and 8 (i.e., with the lowest and highest additions of heavy metal elements) and the experimental sample in group 6 (with the best overall curing effect) have here been selected. The transient states of the five heavy metals in the parent glass, and in the glass-ceramic samples, were then tested by using the BCR (Community Bureau of Reference) extraction method. The glass-ceramic samples used for these tests were GC-1, GC-6, and GC-8, and the parent glass samples were G-1, G-6, and G-8. The BCR results are shown in Figure 4.

The heavy metal Cr element has been found to be predominantly in its residual state in both the glass-ceramic and in the solidified parent glass. The residual state of Cr in GC-1, GC-6, and GC-8 accounts for 99.49%, 98.59%, and 99.45%, respectively. Furthermore, it accounts for more than 98% in the parent glass samples. Moreover, the heavy metal Mn element was found to be predominantly in the form of its residual state and an oxidized state in the parent glass. The residual state accounts for about 60% and the oxidized state for about 15%. After heat treatment (i.e., after micro-crystallization), the percentage of oxidized state has become significantly reduced to a level of only about 7%, while the percentage of the residual state has increased to about 70%. Furthermore, the proportion of the heavy metal Cd element in its residual state has changed significantly, from about 65% in the parent glass to about 75% in the glass-ceramic. The proportion of the oxidized states in G-1,G-6, and G-8 became 15.10%, 17.35%, and 10.38%, respectively. Also, the proportion of the reduced states became 12.66%, 13.72%, and 9.47%, respectively. As a result of the heat treatment, these states became reduced to 4.34%, 7.56%, and 8.44% (oxidized state) and 8.08%, 11.88%, and 9.04% (reduced state). Furthermore, the heavy metal Zn element was found to exist in both the form of its residual state and the oxidation state in the solidified body of the parent glass. In the G-1, G-6 and G-8 samples, the percentage of the residual state was 77.67%, 78.48%, and 71.75%, respectively, and the percentage of the oxidation state was 9.71%, 10.13% and 11.43%, respectively. In the glass-ceramics GC-1, GC-6 and GC-8 samples (i.e., after heat treatment), the proportion of the residual state was observed to increase to about 90% for all three samples, and the proportion of the oxidized state was observed

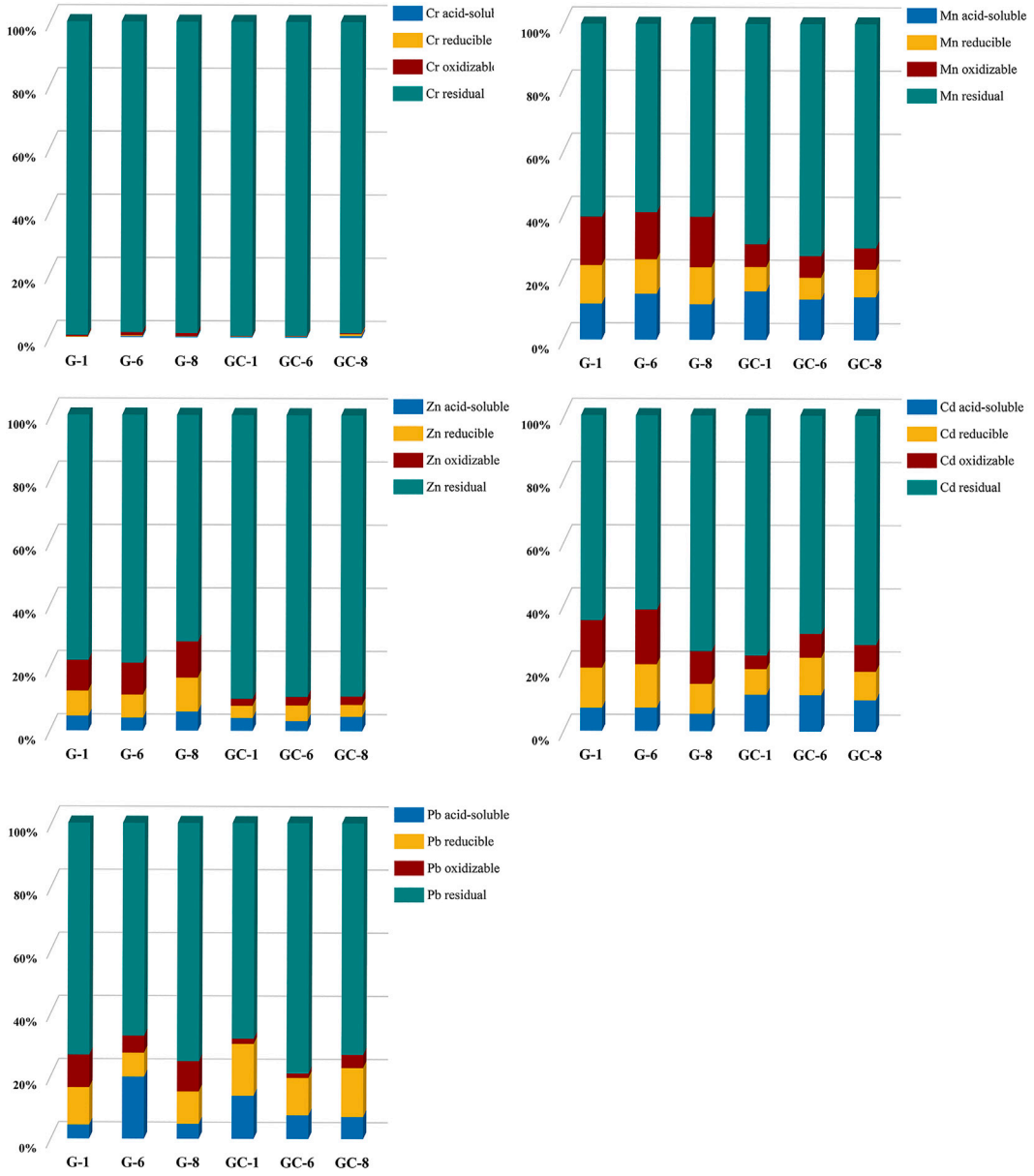

FIGURE 4
Distribution of Cr, Mn, Zn, Cd, and Pb elements in the parent glass and in glass-ceramic samples.

to decrease to 2.21%, 2.70%, and 2.69%, respectively. Furthermore, the oxidized state of the heavy metal Pb element was found to decrease from 10.37%, 9.59%, and 5.39%–1.64%, 4.19%, and 1.47% for the GC-1, GC-6, and GC-8 samples, respectively. In addition, the proportion of the Pb residual state in the glass-ceramic was also found to be higher than its level in the parent glass.

In a comparison of the two states (i.e., the residual state and the oxidized state) in the parent glass and in the glass-ceramic samples, the percentage of Cr, Mn, Cd, Pb, and Zn, in the residual state was observed to increase in glass-ceramic after heat treatment. The percentage of the more unstable acid leaked, oxidized and reduced states in the environment is significantly lower than that of the residual state, especially for the heavy metal Cr element. This is an indication on the fact that after crystallization treatment, the heavy metal elements do all change from the unstable state to the stable one. Thus, the stabilization of the heavy metals in the glass-ceramic has been further improved, as compared with the corresponding parent glass.

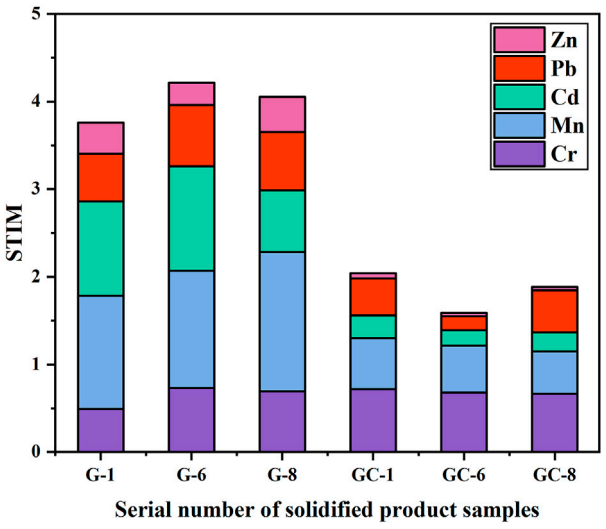

FIGURE 5
Comparison of STIM indices for heavy metal elements in the parent glass and in the glass-ceramic samples.

3.2.3 Comprehensive toxicity assessment of the heavy metals

The ability of the heavy metal elements to migrate and transform in the environment, and their effects on the external conditions, has in the present study been examined by performing a leakage toxicity analysis and a chemical element analysis. However, the potential long-term toxicity effects by the heavy metals in the environment are not only related to the content of these elements, the activity of their chemical forms, and the level of leakage toxicity, but also to their chemical activity and bioavailability. A research group has previously established heavy metal toxicity assessment models by which it is possible to estimate the potential harm heavy metal elements can make to the environment (Zhang, 2016a). In the present study, STIM was been used to evaluate the degree of hazardous for each of the heavy metal elements in the glass-ceramic curing system (Luan et al., 2016).

The results from the heavy metal toxicity analysis, for each group of glass-ceramic solidified bodies, can be seen in Figure 5. Eq. 2 has been used for these calculations.

The comprehensive toxicity indices of the parent glass samples G-1, G-6, and G-8 were found to have values between 3 and 4. Moreover, the STIM indices of the glass-ceramic samples GC-1, GC-6, and GC-8 were all found to be less than, or equal to, 2. Of all heavy metal elements studied in the present investigation, Cr and Mn are the main causes to environmental toxicity. As can be seen in Figure 5, the STIM indices of the glass-ceramic samples GC-1, GC-6, and GC-8 are all smaller than those of the corresponding parent glass samples (i.e., G-1, G-6, and G-8). Thus, the glass-ceramics have been found to effectively reduce the potential pollution risk of heavy metal elements in the ecological environment.

3.3 Heavy metal solidification mechanism

Figure 6A shows the XRD results for each glass-ceramic system (i.e., GC-1, GC-2, GC-3, GC-4, GC-5, GC-6, GC-7, and GC-8). It is obvious that all systems contain both diopside and spinel crystalline phases. The main crystalline diopside phase, tremolite, has a dendritic structure with a width of 1–2 μm (see the SEM images in Figure 7). Furthermore, it has been speculated that the generation of the spinel phase is due to the presence of Cr_2O_3 and Fe_2O_3 in the systems. The "ferrophilicity" and "oxyphilicity" exhibited by Cr^{3+}, and the large field strength induced by the ion itself, will easily interact with the surrounding Mg and Fe plasma agglomerates. Therefore, in the nucleation stage, were the melted system reaches the glass transition temperature, the elements dominated by Cr, Fe, Mn, and Mg have produced inhomogeneous enrichment areas and, thereby, formed spinel phases (Zhao et al., 2019a; Zhao et al., 2019b).

The GC-0 group was added to the group of glass-ceramics to verify the cause of spinel production. The ratios of raw materials in this specific group were identical to those of the CG-6 group (which showed the best curing effect on the heavy metals). As was the situation with the other groups in the present study, the uniformly mixed slag material was annealed until it melted. According to the DSC test results, the nucleation and crystallization temperatures of GC-0 were 700°C and 830°C, respectively. For the nucleation of GC-0, the temperature was kept fixed at 720°C for 2 min. The hereby obtained nucleated glass was named $GC_{2,0}$, and an XRD analysis was performed at this specific nucleation stage (see Figure 6B). It was found that after a short period of nucleation, only the spinel phase appeared in the system. This is a strong indication on the fact that the process of spinel generation started already in the nucleation stage.

The $GC_{2,0}$ material was also analyzed by using SEM and EDS. A small-scale structure, in the form of an octahedron, can be seen in the SEM image in Figure 7. This is most probably the spinel phase that has been generated in the system. Moreover, the EDS results indicate that the material phase contains Cr and Fe elements and has a low Ca content (see Figure 7). This result is also consistent with the spinel characteristics.

$GC_{2,0}$ was further subject to crystallization treatment at 900°C for 1 min, and the obtained crystallized glass was named $GC_{2,1}$. As can be seen in the SEM images of $GC_{2,1}$ in Figure 7, the spinel nuclei have agglomerated and has developed into a typical dendritic pyroxene crystalline structure. This observation gives evidence to the conclusion that the spinel phase has served as a heterogeneous nucleus for the main crystalline phase, tremolite. In other words, the generation of

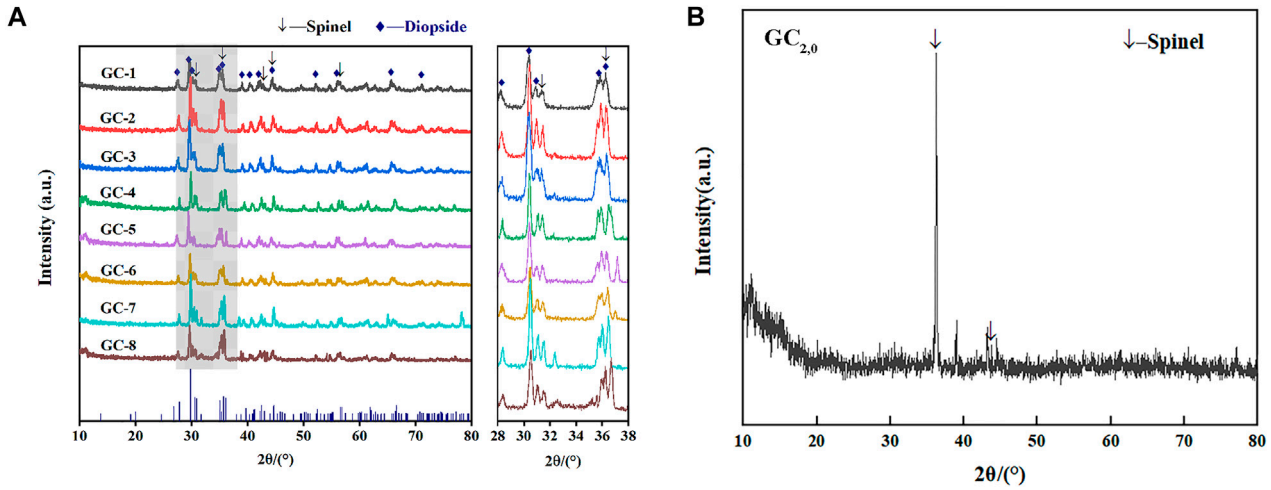

FIGURE 6
Comparison of XRD patterns for each group of glass-ceramic samples. **(A)** XRD patterns of GC1-8 samples; **(B)** XRD patterns of $GC_{2.0}$ sample.

tremolite was induced by the spinel structure (Shi et al., 2018; Ayala Valderrama et al., 2019).

Moreover, Figure 8 shows low- and high-resolution TEM images of the GC-6 sample. Figures 8A–C are images of glass-ceramic powder samples that have passed through a 200-mesh sieve, and Figures 8D,E, and f are images of the FIB-SEM ion thinning samples. The observation and study of the microstructure revealed that the crystalline phase in the system is distributed a small-sized structures that are interleaved with the glass phase. Distinct regions of lattice diffraction streaks can be observed in the high-resolution TEM images in Figures 8B,C. These streaks are not uniquely oriented, with a small amount of an amorphous phase surrounding the region where the crystalline phase region. As demonstrated in Figures 8D,E, the samples were also analyzed by using high-resolution TEM on the ion-thinned samples. Uniform and regular crystal diffraction streaks were then observed, with no obvious amorphous regions. Moreover, only regular diffraction spots appeared in the SAED plot shown in Figure 8F, with no continuous diffraction rings. This indicates that the proportion of the crystalline phase in the glass-ceramic sample is much higher than the proportion of an amorphous phase. The diffraction stripe spacing in the regions shown in Figures 8B,C,E has also been analyzed by using the GMS 3 software. It was possible to find crystal regions with a diffraction stripe spacing of 0.299 nm and 0.323 nm that belong to the (−2 2 1) and (2 2 0) crystal planes of perovskite ($Ca_{1.022}(Mg_{0.857}Fe_{0.122})$ $((Si_{1.877}Fe_{0.144})$ $O_6)$, PDF # 89-0834), respectively. Moreover, the crystalline facets with 0.251 nm and 0.257 nm stripe spacing were found to belong to the (3 1 1) crystalline facets of spinel ($MgFe_{0.9}Cr_{1.1}O_4$ PDF # 71-1255), and $((Mn_{0.113}Fe_{0.977}Ti_{0.91})$ $[(Ti_{0.09}Fe_{0.815}Mn_{0.095})$ $O_4)$ PDF # 82-1293], respectively. It was then confirmed that most of the crystalline phases in the glass-ceramic sample are diopside, in addition to a smaller amount of spinel. In the curing system, heavy metal elements Cr, Mn is mostly atomic substitution, chemical bond binding or solid solution form in spinel phase. After the heat treatment crystallization process, the spinel phase further develops into the diopside phase to form a more stable curing system. Compared with the results of the XRD measurements, the conclusions that can be drawn from the TEM analysis further refer to comparison of lattice parameters, more accurate and effective.

Figure 9 shows the results of the qualitative and semi-quantitative analysis of the crystal phase region of the GC-6 glass-ceramic sample. Electron probe microscopy was used in this analysis, by which the distribution of each element in the micro-phase of the glass-ceramic phase could be obtained. The results from the energy spectrum analysis of points 1 and 2 in Figure 9 are shown in Table 5. The results show that the presence of the heavy metal elements Cr, Mn, and Fe became enriched in the spinel phase. Moreover, the dominating elements were O, Ca, Al, Si, Mg, Fe, Cr, and Mn. The contents of Cr and Mn were 13.52 and 22.42 wt%, respectively (see Figure 9, point 1). Due to the large field strength of the Cr^{3+} ions, and the "ferrophilicity" exhibited by the chromium oxides, the Fe, Mn, and Cr elements could together form a spinel phase which functioned as a heterogeneous nucleation core (Liao et al., 2016; Zhao et al., 2021a). Furthermore, the dominating elements in the diopside phase (see Figure 9, point 2), were O, Ca, Al, Si, Mg, Fe, Mn, and Cr. More specifically, the contents of Cr and Mn were 1.15 and 4.52 wt%, respectively.

The distribution of heavy metal elements in GC-6 is also shown in Figure 9. Combined with the TEM results, two

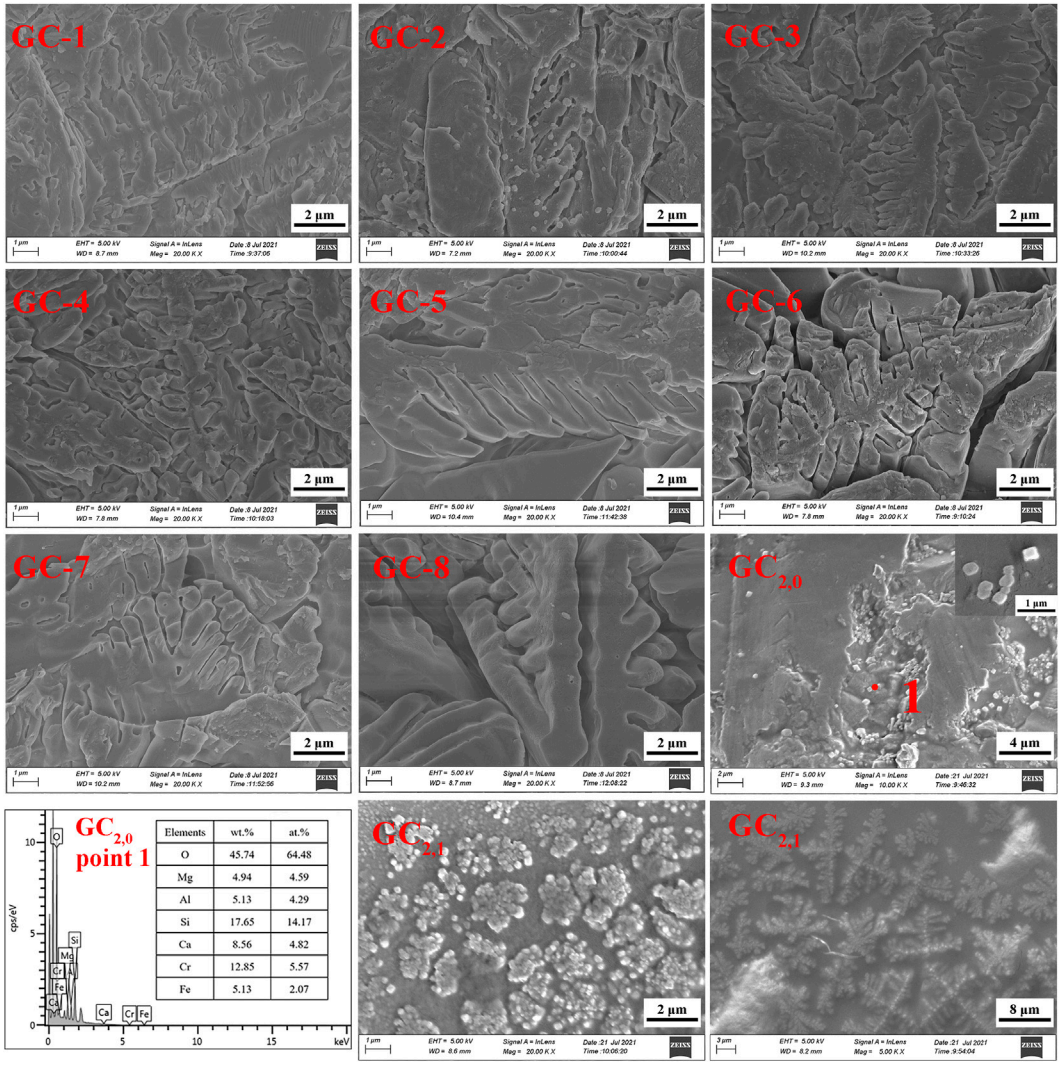

FIGURE 7
Comparison of SEM images for each group of glass-ceramic samples.

elements, Cr and Mn, were found to be enriched in the crystalline phase that consisted of mainly spinel $MgFe_{0.9}Cr_{1.1}O_4$ and $(Mn_{0.113}Fe_{0.977}Ti_{0.91})$ $[(Ti_{0.09}Fe_{0.815}Mn_{0.095})$ $O_4]$. This is an important indication that both Cr and Mn can be effectively solidified by participating in the crystalline phase formation. Combining the results of part 3.2.2, most of the chromium and manganese elements were found to be in the residual state with a good curing effect. It can be concluded that both spinel (which forms a stable crystalline phase) and tremolite (which is formed onto the spinel core) possess an excellent resistance to leakage, making it difficult for heavy metals to migrate. Thus, the escape of harmful elements into the environment has been prevented. Whether heavy metal elements can exist for a long time in the solidified body mainly depends on their chemical form in the system, in addition to the way of solidification and bonding. The way that heavy metals form compounds can facilitate the replacement of heavy metals with elements forming crystal lattice in the process of phase transition (so as to enter the crystal and become solidified) (Zhang et al., 2016b).

Both Cr and Mn became solidified in the crystalline phase of the glass-ceramics, which significantly reduced the leakage toxicity of both elements. This result is consistent with the results in a previous study that showed that the leakage rate of heavy metals in the spinel phase is significantly higher than the leakage rate of heavy metal oxides (Su et al., 2018). Thus, the glass-ceramic solidified body was shown to have an excellent effect on the solidification and stabilization of heavy metals. The remaining three heavy metal elements (Zn, Cd, and Pb) were not concentrated in the crystalline phase but were dispersed and distributed in both the glass phase and in the crystalline phase.

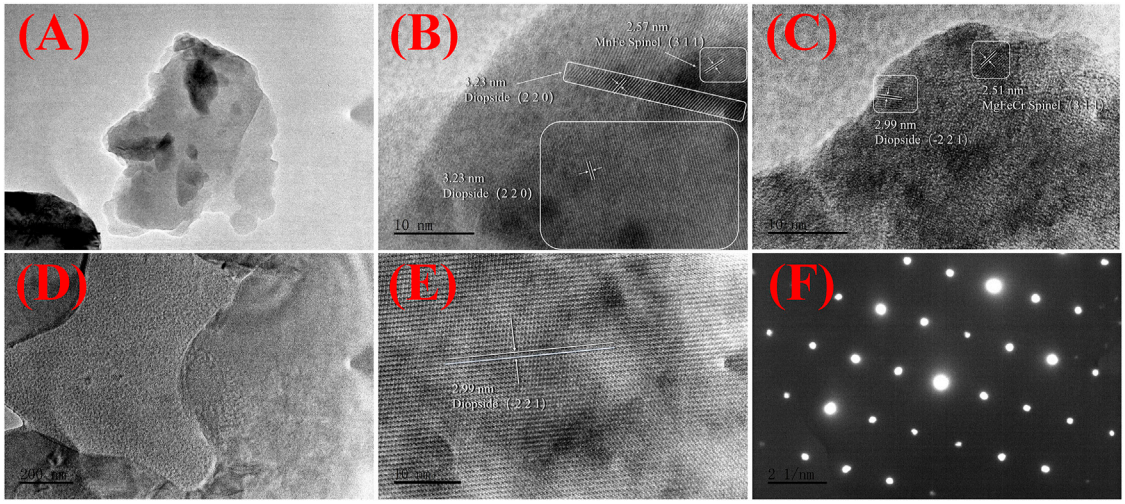

FIGURE 8
Transmission electron microscopy (TEM) characterization of the GC-6 sample: **(A)** A low-resolution TEM image of the GC-6 powder; **(B,C)** High-resolution TEM images of the GC-6 powder; **(D)** A low-resolution TEM image of the FIB-SEM ion thinning GC-6 sample; **(E)** A high-resolution TEM image of the FIB-SEM ion thinning GC-6 sample; **(F)** A SAED image of the FIB-SEM ion thinning GC-6 sample.

The reason may be that these heavy metal elements do not participate in the crystalline phase precipitation process, and the content is also low. They could not either precipitate into an independent phase, so these three elements became wrapped and isolated by a grid formed by the interlacing of crystalline and glass phases. Thus, the curing method for these heavy metal elements is physical wrapping.

X-ray photoelectron spectroscopy was also used in studying the electron binding energies of five heavy metal elements in the glass-ceramic samples of the GC-6 group, the parent glass, and a mixture thereof. Figure 10 shows the XPS spectra of Cr, Cd, Pb, Zn, and Mn. The C 1s peak (BE = 284.8 eV) was calibrated prior to the analysis of the XPS results. As can be seen in Figure 10, the binding energies of Mn 2p 3/2 and Mn 2p 1/2 have the values of 641.5 ± 0.3 eV and 653.5 ± 0.3 eV, respectively. They coincide with the Mn 2p binding energy of Mn (IV), as reported by Ilton et al. (2016) And the binding energy of the Mn 3s orbital, ΔE (Peak position spacing) is about 4.4 eV. This is consistent with the Mn 2p result, proving that Mn was in the form of Mn (IV) in both the curing system and in the feedstock. Furthermore, the binding energies of Cr 2p 3/2 and Cr 2p 1/2 were found to be 576.8 ± 0.3 eV and 586.7 ± 0.3 eV, respectively. These values were identical to the Cr 2p binding energies of Cr (III), as reported by Zhang et al. (2021). Also, the binding energies of Zn 2p 3/2 and Zn 2p 1/2 were found to be 1,020.8 ± 0.3 eV and 1,043.9 ± 0.3 eV, respectively. These ones were identical to the Zn 2p binding energies of Zn (II) reported by Kabongo et al. (2017). Moreover, the binding energies of Cd 3 days 5/2 and Cd 3 days 3/2 were 405.1 ± 0.3 eV and 412.1 ± 0.3 eV, respectively. They were identical to those of Cd (II), as reported by Dou et al. (1998). Finally, the binding energies of Pb 4f 7/2 and Pb 4f 5/2 were 138.3 ± 0.3 eV and 143.1 ± 0.3 eV, respectively. They were identical to those of Pb (II), as reported by Rondon and Sherwood (1998).

For all of these heavy metal elements, the electronic binding energies were found to be very similar for the raw material, base glass, and glass-ceramic samples. This indicated that the valence states did not change during the whole preparation process. The Pb and Zn elements existed in the form of oxides in the raw materials. They did not participate in the formation of phases in the solidified body and were solidified in the form of a physical coating. The respective electron binding energies were, therefore, almost unchanged during the preparation process. Furthermore, the Cd element was added in the form of a nitrate to the raw material. It was transformed into its oxide form during the high temperature melting process. The electronegativity around the Cd atoms did, thereby, slightly increase, which was also the situation for the electron binding energies in the Cd atoms. Furthermore, the Cr and Mn elements were observed to participate in the formation of the crystalline phases. The strong "oxyphilicity" of Cr lead to the formation of Cr^{3+} ions, and Mn^{4+} ions could easily combine with non-bridging oxygens to form bonds. This resulted in higher electronegativity around the heavy metal ions than what is the case in the raw slag system, and thereby, also lead to lower electron binding energies.

In summary, the solidification of heavy metal elements in glass-ceramics was found to take place in either of two different ways. One was the physical encapsulation, in which heavy metal elements became immobilized in a dense structure formed by a close interlacing of crystalline and amorphous phases in the glass-ceramic. The second type of method was the chemically stabilized solidification, where heavy metal ions became

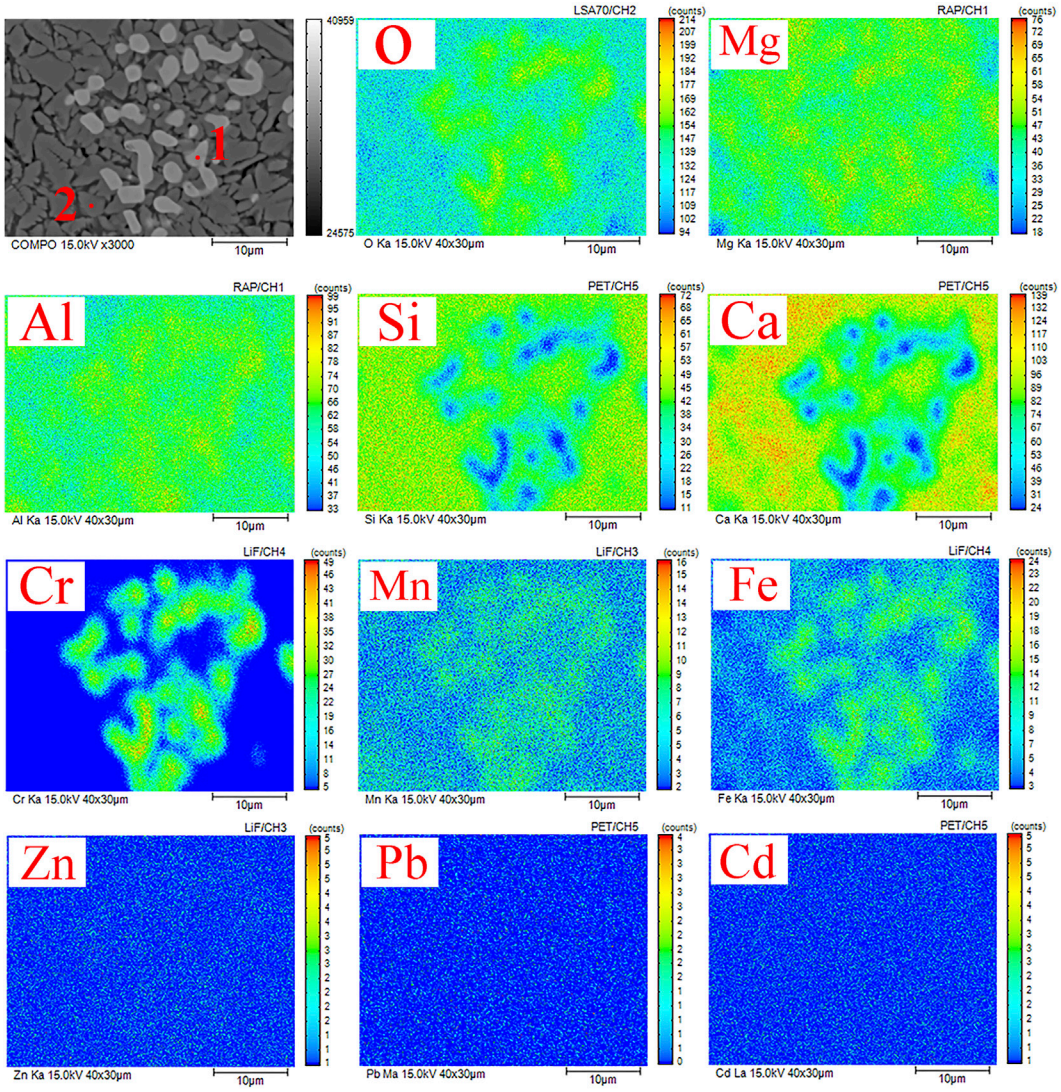

FIGURE 9
EPMA images of the GC-6 sample with its elemental distribution of O, Si, Ca, Mg, Al, Cr, Mn, Fe, Pb, Zn, and Cd.

TABLE 5 Results from the EDS analysis of points 2 and 3 in Figure 9.

Elements	1	2
O	32.18	46.06
Mg	3.22	5.62
Al	5.49	5.16
Si	10.89	20.64
Ca	5.94	12.64
Cr	13.52	1.15
Mn	22.42	4.52
Fe	6.33	4.21

substituted in the crystalline phase, with ions of similar radius size and charge. For instance, Fe and Mn ions could take the place of Al ions in the spinel phase, forming $(Mn_{0.113}Fe_{0.977}Ti_{0.91})[(Ti_{0.09}Fe_{0.815}Mn_{0.095})O_4]$. Alternatively, heavy metals could also use elements in the solidification system to directly form a stable new phase. For example, Cr and Fe could use Mg in the raw material to form $MgFe_{0.9}Cr_{1.1}O_4$. Thus, the solidification of heavy metal elements in glass-ceramics could take place by a combination of physical encapsulation and chemically stabilizing solidification. As a result, in the present study, the three elements Pb, Cd and Zn were not observed to change significantly during the whole crystallization process. On the other hand, Cr^{3+} was found to promote the

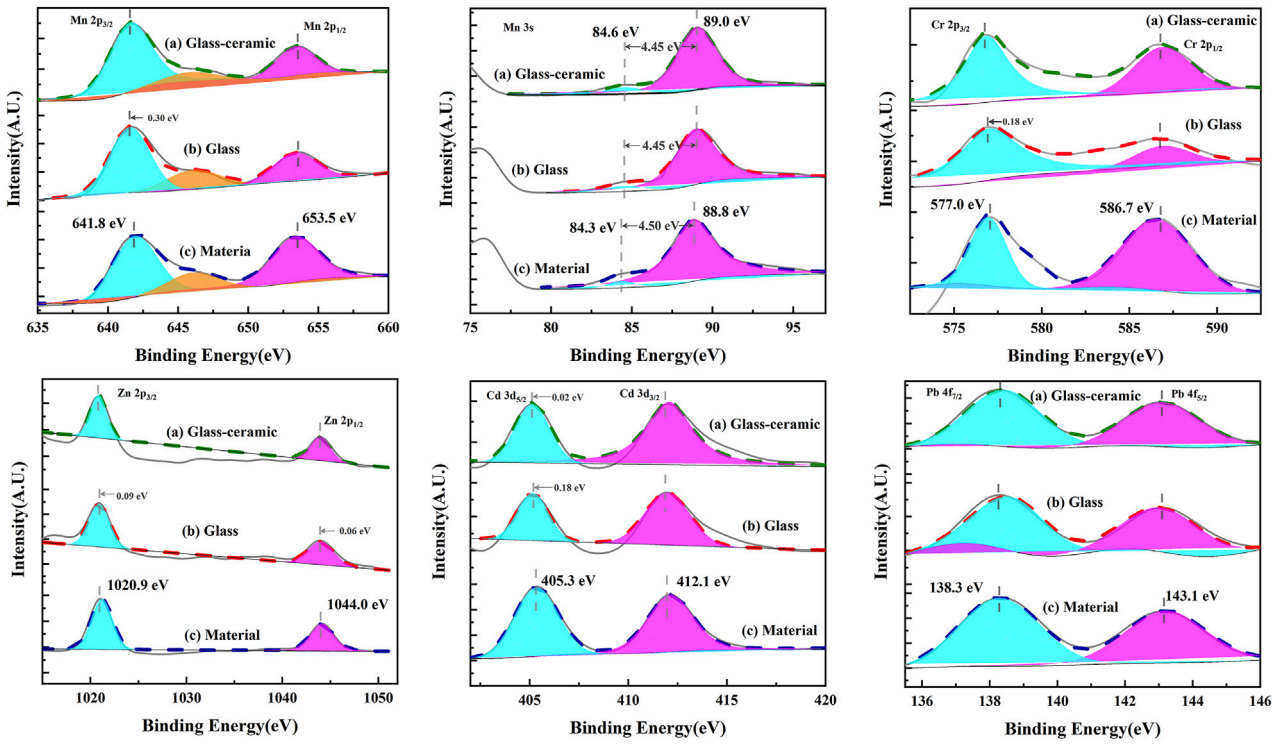

FIGURE 10
XPS spectra of heavy metals in the GC-6 sample.

enrichment of Mn and Fe in forming a spinel phase, which was generated in the nucleation stage and precipitated as a heterogeneous shaped nucleation core in the crystallization stage. This facilitated the generation and growth of crystals in the crystallization stage and promoted the generation of the main crystalline tremolite phase. It can then be concluded that the microcrystalline phase in the glass-ceramic acted synergistically with the glass phase to solidify the heavy metal ions. That is, the generation of stable crystalline phases, or physically encapsulated heavy metal elements in the crystalline and glass phases, was the result of the joint action of the microcrystalline and glass phases.

4 Conclusion

1) Successfully prepared glass-ceramic with the main crystalline phase of diopside using 100% industrial solid waste as raw material. With a high slag elimination capacity, the product performance also reaches the standard of industrial use of plates. Among them, the bending strength of the GC-6 group samples reached 107.35 MPa, Vickers hardness reached 6.67 GPa, density was 3.05 g/cm^3, water absorption was 0.04%, acid and alkali corrosion resistance of 99.38% and 99.86% respectively.
2) The results achieved by treating harmful heavy metals in waste sludge by glass-ceramic curing are obvious. The curing rate of Cr, Mn, Cd, Pb, and Zn all reached 99.9% for five heavy metal elements. Of them, Cr has the highest curing rate of 99.99%. In contrast to unheated base glass, heavy metal elements in glass-ceramic are more often retained in the curing system in a residue state that can be stabilized in the environment. Moreover, the STIM index of glass-ceramic has been reduced from the level of 3–4 in the base glass state to below 2.
3) The heavy metal elements Cr and Mn are mainly solidified by participating in the formation of crystalline phases, while the three elements Pb, Cd, and Zn are stabilized in the system in the form of physical encapsulation. Using the characteristics of the interlaced distribution of glass and crystal phases in the glass-ceramic system, the two approaches work synergistically to achieve a more excellent stabilized curing effect of heavy metals.

Data availability statement

The original contributions presented in the study are included in the article/Supplementary Material, further inquiries can be directed to the corresponding author.

Author contributions

JW: Investigation, data curation, conceptualization, methodology, writing- original draft preparation. FH: Writing—review and editing, sources. BY: Conceptualization. ZX: Writing—Review and editing. TL: Supervision.

Funding

This work was supported by Key R and D project in Ningxia Hui Autonomous Region (Grants No.2021BEG01003).

Conflict of interest

The authors declare that the research was conducted in the absence of any commercial or financial relationships that could be constructed as a potential conflict of interest.

Publisher's note

All claims expressed in this article are solely those of the authors and do not necessarily represent those of their affiliated organizations, or those of the publisher, the editors and the reviewers. Any product that may be evaluated in this article, or claim that may be made by its manufacturer, is not guaranteed or endorsed by the publisher.

References

Author anonymous (2011). *Glass - ceramics plate for industrial application*, JC/T 2097-2011, (in chinese).

Author anonymous (2007a). *Identification standards for hazardous wastes identification for extraction toxicity*. 5085GB .3-2007. (in chinese).

Author anonymous (1996). *Integrated wastewater discharge standard*. GB 8978-1996. (in chinese).

Author anonymous (2007b). *Solid waste - extraction procedure for leaching toxicity - sulphuric acid & nitric acid method*. HJ/T 299-2007. (in chinese).

Author anonymous (1995). *Solid waste-Determination of chromium(VI)-1,5-Diphenylcarbohydrazide spectrophotometric method*. GB/T 15555.4-1995. (in chinese).

Ayala Valderrama, D. M., Gomez Cuaspud, J. A., Roether, J. A., and Boccaccini, A. R. (2019). Development and characterization of glass-ceramics from combinations of slag, fly ash, and glass cullet without adding nucleating agents. *Materials* 12 (12), 2032. doi:10.3390/ma12122032

Chen, L., Ge, X., Long, Y., Zhou, M., Wang, H., and Chen, X. (2020). Crystallization and properties of high calcium glass-ceramics synthesized from ferromanganese slag. *J. Non. Cryst. Solids* 532, 119864. doi:10.1016/j.jnoncrysol.2019.119864

Dou, Y., Egdell, R. G., Walker, T., Law, D. S. L., and Beamson, G. (1998). N-Type doping in CdO ceramics: A study by EELS and photoemission spectroscopy. *Surf. Sci.* 398 (1), 241–258. doi:10.1016/S0039-6028(98)80028-9

Hakanson, L. (1980). An ecological risk index for aquatic pollution control.a sedimentological approach. *Water Res.* 14 (8), 975–1001. doi:10.1016/0043-1354(80)90143-8

He, D., Shu, J., Wang, R., Chen, M., Wang, R., Gao, Y., et al. (2021a). A critical review on approaches for electrolytic manganese residue treatment and disposal technology: Reduction, pretreatment, and reuse. *J. Hazard. Mat.* 418, 126235. doi:10.1016/j.jhazmat.2021.126235

He, S., Jiang, D., Hong, M., and Liu, Z. (2021b). Hazard-free treatment and resource utilisation of electrolytic manganese residue: A review. *J. Clean. Prod.* 306, 127224. doi:10.1016/j.jclepro.2021.127224

Ilton, E. S., Post, J. E., Heaney, P. J., Ling, F. T., and Kerisit, S. N. (2016). XPS determination of Mn oxidation states in Mn (hydr)oxides. *Appl. Surf. Sci.* 366, 475–485. doi:10.1016/j.apsusc.2015.12.159

Kabongo, G. L., Mhlongo, G. H., Mothudi, B. M., Hillie, K. T., Mbule, P. S., and Dhlamini, M. S. (2017). Structural, photoluminescence and XPS properties of Tm3+ ions in ZnO nanostructures. *J. Lumin.* 187, 141–153. doi:10.1016/j.jlumin.2017.02.024

Liao, C., Tang, Y., Liu, C., Shih, K., and Li, F. (2016). Double-barrier mechanism for chromium immobilization: A quantitative study of crystallization and leachability. *J. Hazard. Mat.* 311, 246–253. doi:10.1016/j.jhazmat.2016.03.020

Liu, S., Li, A., and Yuan, W. (2008). Research on the hybrid anaerobic technology and its design and start -up for low temperature home-sewage treating. *J. Saf. Environ.* 01, 43–47. doi:10.3969/j.issn.1009-6094.2008.01.013

Liu, Z., Zheng, J., Liu, W., Liu, X., Chen, Y., Ren, X., et al. (2020). Identification of the key host phases of Cr in fresh chromite ore processing residue (COPR). *Sci. Total Environ.* 703, 135075. doi:10.1016/j.scitotenv.2019.135075

Luan, J., Chai, M., and Li, R. (2016). Heavy metal migration and potential environmental risk assessment during the washing process of MSW incineration fly ash and molten slag. *Procedia Environ. Sci.* 31, 351–360. doi:10.1016/j.proenv.2016.02.047

Miah, M. R., Ijomone, O. M., Okoh, C. O. A., Ijomone, O. K., Akingbade, G. T., Ke, T., et al. (2020). The effects of manganese overexposure on brain health. *Neurochem. Int.* 135, 104688. doi:10.1016/j.neuint.2020.104688

Ning, D., Wang, F., Zhou, C., Zhu, C., and Yu, H. (2010). Analysis of pollution materials generated from electrolytic manganese industries in China. *Resour. Conserv. Recycl.* 54 (8), 506–511. doi:10.1016/j.resconrec.2009.10.007

Röllin, H. B., and Nogueira, C. M. C. A. (2011). "Manganese: Environmental pollution and health effects," in *Encyclopedia of environmental health*. Editor J. O. Nriagu (Burlington: Elsevier), 617–629.

Rondon, S., and Sherwood, P. M. A. (1998). Core level and valence band spectra of PbO by XPS. *Surf. Sci. Spectra.* 5 (2), 97–103. doi:10.1116/1.1247866

Shi, Y., Li, B.-W., Zhao, M., and Zhang, M.-X. (2018). Growth of diopside crystals in CMAS glass-ceramics using Cr2O3 as a nucleating agent. *J. Am. Ceram. Soc.* 101 (9), 3968–3978. doi:10.1111/jace.15700

Shu, J., Li, B., Chen, M., Sun, D., Wei, L., Wang, Y., et al. (2020). An innovative method for manganese (Mn2+) and ammonia nitrogen (NH4+-N) stabilization/solidification in electrolytic manganese residue by basic burning raw material. *Chemosphere* 253, 126896. doi:10.1016/j.chemosphere.2020.126896

Shu, J., Wu, H., Chen, M., Peng, H., Li, B., Liu, R., et al. (2019). Fractional removal of manganese and ammonia nitrogen from electrolytic metal manganese residue leachate using carbonate and struvite precipitation. *Water Res.* 153, 229–238. doi:10.1016/j.watres.2018.12.044

State Environmental Protection, A., and China Environmental Monitoring, S. (1990) *Chinese soil element background values*, China, Environ. Sci. Press.

Su, M., Liao, C., Chan, T., Shih, K., Xiao, T., Chen, D., et al. (2018). Incorporation of cadmium and nickel into ferrite spinel solid solution: X-Ray diffraction and X-ray absorption fine structure analyses. *Environ. Sci. Technol.* 52 (2), 775–782. doi:10.1021/acs.est.7b04350

Sun, D., Yang, L., Liu, N., Jiang, W., Jiang, X., Li, J., et al. (2020). Sulfur resource recovery based on electrolytic manganese residue calcination and manganese oxide ore desulfurization for the clean production of electrolytic manganese. *Chin. J. Chem. Eng.* 28 (3), 864–870. doi:10.1016/j.cjche.2019.11.013

Xu, Y., Liu, X., Zhang, Y., Tang, B., and Mukiza, E. (2019). Investigation on sulfate activation of electrolytic manganese residue on early activity of blast furnace slag in cement-based cementitious material. *Constr. Build. Mater.* 229, 116831. doi:10.1016/j.conbuildmat.2019.116831

Xu, Z., Ni, S., Tuo, X., and Zhang, C. (2008). Calculation of heavy metals ' toxicity coefficient in the evaluation of potential ecological risk index. *Environ. Sci. Technol.* 02, 112–115. doi:10.19672/j.cnki.1003-6504.2008.02.030

Zhang, W., Song, S., Nath, M., Xue, Z., Ma, G., and Li, Y. (2021). Inhibition of Cr6+ by the formation of *in-situ* Cr3+ containing solid-solution in Al2O3-CaO-Cr2O3-SiO2 system. *Ceram. Int.* 47 (7), 9578–9584. doi:10.1016/j.ceramint.2020.12.092

Zhang, Y., Sun, Y., Qi, Z., Xing, Z., and Zhang, C. (2013). Research on the harmless disposal technology of chrome residue. *Environ. Sci. Technol.* 05, 41–44. doi:10.3969/j.issn.1674-4829.2013.05.010

Zhang, Z., Li, A., Wang, X., and Zhang, L. (2016b). Stabilization/solidification of municipal solid waste incineration fly ash via co-sintering with waste-derived vitrified amorphous slag. *Waste Manag.* 56, 238–245. doi:10.1016/j.wasman.2016.07.002

Zhang, Z. (2016a). *Preparation of glass-ceramic and solidification of solid waste incineration fly ash using oil shale fly ash-based composite ashes*. Dalian: Dalian University of Technology. [dissertation]. [Dalian].

Zhao, M., Cao, J., Wang, Z., and Li, G. (2019a). Insight into the dual effect of Fe2O3 addition on the crystallization of CaO-MgO-Al2O3-SiO2 glass-ceramics. *J. Non. Cryst. Solids* 513, 144–151. doi:10.1016/j.jnoncrysol.2019.03.021

Zhao, M., Cao, J., Wang, Z., and Li, G. (2019b). Precipitating spinel into precursor glass and its assistance in crystallization. *J. Eur. Ceram. Soc.* 39 (7), 2427–2435. doi:10.1016/j.jeurceramsoc.2019.02.012

Zhao, S., Wen, Q., Zhang, X., Liu, B., and Zhang, S. (2021a). Migration, transformation and solidification/stabilization mechanisms of heavy metals in glass-ceramics made from MSWI fly ash and pickling sludge. *Ceram. Int.* 47 (15), 21599–21609. doi:10.1016/j.ceramint.2021.04.172

Zhao, S., Zhang, X.-Y., Liu, B., Zhang, J.-J., Shen, H.-L., and Zhang, S.-G. (2021b). Preparation of glass-ceramics from high-chlorine MSWI fly ash by one-step process. *Rare Met.* 40 (11), 3316–3328. doi:10.1007/s12598-021-01770-9

Zhou, Y. (2021). Reusing electrolytic manganese residue as an activator: The effect of calcination on its mineralogy and activity. *Constr. Build. Mat.* 294, 123533. doi:10.1016/j.conbuildmat.2021.123533

frontiers | Frontiers in Chemistry

TYPE Original Research
PUBLISHED 28 September 2022
DOI 10.3389/fchem.2022.1014441

Check for updates

OPEN ACCESS

EDITED BY
Mohd Hazwan Hussin,
Universiti Sains Malaysia (USM), Malaysia

REVIEWED BY
Fernando Pita,
University of Coimbra, Portugal
Yuran Chen,
Zhengzhou University, China

*CORRESPONDENCE
Theerayut Phengsaart,
theerayut.p@chula.ac.th

SPECIALTY SECTION
This article was submitted to Green and Sustainable Chemistry, a section of the journal Frontiers in Chemistry

RECEIVED 08 August 2022
ACCEPTED 09 September 2022
PUBLISHED 28 September 2022

CITATION
Phengsaart T, Manositchaikul C, Srichonphaisarn P, Juntarasakul O, Maneeintr K, Jeon S, Park I, Tabelin CB, Hiroyoshi N and Ito M (2022), Reverse hybrid jig separation efficiency estimation of floating plastics using apparent specific gravity and concentration criterion. *Front. Chem.* 10:1014441. doi: 10.3389/fchem.2022.1014441

COPYRIGHT
© 2022 Phengsaart, Manositchaikul, Srichonphaisarn, Juntarasakul, Maneeintr, Jeon, Park, Tabelin, Hiroyoshi and Ito. This is an open-access article distributed under the terms of the Creative Commons Attribution License (CC BY). The use, distribution or reproduction in other forums is permitted, provided the original author(s) and the copyright owner(s) are credited and that the original publication in this journal is cited, in accordance with accepted academic practice. No use, distribution or reproduction is permitted which does not comply with these terms.

Reverse hybrid jig separation efficiency estimation of floating plastics using apparent specific gravity and concentration criterion

Theerayut Phengsaart[1]*, Chaiwat Manositchaikul[1], Palot Srichonphaisarn[1], Onchanok Juntarasakul[1], Kreangkrai Maneeintr[1], Sanghee Jeon[2], Ilhwan Park[2], Carlito Baltazar Tabelin[3], Naoki Hiroyoshi[2] and Mayumi Ito[2]

[1]Department of Mining and Petroleum Engineering, Faculty of Engineering, Chulalongkorn University, Bangkok, Thailand, [2]Division of Sustainable Resources Engineering, Faculty of Engineering, Hokkaido University, Sapporo, Japan, [3]Department of Materials and Resources Engineering Technology, College of Engineering and Technology, Mindanao State University-Iligan Institute of Technology, Iligan City, Philippines

We developed a technique called the reverse hybrid jig, an advanced physical separation technique that combines the principles of jig and flotation to separate floating plastics. This technique is a promising green technology that is more economical and environmentally friendly compared with the conventional flotation. Although the applicability of this technique to separate PP/PE have been reported, the index to illustrate the possibility of separation for the reverse hybrid jig is still not available. In this study, a reverse apparent concentration criterion (CC_{RA}) is proposed to estimate reverse hybrid jig separation efficiency. This modified concentration criterion can be calculated using the specific gravity (SG) of particle with attached bubbles called the apparent specific gravity (SG_A). To determine the volume of attached bubbles on plastic surfaces under water pulsation, a laser-assisted apparatus was used under various conditions, including plastic type, air flow rate, dosage, and type of wetting agent. The results of attached bubble volume measurements were used to calculate the SG_A and CC_{RA}. The estimated values were then compared with the results of reverse hybrid jig separation. It was found that higher CC_{RA} resulted in better separation efficiency. In addition, an empirical linear equation for estimating the reverse hybrid jig separation efficiency is proposed.

KEYWORDS

recycling, plastic, polyolefin, gravity separation, bubble attachment

1 Introduction

Management of municipal solid wastes (MSW) is a big global challenge particularly because of the increasing amount of their associated plastic waste fraction (Geyer et al., 2017). During the Coronavirus disease (COVID-19) pandemic, the situation with plastic wastes worsened as consumption of single-use plastics in households skyrocketed. Various types of single-used plastics (e.g., surgical mask, plastic glove, and packaging from food delivery) are not treated properly and often mixed with MSW. Prata et al. (2020), for example, estimated that the monthly use of personal protective equipment (PPE) worldwide was approximately 129 billion face masks and 65 billion gloves. Furthermore, lockdowns in many countries around the world due to the pandemic led to the growth of e-commerce and food delivery services that increased plastic packaging waste generation by 53% in 2021 (Filho et al., 2021).

Almost half of plastics produced worldwide (46%) and more than half of plastic used in the global packaging industry (69.5%) is made up of polyolefin (Rabnawaz et al., 2017). Polyolefin—floating plastics like polypropylene (PP) and polyethylene (PE)—is the most widely produced and consumed type of thermoplastics due to its low cost, light weight, easy processability, and good recyclability (Gopanna et al., 2019). Moreover, PP is one of the most important plastics used to fabricate medical face masks (Irez et al., 2022).

Resources recovery, the concept of waste reduction by extracting valuable materials from waste streams, is a promising strategy for the management of plastic wastes in MSW. Recovered plastic wastes can be recycled to generate new plastic materials (i.e., resources recycling) and/or used as supplementary fuel for cement production, pyrometallurgical operations and electricity generation (i.e., energy recovery) (Tabelin et al., 2021). Compared with landfilling, incineration, and energy recovery, resources recycling is a more sustainable approach because plastic materials are recirculated back into the economy (Demirbas, 2011). Therefore, resources recycling is an important way of minimizing the amounts of plastic wastes disposed of in landfills or burned in incinerators. It means that recycling of mixed plastic wastes is critical to limit the negative environmental impacts of plastics as well as to conserve finite natural resources. It is also included in the United Nation Sustainable Development Goals (UN-SDGs): Goal 12 "Responsible production and consumption" (United Nations, 2015). To effectively recycle plastics, separation of various plastic types in mixed-plastic wastes is essential. Sink-float separation in water is commonly used to separate polyolefins from other mixed plastics because they have lower densities than water causing them to float while other types of plastics sink with their heavier density. The sink-float separation of various polyolefins like PP and PE, however, is expensive because it requires the use of water-ethanol mixtures as medium (Mumbach et al., 2019).

An alternative to sink-float separation for the separation of mixed-plastics is the use of jig, a gravity concentration technique that uses vertical expansion and contraction of a bed of particles by a pulse of fluid to separate the particle based on difference of specific gravity (*SG*) and settling velocity (v). It is one of the oldest mineral processing methods and still used due to its simple operation, low cost, and high efficiency. Among the many types of jigs, four advanced jig separation technology—RETAC jig, reverse jig, hybrid jig, and reverse hybrid jig (Figure 1)—were developed in the Laboratory of Mineral Processing and Resources Recycling, Hokkaido University, Japan for plastic-plastic separation. First, the RETAC jig, modified from coal cleaning TACUB (Tsunekawa Air Chamber Under Bed) jig (commercially called as BATAC jig) (Hori et al., 2009a; Tsunekawa et al., 2012; Phengsaart et al., 2020, 2021), was successfully applied to recover plastics and other valuable materials from copy machines (Tsunekawa et al., 2005), automobile shredded residues (ASR) (Kuwayama et al., 2014), small home appliances (Phengsaart et al., 2018), mobile phones (Jeon et al., 2019) in both laboratory- and pilot-scales. Second, the reverse jig, which is the RETAC jig with top screen, was developed to separate plastics lighter than water (e.g., PP and high-density polyethylene (HDPE) from packaging containers) by their difference in levitating velocity (Ito et al., 2010). Third, the hybrid jig was developed to separate plastics with similar *SG*s but different surface wettabilities by combining density- and surface-based separation concepts. In this type of jig, an aeration tube is installed under the screen to generate air bubbles introduced into the jig separation chamber. Separation occurs when the *SG* of one type of plastic is reduced and changed into apparent specific gravity (SG_A) due to the attachment of bubbles. This causes stratification during water pulsation, so the lower SG_A (more hydrophobic) plastic is recovered on top while that with higher SG_A (more hydrophilic) is recovered at the bottom. The hybrid jig effectively separated various types of mixed-plastics like polyethylene terephthalate (PET)/polyvinyl chloride (PVC) (Hori et al., 2009b; Ito et al., 2019a, 2020), polypropylene with glass fiber (PPGF)/high impact polystyrene (HIPS) (Ito et al., 2019b, 2020), and PVC/polyamide (nylon-66 or PA) (Ito et al., 2019b). Finally, the reverse hybrid jig—a combination of reverse and hybrid jigs—was developed to separate floating plastics having similar *SG*s like PE/cross-linked polyethylene (XLPE) mixtures (Ito et al., 2021).

For separation to occur, less selectivity of bubble attachment is required for hybrid and reverse hybrid jigs compared with flotation. Very high bubble attachment selective is crucial in flotation because bubbles are used to separate and carry hydrophobic particles to froth products while hydrophilic particles are left in suspension. Because of this, the high consumption of chemical reagents (e.g., wetting agents and frothers) are required for high selectivity and efficiency (Aikawa et al., 2020; Hornn et al., 2020, 2021). In contrast, only few bubbles with low selectivity are needed for effective

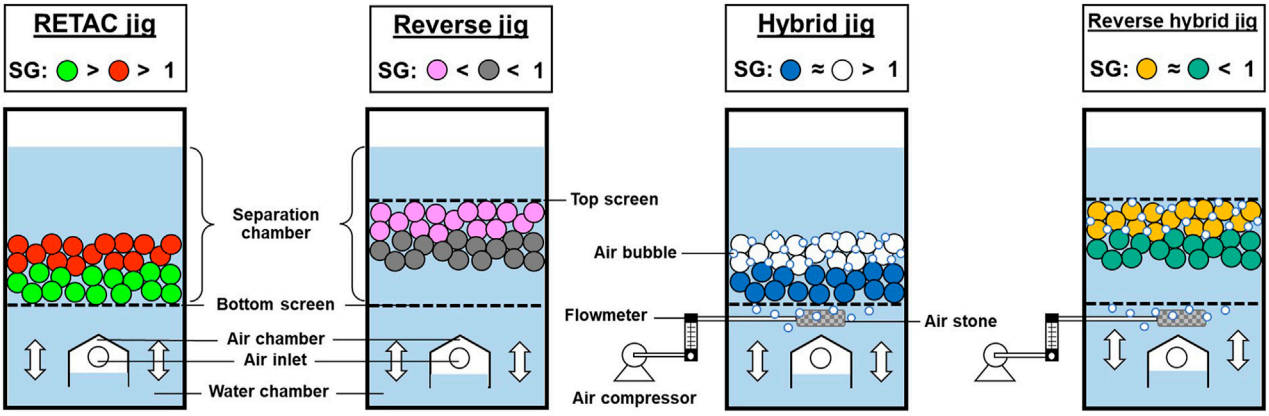

FIGURE 1
Schematic illustrations of advanced jigs.

separation in hybrid and reverse hybrid jigs because their main role is only to change the *SG* of more hydrophobic plastics. Meanwhile, water pulsations are introduced to stratify the particles into different layers in the separation chamber, so little consumption of chemical reagents is required (Ito et al., 2019b). Therefore, advanced jigs are both green and sustainable technologies.

To obtain high quality recycled plastics with similar physical/chemical properties of virgin resins, high separation efficiency is required. In the previous studies of the authors about advanced jig separation efficiency, the concentration criterion (*CC*)—an index illustrates the possibility of gravity separation—was modified to estimate the separation efficiency of the RETAC jig, reverse jig, and hybrid jig. However, the estimation of *CC* for floating plastics using the reverse hybrid jig separation is still lacking in the literature.

In this study, a laser-assisted measurement apparatus was used to measure attached-bubble volume on plastics during water pulsation and determine the SG_A of plastics under various conditions (i.e., plastic type, air flow rate, dosage and type wetting agents). Finally, a new index based on *CC* is proposed to estimate the separation efficiency of reverse hybrid jig separation.

2 Concentration criteria for advanced jig separation

The concentration criterion (*CC*) is an index used to determine the possibility of separation by gravity concentrators like conventional jigs. The higher the value of *CC*, the easier it is to separate materials in the sample (Wills and Finch, 2015; Gupta and Yan, 2016). It is calculated using the following equation (Wills and Finch, 2015; Gupta and Yan, 2016):

$$CC = \frac{\rho_H - \rho_F}{\rho_L - \rho_F} \tag{1}$$

where ρ_H and ρ_L are the mass density of heavy (*H*) and light (*L*) materials, respectively while ρ_F is the mass density of fluid medium used for separation.

In terms of *SG*, Eq. 1 can be rewritten as

$$CC = \frac{SG_H - SG_F}{SG_L - SG_F} \tag{2}$$

where SG_H and SG_L are the specific gravities of *H* and *L* materials, respectively while SG_F is the specific gravity of fluid medium.

In gravity separation, particles with different densities are separated by the difference of their settling velocities (v) in fluid usually water. The settling of a particle in water is strongly influenced by three forces—gravity force (F_G; Eq. 3), buoyancy force (F_B; Eq. 4) and drag force (F_D; Eq. 5)—while its *v* is determined by the balance between these three forces (Eq. 6).

$$F_G = mg \tag{3}$$

$$F_B = \frac{m}{\rho_P}\rho_F g \tag{4}$$

$$F_D = C_D A \frac{\rho_F v^2}{2} \tag{5}$$

$$m\frac{dv}{dt} = mg - \frac{m}{\rho_P}\rho_F g - C_D\left(\frac{\rho_F v^2}{2}\right) \tag{6}$$

where *m* is the mass of the particle [kg], *v* is the velocity of particle [m/s], *t* is time [s], *g* is gravitational acceleration [m/s^2], ρ_P is density of particle [kg/m^3], ρ_F is density of fluid [kg/m^3], C_D is drag coefficient, and *A* is the projection area of particle [m^2].

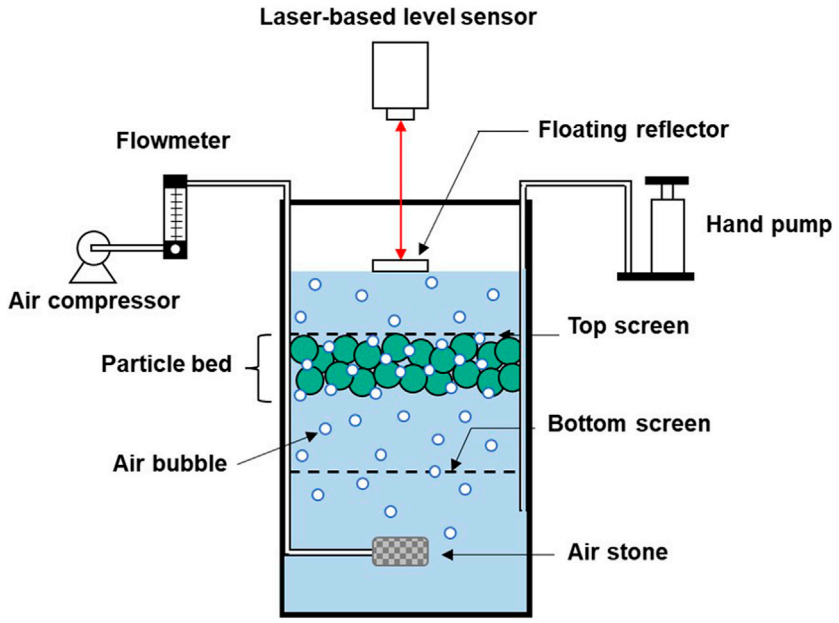

FIGURE 2
A schematic diagram of the laser-assisted measurement setup for the determination of attached-bubble volume.

$$m = \rho_P V \tag{7}$$

where V = volume of particle [m^3].

When a particle reaches terminal velocity (v_∞), its acceleration (dv/dt) becomes zero and Eqs 6, 7 can be simplified to the following equation:

$$0 = (\rho_P - \rho_F)gV - C_D A\left(\frac{\rho_F v_\infty^2}{2}\right) \tag{8}$$

If the particle is a sphere (*), its projection area (A^*) and volume (V^*) are given by Eqs 9, 10.

$$A^* = \frac{\pi D^2}{4} \tag{9}$$

$$V^* = \frac{\pi D^3}{6} \tag{10}$$

The drag coefficient (C_D) in Eqs 5, 6 could also be expressed as a function of the Reynolds number (Re_p) assuming a laminar flow regime during particle settling ($Re_p < 1$) (Eqs 11, 12).

$$Re_p = \frac{vD\rho_f}{\mu} \tag{11}$$

$$C_D = \frac{24}{Re_p} \tag{12}$$

where μ is the viscosity of fluid [Pa,s].

In a laminar or Stokes' flow regime, the terminal velocity of a sphere ($v_\infty{}^*$) could be calculated and is given as Eq. 13 by substituting Eqs 9–12 to Eq. 8.

$$v_\infty^* = \frac{(\rho_P - \rho_F)gD^2}{18\mu} \tag{13}$$

Using Stokes' law (Eq. 13), CC (Eq. 1) can be expressed by the ratio of v_∞ of heavy and light particles.

$$CC = \frac{v_{\infty H}^*}{v_{\infty L}^*} \tag{14}$$

where $v_\infty{}^*{}_H$ and $v_\infty{}^*{}_L$ are the terminal velocities of heavy and light materials with spherical shape, respectively.

The equations of conventional CC (Eqs 1, 2 and Eq. 14), however, are not applicable for non-spherical particles. To modify the CC and capture the effects of particle shape, a dynamic shape factor called shape settling factor (SSF) was introduced (Eq. 15) (Gupta and Yan, 2016).

$$SSF = \frac{v_\infty}{v_\infty^*} \tag{15}$$

The SSF is defined as the ratio of the terminal velocity in static water of a non-spherical particle (v_∞) and the terminal velocity in static water of a spherical particle having the same D ($v_\infty{}^*$). Using SSF (Eq. 15), the modified concentration criterion for non-spherical particles (CC_S) were obtained as follows (Pita and Castilho, 2016):

$$CC_S = \frac{\rho_H - \rho_F}{\rho_L - \rho_F} \times \frac{SSF_H}{SSF_L} \tag{16}$$

where SSF_H and SSF_L are the shape settling factor of heavy and light materials, respectively.

TABLE 1 Reverse apparent concentration criterion (CC_{RA}) of each plastic mixtures (i.e., PP/LDPE and PP/HDPE) and sharpness index (SI) of reverse hybrid jig separation experiments without bubble generation during pulsation at air flow rate (i.e., 0.5, 1.0, and 1.5 L/min) and wetting agent of 0 ppm.

Plastic mixtures	Air flow rate [L/min]	CC_{RA}	SI
PP/LDPE	0.5	1.39	0.95
	1.0	1.22	0.96
	1.5	1.23	0.88
PP/HDPE	0.5	1.56	0.82
	1.0	1.47	0.94
	1.5	1.28	0.77

Then,

$$CC_S = \frac{\rho_H - \rho_F}{\rho_L - \rho_F} \times \frac{\frac{v_{\infty H}}{v^*_{\infty H}}}{\frac{v_{\infty L}}{v^*_{\infty L}}} \tag{17}$$

where $v_{\infty H}$ is the terminal velocity in static water of a heavy, non-spherical particle, $v_{\infty L}$ is the terminal velocity in static water of a light, non-spherical particle, $v_{\infty}{}^*{}_H$ is the terminal velocity in static water of heavy, spherical particle having the same D as the heavy, non-spherical particle, and $v_{\infty}{}^*{}_L$ is the terminal velocity in static water of a light, spherical particle having same D as a light, non-spherical particle.

Finally,

$$CC_S = \frac{v_{\infty H}}{v_{\infty L}} \tag{18}$$

However, CC and CC_S are suitable for estimate the separation efficiency of sinking plastics using conventional and RETAC jigs. To estimate the results of reverse jig separation that separate the particles based on levitation velocity difference, Eqs 1, 2 were modified into reverse concentration criterion (CC_R) as shown in Eq. 19 (Ito et al., 2010).

$$CC_R = \frac{SG_L - SG_F}{SG_H - SG_F} \tag{19}$$

Similarly, for hybrid jig separation, since the apparent specific gravity (SG_A)—SG changed by bubble attachment—affects the separation efficiency more than the inherent SGs of plastics therefore, SG_A (Eq. 20) calculated from the inherent specific gravity of materials (SG_P) and volume of attached bubbles on particles during water pulsation ($V_0{}^*$) need to be considered (Ito et al., 2020).

$$SG_A = \frac{SG_P}{1 + V_0^*} \tag{20}$$

From Eqs 2, 20, the apparent concentration criterion (CC_A) —modified CC based on SG_A—was proposed as Eq. 21 to determine the efficiency of hybrid jig separation (Ito et al., 2020).

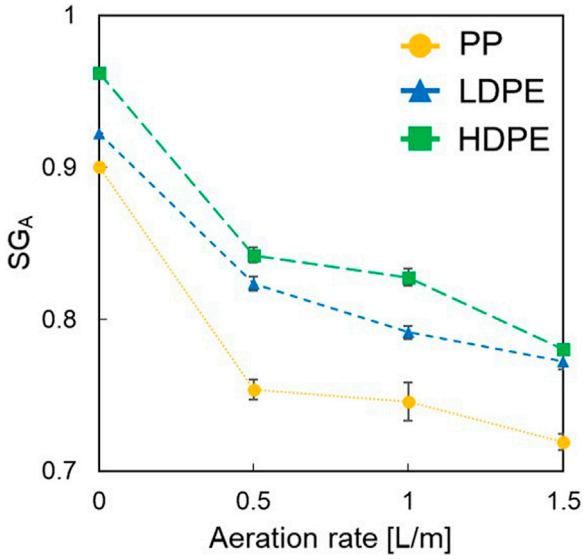

FIGURE 3
Apparent specific gravities of PP, LDPE, and HDPE at different air flow rates (i.e., 0, 0.5, 1.0, and 1.5 L/min) in water (i.e., without wetting agent).

$$CC_A = \frac{SG_{AH} - SG_F}{SG_{AL} - SG_F} \tag{21}$$

where SG_{AH} and SG_{AL} are the SG_A of H and L materials, respectively.

These CC, CC_S, CC_R, and CC_A have been successfully applied to estimate the separation efficiency of various jig separation of plastics (Ito et al., 2010, 2020; Pita and Castilho, 2016). However, an index to illustrate the possibility of separation for reverse hybrid jig is still not available. In this study, reverse apparent concentration criterion (CC_{RA})—modified CC combining the principles of reverse jig and hybrid jig (Eqs 19, 21)—was proposed to estimate reverse hybrid jig separation efficiency (Eq. 22) The experiments to confirm this proposed equation were carried out as explained in the next section.

$$CC_{RA} = \frac{SG_{AL} - SG_F}{SG_{AH} - SG_F} \tag{22}$$

3 Materials and methods

3.1 Samples

The samples used in this study are virgin plastic pellets about 3.5–4.0 mm in size, spherically shaped and without additives. Two types of polyolefins, PP (PP1100NK, POLIMAXX, IRPC

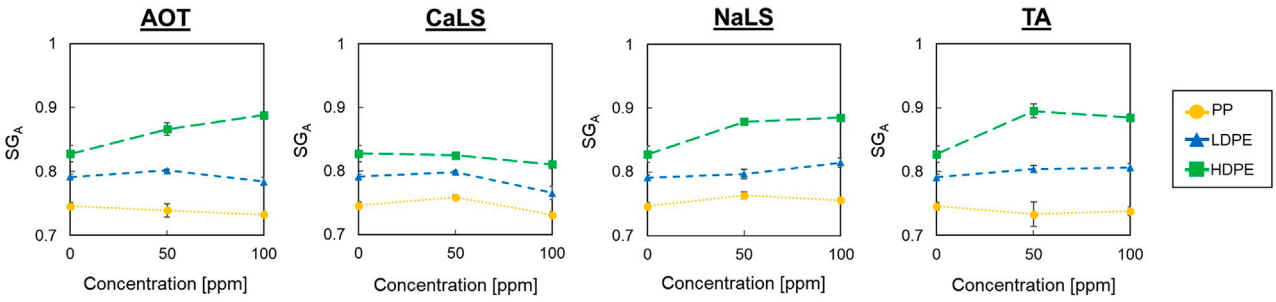

FIGURE 4
Apparent specific gravities of PP, LDPE, and HDPE at air flow rate of 1.0 L/min with AOT, CaLS, NaLS, and TA at concentrations of 0, 50, and 100 ppm.

TABLE 2 Reverse apparent concentration criterion (CC_{RA}) of each plastic mixtures (i.e., PP/LDPE and PP/HDPE) and sharpness index (*SI*) of reverse hybrid jig separation experiments without bubble generation during pulsation at different air flow rate of 1.0 L/min and wetting agents (i.e., AOT, CaLS, NaLS, and TA) of 50 and 100 ppm.

Separation test	Wetting agents		CC_{RA}	SI
	Types	Concentrations [ppm]		
PP/LDPE	AOT	50	1.31	0.93
		100	1.24	0.78
	CaLS	50	1.20	1.00
		100	1.15	1.00
	NaLS	50	1.17	0.95
		100	1.32	0.97
	TA	50	1.36	1.00
		100	1.35	0.87
PP/HDPE	AOT	50	1.95	0.52
		100	2.40	0.49
	CaLS	50	1.38	1.00
		100	1.42	0.96
	NaLS	50	1.96	0.47
		100	2.13	0.54
	TA	50	2.54	0.50
		100	2.27	0.50

Public Co., Ltd., Thailand) with *SG* of 0.90 and PE, which is further subdivided into low-density polyethylene (LDPE; LDJJ4324, POLENE, TPI Polene Public Co. Ltd., Thailand) with *SG* of 0.92 and high-density polyethylene (HDPE; HD2308J, InnoPlus, PTT Global Chemical Public Co., Ltd., Thailand) with *SG* of 0.96.

3.2 Reagents

Four types of wetting agents were used: 1) docusate sodium salt (Aerosol OT; AOT), 2) calcium lignosulfonate (CaLS), 3) sodium lignosulfonate (NaLS), and 4) tannic acid (TA). Methyl isobutyl carbinol (MIBC), a reagent widely utilized in flotation as a frother, was used to stabilize bubbles in solution. All chemicals used in the experiments are reagent grade obtained from Sigma-Aldrich Co., United States .

3.3 Measurements of attached-bubble volume

Because SG_A (Eq. 20) is an important factor to estimate the reverse hybrid jig separation efficiency, determination of

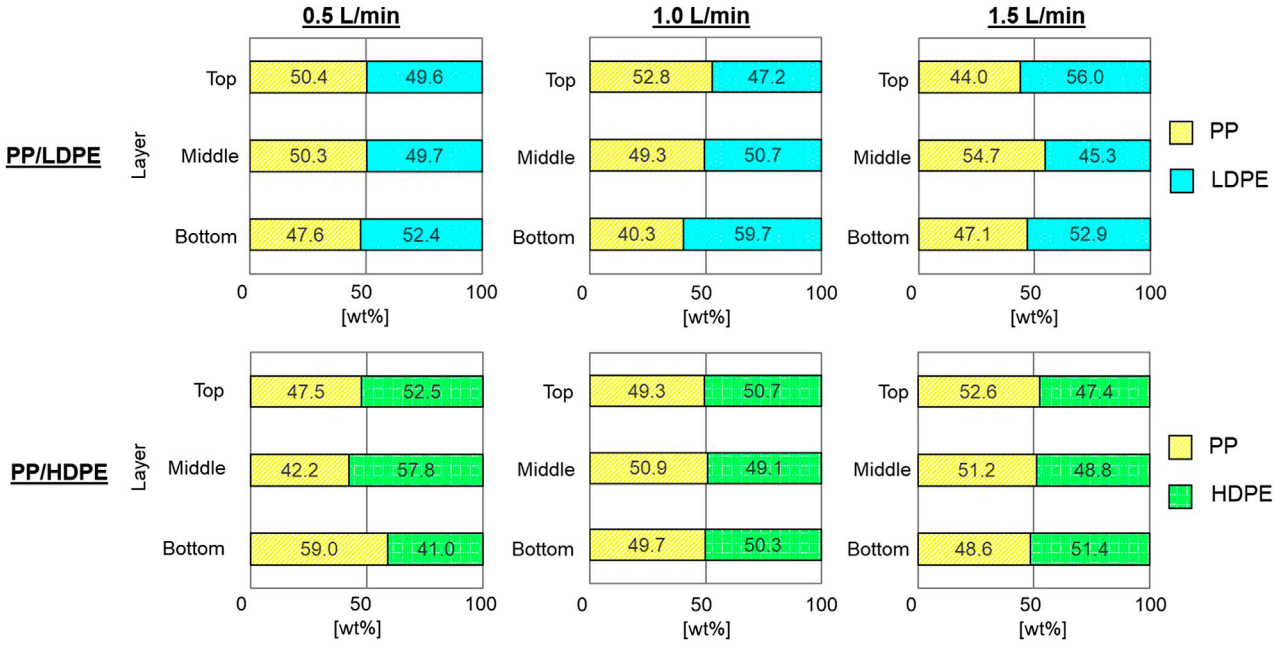

FIGURE 5
The proportion of plastics in each layer after reverse hybrid jig separation of PP/LDPE and PP/HDPE with continuous bubble generation at different air flow rate of 0.5, 1.0, and 1.5 L/min in water (i.e., without wetting agent).

attached-bubble volume on plastic surfaces during water pulsation (V_0*) were carried out under various conditions using the apparatus shown in Figure 2 (Ito et al., 2020, 2021).

In these tests, a reverse hybrid jig with a separation chamber 60 mm long, 60 mm wide, and 150 mm high were used. A hand-pump connected to the air chamber was used for water pulsation while an air pump introduces air into the jig through a tube connected to porous rock for creating air bubbles under the separation chamber. Air bubbles are introduced under the particle bed, and when bubbles attached to particles, an equivalent water level rise is recorded. This water level rise is accurately measured and recorded by a laser-based level sensor (HG-C1050, Panasonic Corporation, Japan) with a floating reflector on top of the water surface. The attached-bubble volume can then be calculated from changes in water level inside the separation chamber before and after bubble introduction (Ito et al., 2020, 2021).

Supplementary Figure S1 shows the procedure of this measurement in which 50 g of a single-type plastic sample (i.e., PP, LDPE, or HDPE) was fed into a separate chamber then, 1.2 L of water containing 20 ppm of MIBC were added. The experiments were carried out with wetting agents (i.e., AOT, CaLS, NaLS, or TA) at concentrations of 0, 50, and 100 ppm. The water pulsation was controlled by hand-pump at a displacement of 20 mm and frequency equal to 30 cycles/min with air bubbles generated using an air pump at flow rates of 0.5, 1, and 1.5 L/min for 3 min. The measurement was carried out by following the procedure in the published paper of Ito et al. (2020, 2021). After finished the aeration with water pulsation, the change in water height were recorded using a laser-based level sensor. Then, four more water pulsation were introduced to remove air bubbles that were trapped in the void between plastic pallets and the height of the water surface of each pulsation were also recorded. These data were used to determine the V_0* (Ito et al., 2020).

3.4 Reverse hybrid jig separation experiments

The reverse hybrid jig separation experiments were carried out using the same reverse hybrid jig used in the attached-bubble volume measurements. 60 g of PP/LDPE, and PP/LDPE mixtures with 1:1 mixing ratio (by weight) were used for the experiments. All conditions were the same as that of the attached-bubble volume measurements. Experiments were carried out under two different methods below (Supplementary Figure S2) (Ito et al., 2021):

3.4.1 Reverse hybrid jig separation experiments with continuous bubble generation

In these tests, air bubbles were introduced for 5 min as a kind of “conditioning” process. This was followed by water

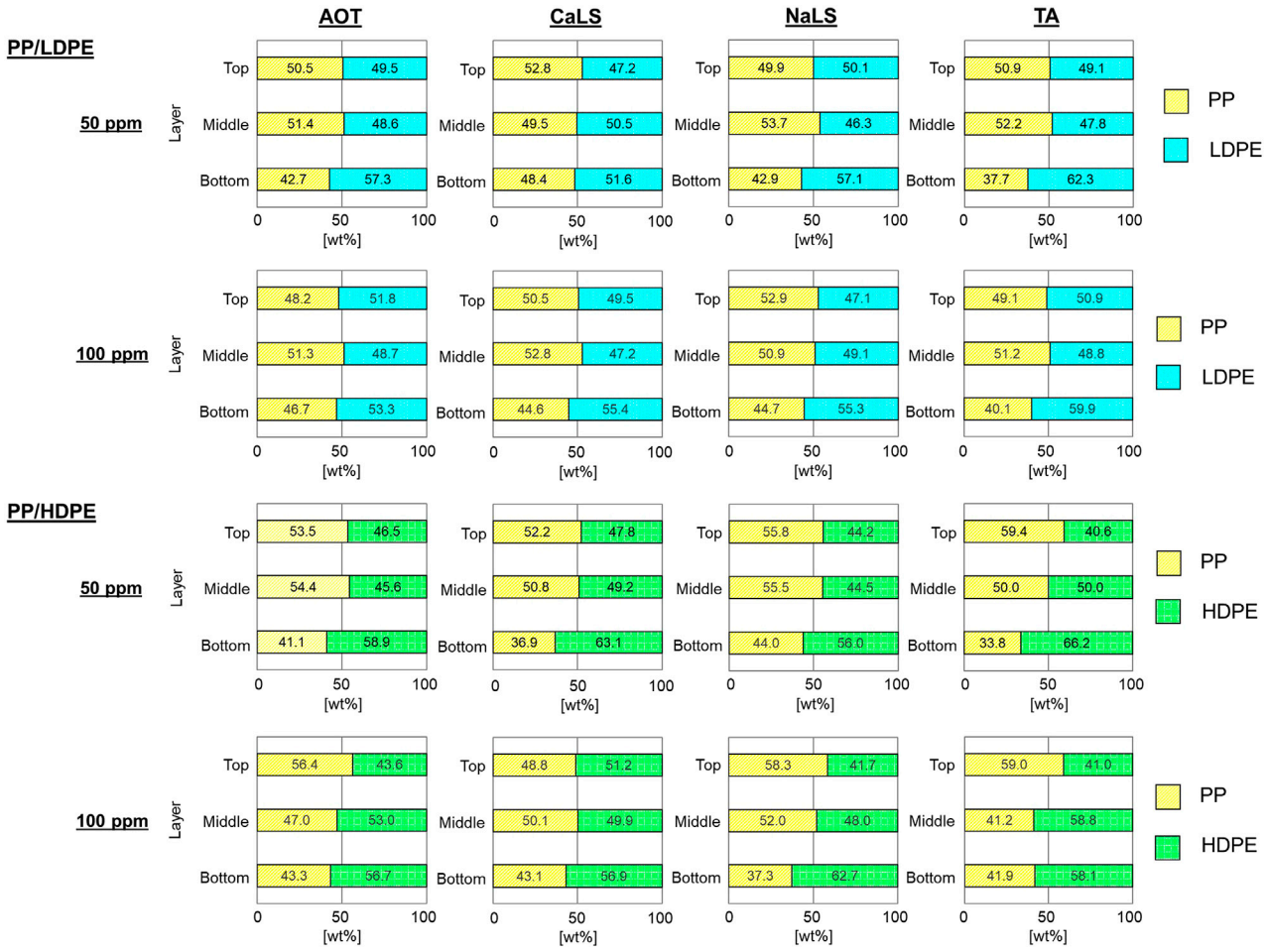

FIGURE 6
The proportion of plastics in each layer after reverse hybrid jig separation of PP/LDPE and PP/HDPE with continuous bubble generation at air flow rate of 1.0 L/min in the solution with AOT, CaLS, NaLS, and TA at concentration of 50 and 100 ppm.

pulsation for 3 min with continuous bubble generation bubble. After the separation, products were collected into three layers from the top. The products in each layer were then separated by sink-float separation using 50 wt% ethanol (prepared using 99.9% C_2H_6O, AR grade, Qchemical Co. Ltd., Thailand) solution (SG: ~0.91) as medium to determine the purity of each layer.

3.4.2 Reverse hybrid jig separation experiments without bubble generation during pulsation

Similar to the tests in Section 3.4.1, air bubbles were introduced for 5 min, but after conditioning, air introduction was stopped and water pulsation was introduced for 3 min. For the determination of purity of products in each layer, the same sink-float separation method was used as outlined previously.

4 Results and discussion

4.1 Effects of air flow rate and wetting agents on the apparent specific gravity

Figure 3 shows the SG_A of plastics measured using the laser-assisted measurement apparatus without wetting agent at air flow rates of 0, 0.5, 1.0, and 1.5 L/min. HDPE had the highest SG_A regardless of the air flow rate and was followed by LDPE and PP. It was also found that the SG_A of all types of plastics decreased with increasing air flow rate, which could be attributed to the higher volume of bubbles attached to plastic surfaces (Eq. 20).

After determining the values of SG_A, these were used to calculate CC_{RA} using Eq. 22, and the results are presented in Table 1. The plastic mixtures of PP/HDPE showed higher CC_{RA} compared with that of PP/LDPE because of larger differences in

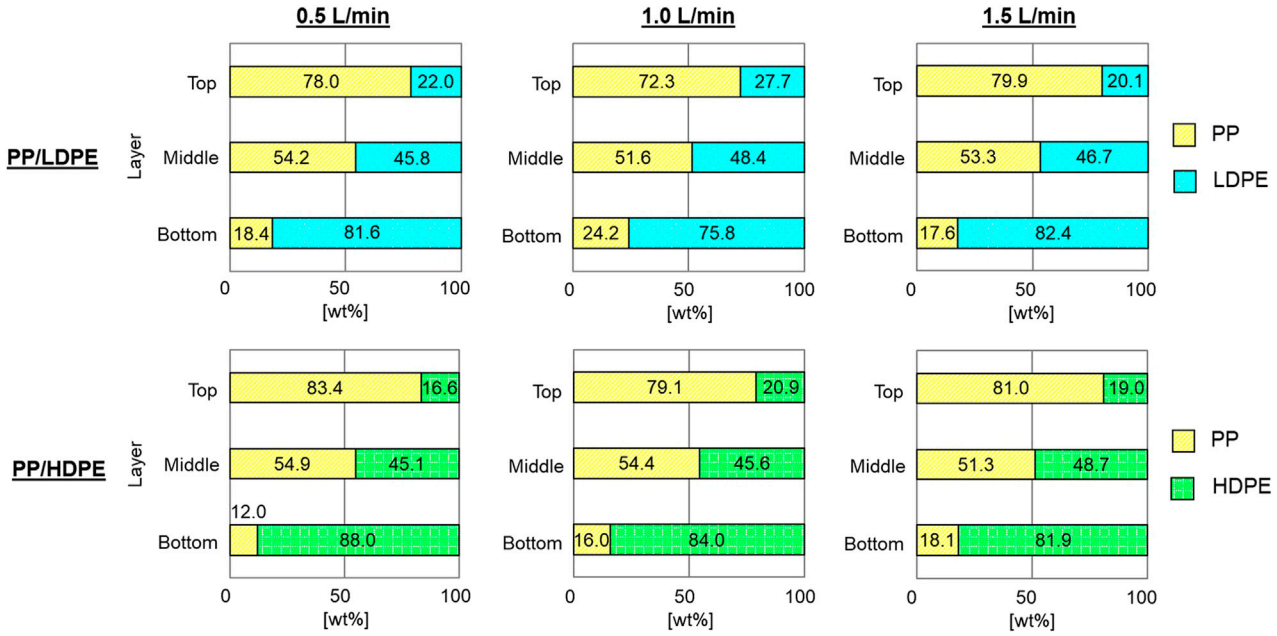

FIGURE 7
The proportion of plastics in each layer after reverse hybrid jig separation of PP/LDPE and PP/HDPE without bubble generation during pulsation at different air flow rates of 0.5, 1.0, and 1.5 L/min in water (i.e., without wetting agent).

SG_A of the former than the latter. It is also interesting to note was also found that the CC_{RA} were higher when lower air flow rate was used. These results indicate that the conditions with lower air flow rate should achieve higher separation efficiency if the proposed equation (Eq. 22) is correct as well as the separation of PP/HDPE should be better than that of PP/LDPE.

Figure 4 shows the SG_A of PP, LDPE, and HDPE at air flow rate of 1.0 L/min in the solution with wetting agent (i.e., AOT, CaLS, NaLS, and TA) of 0, 50, and 100 ppm. HDPE shows the highest SG_A in all conditions followed by LDPE and PP, a trend similar to the SG_A results in water (Figure 3). It was also found that SG_A of HDPE drastically changed with the concentration and type of wetting agents but those of LDPE and PP changed only slightly. To explore these discrepancies more, CC_{RA} were calculated from SG_A of each condition as shown in Table 2. The PP/HDPE mixtures always had higher CC_{RA} compared with the PP/LDPE mixtures under the same conditions due to their higher SG_A difference. Also, most conditions with wetting agents had higher CC_{RA} than without wetting agents when the same air flow rate (i.e., 1.0 L/min) was used, indicating that the addition of wetting agents could improve the reverse hybrid jig separation efficiency if this proposed index (Eq. 22) is correct.

The SG_A of HDPE increased with the addition of AOT with the highest SG_A difference and CC_{RA} value between PP and HDPE obtained at 100 ppm. This means that 100 ppm AOT could achieve better separation efficiency than pure water or lower AOT concentrations. For NaLS and TA, the SG_A of HDPE only increased until 50 ppm. After this dosage, the SG_A like that of AOT remained constant. Meanwhile, contrast, CaLS had negligible effects on the SG_A of HDPE. Also, because this agent has very low effect influence on the apparent density of the three plastics. It can be said that it does not change the hydrophobicity of the three plastics. These results indicate that AOT, NaLS, and TA are capable of selectively modifying the hydrophobic surface of HDPE to become more hydrophilic. It follows that surface modification using wetting agents like AOT, NaLS, and TA could enhance the separation of PP/HDPE since CC_{RA} could be increased.

In the case of PP/LDPE mixtures, the results are still unclear and difficult to interpret due to the unnoticeable changes of SG_A. Based on the *CC* guide for gravity separation of Gupta and Yan (2016), PP/LDPE separation might not because particles with 3.5–4.0 mm size requires *CC* to be larger than 1.7. To confirm these hypothesis, the reverse hybrid jig separation experiments with the condition above were carried out.

4.2 Effects of air flow rate and wetting agents on reverse hybrid jig separation

The results of reverse hybrid jig separation experiments with continuous bubble generation of PP/HDPE and PP/LDPE plastic mixtures using various air flow rates as well as different wetting agent types and concentrations are presented in Figure 5. It was

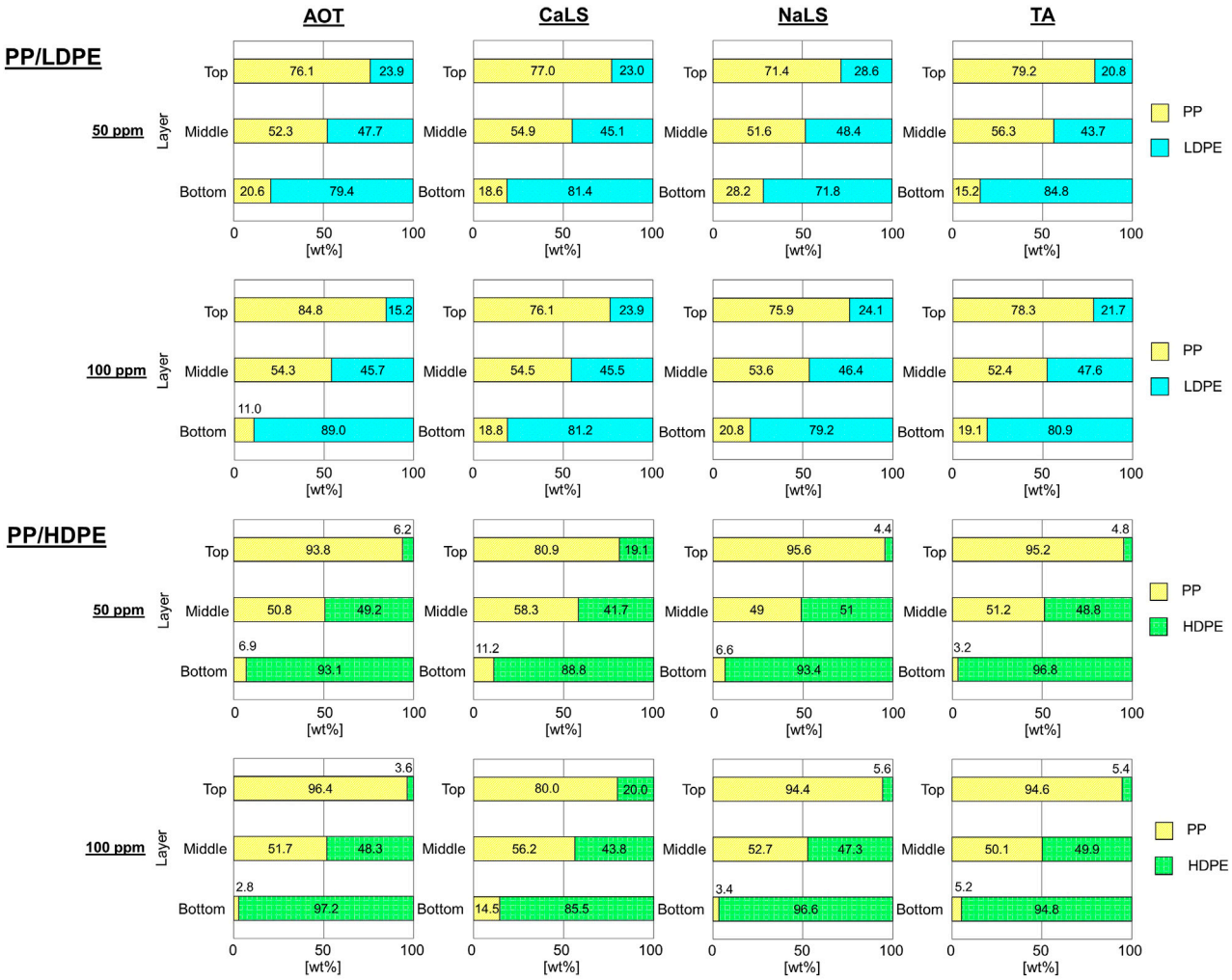

FIGURE 8
The proportion of plastics in each layer after reverse hybrid jig separation of PP/LDPE and PP/HDPE without bubble generation during pulsation at air flow rate of 1.0 L/min with AOT, CaLS, NaLS, and TA at concentrations of 50 and 100 ppm.

found that after separation, each layers contained similar amounts of PP and PE (i.e., LDPE or HDPE), indicating that separation did not occur. Visual observations suggest that separation was disturbed by the rising motion of air bubbles, which influence the fluidization behavior of the particle bed during water pulsation. However, there were slight improvements in PP/HDPE separation when wetting agents, particularly in TA, were added (Figure 6). These results confirmed that wetting agents could change the surface wettability of HDPE particles and improve the efficiency of reverse hybrid jig separation.

In contrast, the separation could occur for reverse hybrid jig separation experiments without bubble generation during pulsation (Figure 7). Compared with that of continuous bubble generation, the particle layer expanded more freely when bubbles were not introduced during pulsation. The particles with attached bubbles also stratified based on their SG_A without excess bubbles. Moreover, separation was possible even when CC_{RA} are less than 1.7 (Table 1). This improvement to the *CC* guide of Gupta and Yan (2016) could be attributed to the high precision control of water pulsation in advanced jig (Phengsaart et al., 2021). It was found that PP was concentrated in the top layers while PE (i.e., LDPE or HDPE) was concentrated in bottom layers. The results confirmed that separation of PP and HDPE was more effective than that of PP and LDPE in all air flow rates and was consistent with the results discussed previously (Figure 3 and Table 1). While air flow rate did not have significant effect

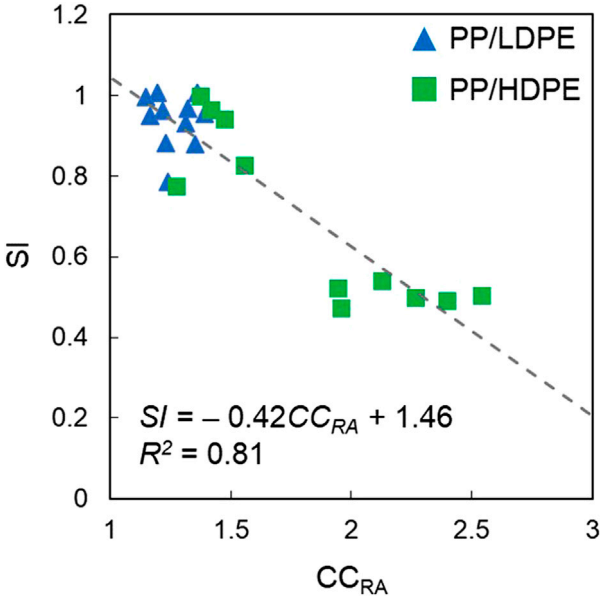

FIGURE 9
Relationship between sharpness index (*SI*) and reverse apparent concentration criterion (CC_{RA}).

on the separation. These indicate that SG_P was important for the separation. However, to prove that SG_A has more influence on gravity-wettability hybrid separation, more reverse hybrid jig separation experiments without bubble generation during pulsation were done with surface modification using wetting agents at air flow rate of 1.0 L/min (Figure 8 and Table 2). Similarly, PP and PE (i.e., LDPE or HDPE) were concentrated in the top and bottom layers, respectively. The results showed that the separation of PP and HDPE using AOT, NaLS, and TA improved but not for CaLS. While for PP/LDPE mixtures, the separation could not be improved. These reverse hybrid jig separation results were in line with the results of SG_A obtained from attached-bubbles volume measurements, indicating that separation efficiency has a stronger relationship with SG_A than SG_P. Also, the CC_{RA} could be used to estimate the efficiency of reverse jig separation.

4.3 Relationship of sharpness index of reverse hybrid jig separation without bubble generation during pulsation and reverse apparent concentration criterion

To determine the separation efficiency, purity distribution curves (Supplementary Figure S3, S4) were plotted from the results of Figure 7 and Figure 8, respectively. The horizontal axis (X) refers to the height (distance between the center position of each product layer and the lowest point of particle bed) and the vertical axis is the purity of PP while the horizontal axis (Y) refers to the purity of lighter plastic (i.e., PP) of each layer products.

From these purity distribution curves, the sharpness index (*SI*) could be calculated by Eq. 23 (Ito et al., 2020).

$$SI = \frac{X_{84.13} - X_{50}}{X_{50}} \tag{23}$$

where $X_{84.13}$ and X_{50} are the heights when purities of PP are 84.13 and 50%, respectively.

The value of CC_{RA} and *SI* under various conditions of air flow rate and surface modifications using wetting agents are shown in Table 1 and Table 2. It was found that the *SIs* were low (high separation efficiency) when CC_{RA} were high.

To understand the relationship of CC_{RA} and *SI* more clearly, the data in Table 1 and Table 2 were plotted into Figure 9. An empirical linear equation (Eq. 24) as a function of CC_{RA} and *SI* was obtained using least-squares method with a coefficient of determination (R^2) of 0.81.

$$SI = -0.42CC_{RA} + 1.46 \tag{24}$$

This relationship showed that the higher the values of CC_{RA}, the lower are the values of *SI*, which means that higher separation efficiency and CC_{RA} as well as attached-bubble volume measurement could be used to estimate the reverse jig separation efficiency when air bubbles are not introduced during water pulsation.

5 Conclusions

In this study, a new index called the reverse apparent concentration criterion (CC_{RA}) is proposed to estimate the efficiency of reverse jig separation at various air flow rates and surface modifications using wetting agents. The findings of this study are summarized as follows:

- Higher air flow rate deceased the SG_A of plastics because more air bubbles were generated and attached on plastic surfaces.
- Reverse hybrid jig separation with continuous bubble generation could not be used to separate mixed plastics because the rising motion of air bubbles disturbed particle fluidization. By stopping bubble generation during pulsation, separation occurred because the particle bed could expand more freely.
- Except for CaLS, AOT, NaLS, and TA could selectively modify the surface of HDPE from hydrophobic to become more hydrophilic that improved the separation of PP/HDPE plastic mixtures.
- CC_{RA}, a modified *CC* for reverse hybrid jig, obtained using SG_A and V_0^* from the attached-bubble volume measurement could be used to estimate the efficiency of reverse hybrid jig separation.

Data availability statement

The original contributions presented in the study are included in the article/Supplementary Material, further inquiries can be directed to the corresponding author.

Author contributions

TP: conceptualization, methodology, validation, formal analysis, investigation, data curation, writing—original draft, writing editing, visualization, project administration. CM: methodology, validation, formal analysis, investigation, data curation, writing—original draft, writing—editing, visualization. PS: validation, writing—editing. OJ: methodology, supervision. KM: supervision. SJ: supervision. IP: supervision. CT: writing—editing, supervision. NH: supervision. MI: conceptualization, validation, writing—editing, supervision.

Funding

This work (Grant No. RGNS 64-009) was supported by the Office of the Permanent Secretary, Ministry of Higher Education, Science, Research, and Innovation (OPS MHESI), Thailand Science Research and Innovation (TSRI) and Chulalongkorn University.

Acknowledgments

The authors wish to thank the editor and reviewers for their valuable inputs to this paper.

Conflict of interest

The authors declare that the research was conducted in the absence of any commercial or financial relationships that could be construed as a potential conflict of interest.

Publisher's note

All claims expressed in this article are solely those of the authors and do not necessarily represent those of their affiliated organizations, or those of the publisher, the editors and the reviewers. Any product that may be evaluated in this article, or claim that may be made by its manufacturer, is not guaranteed or endorsed by the publisher.

Supplementary material

The Supplementary Material for this article can be found online at: https://www.frontiersin.org/articles/10.3389/fchem.2022.1014441/full#supplementary-material

References

Aikawa, K., Ito, M., Segawa, T., Jeon, S., Park, I., Tabelin, C. B., et al. (2020). Depression of lead-activated sphalerite by pyrite via galvanic interactions: Implications to the selective flotation of complex sulfide ores. *Min. Eng.* 152, 106367. doi:10.1016/j.mineng.2020.106367

Demirbas, A. (2011). Waste management, waste resource facilities and waste conversion processes. *Energy Convers. Manag.* 52 (2), 1280–1287. doi:10.1016/j.enconman.2010.09.025

Filho, W. L., Voronova, V., Kloga, M., Paço, A., Minhas, A., Salvia, A. L., et al. (2021). COVID-19 and waste production in households: A trend analysis. *Sci. Total Environ.* 777, 145997. doi:10.1016/j.scitotenv.2021.145997

Geyer, R., Jambeck, J. R., and Law, K. L. (2017). Production, use, and fate of all plastics ever made. *Sci. Adv.* 3, e1700782. doi:10.1126/sciadv.1700782

Gopanna, A., Rajan, K. P., Thomas, S. P., and Chavali, M. (2019). "Polyethylene and polypropylene matrix composites for biomedical applications," in *Materials for biomedical engineering*. Editors V. Grumezescu and A. M. Grumezescu, 175–216. doi:10.1016/B978-0-12-816874-5.00006-2

Gupta, A., and Yan, D. (2016). "Gravity separation," in *Mineral processing design and operations*. Editors A. Gupta and D. Yan, 563–628. doi:10.1016/B978-0-444-63589-1.00016-2

Hori, K., Tsunekawa, M., Hiroyoshi, N., and Ito, M. (2009a). Optimum water pulsation of jig separation for crushed plastic particles. *Int. J. Min. Process.* 92 (3–4), 103–108. doi:10.1016/j.minpro.2009.01.001

Hori, K., Tsunekawa, M., Ueda, M., Hiroyoshi, N., Ito, M., and Okada, H. (2009b). Development of a new gravity separator for plastics —A hybrid-jig. *Mater. Trans.* 50 (12), 2844–2847. doi:10.2320/matertrans.M-M2009825

Hornn, V., Ito, M., Shimada, H., Tabelin, C. B., Jeon, S., Park, I., et al. (2020). Agglomeration-flotation of finely ground chalcopyrite and quartz: Effects of agitation strength during agglomeration using emulsified oil on chalcopyrite. *Minerals* 10, 380. doi:10.3390/min10040380

Hornn, V., Park, I., Ito, M., Shimada, H., Suto, T., Tabelin, C. B., et al. (2021). Agglomeration-flotation of finely ground chalcopyrite using surfactant-stabilized oil emulsions: Effects of co-existing minerals and ions. *Min. Eng.* 171, 107076. doi:10.1016/j.mineng.2021.107076

Irez, A. B., Okan, C., Kaya, R., and Cebe, E. (2022). Development of recycled disposable mask based polypropylene matrix composites: Microwave self-healing via graphene nanoplatelets. *Sustain. Mater. Technol.* 31, e00389. doi:10.1016/j.susmat.2022.e00389

Ito, M., Tsunekawa, M., Ishida, E., Kawai, K., Takahashi, T., Abe, N., et al. (2010). Reverse jig separation of shredded floating plastics — separation of polypropylene and high density polyethylene. *Int. J. Min. Process.* 97 (1–4), 96–99. doi:10.1016/j.minpro.2010.08.007

Ito, M., Saito, A., Murase, N., Phengsaart, T., Kimura, S., Tabelin, C. B., et al. (2019a). Development of suitable product recovery systems of continuous hybrid jig for plastic-plastic separation. *Min. Eng.* 141, 105839. doi:10.1016/j.mineng.2019.105839

Ito, M., Takeuchi, M., Saito, A., Murase, N., Phengsaart, T., Tabelin, C. B., et al. (2019b). Improvement of hybrid jig separation efficiency using wetting agents for the recycling of mixed-plastic wastes. *J. Mater. Cycles Waste Manag.* 21, 1376–1383. doi:10.1007/s10163-019-00890-w

Ito, M., Saito, A., Murase, N., Phengsaart, T., Kimura, S., Kitajima, N., et al. (2020). Estimation of hybrid jig separation efficiency using a modified concentration criterion based on apparent densities of plastic particles with attached bubbles. *J. Mater. Cycles Waste Manag.* 22, 2071–2080. doi:10.1007/s10163-020-01090-7

Ito, M., Saito, A., Takeuchi, M., Murase, N., Phengsaart, T., Tabelin, C. B., et al. (2021). Development of the reverse hybrid jig: Separation of polyethylene and cross-

linked polyethylene from eco-cable wire. *Min. Eng.* 174, 107241. doi:10.1016/j.mineng.2021.107241

Jeon, S., Ito, M., Tabelin, C. B., Pongsumrankul, R., Tanaka, S., Kitajima, N., et al. (2019). A physical separation scheme to improve ammonium thiosulfate leaching of gold by separation of base metals in crushed mobile phones. *Min. Eng.* 138, 168–177. doi:10.1016/j.mineng.2019.04.025

Kuwayama, Y., Ito, M., Hiroyoshi, N., and Tsunekawa, M. (2014). Jig separation of crushed automobile shredded residue and its evaluation by float and sink analysis. *J. Mater. Cycles Waste Manag.* 13, 240–246. doi:10.1007/s10163-011-0008-y

Mumbach, G. D., de Sousa Cunha, R., Machado, R. A. F., and Bolzan, A. (2019). Dissolution of adhesive resins present in plastic waste to recover polyolefin by sink-float separation processes. *J. Environ. Manage.* 243, 453–462. doi:10.1016/j.jenvman.2019.05.021

Phengsaart, T., Ito, M., Hamaya, N., Tabelin, C. B., and Hiroyoshi, N. (2018). Improvement of jig efficiency by shape separation, and a novel method to estimate the separation efficiency of metal wires in crushed electronic wastes using bending behavior and "entanglement factor". *Min. Eng.* 129, 54–62. doi:10.1016/j.mineng.2018.09.015

Phengsaart, T., Ito, M., Azuma, A., Tabelin, C. B., and Hiroyoshi, N. (2020). Jig separation of crushed plastics: The effects of particle geometry on separation efficiency. *J. Mater. Cycles Waste Manag.* 22, 787–800. doi:10.1007/s10163-019-00967-6

Phengsaart, T., Ito, M., Kimura, S., Azuma, A., Hori, K., Tanno, H., et al. (2021). Development of a restraining wall and screw-extractor discharge system for continuous jig separation of mixed plastics. *Min. Eng.* 168, 106918. doi:10.1016/j.mineng.2021.106918

Pita, F., and Castilho, A. (2016). Influence of shape and size of the particles on jigging separation of plastics mixture. *Waste Manag.* 48, 89–94. doi:10.1016/j.wasman.2015.10.034

Prata, J. C., Silva, A. L. P., Walker, T. R., Duarte, A. C., and Rocha-Santos, T. (2020). COVID-19 pandemic repercussions on the use and management of plastics. *Environ. Sci. Technol.* 54 (13), 7760–7765. doi:10.1021/acs.est.0c02178

Rabnawaz, M., Wyman, I., Auras, R., and Chenga, S. (2017). A roadmap towards green packaging: The current status and future outlook for polyesters in the packaging industry. *Green Chem.* 1920, 4737–4753. doi:10.1039/C7GC02521A

Tabelin, C. B., Park, I., Phengsaart, T., Jeon, S., Villacorte-Tabelin, M., Alonzo, D., et al. (2021). Copper and critical metals production from porphyry ores and E-wastes: A review of resource availability, processing/recycling challenges, socio-environmental aspects, and sustainability issues. *Resour. Conserv. Recycl.* 170, 105610. doi:10.1016/j.resconrec.2021.105610

Tsunekawa, M., Naoi, B., Ogawa, S., Hori, K., Hiroyoshi, N., Ito, M., et al. (2005). Jig separation of plastics from scrapped copy machines. *Int. J. Min. Process.* 76 (1-2), 67–74. doi:10.1016/j.minpro.2004.12.001

Tsunekawa, M., Kobayashi, R., Hori, K., Okada, H., Abe, N., Hiroyoshi, N., et al. (2012). Newly developed discharge device for jig separation of plastics to recover higher grade bottom layer product. *Int. J. Min. Process.* 114-117, 27–29. doi:10.1016/j.minpro.2012.09.003

United Nations (2015). *Transforming our world: the 2030 agenda for sustainable development*, Available at: https://sustainabledevelopment.un.org/post2015/summit (Accessed July 28, 2022).

Wills, B. A., and Finch, J. A. (2015). "Gravity concentration," in *Wills' mineral processing technology*. Editors B. A. Wills and J. A. Finch, 223–244. doi:10.1016/B978-0-08-097053-0.00010-8

frontiers | Frontiers in Chemistry

TYPE Original Research
PUBLISHED 05 October 2022
DOI 10.3389/fchem.2022.1038555

Check for updates

OPEN ACCESS

EDITED BY
Ugur Ulusoy,
Cumhuriyet University, Turkey

REVIEWED BY
Li Yu,
Northeastern University, China
Yuran Chen,
Zhengzhou University, China

*CORRESPONDENCE
Li Bao,
baoli-1983@163.com
Jiao Yang,
2924719578@qq.com

SPECIALTY SECTION
This article was submitted to Green and Sustainable Chemistry, a section of the journal Frontiers in Chemistry

RECEIVED 07 September 2022
ACCEPTED 20 September 2022
PUBLISHED 05 October 2022

CITATION
Yang J, Bao L, Long W, Zhong S, Qin J and Qiao R (2022), Microstructure and properties analysis of the brazing alloy prepared from recycled E-waste. *Front. Chem.* 10:1038555. doi: 10.3389/fchem.2022.1038555

COPYRIGHT
© 2022 Yang, Bao, Long, Zhong, Qin and Qiao. This is an open-access article distributed under the terms of the Creative Commons Attribution License (CC BY). The use, distribution or reproduction in other forums is permitted, provided the original author(s) and the copyright owner(s) are credited and that the original publication in this journal is cited, in accordance with accepted academic practice. No use, distribution or reproduction is permitted which does not comply with these terms.

Microstructure and properties analysis of the brazing alloy prepared from recycled E-waste

Jiao Yang[1]*, Li Bao[1]*, Weimin Long[1], Sujuan Zhong[1], Jian Qin[1,2] and Ruilin Qiao[1]

[1]State Key Laboratory of Advanced Brazing Filler Metals and Technology of Zhengzhou Research Institute of Mechanical Engineering Co., Ltd., Zhengzhou, Henan, China, [2]Beijing University of Science and Technology, Beijing, China

In order to realize the efficient and comprehensive utilization of e-waste resources and short process preparation of alloy brazing materials, this study has analyzed the microstructure and properties of e-waste recycled brazing alloys by the analysis methods of inductively coupled plasma emission spectrometer, differential scanning calorimeter, scanning electron microscope, metalloscope, X-ray diffractometer, micro-hardness tester. Experimental results showed that phase compositions are significant differences between the alloys prepared by the recycled e-waste and the pure metals. The circuit board recycling alloy mainly consisted of α-Fe dendrites, (Cu, Sn) phases, Sn-rich phases and Cu matrix, while the alloy obtained by pure metals is composed of (Cu, Sn) phase, Sn-rich phase and Cu matrix. The melting temperature of alloy obtained by melting the circuit board is in the range of 985.3°C–1,053.0°C, which was wider and higher than that of alloy obtained by pure metal smelting. The shear strengths of the joints brazed by the brazing alloys prepared by the recycle e-waste and pure metals are 182.21 MPa and 277.02 MPa, respectively. There is little difference in hardness between the two types of brazed joints. In addition, there are a large number of precipitated phases in alloy obtained by the recycled circuit board, owing to the precipitation strengthening mechanism. The main strengthening mechanism of alloy obtained by pure metals is solid-solution strengthening. The paper focused primarily on alloy obtained by melting the circuit board and studying the specific composition, melting temperature, structure, and properties of alloys formed by melting the circuit board and pure metals. Meawhile, the size, morphology and other microstructure evolution of the second phase of brazing alloy were investigated to provide theoretical guidance for the brazing alloy in the subsequent actual production process.

KEYWORDS

electronic waste alloy, copper based brazing filler metals, microstructure, wettability, mechanical properties

Introduction

Electronic waste, also called e-waste, includes a variety of obsolete computers, waste air conditioning, waste washing machines, and other household appliances, as well as some communication equipment. China generates a vast quantity of e-waste, which is continually increasing (Guo and Yan, 2017; Kang et al., 2020; Rao et al., 2020). It is rich in various metals, non-metallic substances, and organic materials in waste electrical and electronic equipment. With the global shortage of resources, e-waste as a critical "urban mine" attracts much attention and concern from society. E-waste is mainly composed of plastics, inert oxides, and metals. Taking circuit boards as an example, the metal content is high in circuit boards, with the majority of being common metals like Cu, Sn, Fe, Ni, Al, and Zn. Mo, Sb, and rare and precious metals, such as, Au and Ag (Jiang et al., 2016), have a comparatively low concentration. The research reports that a number of methods of recovering metal from circuit boards in China and abroad are dominated by physical separation extractive techniques such as magnetic separation, electrical separation, eddy current separation (Zheng et al., 2016; Gu et al., 2019), pyrometallurgy (Park and Kim, 2019; Habibi et al., 2020; Yue et al., 2021), hydrometallurgy (Díaz-Martínez et al., 2019), Bio-hydrometallurgy (Gu, 2016), and other extractive techniques. Due to the characteristics of e-waste, including its large quantity, complicated constituents, great harm, high potential value, and difficulty in treatment (Cao et al., 2003; Zhu et al., 2018), the recovery of valuable metals is the focus of attention for metal resource recovery from e-waste. Additionally, most of them are mainly recycling valued metals, which have many problems, such as long process flows, high energy consumption, and the generation of new pollutants like electrolytes and residue.

There is a high demand for multi-component alloys in China. For example, China consumes around 100,000 tons of copper-base brazing filler metals annually. The application of multi-component alloys is very wide. It is primarily employed in the production of diamond tools. Specifically, it could be widely applied in numerous engineering technical fields, such as automobiles, engineering machinery, aeronautics, and astronautics. Multi-component alloys usually contain Cu, Fe, Sn, Ni, Ag, Zn, and other elements. Consequently, the highest content of Cu in circuit board alloys can be used as the main component of brazing materials to produce copper-based brazing alloys. The brazing properties of alloys can be increased by adding Zn, Ni, and Sn elements (Long et al., 2017; Rene et al., 2021; Yang et al., 2022). Long Weimin (Long et al., 2017) studied the copper-base brazing alloys containing silver to braze. It was concluded that the addition of silver could improve the wettability of copper-base brazing alloys, hence greatly reducing the thickness of the copper-phosphorus/carbon steel interface compound layer and efficiently enhancing the strength and toughness of the brazed joint. Yang Jiao and Bao Li (Yang et al., 2022) summarized several typical copper-based brazing filler metals and mentioned that Zn additive can improve the wettability of copper-based brazing alloy and reduce the melting temperature of alloy. Ni element can refine crystalline, increase sintered body density, strengthen phase microstructure, and prevent crack propagation.

Most of the metals in circuit boards are feasible as components of the multi-element alloy brazing alloy. Besides, this may lower the melting point, solve problems of uneven composition, poor alloying extent and poor stability (Long et al., 2015). If the e-waste recycling target is used as an alloy preparation, the difficulties associated with refining individual metals can be avoided one by one. So that most of the metal elements can be recycled and utilized to achieve efficient recycling and comprehensive utilization of resources. However, most researches have concentrated on how to extract the required singlet metals from electronic wastes, but few reports on the composition, microstructure, and properties of alloy obtained by melting the circuit board. Therefore, this paper has focused primarily on melting the circuit board and studying the specific composition, melting temperature, structure, and properties of alloys formed by melting the circuit board and pure metals (Xue, 2018), (Wang et al., 2021). Meawhile, the size, morphology and other microstructure evolution of the second phase of brazing alloy were investigated to provide theoretical guidance for the brazing alloy in the subsequent actual production process.

Experiments

Materials

Circuit boards from discarded mobile phones served as the basic material. The recycled alloy is obtained by shearing, crushing, pretreatment, and high-temperature smelting. In addition, based on the composition ratio of brazing alloy obtained by melting the circuit board, materials including copper plate and tin block with a purity of 99.99%, Cu-37% Zn and Fe-36% Ni master alloys were utilized to quantitatively melt the alloy using induction heating equipment. The resulting alloy was then compared to that obtained by melting the circuit board.

Methods

After the melting process was completed, the alloy elements were quantitatively analyzed by an inductively coupled plasma emission spectrometer (ICP-OES) to measure the types and contents of the contained elements. The melting points of the two alloys were measured by differential scanning calorimeter (DSC), and the specimens were taken at 30 mg, heated to 1,300°C

TABLE 1 Main chemical compositions of the two alloy specimens (wt%).

Element	Cu	Sn	Fe	Ni	Pb	Ag
Sample 1	Bal.	4.85	3.29	0.66	0.82	0.3
Sample 2	Bal.	4.48	0.53	0.72	31ppm	0.13

at a heating rate of 15°C/min; Then, the solid and liquid phase lines were determined based on the DSC curves; The metallographic specimens and hardness specimens were intercepted by wire cutting, inlaid, polished, and then observed by a JEOL JSM-700F scanning electron microscope (SEM). Polycrystal X - Ray Diffractometer was used for detection. The target used in the experiment was copper target (Cu-Kα Rays, λ= 0.15405 nm), the current and voltage were 40 mA and 40 kV respectively, and the scanning angle ranged from 30° to 90°. It combined with energy spectrum analyzer (EDS)microstructure and phase of the alloy were analyzed; HV-1000 microhardness tester was used to measure the specimen's Vickers hardness; Loading load was 0.1 kN, the loading time was 10 s, and a point was selected at every 0.2 mm interval, with 10 points being the average value of the hardness test.

According to the national standard GB/T 11364-2008 "brazing material wettability test method," the Wetting test was carried out on the molten brazing alloy. The brazing alloys were wholly melted, maintained for 10 s, and then air-cooled. After wetting and spreading, the spread area of the brazing alloy was measured by image analysis software. The test was repeated five times, with the results being averaged. After welding the two brazing alloys onto stainless steel, joint shear tests were carried out. The shear strength of the joint specimen was evaluated using a universal testing equipment. The shear test was repeated three times, and the results were averaged.

Results and discussion

Composition analysis

The main chemical composition of brazing alloy was obtained by melting the circuit board sample No. 1. According to the composition ratio of the melting alloy, melting, the main chemical composition of the alloy No. 2 sample is shown in Table 1.

Compared the composition of alloy obtained by melting the circuit board and pure metal, it was found that the alloy obtained by pure metal iron content has a quit low iron content. In contrast, the proportional melting alloy added to the iron content of 3.5% results in measured iron content of 0.53% at the end of melting. According to the Cu-Fe binary phase diagrams, it can be seen that the solubility of Fe in Cu is low at room temperature, and the melting process is heated by conventional methods and cooled by air-cooling, resulting in insufficient iron content.

DSC analysis

Figure 1 depicts the melting curve for the alloy obtained by melting the circuit board, which was analyzed by using DSC analysis with alloy obtained by the pure metal. Figure 2B reveals alloy obtained by the pure metal has only one endothermic peak,

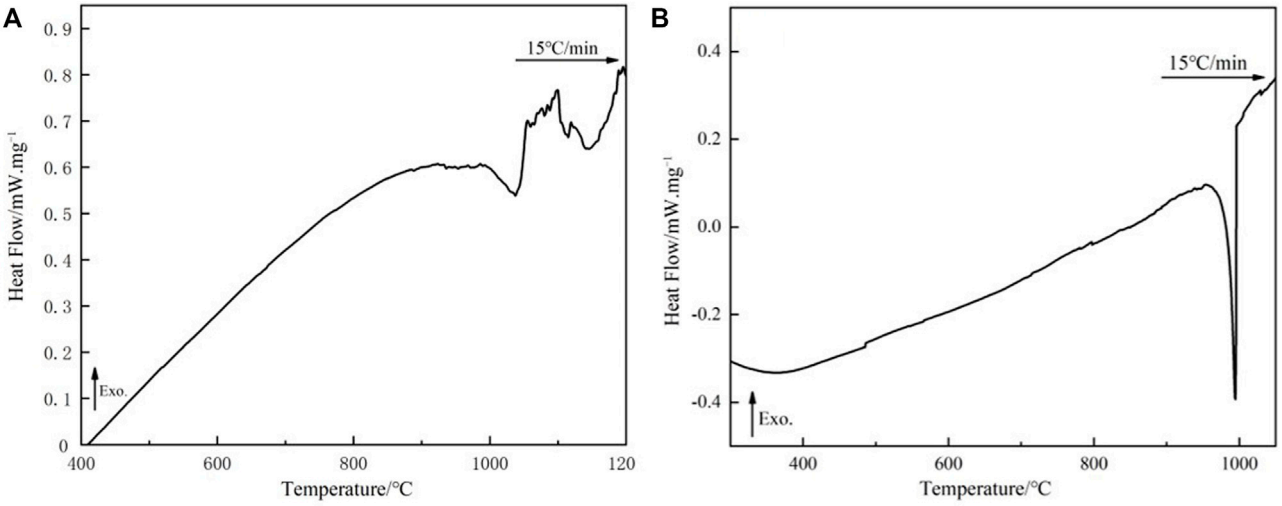

FIGURE 1
DSC curves of brazing alloys: **(A)** melting circuit board and **(B)** melting pure metals.

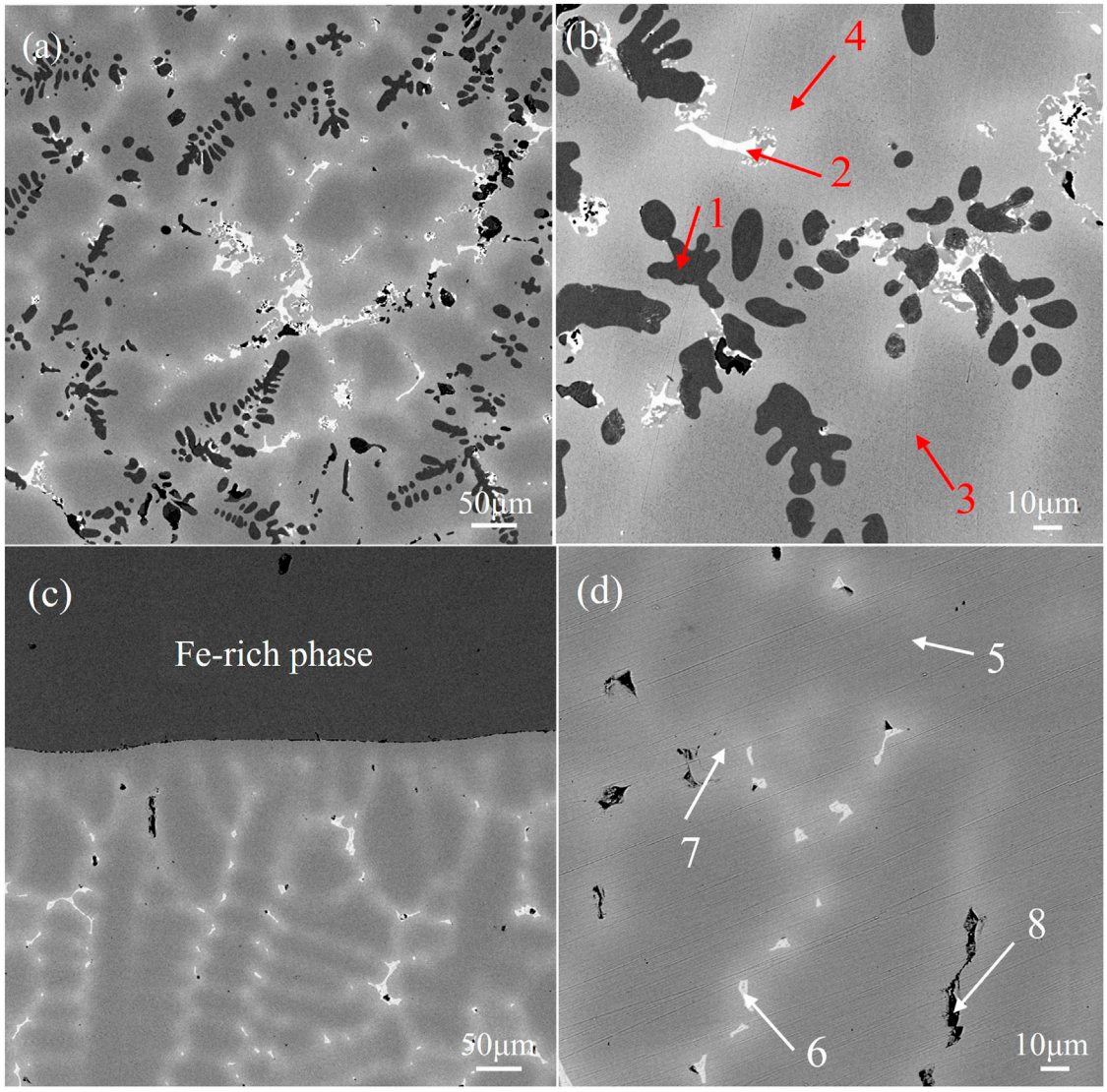

FIGURE 2
Microstructure of alloys **(A)** **(B)** alloy obtained by melting the circuit board and**(C)** **(D)** alloy obtained by pure metals.

with a peak temperature of 994.5°C. Correspondingly, it has a narrow melting temperature range of 941.0–996.1°C and good wettability. As shown in Figure 2A, the alloy obtained by the circuit board has two reaction heat endothermic peaks, with peaks at 1,037.2 °C and 1,144.7°C, corresponding to the heat endothermic peak temperature of 985.3–1,053.0°C and 1,099.4–1,189.2°C, respectively. The difference between this temperature melting interval and the melting temperature interval in the phase diagram is obvious. This difference in the melting temperature interval is related to experimental conditions and the change in elemental composition. The combined alloys obtained by the pure metal have an exothermic peak, showing that only one reaction occurs; While the.

Recycling alloy has two exothermic peaks, indicating that two reactions occur. Compared to the melting characteristics of alloy obtained by the pure metal, it indicates that the second peak of the recycling alloy might be a non-metallic reaction occurs. Therefore, the melting temperature range of the alloy obtained by melting the circuit board should be 985.3–1,053.0°C, which is higher than the alloy obtained by the pure metal.

Microstructure analysis of brazing alloys

Figure 2 shows the microscopic morphological SEM images of the two brazing alloys. Figure 2A is a low magnification image

10.3389/fchem.2022.1038555

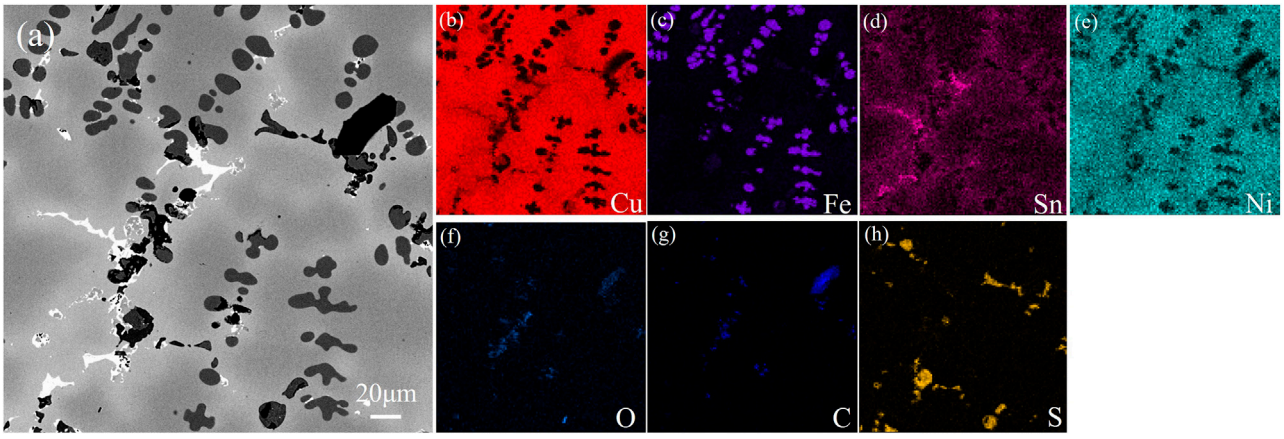

FIGURE 3
Microstructure and EDS distribution of alloy obtained by melting the circuit board.

TABLE 2 Analysis results of energy spectrum components at each point (wt%).

Region	Cu	Fe	Ni	Sn	Ag	Pb	Zn	C	O
1	15.64	79.12	3.65	0.61	—	0.43	0.19	0.36	—
2	57.02	1.08	4.12	30.54	0.97	0.41	—	0.50	5.35
3	90.28	2.17	1.17	3.26	0.24	0.72	—	0.97	1.24
4	80.38	1.04	1.28	11.76	0.41	0.59	—	0.69	3.85
5	93.50	1.61	1.58	1.72	0.23	—	0.35	1.01	—
6	59.77	0.17	1.47	30.04	1.78	—	1.03	0.77	4.97
7	81.49	1.07	12.76	6.56	0.89	—	0.40	0.98	2.21
8	73.54	0.41	—	12.68	0.91	—	—	3.82	8.63
9	3.41	62.77	31.48	—	—	—	—	0.75	1.59

of alloy obtained by melting the circuit board, which shows the distribution of black dendrites, bright white phase, peripheral gray-white phase, and dark gray Cu matrix in the figure. The dendrites are precipitated on the Cu matrix with a volume fraction as high as 79.12%, showing obvious dendrite segregation. This resembles the casting microstructure image of Cu-Fe alloy observed by Yue Shipeng et al. (Xue, 2018), displaying the characteristics of uneven distribution; Figure 2B shows the magnified image of Figure 3A, and the marked points 1–4 use the EDS elemental analysis. The analysis results are shown in Table 2; The black phase is the Fe-rich intermetallic compounds, and the bright white phase is the Sn-rich phase combined with the relevant references and EDS analysis. Figure 2C is a low-power electron microscope image of an alloy sample obtained by melting the pure metal. Large pieces of unmelted Fe-Ni alloy can be seen to occur a severe macroscopic segregation which is easy to produce when melting Cu alloy with high Fe content. Magnification of the copper matrix can be seen in the high magnification image, as shown in Figure 2D; It can be seen that alloy obtained by melting the.

Pure metal has the same the bright white phase, peripheral gray-white phase and dark gray Cu matrix composition, except for the lack of black phase in the microstructure of the alloy obtained by melting circuit boards. The composition of points 5-8 and 1-4 in Table 2 shows that the bright white phase is the Sn-rich phase. However, compared to the thinner and more uniform alloy sample size obtained by melting the circuit board, the Cu matrix appears dark gray. There is no Fe-rich phase precipitation, and the solid solution degree is better.

Figures 3 and 4 show the photos of area scan by SEM and EDS about the two alloy samples. The photos of area scan by SEM in Figure 3A and Figure 4A. The main element of the black precipitated phase in Figure 3C mainly contains Fe. Moreover, based on the XRD patterns in Figure 5 and some references, the precipitated phase should be α-Fe dendrites, and Ni elements in Figure 3E are less solidly soluble in α-Fe dendrites; More Ni elements are solidly soluble in the dark gray Cu matrix in Figure 3B with a small amount of Sn in Figure 3D, which is uniformly diffused; Most of the Sn elements form a bright white (Cu, Sn) phase, in which O elements in Figure 3F are also distributed, forming compound inclusions; The surrounding diffuse distribution of Sn-rich phase, with a medium Sn content; Non-metallic impurities such as C and S can be seen in Figure 3G,H , which may be residues from the incomplete separation of e-waste or inclusions generated during the pyrometallurgical melting process. As can be seen from Figure 4, microelement Fe in Figure 4C is diffusely distributed on the Cu matrix in Figure 3B, and most Ni elements in Figure 3E are solidly dissolved in the Cu matrix; The precipitated phase is only the bright white phase formed by the enrichment of Sn elements, while Ag in Figure 3F, C in Figure 3G elements are

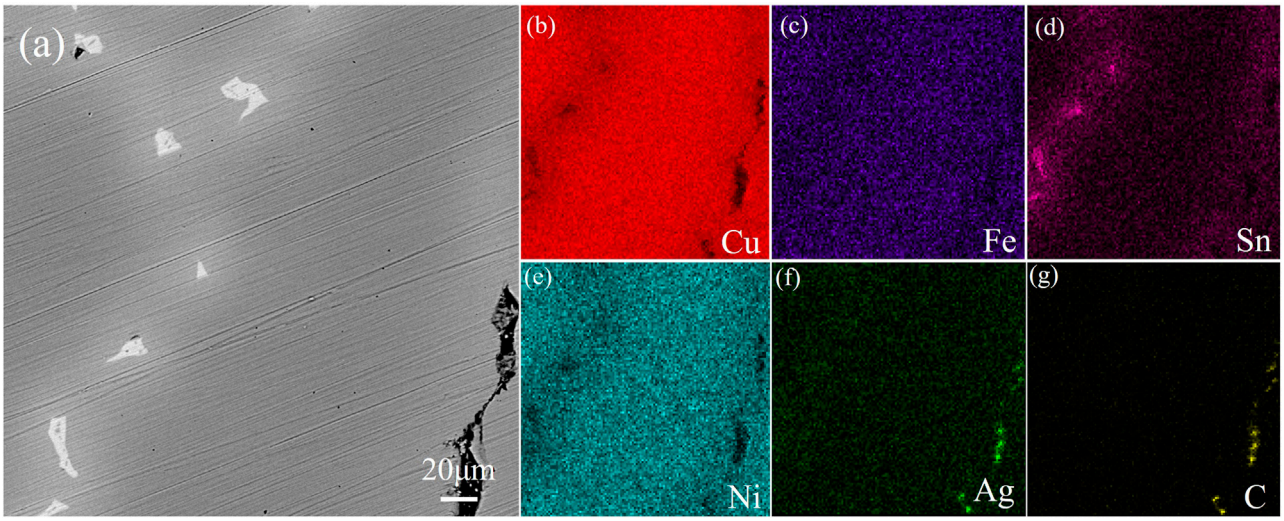

FIGURE 4
Microstructure and EDS distribution of alloy obtained by pure metals.

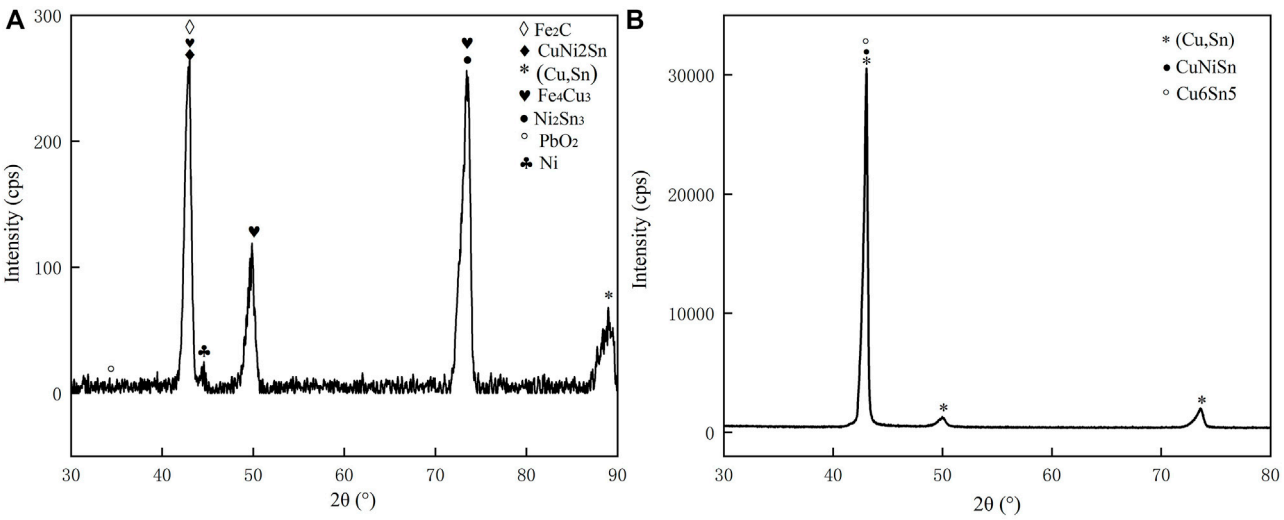

FIGURE 5
XRD analysis **(A)** alloy obtained by melting the circuit board **(B)** alloy obtained by pure metals.

TABLE 3 Microhardness at each area of alloys obtained by melting the circuit board sample 1 and pure metals sample 2.

Sample	Location	1	2	3	4	5	6	7	8	9	10	Average/HV10
Sample 1	Matrix	99.8	111.7	109.6	121.4	105.9	102.8	106.3	112.6	116.5	115.3	112.68
	Black phase	163.2	164.6	155.8	138.6	153.5	177.8	145.0	134.7	183.9	133.0	159.30
Sample 2	——	98.3	96.8	117.5	95.5	95.9	109.6	105.9	120.0	108.4	100.2	104.83

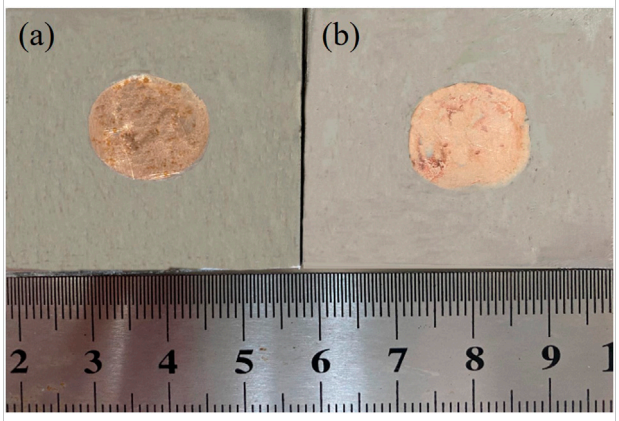

FIGURE 6
Spreading area of two alloys on 304 stainless steels: alloy obtained by melting the circuit board **(A)** and pure metals **(B)**.

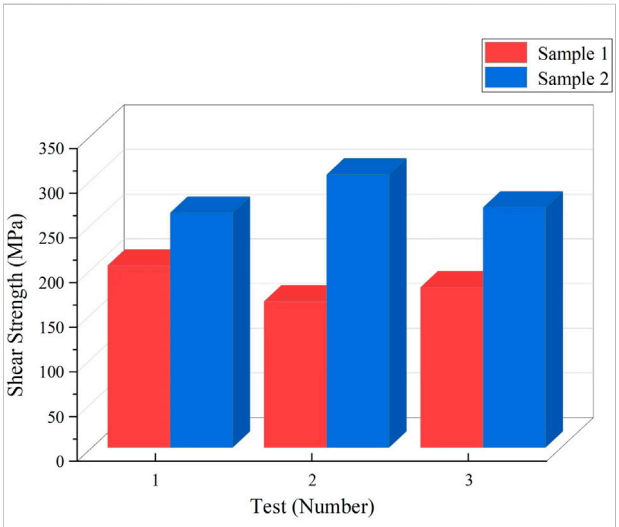

FIGURE 7
Shear strength of brazed joints with different brazing alloys.

gathered and distributed on the black irregular shape. The appearance of C may be from the inclusion produced in the smelting process.

XRD analysis

The XRD patterns of the alloys with varied compositions are shown in Figure 5. As can be seen, the content of precipitated iron leads to some differences in the diffraction patterns of the two groups of alloys, indicating a shift in their phase composition changes, with the higher content of Fe precipitated in the form of α-Fe dendrites. In contrast, the lower Fe content primarily exists as a solid solution in the copper matrix, which is consistent with the previous EDS analysis. In addition, it is evident from its diffraction pattern that the alloy obtained by melting the circuit board consists of α-Fe dendrites, (Cu, Sn) phase, Sn-rich phase, and Cu matrix. Alloys obtained by the pure metal consist of (Cu, Sn) phase, Sn-rich phase, and Cu matrix, which is different with the phase composition of recycled samples.

Hardness analysis

As demonstrated in Table 3, alloys obtained by recycling and melting the circuit board were subjected to hardness analysis with alloys obtained by the pure metal. The average microhardness of the black phase in the recycling alloy for circuit boards is 159.30 $HV_{0.1}$, which is relatively high. The microhardness at the copper matrix of the two brazing alloys is 112.68 $HV_{0.1}$ and 104.83 $HV_{0.1}$, respectively. Overall, the recycling alloy for circuit boards has a little higher than the.

Melting alloy for pure metal. According to the analysis depicted in Figure 3, the high hardness of alloys obtained by recycling and melting the circuit board is a result of the α-Fe dendrites created when the Fe content is excessive. The precipitation of Fe significantly increases the hardness of the alloy, but the overall hardness does not change significantly.

Wettability

Two brazing alloys were used for wetting test in stainless steel at a temperature of 1,080°C, and Figure 6 depicts the macroscopic morphology after the wetting experiment. Figure 6A is the spreading area of alloys obtained by melting the circuit board, with an average of 198 mm^2, while Figure 6B is the spreading area of brazing alloy obtained by the pure metal, with an average of 180 mm^2. The alloys obtained by melting the circuit board than alloy by melting pure metal in wettability is slightly better. Nevertheless, based on the DSC curve, the melting temperature interval of alloy obtained by the pure metal is narrower. On the one hand, it could be due to the higher temperature, on the other hand, the presence of the Fe element enhances the wettability of the brazing alloy on 304 stainless steels. The strong activite effect of brazing flux played a good role in de-filming, protecting the liquid brazing alloy, and reducing interfacial tension.

Properties and microstructure of brazed joint

Three shear tests were carried out separately for the two brazed joints, and the comparison of the mechanical properties of brazed joints is shown in Figure 7. Samples 1 and 2 represent

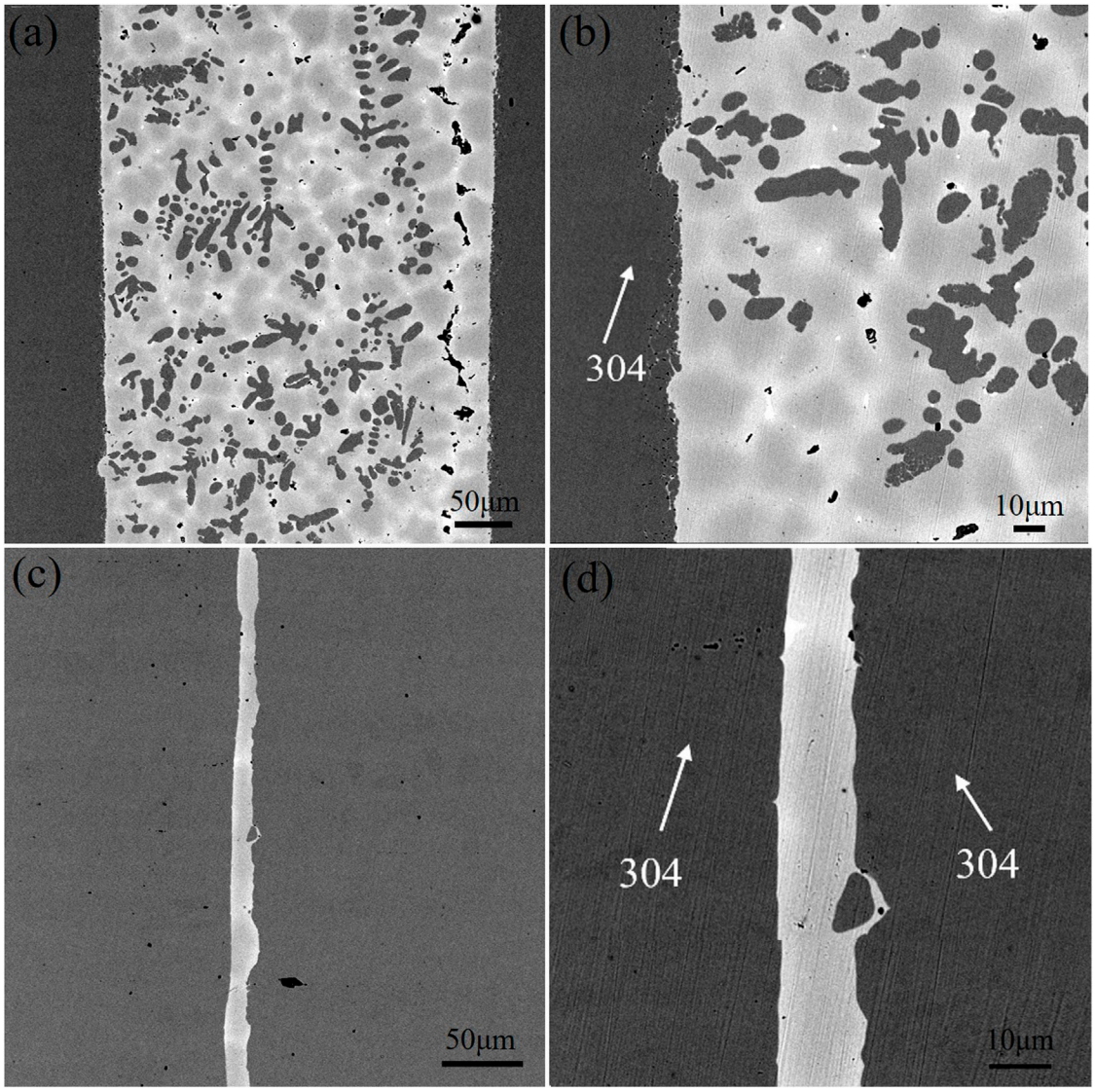

FIGURE 8
Microstructure of brazed joints with two brazing alloys **(A)** **(B)** brazed joint with alloy obtained by melting the circuit board and**(C)** **(D)** alloy obtained by pure metals.

alloy obtained by melting the circuit board and alloy obtained by melting pure metal, with average shear strengths of 182.21 MPa and 277.02 MPa, respectively. The brazing joint strength of alloy obtained by melting the circuit board is lower than that of pure metal melting alloy obtained by pure metal by 94.81 MPa. The fracture occurred at the brazed joints. According to the related.

Research (Wang et al., 2021), it is judged that the strengthening mechanism of alloy obtained by melting the circuit board is precipitation strengthening, while that of alloy sample No. 1 obtained by the pure metal is mainly solid solution strengthening. However, the alloy obtained by melting the circuit board appears segregated, resulting in the shear strength obviously inferior to the strength of the brazed joints of the No. 2 alloy. Figure 8 shows photos of the brazed joints microstructure about alloy obtained by melting the circuit board and alloy obtained by pure metal. From Figures 8A–B, it can be seen that the brazed joint seam of alloy obtained by melting the circuit board is densely.

Organized, mainly with α-Fe dendrites and Cu matrix. Meanwhile, diffusion occurs at the interface between the brazing joint and 304 stainless steels, and the microstructure of base metal near the interface is partially dissolved and enters the brazing seam. In addition, the brazing seam is wider, ranging from 275 to 283 μm. As can be seen in Figures 8C,D, the brazing

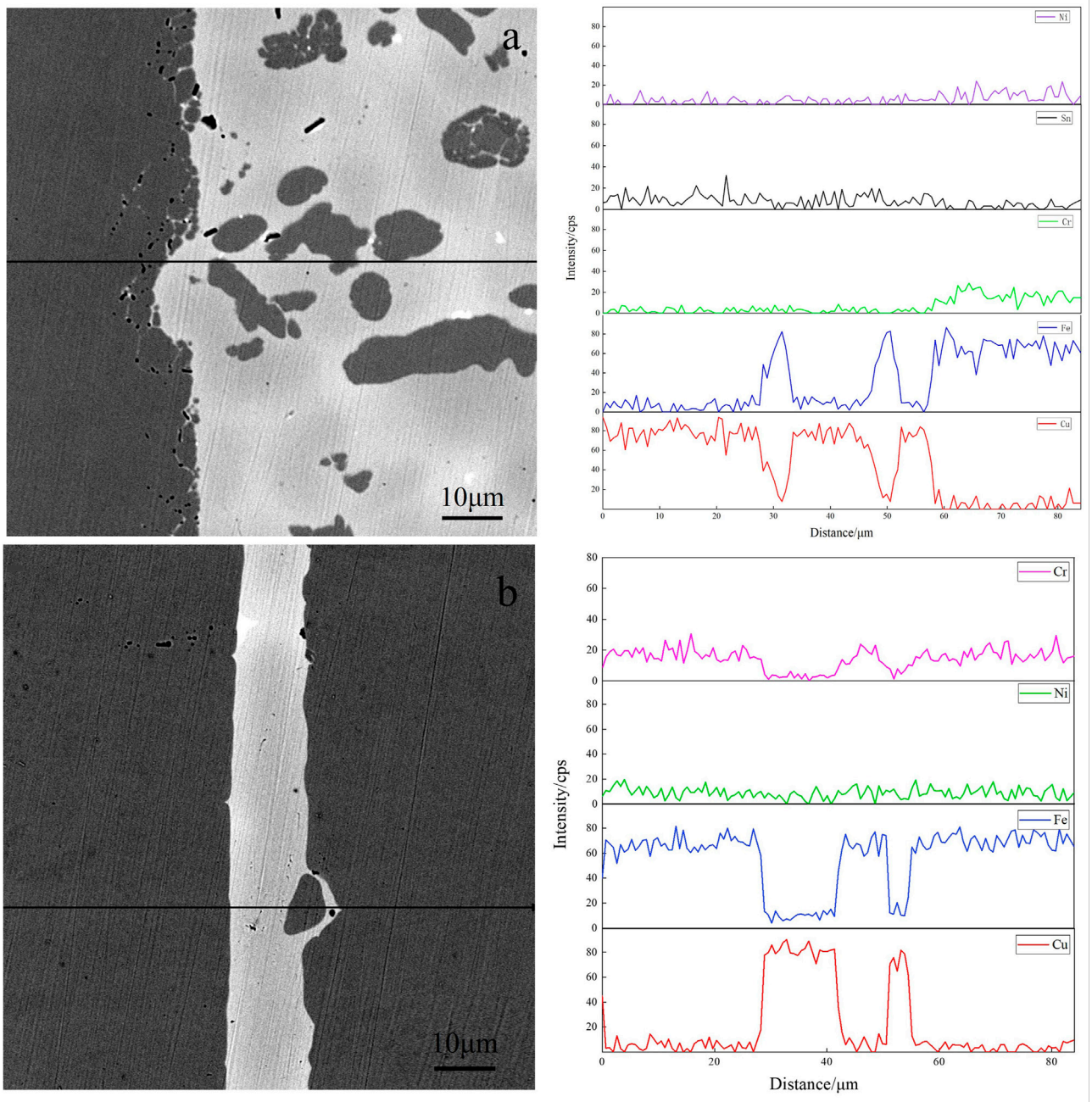

FIGURE 9
SEM image and EDS line scanning of elements with two brazed joints **(A)** alloy obtained by melting the circuit board and**(B)** alloy obtained by pure metals.

seam of alloy obtained by the pure metal is free of black α-Fe dendrites, and the brazing seam is mainly dominated by Cu matrix with the tiny microstructure of the brazing seam. The diffusion of the base metal can be observed on the high magnification image. Figure 9 shows the SEM images of the brazing seam and the line distributions of elements in two brazed joints by EDS. The line scan of Figure 9A from left to right through the areas of 304L stainless steel parent material, 304L-braze interface, and braze zone; Figure 9B from left to right for base metal of 304L stainless steel, 304L-brazing seam interface, brazing seam area, brazing seam-304L interface, the base metal of 304L. Figure 9B displays from left to the right base metal of 304L stainless steel, 304L- brazing seam interface, brazing seam area, brazed seam-304L interface, and 304L base metal. As can be seen

from Figure 9, the width of the two brazing seam area and the corresponding intermetallic compounds are obviously different. At the interface between the base metal of 304L and alloy brazing filler metal obtained by melting the circuit board, the elemental content of Fe gradually decreases, and the elemental content of Cu gradually increases, which form a transition phase of diffusion distribution. Consequently, the microstructure and morphology of the interface region are closer to that of α-Fe dendrites without obvious demarcation. The interface between the brazing seam of alloy obtained by the pure metal and the base metal is similar to that of the brazing seam of alloy obtained by melting the circuit board, where the Cu and Fe elements diffuse into each other. Due to limited diffusion ability of Cu in Fe, the thickness of the brazing seam interface layer is only 13–20 μm with uneven thickness distribution.

Conclusion

1) This study focuses on the microstructure and phase composition of the brazing alloys obtained by recycling and melting circuit boards. The alloys consist of α-Fe dendrites, (Cu, Sn) phase, Sn-rich phase, and copper matrix.
2) Compared to alloy obtained by the pure metal, the melting temperature range of alloy obtained by melting the circuit board expands, the melting temperature becomes higher, the shear strength is reduced, and the shear strength of the two multi-component brazing alloys is 182.21 MPa and 277.02 MPa, respectively. In addition, there are a large number of precipitated phases in the brazing alloy obtained by melting the circuit board, and the primary strengthening mechanism is determined as precipitation strengthening. Solid solution strengthening is the main strengthening mechanism of alloy obtained by the pure metal.
3) There are primarilyα-Fe dendrites and Cu matrix tissue with dense microstructure in the brazing seam of alloys obtained by melting circuit board. Diffusion occurs at the interface between the brazing seam and 304 stainless steels; The tissue of the base metal near the interface is partially dissolved and enters the brazing seam. In addition, the thickness in the brazing seam is wider, at 275–283 μm. The interface between the brazing seam of alloy obtained by melting the pure metal and the base metal is similar, where the Cu and Fe elements diffuse into each other; The thickness of the interface layer is only 13–20 μm with uneven thickness distribution due to the limited diffusion ability of Cu in Fe.

Data availability statement

The original contributions presented in the study are included in the article/Supplementary Material, further inquiries can be directed to the corresponding author.

Author contributions

JY: performed the experiment; performed the data analyses and wrote the manuscript; LB: helped perform the analysis with constructive discussions; WL: contributed significantly to analysis and manuscript preparation; SZ: contributed to the conception of the study; JQ: contributed to analysis and manuscript preparation; RQ: contributed to analysis and experiment.

Funding

This article was supported by National Natural Science Foundation of China (Grant No. 52005452).

Conflict of interest

Authors JY, LB, WL, SZ and JQ, and RQ were employed by State Key Laboratory of advanced brazing filler metals and technology of Zhengzhou Research Institute of Mechanical Engineering Co., Ltd.

Publisher's note

All claims expressed in this article are solely those of the authors and do not necessarily represent those of their affiliated organizations, or those of the publisher, the editors and the reviewers. Any product that may be evaluated in this article, or claim that may be made by its manufacturer, is not guaranteed or endorsed by the publisher.

References

Cao, Y. J., Zhao, Y. M., and Wen, X. F. (2003). Current status of research and development on the resourceization of waste electronic equipment [J]. *Environ. Pollut. Prev.* 25 (5), 289–292. doi:10.3969/j.issn.1001-3865.2003.05.013

Díaz-Martínez, M. E., Argumedo-Delira, R., Sánchez-Viveros, G., Alarcón, A., and Mendoza-López, M. (2019). Microbial bioleaching of Ag, Au and Cu from printed circuit boards of mobile phones. *Curr. Microbiol.* 76 (5), 536–544. doi:10.1007/s00284-019-01646-3

Gu, F., Summers, P. A., and Hall, P. (2019). Recovering materials from waste mobile phones: Recent technological developments. *J. Clean. Prod.* 237, 117657. doi:10.1016/j.jclepro.2019.117657

Gu, Y. W. (2016). *Study on the recovery of valuable metals by high temperature melting of used cell phones with Al2O3-FeOx-SiO2-CaO slag system[D]*. Maanshan: Anhui University of Technology.

Guo, X., and Yan, K. (2017). Estimation of obsolete cellular phones generation: A case study of China. *Sci. Total Environ.* 575, 321–329. doi:10.1016/j.scitotenv.2016.10.054

Habibi, A., Shamshiri Kourdestani, S., and Hadadi, M. (2020). Biohydrometallurgy as an environmentally friendly approach in metals recovery from electrical waste: A review. *Waste Manag. Res.* 38 (3), 232–244. doi:10.1177/0734242x19895321

Jiang, X. J., Liu, J. X., and Yan, K. (2016). Forecast of e-waste generation and characteristics analysis of metal accumulation in China [J]. *Nonferrous Metal Sci. Eng.* 7 (5), 104–109. doi:10.13264/j.cnki.ysjskx.2016.05.019

Kang, K. D., Kang, H., Ilankoon, I. M. S. K., and Chong, C. Y. (2020). Electronic waste collection systems using Internet of Things (IoT): Household electronic waste management in Malaysia. *J. Clean. Prod.* 252, 119801. doi:10.1016/j.jclepro.2019.119801

Long, W. M., Dong, B. W., Zhang, Q. K., He, P., and Xue, P. (2017). Copper-phosphorus brazing of steel based on the pilot wetting of silver alloy[J]. *J. Weld.* 38 (01), 1–4+129.

Long, W. M., Zhang, G. X., Zhang, Q. K., Zhang, Q. K., and He, P. (2015). Study on *in situ* synthesis of high-strength ZnAgCu brazing materials[J]. *Welding* 21 (07), 6–9+73. doi:10.3969/j.issn.1001-1382.2015.07.002

Park, H. S., and Kim, Y. J. (2019). A novel process of extracting precious metals from waste printed circuit boards: Utilization of gold concentrate as a fluxing material. *J. Hazard. Mater.* 365, 659–664. doi:10.1016/j.jhazmat.2018.11.051

Rao, M. D., Singh, K. K., Morrison, C. A., and Love, J. B. (2020). Challenges and opportunities in the recovery of gold from electronic waste. *RSC Adv.* 10 (8), 4300–4309. doi:10.1039/c9ra07607g

Rene, E. R., Sethurajan, M., Ponnusamy, V. K., Kumar, G., Dung, T. N. B., Brindhadevi, K., et al. (2021). Electronic waste generation, recycling and resource recovery: Technological perspectives and trends. *J. Hazard. Mater.* 416, 125664. doi:10.1016/j.jhazmat.2021.125664

Wang, L. M., Yang, Q. R., Jiang, Y. B., Li, Z., Xiao, Z., Gong, S., et al. (2021). Effects of Fe content on microstructure and properties of Cu–Fe alloy. *Trans. Nonferrous Metals Soc. China* 31 (10), 3039–3049. doi:10.1016/s1003-6326(21)65713-8

Xue, H. Y. (2018). *Study on the effect of phosphorus-containing pre-alloy powder on the tissue properties of iron-based diamond tool carcasses[D]*. Durgapur: General Research Institute of Mechanical Sciences.

Yang, J., Long, W. M., Bao, L., Liu, P., and Yang, H. Z. (2022). Research progress and application of copper-based brazing materials[J]. *Electr. Weld. Mach.* 52 (04), 21–28. doi:10.7512/j.issn.1001-2303.2022.04.04

Yue, S. H., Jie, J. C., Qu, J. P., and Li, Y. J. (2021). Effect of Ni and Si elements on Microstructure and mechanical properties of Cu Fe alloy [j]. *Chin. J. nonferrous metals* 31 (06), 1485–1493. doi:10.11817/j.ysxb.1004.0609.2021-39798

Zheng, Y., Yan, J. Z., Li, N., Cao, Y. T., and Shuai, F. (2016). Microstructure and properties of high-frequency induction brazed joints of 2Cr13 stainless steel with Cu-Mn-Ni-Ag brazing material[J]. *Chin. J. Nonferrous Metals* 26 (05), 988–994. doi:10.19476/j.ysxb.1004.0609.2016.05.006

Zhu, M. J., Wan, L. J., Ji, X. Q., and Liu, D. M. (2018). Analysis of the current situation and problems of e-waste recycling--Jiangsu Province Yangzhou City as an example[J]. *China Resour. Compr. Util.* 36 (04), 71–74. doi:10.3969/j.issn.1008-9500.2018.04.027

frontiers | Frontiers in Chemistry

TYPE Original Research
PUBLISHED 10 October 2022
DOI 10.3389/fchem.2022.1025990

Check for updates

OPEN ACCESS

EDITED BY
Xiangning Bu,
China University of Mining and Technology, China

REVIEWED BY
Ugur Ulusoy,
Cumhuriyet University, Turkey
Sabereh Nazari,
China University of Mining and Technology, China
Ma Guangxi,
Shandong University of Technology, China
Xinbo Yang,
The University of Utah, United States

*CORRESPONDENCE
Xuexia Wang,
wxuexia1989@163.com

SPECIALTY SECTION
This article was submitted to Green and Sustainable Chemistry, a section of the journal Frontiers in Chemistry

RECEIVED 23 August 2022
ACCEPTED 26 September 2022
PUBLISHED 10 October 2022

CITATION
Wang Y, Wang X and Bilal M (2022), Recovery of carbon and cryolite from spent carbon anode slag of electrolytic aluminum by flotation based on the evaluation of selectivity index. *Front. Chem.* 10:1025990. doi: 10.3389/fchem.2022.1025990

COPYRIGHT
© 2022 Wang, Wang and Bilal. This is an open-access article distributed under the terms of the Creative Commons Attribution License (CC BY). The use, distribution or reproduction in other forums is permitted, provided the original author(s) and the copyright owner(s) are credited and that the original publication in this journal is cited, in accordance with accepted academic practice. No use, distribution or reproduction is permitted which does not comply with these terms.

Recovery of carbon and cryolite from spent carbon anode slag of electrolytic aluminum by flotation based on the evaluation of selectivity index

Yemin Wang[1], Xuexia Wang[1]* and Muhammad Bilal[2]

[1]Department of Mining Engineering, Shanxi Institute of Technology, Yangquan, China, [2]Department of Mining Engineering, Balochistan University of Information Technology, Engineering and Management Sciences (BUITEMS), Quetta, Pakistan

One of the main electrolytic aluminum production costs is the consumption of carbon anodes, and carbon anode slag is a common hazardous waste in the aluminum industry. In this work, electrolytic aluminum carbon anode slag was separated by flotation. Using the selectivity index (*SI*) as an indicator, the influencing factors of the carbon slag flotation process were optimized, and the separation performance of carbon and cryolite in the carbon anode slag was investigated. The raw carbon anode slag was ground for 40 min to achieve dissociation of the cryolite from the carbon, the optimized *SI* value was then used to determine the optimal flotation test conditions. The test results showed that the *SI* value under the optimal grinding flotation was approximately four times larger than the value of direct flotation. This indicated that carbon anode slag had a better flotation selectivity under the grinding flotation, which significantly improved the flotation performance.

KEYWORDS

carbon anode slag, grinding flotation, carbon, cryolite, selectivity index

1 Introduction

Cryolite-alumina molten salt electrolysis has been the most commonly used process for producing aluminum since its invention (Grjotheim, 1982). This process uses carbon as its electrolytic anode in industrial production. The carbon anode often bursts during electrolysis due to uneven combustion, and the carbon slag particles fall off from the anode surface and then come into the electrolyte thus affecting the production. At present, carbon anode slag from aluminum electrolysis is generally discarded as waste or used as fuel. Carbon anode slag is primarily composed of cryolite (Na_3AlF_6) and carbon, which are valuable raw materials for aluminum electrolysis, and carbon can also be used as raw materials for the preparation of porous carbon materials (Li et al., 2021). When the carbon anode slag is discarded directly, it will pollute the environment; when it is burned as fuel, it will waste the high extra value electrolyte. The comprehensive recovery and utilization of electrolytic aluminum spent carbon anode slag (Hereinafter simplified as "carbon anode slag") are therefore necessary.

Flotation is a physical separation method used to separate particles by using the difference in surface property of particles (Chen et al., 2022; Ni et al., 2022). However, the flotation method is generally considered to be difficult to improve carbon purity and recovery efficiency, because cryolite are embedded during the process of carbon anode slag formation. In the mineral flotation, if there are different mineral embedding or locked bodies in the feed particles, grinding for mineral liberation is a prerequisite for a successful flotation separation (Li and Gao, 2017; Mathe et al., 2021). A grinding flotation process was proposed to separate and recover the $LiCoO_2$ and graphite from spent lithium-ion batteries (Yu et al., 2018). The flotation performance of carbon anode slag through process optimization (a closed-circuit process of one roughing, one scavenging and two cleaning) was significantly improved (Mei et al., 2016). Li et al. (2021) studied the effects of particle size distribution of carbon anode slag, impeller speed, slurry concentration, reagent addition, and flotation time on the flotation performance of electrolysis aluminum carbon anode slag basing on the carbon recovery rate and separation flotation efficiency index. They concluded that the carbon recovery rate in the optimization experiment was increased by 1.7%, and the separation flotation efficiency index was improved by 4.1%. Grinding flotation performance is significantly affected by grinding parameters such as wet or dry conditions, grinding time, and grinding devices. Compared to dry-ground particles, wet-ground particles had more irregular shape factors and smoother surfaces, resulting in shorter induction times and higher floatation recovery rates (Bu et al., 2019). Ulusoy et al. researched the relationship between the shape, surface roughness values and wettability of various minerals (quartz, barite, and calcite) under different dry mills (ball, rod, and autogenous) (Ulusoy et al., 2003; Ulusoy and Yekeler, 2004, Ulusoy and Yekeler, 2007). Thus, for different minerals, shape and roughness affect surface hydrophobicity differently. Given this, there is no systematic study on grinding flotation of carbon anode slag.

Flotation kinetics results are often described using cumulative recovery *versus* time in batch flotation. Typically, the widely used and classical first-order kinetic model is applied to analyze the effects of different factors (i.e., emulsified reagent, salt ions, and operation parameters) on the flotation performance of the minerals (Bu et al., 2017a; Chen et al., 2019; Zheng et al., 2020; Zhou et al., 2020). In terms of the correlation of flotation kinetics for carbon anode slag, currently, fewer studies have examined the influence of different operating factors on flotation performance.

Therefore, in this study, the flotation performance of carbon anode slag under different factors (grinding time, flotation feed solid concentration, collector dosage, frother dosage, and pH of slurry) was investigated using selectivity index (*SI*), and optimal conditions for grinding flotation were optimized. As a next step, the flotation performance of direct flotation and optimal grinding flotation of carbon anode slag was compared based on the ash content of the flotation products. Finally, to compare the differences in the recovery rates of combustible materials (R_c) and ash (R_a) for concentrate, the kinetic analyses of direct flotation and optimal grinding flotation of carbon anode slag were carried out. Thus, the flotation selectivity of carbon anode slag under each method was evaluated.

2 Materials and methods

2.1 Materials

Carbon anode slag was obtained from Shandong Province, containing 87%–90% cryolite and 10%–13% carbon. After drying, the representative sub-samples, used in the whole experiments, were obtained through mixing the carbon anode slag by thorough coning and quartering. The carbon anode slag was sieved with the help of a RK/ZSP-Φ200 slapping sieve shaker (Wuhan Rock Crush & Grinding Equipment Manufacture Co., Ltd. Wuhan, China) to determine the particle size distribution. The carbon anode slag was characterized by X-Ray diffraction (XRD), X-Ray fluorescence (XRF), and field emission scanning electron microscopy (FESEM).

2.2 Methods

2.2.1 Grinding experiments

The grinding tests were conducted under dry conditions using a QM-5 laboratory-scale ball mill (Changsha Tianchuang Powder Technology Co., Ltd. Changsha, China) equipped with a 2.0 L stainless steel cylinder (Diameter 12.5 cm and length 16.0 cm). A total of 2.22 kg of stainless steel balls were used as milling media. The diameters of the stainless steel balls were 1.20 cm, 0.90 cm, 0.62 cm, and 0.55 cm and their mass percentages were 33.75%, 31.40%, 18.37%, and 16.48%, respectively. The operational speed of the ball mill was set at 115 rpm (62.16% of critical rotational speed). The calculation of critical rotational speed for ball mill refers to the published literature (Ni et al., 2022). A mass of 200 g carbon anode slag with the size of −1 mm was fed into the ball mill.

2.2.2 Flotation experiments

A 0.5 L RK/FD-II flotation machine (Wuhan Rock Crush & Grinding Equipment Manufacture Co., Ltd. Wuhan, China) was used for flotation tests with the impeller speed of 1900 rpm and 200 L/h of airflow rate. Kerosene and terpenic oil were used as collector and frother, respectively. The specific operation steps of flotation were as follows. First, carbon anode slag was pre-wetted and then poured into the flotation machine. Next, kerosene was added after 2 min of agitation, and then the slurry was mixed for

2 min. After which terpenic oil was added and the slurry was stirred for 0.5 min. Following this, the air was introduced, and after 0.5 min of aeration, scraping of froth was started. Flotation concentrates were collected at intervals of 0.5, 1, 2, 3, and 5 min. Following flotation, the concentrates and tailings were filtered, dried, weighed, and analyzed.

2.2.3 XRD and XRF tests

The sample was ground to −0.074 mm using an HLXPM-Φ120 × 3 three-headed grinding machine (Wuhan Hengle Mineral Engineering Equipment Co., Ltd. Wuhan, China). The XRD and XRF tests were conducted with a D8 Advance X-Ray diffractometer (Bruker Company, Germany) and a ZSX Primus IV XRF (Rigaku Company, Japan), respectively. The tube current and voltage of XRD were 30 mA and 40 kV respectively. The anode target material used was Cu target, Kα radiation. The sample for XRD analysis was measured from 5 to 85° (2θ) with the scanning rate of 5°/min. The chemical composition of the carbon anode slag was acquired through XRF.

2.2.4 FESEM measurement

A high-resolution FESEM (MA1A3 LMH, Tescan Company, Czech) equipped with an energy dispersive spectroscopy (EDS) was applied to analyze the surface morphology and element distribution of carbon anode slag. The FESEM was operated at an accelerating voltage of 10.0 kV and with secondary electron detector. Before the FESEM experiments, all samples were sputtered with the gold-palladium layer to promote the surface conductivity.

2.2.5 Polarized light microscopy measurement

Thin sections were made from raw carbon anode slag, the product of carbon anode slag after 40 min, and optimal grinding flotation tailings. The particle size for the preparation of thin sections was + 45 μm. The embedding and liberation state between cryolite and carbon particles was then observed using the Polarizing microscope CX40P (Sunny optical instrument, Zhejiang, China).

2.3 Evaluation index of flotation

The first-order kinetic model, given in Eq. 1 (Sokolović and Miskovic, 2018), is used to obtain the parameters of K and R_{∞} through fitting the flotation test data. After that, the two parameters are used to evaluate the effect of the variables on flotation (Lynch et al., 1981). However, it is difficult to establish a trend for K and R_{∞} values under various conditions using this approach. Therefore, the modified rate constant (K_m), defined as the product of R_{∞} and K, was given in Eq. 2 (Xu, 1998). Xu et al. defined the ratio of K_m between mineral I and mineral II as the selectivity index (*SI*) (Xu, 1998). The expression of *SI* is presented in Eq. 3. Since K and R_{∞} were comprehensively considered in the calculation of *SI*, some researchers have applied *SI* to compare the effects of different factors on flotation performance (Sripriya et al., 2003; Vapur et al., 2010; Marion et al., 2017; Zheng et al., 2020).

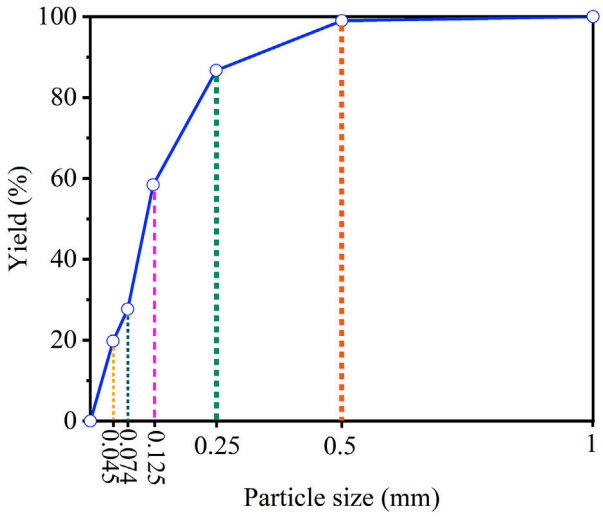

FIGURE 1
Cumulative particle size curve of carbon anode slag.

$$R = R_{\infty}.\left(1 - e^{-K.t}\right) \tag{1}$$

Where, R is the combustible/ash matter recovery in %; R_{∞} is the ultimate percentage (%) recovery; K is the first-order rate constant (min^{-1}), and t refers to the cumulative flotation time (min). MATLAB software was used to fit the first-order kinetic model to the flotation test results to obtain R_{∞} and K values. Coefficient of determination (R^2) was used to evaluate the accuracy of the model fit, and if it was higher than 0.8, Eq. 1 can be applied (Wang et al., 2021b).

$$K_m = R_{\infty}.K \tag{2}$$

$$SI\left(\frac{\mathrm{I}}{\mathrm{II}}\right) = \frac{K_m \text{ of mineral I}}{K_m \text{of mineral II}} \tag{3}$$

Where, minerals I and II represent the combustible and the ash materials in the flotation concentrate, respectively. The greater the *SI* value, the better the flotation selectivity. The expressions of R_c and R_a for flotation concentrate are shown in Eqs 4, 5, respectively.

$$R_c = \frac{\gamma_c.(100 - A_c)}{100 - A_f} \tag{4}$$

$$R_a = \frac{\gamma_c.A_c}{A_f} \tag{5}$$

Where, γ_c refers to the yield of flotation concentrate (%); A_c (%) and A_f (%) are the ash content of flotation concentrate and feed material, respectively.

10.3389/fchem.2022.1025990

TABLE 1 Element components from XRF analysis.

Element	F	Na	Mg	Al	Si	S	K	Ca
wt (%)	52.77	22.10	0.27	15.83	0.10	0.39	0.19	2.54

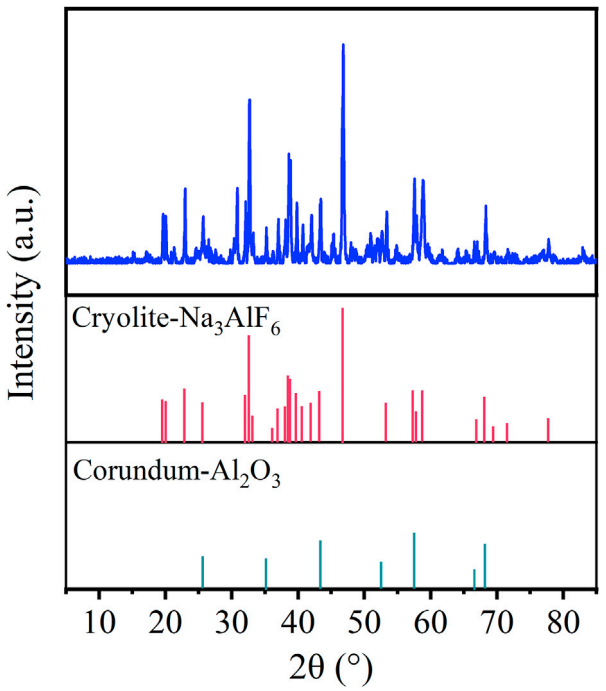

FIGURE 2
XRD pattern of carbon anode slag.

3 Results and discussion

3.1 Characterization of raw carbon anode slag

The cumulative particle size result is shown in Figure 1. From Figure 1, the content of fraction size of 0.125 mm–0.074 mm (30.76%) was the most, followed by 0.25 mm–0.125 mm (28.29%). The content of −0.045 mm fraction size was 19.74%, and the proportion of this micro-fine fraction was small. The chemical composition is provided in Table 1. As given in Table 1, the major elements in the carbon anode slag were fluorine (F, 52.77%), sodium (Na, 22.10%), and aluminum (Al, 15.83%). The XRD pattern is illustrated in Figure 2. The mineral components of carbon anode slag contained cryolite and corundum, which were in agreement with the content of major elements determined by XRF. The surface morphology and element distribution images of carbon anode slag are demonstrated in Figure 3. As shown in Figures 3A,B, the particle shape was irregular, and the particle surface was rough. The distribution of Na, Al, and F elements in Figure 3C indicated that the component of carbon anode slag was mainly cryolite. Here, the C element detected by EDS was primarily the C element on the conductive tape.

3.2 Effect of different factors on flotation performance of carbon anode slag

3.2.1 Grinding time

To improve flotation performance, the cryolite bound to carbon in carbon anode slag must be ground to be liberated from carbon. Therefore, carbon anode slag was ground before flotation to investigate the effect of grinding time on flotation performance. Figure 4 illustrates the effect of grinding time on the *SI* of carbon anode slag. From Figure 4, when the grinding time increased, the *SI* value first increased, then decreased. When the grinding time was 40 min, the *SI* value reached the maximum value of 41.89, which was about three times that of 0 min grinding time (i.e., direct flotation of carbon anode slag). These results indicate that grinding pretreatments significantly improved flotation recovery; because the carbon and cryolite separated in the carbon anode slag after grinding. When the grinding time was shorter than 40 min, the particles were dissociated to a certain extent, but they were also prone to detachment in the flotation process due to their large gravity, which did not permit the recovery of carbon particles. When the grinding time was longer than 40 min, carbon anode slag was over-grinding, thus causing more micro-cryolite particles to enter the froth concentrate (Wang et al., 2021a). Floatability was poor due to the excessive fine particles. The optimal grinding time was determined to be 40 min. Therefore, the subsequent flotation experiments were performed on the carbon anode slag after 40 min grinding treatment.

The ash content of flotation concentrate with different sizes under direct flotation and flotation after 40 min grinding treatment of carbon anode slag is illustrated in Figure 5. From Figure 5, it can be seen that the ash content of + 0.125 mm and 0.125–0.074 mm in the concentrate under the flotation after 40 min grinding treatment were 6.42% and 35.02%, respectively, which were significantly lower than that of the corresponding particle size in the direct flotation. It indicated that the grinding treatment had effectively separated the cryolite adhering to the coarser carbon particles, thus improving the flotation selectivity of the coarser carbon particles and promoting the flotation process. The microscope observations of the raw carbon anode slag and the product of carbon anode slag after 40 min grinding were demonstrated in Figure 6. Comparing Figures 6A,B, it is found that there were significantly more black carbon particles in the product after grinding treatment than in the raw carbon anode slag, indicating that cryolite

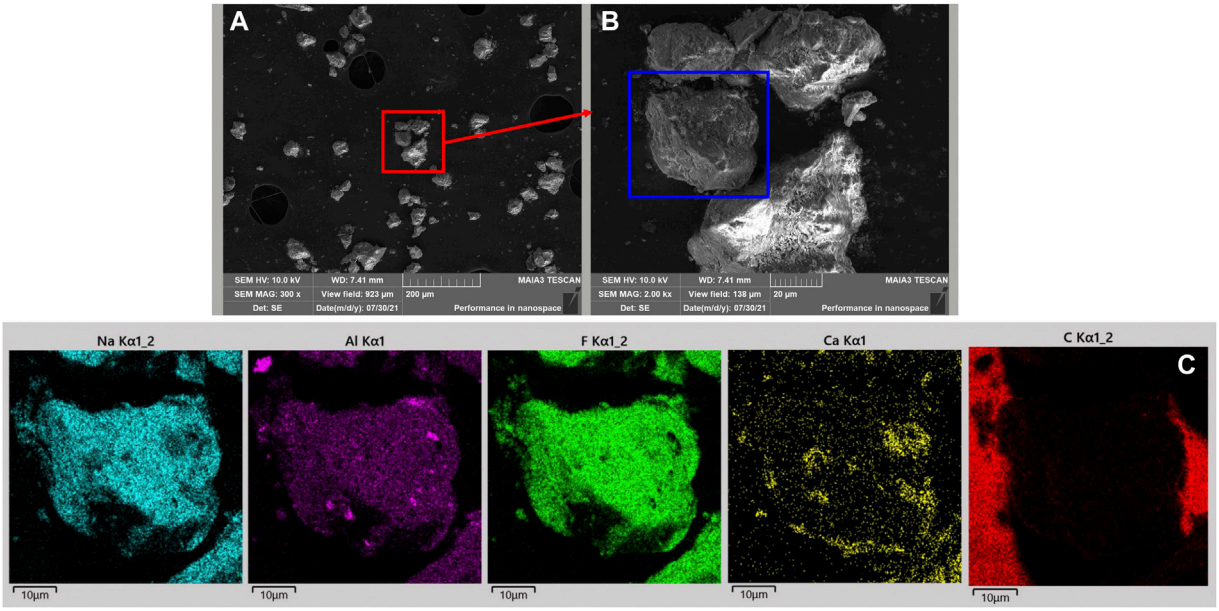

FIGURE 3
Images of **(A)**, **(B)** surface morphology and **(C)** element distribution in the carbon anode slag. Image **(B)** is an enlarged view of image **(A)** where is highlighted with a red rectangle. The area captured in image **(C)** was highlighted with a blue rectangle in image **(B)**.

particels were enriched in the fine-grainded fraction; carbon particles were enriched in the coarse-grainded fraction. This was because there was a difference in hardness between cryolite and carbon particles, which led to the selective crushing of carbon anode slag in the grinding process (Ni et al., 2022).

3.2.2 Effects of feed solid concentration

The effects of feed solid concentration on the flotation performance are mainly reflected in the change of flotation time, the "excess" and "insufficient" flotation reagent, and the change of aeration rate, which directly affects the recovery and ash content of the concentrate. Figure 7 shows the effect of feed

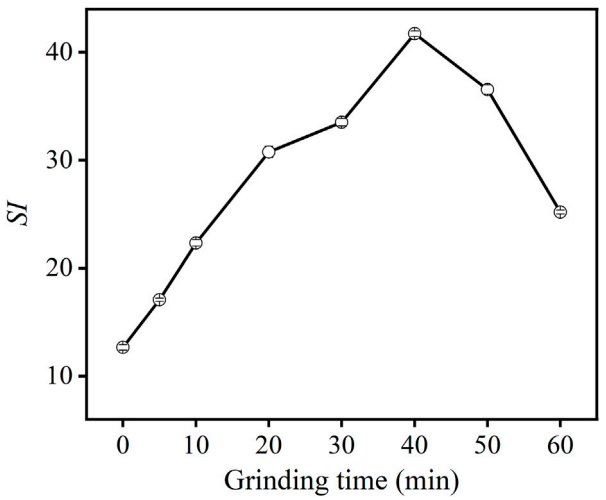

FIGURE 4
Effect of grinding time on *SI* of carbon anode slag flotation (feed solid concentration 200 g/L, colletor dosage 1,000 g/t, frother dosage 500 g/t).

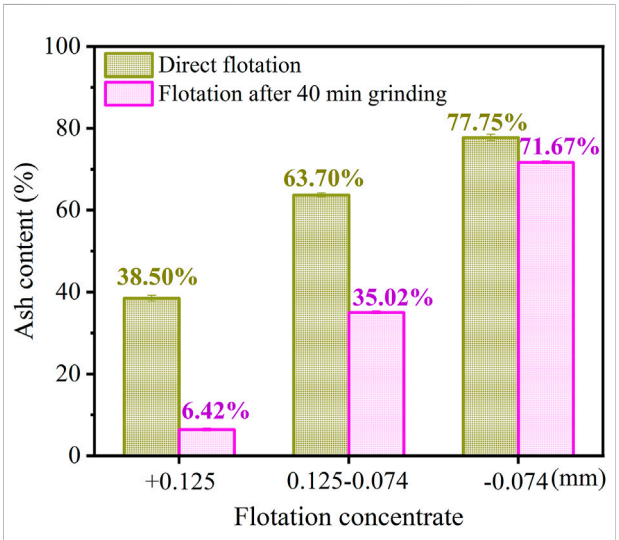

FIGURE 5
Comparison diagram of ash content of flotation concentrate with different sizes under different methods.

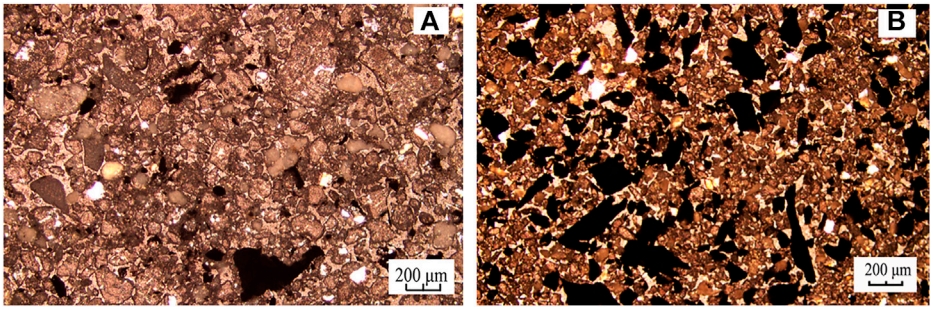

FIGURE 6
Microscope photographs of thin sections of **(A)** raw carbon anode slag and **(B)** the product of carbon anode slag after 40 min grinding.

solid concentration on the flotation performance of carbon anode slag. As can be seen in Figure 7, the *SI* value tended to increase and then decrease as the feed solid concentration increased, and the *SI* reached a maximum value at a feed solid concentration of 140 g/L.

When the feed solid concentration was lower (<140 g/L), the *SI* value increased with the increase in the feed solid concentration, which is consistent with the literature (Luo et al., 2016; Bu et al., 2017b). The increase in the solid concentration is helpful for the collison between bubbles and particles, which leads to the improvement in the flotation recovery of valuable particles. When the feed solid concentration was higher than 140 g/L, the reduction of *SI* was observed. This could be attributed to the detachment of bubbles from particle surfaces and also reduction of bubble numbers with increasing of pulp density for a given air flow rate (Mowla et al., 2008). Furthermore, the flotation time of the particles was relatively long, and there existed entrainment of more micro-cryolite particles, in turn leading to a lower *SI* (Wang et al., 2015). Therefore, 140 g/L was selected as the optimal value for feed solid concentration.

3.2.3 Collector dosage

The effect of collector dosage on *SI* is illustrated in Figure 8. From Figure 8, when the collector dosage increased from 600 g/t to 1,000 g/t, the *SI* showed an increasing trend; when the dosage of the collector continued to increase, the *SI* value showed a decreasing trend. When the dosage of the collector was not enough, the collector's ability to capture particles was

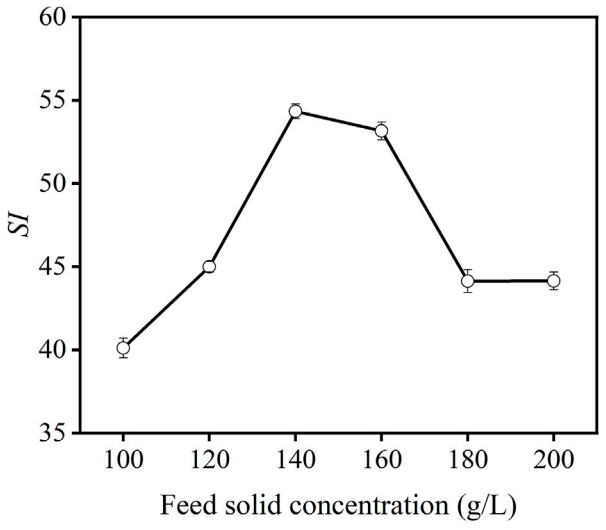

FIGURE 7
Effect of feed solid concentration on *SI* of carbon anode slag flotation (grinding time 40 min, colletor dosage 1,000 g/t, frother dosage 500 g/t).

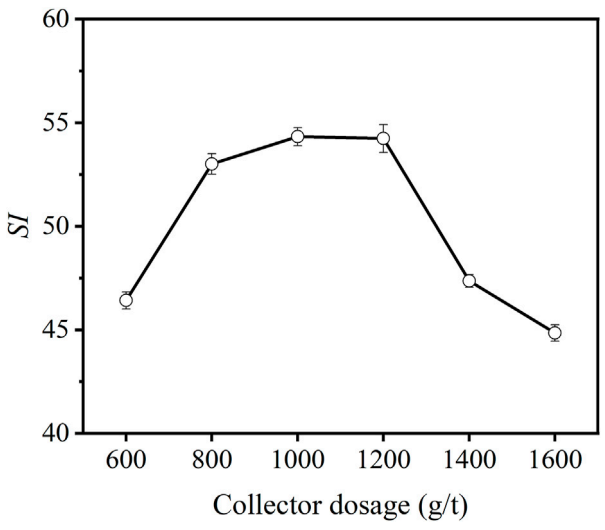

FIGURE 8
Effect of collector dosage on *SI* of carbon anode slag flotation (grinding time 40 min, feed solid concentration 140 g/L, frother dosage 500 g/t).

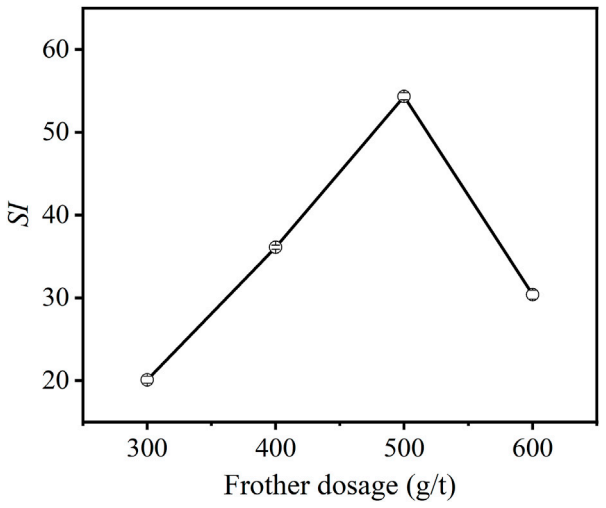

FIGURE 9
Effect of frother dosage on *SI* of carbon anode slag flotation (grinding time 40 min, feed solid concentration 140 g/L, collector dosage 1,000 g/t).

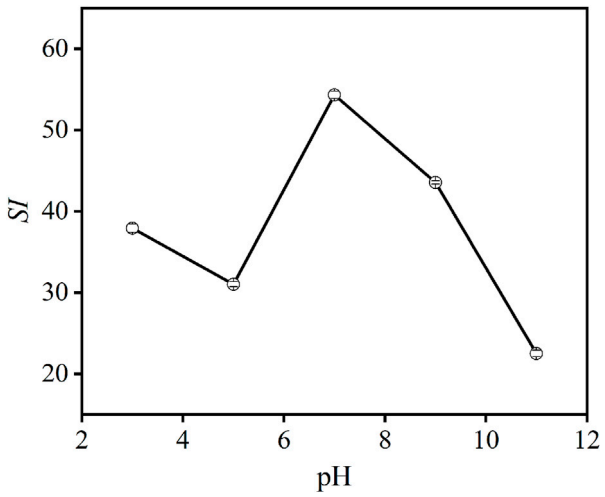

FIGURE 10
Effect of pH on *SI* of carbon anode slag flotation (grinding time 40 min, feed solid concentration 140 g/L, collector dosage 1,000 g/t, frother dosage 500 g/t).

inadequate. When the collector dosage was gradually increased, the hydrophobic particles were promoted into the froth concentrate, thus increasing *SI*. When the collector dosage was 1,000 g/t, the *SI* value reached its maximum. When the collector dosage was >1,000 g/t, due to the excessive collector dosage, solid particle selectivity in the slurry was poor, resulting in a decrease in *SI* (Bu et al., 2018). Further more, oil droplet can promote the liquid drainage of froth, leading to bubble coalescence and breakup (Zhou et al., 2020). Thus, the poor flotation performance at excessively high collector dosage can be due to the poor froth stability resulting from the oil droplets.

3.2.4 Effects of frother dosage

Figure 9 provides the effect of frother dosage on the flotation performance of carbon anode slag. As can be seen from Figure 9, *SI* values increased with increasing frother dosage, followed by decreasing trends. The low *SI* value at low frother dosage is due to the poor bubble stability. With the increasing frother dosage, the froth become stable, which is helpful for the collection of mineralized bubble *via* the froth zone (Farrokhpay, 2011). At a dosage of 500 g/t, the *SI* reached its maximum value. Increasing the frother dosage over 500 g/t resulted in more froth entrainment due to the sticky froth of terpenic oil, so the *SI* value decreased again (Nguyen and Schultze, 2004). Therefore, 500 g/t was chosen as the optimal froth dosage.

3.2.5 pH of the slurry

The effect of slurry pH on the flotation performance of carbon anode slag is illustrated in Figure 10. It can be seen that, when pH is <7 or >7, the *SI* value is decreased in both

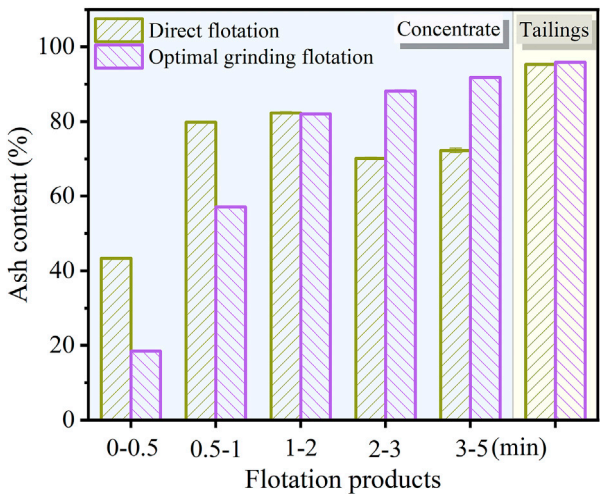

FIGURE 11
Comparison diagram of ash content of flotation products under different periods.

cases, indicating that when the flotation slurry was acidic or alkaline, it was not conducive to the flotation of carbon anode slag, thus resulting in poor flotation performance. This is because the molecular activity of the surfactant was inhibited by acidic or alkaline solution environments, thereby reducing the flotation selectivity of carbon anode slag. Accordingly, pH seven was determined to be the optimal pH of the flotation slurry.

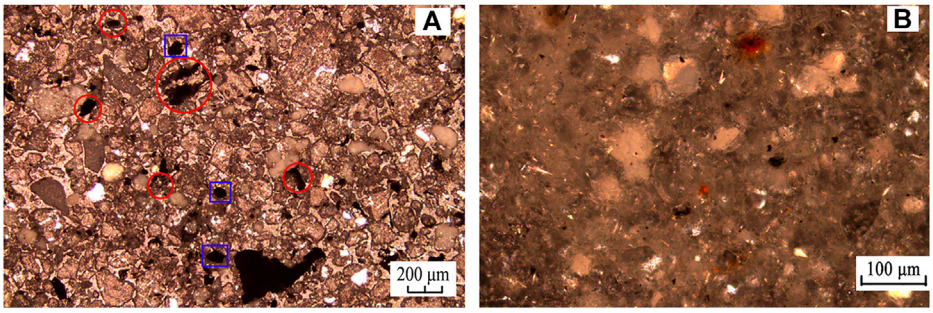

FIGURE 12
Microscope photographs of thin sections of **(A)** raw carbon anode slag and **(B)** tailings of optimal grinding flotation.

The optimal experiment conditions for grinding flotation of carbon anode slag were: grinding time 40 min, feed solid concentration 140 g/L, pH 7, collector dosage 1,000 g/t, and frother dosage 500 g/t.

3.3 Comparative analysis of flotation performance

3.3.1 Ash content comparison of flotation products under different periods

The ash content of carbon anode slag flotation products under direct flotation and optimal grinding flotation is shown in Figure 11. According to Figure 11, the ash content of carbon collected in 0–0.5 min and 0.5–1 min under the optimal grinding flotation was significantly lower than that direct flotation, because the carbon and cryolite in carbon anode slag were effectively dissociated after grinding treatment. Tailings obtained by this method had a higher ash content than tailings obtained by direct flotation. In the flotation process, carbon particles are recovered in the early stages and cryolite (hydrophobic particles) are recovered in the later stage due to entrainment. Thus, under the direct flotation, the carbon anode slag was not dissociated, and the locked bodies of cryolite and carbon were collected at the stage of 2–3 min and 3–5 min, resulting in lower ash content of concentrate than that under the optimal grinding flotation. This revealed that when carbon anode slag was ground and floated, the dissociated carbon particles mainly floated out during the periods 0–0.5 min and 0.5–1 min, resulting in good separation efficiency.

3.3.2 Analysis of microscope photographs

Figure 12 shows the microscope observations of the raw carbon anode slag and the tailings under the optimal grinding flotation. In Figure 12A, the black particles marked by blue box lines were monomeric carbon particles, and the particles marked by red box lines were carbon and cryolite in an embedded state. It indicated that there were more locked bodies of carbon and cryolite and less monomeric carbon, further dissociation of locked bodies of carbon and cryolite can improve carbon anode slag flotation performance. As can be seen from Figure 12B, there were fewer black carbon particles in the flotation tailings, demonstrating that the effective separation of carbon and cryolite particles can be achieved through grinding treatment. After grinding, the carbon and cryolite were sufficiently dissociated, and the carbon was enriched into the froth concentrate, thereby improving the cryolite tailings ash content. As a result, it was confirmed that optimal grinding flotation of carbon anode slag produced a better flotation performance than direct flotation.

3.4 Comparison of the recovery rate of flotation concentrate

The recovery rate of combustible materials (R_c) and ash materials (R_a) of concentrate (direct flotation vs. optimal grinding flotation) as a function of time is shown in Figure 13. According to Figure 13A, the R_c of the concentrate at 0.5–5 min under the method of optimal grinding flotation was higher than that of direct flotation, indicating that the carbon could be recovered from carbon anode slag efficiently through grinding treatment before flotation. As shown in Figure 13B, the R_a of the concentrate for optimal grinding flotation was lower than that of direct flotation. Moreover, under the grinding flotation method, the ash content in the concentrate was significantly reduced, and micro-cryolite particles were significantly reduced from entering the froth concentrate. Table 2 gives the R_{co} and K values of flotation concentrate combustible/ash materials for each method. As can be seen in Table 2, the SI values for direct flotation and optimal grinding flotation were 12.82 and 54.64, respectively, and the latter was approximately four times larger than the former; indicating that grinding flotation has a better flotation selectivity for carbon anode slag than direct flotation.

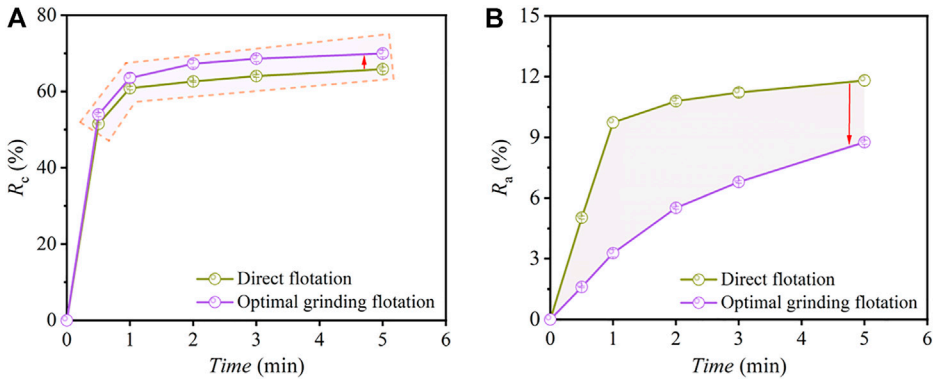

FIGURE 13
R_c **(A)** and R_a **(B)** of concentrate *versus* time under the methods of direct flotation and optimal grinding flotation.

TABLE 2 Output of non-linear regression fitting to first-order rate equation for a recovery rate of combustible and ash materials for flotation concentrate.

Flotation method	Combustible material				Ash material				*SI*
	K (min^{-1})	$R_{c\infty}$ (%)	R^2	K_m	K (min^{-1})	$R_{a\infty}$ (%)	R^2	K_m	
Direct flotation	3.22	63.77	0.9985	205.21	1.39	11.53	0.9855	16.00	12.82
Optimal grinding flotation	3.03	67.68	0.9980	204.73	0.36	10.42	0.9993	3.75	54.64

4 Conclusion

The effects of grinding time, flotation feed solid concentration, collector dosage, frother dosage, and pH of slurry on the flotation performance of carbon anode slag were investigated, and the flotation selectivity of carbon anode slag under the methods of direct flotation and grinding flotation was analyzed and compared. The following conclusions were drawn.

1) Carbon anode slag flotation separation is affected by all five factors. Based on the optimization value of *SI*, the optimal test conditions for grinding flotation were determined as follows: grinding time 40 min, feed solid concentration 140 g/L, collector dosage 1,000 g/t, frother dosage 500 g/t, and pH of slurry 7.
2) Under the optimal grinding flotation, the separated carbon particles were mainly recovered at the stages of 0–0.5 min and 0.5–1 min. This led to a better flotation performance for the carbon anode slag because the carbon and cryolite were separated.
3) Under grinding flotation, carbon anode slag had a higher recovery rate of combustible material in the concentrate than direct flotation.
4) The *SI* value of carbon anode slag under the optimal grinding flotation was approximately four times larger than the direct flotation. Consequently, carbon anode slag showed better flotation selectivity under the grinding flotation than direct flotation.

Data availability statement

The original contributions presented in the study are included in the article/Supplementary Material, further inquiries can be directed to the corresponding author.

Author contributions

YW and XW conceived the research, designed the tests, and analyzed the data. YW, XW, and MB wrote and revised the manuscript.

Conflict of interest

The authors declare that the research was conducted in the absence of any commercial or financial relationships that could be construed as a potential conflict of interest.

Publisher's note

All claims expressed in this article are solely those of the authors and do not necessarily represent those of their affiliated organizations, or those of the publisher, the editors and the reviewers. Any product that may be evaluated in this article, or claim that may be made by its manufacturer, is not guaranteed or endorsed by the publisher.

References

Bu, X., Xie, G., Peng, Y., Ge, L., and Ni, C. (2017a). Kinetics of flotation. Order of process, rate constant distribution and ultimate recovery. *Physicochem. Probl. Mineral. Pro.* 53 (1), 342–365. doi:10.5277/ppmp170128

Bu, X., Zhang, T., Chen, Y., Xie, G., and Peng, Y. (2017b). Comparative study of conventional cell and cyclonic microbubble flotation column for upgrading a difficult-to-float Chinese coking coal using statistical evaluation. *Int. J. Coal Prep. Util.* 40 (6), 359–375. doi:10.1080/19392699.2017.1359577

Bu, X., Zhang, T., Chen, Y., Peng, Y., Xie, G., and Wu, E. (2018). Comparison of mechanical flotation cell and cyclonic microbubble flotation column in terms of separation performance for fine graphite. *Physicochem Probl. Miner.* 54 (3), 732–740.

Bu, X., Chen, Y., Ma, G., Sun, Y., Ni, C., and Xie, G. (2019). Differences in dry and wet grinding with a high solid concentration of coking coal using a laboratory conical ball mill: Breakage rate, morphological characterization, and induction time. *Adv. Powder Technol.* 30, 2703–2711. doi:10.1016/j.apt.2019.08.016

Chen, Y., Bu, X., Truong, V. N. T., Peng, Y., and Xie, G. (2019). Study on the effects of pre-conditioning time on the floatability of molybdenite from the perspective of cavitation threshold. *Min. Eng.* 141, 105845. doi:10.1016/j.mineng.2019.105845

Chen, Y., Li, P., Bu, X., Chehreh Chelgani, S., Kong, Y., and Liang, X. (2022). Resource utilization strategies for spent pot lining: A review of the current state. *Sep. Purif. Technol.* 300, 121816. doi:10.1016/j.seppur.2022.121816

Farrokhpay, S. (2011). The significance of froth stability in mineral flotation--a review. *Adv. Colloid Interface Sci.* 166 (1-2), 1–7. doi:10.1016/j.cis.2011.03.001

Grjotheim, K. (1982). *Aluminium electrolysis: fundamentals of the Hall-Héroult process*. Incorporated. Düsseldorf: Aluminium-Verlag.

Li, C., and Gao, Z. (2017). Effect of grinding media on the surface property and flotation behavior of scheelite particles. *Powder Technol.* 322, 386–392. doi:10.1016/j.powtec.2017.08.066

Li, B., Zhou, J., Yao, Z., Peng, Q., Liu, M., Li, X., et al. (2021a). Advances in the safe disposal and comprehensive utilization of spent carbon anode from aluminum electrolysis: Prospects for extraction and application of carbon resources from hazardous waste. *Front. Energy Res.* 9, 1–10. doi:10.3389/fenrg.2021.779476

Li, H., Wang, J., Hou, W., Li, M., Cheng, B., Feng, Y., et al. (2021b). The study of carbon recovery from electrolysis aluminum carbon dust by froth flotation. *Metals* 11 (1), 145. doi:10.3390/met11010145

Luo, X., Feng, B., Wong, C., Miao, J., Ma, B., and Zhou, H. (2016). The critical importance of pulp concentration on the flotation of galena from a low grade lead–zinc ore. *J. Mat. Res. Technol.* 5 (2), 131–135. doi:10.1016/j.jmrt.2015.10.002

Lynch, A. J., Johnson, N., Manlapig, E., and Thorne, C. (1981). *Mineral and coal flotation circuits: Their simulation and control*. Amsterdam: Elsevier.

Marion, C., Jordens, A., Li, R., Rudolph, M., and Waters, K. E. (2017). An evaluation of hydroxamate collectors for malachite flotation. *Sep. Purif. Technol.* 183, 258–269. doi:10.1016/j.seppur.2017.02.056

Mathe, E., Cruz, C., Lucay, F. A., Gálvez, E. D., and Cisternas, L. A. (2021). Development of a grinding model based on flotation performance. *Min. Eng.* 166, 106890. doi:10.1016/j.mineng.2021.106890

Mei, X., Li, J., and Yu, Z. (2016). The research on recycling carbon residue by floatation process. *Light Met.* 4, 28–30.

Mowla, D., Karimi, G., and Ostadnezhad, K. (2008). Removal of hematite from silica sand ore by reverse flotation technique. *Sep. Purif. Technol.* 58 (3), 419–423. doi:10.1016/j.seppur.2007.08.023

Nguyen, A. V., and Schultze, H. J. (2004). *Colloidal science of flotation*. New York: Marcel Dekker.

Ni, C., Zhou, S., Gao, J., Bu, X., Chen, Y., Alheshibri, M., et al. (2022). Selective comminution and grinding mechanisms of spent carbon anode from aluminum electrolysis using ball and rod mills. *Physicochem Probl. Miner.* 58 (3), 1–15.

Sokolović, J., and Miskovic, S. (2018). The effect of particle size on coal flotation kinetics: A review. *Physicochem. Probl. Miner. Process.* 54. doi:10.5277/PPMP18155

Sripriya, R., Rao, P., and Choudhury, B. R. (2003). Optimisation of operating variables of fine coal flotation using a combination of modified flotation parameters and statistical techniques. *Int. J. Min. Process.* 68 (1-4), 109–127. doi:10.1016/s0301-7516(02)00063-7

Ulusoy, U., and Yekeler, M. (2004). Variation of critical surface tension for wetting of minerals with roughness determined by Surtronic 3+ instrument. *Int. J. Min. Process.* 74 (1), 61–69. doi:10.1016/j.minpro.2003.09.001

Ulusoy, U., and Yekeler, M. (2007). Flotability of barite particles with different shape and roughness. *Indian J. Chem. Technol.* 14 (6), 616–625.

Ulusoy, U., Yekeler, M., and Hicyilmaz, C. (2003). Determination of the shape, morphological and wettability properties of quartz and their correlations. *Min. Eng.* 16 (10), 951–964. doi:10.1016/j.mineng.2003.07.002

Vapur, H., Bayat, O., and Uçurum, M. (2010). Coal flotation optimization using modified flotation parameters and combustible recovery in a Jameson cell. *Energy Convers. Manag.* 51 (10), 1891–1897. doi:10.1016/j.enconman.2010.02.019

Wang, L., Peng, Y., Runge, K., and Bradshaw, D. (2015). A review of entrainment: Mechanisms, contributing factors and modelling in flotation. *Min. Eng.* 70, 77–91. doi:10.1016/j.mineng.2014.09.003

Wang, X., Bu, X., Alheshibri, M., Bilal, M., Zhou, S., Ni, C., et al. (2021a). Effect of scrubbing medium's particle size distribution and scrubbing time on scrubbing flotation performance and entrainment of microcrystalline graphite. *Int. J. Coal Prep. Util.* 163, 1–22. doi:10.1080/19392699.2021.1932843

Wang, X., Shaoqi, Z., Bu, X., Ni, C., Xie, G., and Peng, Y. (2021b). Investigation on interaction behavior between coarse and fine particles in the coal flotation using focused beam reflectance measurement (FBRM) and particle video microscope (PVM). *Sep. Sci. Technol.* 56 (8), 1418–1430. doi:10.1080/01496395.2020.1777428

Xu, M. (1998). Modified flotation rate constant and selectivity index. *Min. Eng.* 11 (3), 271–278. doi:10.1016/s0892-6875(98)00005-3

Yu, J., He, Y., Ge, Z., Li, H., Xie, W., and Wang, S. (2018). A promising physical method for recovery of LiCoO 2 and graphite from spent lithium-ion batteries: Grinding flotation. *Sep. Purif. Technol.* 190, 45–52. doi:10.1016/j.seppur.2017.08.049

Zheng, K., Bu, X., Zhou, S., Zhang, J., Shao, H., Sha, J., et al. (2020). Effects of monovalent and divalent ions in coal gasification brine on the froth entrainment and flotation kinetics of anthracite coal. *Physicochem. Probl. Min. Process.* 56 (5), 960–974. doi:10.37190/ppmp/127501

Zhou, S., Wang, X., Bu, X., Shao, H., Hu, Y., Alheshibri, M., et al. (2020). Effects of emulsified kerosene nanodroplets on the entrainment of gangue materials and selectivity index in aphanitic graphite flotation. *Min. Eng.* 158, 106592. doi:10.1016/j.mineng.2020.106592

frontiers | Frontiers in Chemistry

TYPE Original Research
PUBLISHED 10 October 2022
DOI 10.3389/fchem.2022.1011518

Check for updates

OPEN ACCESS

EDITED BY
Ilhwan Park,
Hokkaido University, Japan

REVIEWED BY
Kyoungkeun Yoo,
Korea Maritime and Ocean University, South Korea
Marthias Silwamba,
University of Zambia, Zambia
Carlito Baltazar Tabelin,
University of New South Wales, Australia

*CORRESPONDENCE
Naoko Okibe,
okibe@mine.kyushu-u.ac.jp

SPECIALTY SECTION
This article was submitted to Green and Sustainable Chemistry, a section of the journal Frontiers in Chemistry

RECEIVED 04 August 2022
ACCEPTED 23 September 2022
PUBLISHED 10 October 2022

CITATION
Phann I, Tanaka Y, Yamamoto S and Okibe N (2022), Utilization of amino acid for selective leaching of critical metals from spent hydrodesulfurization catalyst. *Front. Chem.* 10:1011518. doi: 10.3389/fchem.2022.1011518

COPYRIGHT
© 2022 Phann, Tanaka, Yamamoto and Okibe. This is an open-access article distributed under the terms of the Creative Commons Attribution License (CC BY). The use, distribution or reproduction in other forums is permitted, provided the original author(s) and the copyright owner(s) are credited and that the original publication in this journal is cited, in accordance with accepted academic practice. No use, distribution or reproduction is permitted which does not comply with these terms.

Utilization of amino acid for selective leaching of critical metals from spent hydrodesulfurization catalyst

Idol Phann, Yu Tanaka, Sae Yamamoto and Naoko Okibe*

Department of Earth Resources Engineering, Kyushu University, Fukuoka, Japan

While spent catalysts can cause serious environmental pollution, they can be considered an essential secondary metal source due to their high critical metal grades. The formation of the amino acid-metal complex is often seen in nature, and its potential application in hydrometallurgy can be foreseen. Alanine (Ala) was first screened as the most effective type of amino acid to be used for the selective leaching of spent hydrodesulfurization catalyst (consisting of MoS_2 and Co_3S_4 supported on Al_2O_3, at 10% Mo and 2.4% Co grades). The sequential 3-step leaching (Step-1: Alkaline Ala leaching at 45°C, Step-2: Hot water leaching at 70°C, Step-3: Second alkaline Ala leaching at 45°C) was conducted where the role of Ala was found to be at least three-fold; 1) maintaining alkalinity by amino acid's buffering capacity to assist Mo leaching, 2) selectively precipitating Co by forming Co-Ala complex with a distinctive pink color, which can readily re-dissolve in hot water to be separated from spent catalyst particles. 3) Effectively suppressing unwanted dissolution of Al throughout the reaction without needing pH control. Consequently, highly metal-selective, two separate Co-rich (<1% Mo and 79% Co dissolved, Al not detected) and Mo-rich (96% Mo, 19% Co, and 2.1% Al dissolved) leachates were obtained. This study highlighted the potential utility of amino acids as non-toxic, alternative metal lixiviant as well as a metal precipitant for selective leaching of critical metals from spent hydrodesulfurization catalyst.

KEYWORDS

spent catalyst, amino acid, alanine, critical metals, molybdenum, cobalt

1 Introduction

The demand for low-sulfur fuels is increasing due to the implementation of stricter environmental regulations in the last decade worldwide. Nonetheless, the processing of heavier crude oil with higher sulfur, nitrogen and metal contents is growing, necessitating the increased use of hydrodesulfurization catalysts in petroleum refineries (Marafi and Stanislaus, 2007; Akcil et al., 2015; Li et al., 2015). Hydrodesulfurization catalysts generally consist of the MoS_2 active phase with Co or Ni promoters supported on γ-Al_2O_3 (Ihan, 2020). Deactivated catalysts (due to deposition of C, S and other heavy metals deriving from crude oil) are usually regenerated and reused multiple times before the end of the cycle. If not correctly

handled, the spent catalysts can cause serious environmental pollution through the dissolution of toxic heavy metals and are thus classified as hazardous waste by the environmental protection agency in the United States (Ihan, 2020).

Despite such environmental concerns, spent catalysts are regarded as an essential secondary metal source due to their high metal grades (e.g., 4%–12% Mo, 1%–5% Ni, 0%–4% Co, 0%–0.5% V, 15%–30% Al; Park et al., 2006; Pinto and Soares, 2012, Ilhan, 2020). Hence, a number of studies attempted to recover valuable metals from spent catalysts through pyrometallurgical, hydrometallurgical and pyrohydrometallurgical routes (Zeng and Cheng, 2009). Pyrometallurgical processes are generally highly energy intensive, and the emission of harmful gases is a major disadvantage (Ihan, 2020). Although hydrometallurgical processes are considered less energy-consuming and the reactions more flexible and readily controllable, the use of concentrated acids, ammonia and other harmful chemicals can still cause secondary pollution and health and safety concerns.

Due to the toxic nature of such chemical lixiviant used in the conventional hydrometallurgy processes, researchers have been attempting to search for more environmentally benign, sustainable alternatives for the leaching of valuable metals from both natural ores and waste materials (Asghari et al., 2013; Astuti et al., 2016; Dewi et al., 2020). Organic acids such as citric acid, oxalic acid, gluconic acid, malic acid and succinic acid can be fermented by some filamentous fungi and/or bacteria out of renewable and waste materials as feedstock (Alonso et al., 2015). The mechanism of metal leaching with chemical or biogenic organic acids is based on the combination of the acid leaching reaction (Eq. 1) and metal-organic acid complexation (Eq. 2).

$$MeO + 2H^+ = Me^{2+} + H_2O \quad (1)$$

$$Me^{2+} + H_2 - A = Me - A + 2H^+ \quad (2)$$

More recently, the utility of glycine (Gly), the simplest amino acid, was reported to be effective as a "green" metal lixiviant (Eksteen et al., 2017; O'Connor et al., 2018; Oraby et al., 2019; Li et al., 2020). In the alkali condition, Gly (plus oxidizing agent such as air/O_2, H_2O_2, Cu^{2+}) leached Cu, Au and Ag from their pure foils and oxide/sulfide minerals. Gly exists as $H_2NCH_2COO^-$ (Gly^-, glycinate anion), $^+H_3NCH_2COO^-$ (H(Gly), zwitterion) or $^+H_3NCH_2COOH$ ($H_2(Gly)^+$, glycinium cation) depending on the solution pH. Cuprous (Cu^+) and cupric (Cu^{2+}) ions were suggested to complex with both zwitterion and glycinate anion, with the latter being more stable (Li et al., 2020). Glycine solution was also shown to be effective in extracting base and precious metals from waste printed circuit boards by employing a two-stage process: Alkaline Gly solution was applied to leach Cu, Al, Pb, and Zn in the first stage, followed by the second stage for Au and Ag leaching in Gly solution in the starved cyanide environment (Oraby et al., 2019).

In hydrometallurgical reactions in general, the recovery of target metals from polymetallic leachates can become complicated, especially by the excessive solubilization of non-target metals (Hamza et al., 2018). In the case of spent hydroprocessing catalysts, the wide usage of porous media as the catalyst support leads to the unwanted dissolution of Al along with the target metals (Angelidis et al., 1995). Previous leaching studies on this particular waste stream utilized conventional inorganic acid or base (Angelidis et al., 1995; Barik et al., 2012; Pinto and Soares, 2012) as well as organic acids (Arslanoğlu and Yaraş, 2019). However, the low leaching selectivity remained to be solved. While use of EDTA for Ni recovery under the microwave condition led to a better selectivity (Pinto and Soares, 2013), its cost effectiveness needs to be improved especially for complex multi-metal compounds (Feng and van Deventer, 2011). The use of amino acids for this waste stream has not been reported yet. However, amino acids were shown to have little to no interaction with acid-consuming components such as Al and Fe, thus thought to be a good replacement for many other lixiviant in the leaching of natural minerals as well as waste printed circuit boards (Feng and van Deventer, 2011; Oraby and Eksteen, 2013; Oraby et al., 2019). The economic and environmental merits of using Gly-based leaching at the industrial scale were emphasized by Eksteen et al. (2017).

In nature, the formation of amino acid-metal complexes is often seen within biological systems as metals are essential cellular components. Many living organisms make extensive use of transition metals (e.g., Co, Fe, and Mn), which are involved in various biochemical functions (such as electron carrier, catalysis and structural roles) and are frequently associated with active sites of proteins and enzymes. Such properties of transition metals led to the development of medicinal inorganic chemistry to design new metal-based drugs (Sodhi and Paul, 2019). Han and Chi (2010) also synthesized a variety of amino acid (Ala, Asn, Gln, His, Ile, Lys, and Pro)-metal (Fe, Cu, and Zn) complexes and emphasized the importance of the study in the applied biochemistry field. All 20 common amino acids (except for the simplest amino acid Gly; R = H) contain a chiral α-carbon. Each amino acid processes unique characteristics deriving from the size, shape, solubility and ionization properties of its side chain. Consequently, diverse reactions can be expected between different amino acids and metals. Furthermore, several amino acids (e.g., glutamic acid, alanine, aspartic acid, serine, tryptophan, isoleucine; Okafor, 2007) can be produced *via* fermentation. By fermenting such amino acids from organic waste streams eventually, additional values can be added to the process being sustainable, low cost, and environmentally friendly. Despite the potential application of such naturally-occurring amino acid-metal complexes in the field of hydrometallurgy, studies on this topic are yet highly limited (except for the study of Gly as mentioned above).

In order to address the above issues, this study attempted to exploit the potential utility of amino acids as non-toxic, alternative metal lixiviant for selective leaching of spent hydrodesulfurization catalyst. To our knowledge, this is the first report utilizing amino acids for the selective leaching of critical metals (Mo and Co).

2 Materials and methods

2.1 Sample preparation and characterization of spent hydrodesulfurization catalyst

The Mo-Co/Al_2O_3 type hydrodesulfurization catalyst (PT Pertamina (Persero), Refinery Unit IV Cilacap, Indonesia) was used in this study. As-received spent catalyst sample was ground by a planetary ball mill (Pulverisette-6; Fritsch, Tokyo, Japan) and dry-sieved to obtain a particle size of 75–150 μm prior to the leaching tests. The particle size distribution analysis was conducted using a laser diffraction particle size analyzer (Horiba, Partica LA-950). The mineralogical composition was analyzed by X-ray diffraction (XRD; Ultima IV; Rigaku, Tokyo, Japan) using Cu Kα radiation, 40 mV, 40 kV, and a scanning speed of 2°/min. To analyze the elemental composition, 0.5 g of ground spent catalyst was digested in 9 ml of reverse aqua regia solution (HCl: HNO_3 = 1:2 v/v) in the microwave (Ethos Plus, Milestone) by heating at 1,000 W to achieve 230°C in 30 min, and keeping at 230°C for 15 min, then allowing to cool to room temperature. The acid digestion leachate after the microwave treatment was left to evaporate before diluting with deionized water for ICP-OES analysis. The acid digestion was done in triplicate set-ups. The elemental composition was also analyzed by X-ray fluorescence spectroscopy (XRF) (Rigaku, ZSX Primus II, Akishima, Japan) as a comparison. The spent catalyst surface was sputter-coated with Au using a magnetron sputter (MPS-1S; Vacuum Device Inc., Tokyo, Japan) and observed by scanning electron microscope (SEM; Hitachi SU1000 FlexSEM 1000II, Tokyo, Japan) at an accelerated voltage of 20 kV.

2.2 Comparison of different acids as metal lixiviant

Analytical-grade reagents were used as lixiviant. All tests were carried out in 300 ml Erlenmeyer flasks containing 100 ml of different lixiviant and ground spent catalysts at a pulp density of 10% (w/v). Several amino acids (L-alanine (Ala), L-glycine (Gly), L-phenylalanine (Phe), L-glutamine (Gln) and L-arginine (Arg) at 0.5 M, $pH_{initial}$ 11 with NaOH) as well as 0.5 M H_2SO_4 and 0.5 M citric acid were compared as representative inorganic and organic acids, respectively. All tests were done in duplicated flasks, incubated shaken at 150 rpm and 45°C. Samples were regularly taken to measure pH and metal concentrations (Mo, Co, and Al) by ICP-OES (LOD: Mo 7.9 μg/L; Co 7 μg/L; Al 28 μg/L).

2.3 Three-step leaching of spent catalyst

2.3.1 Step-1: Alkaline L-alanine leaching

Erlenmeyer flasks (500 ml) containing 200 ml of 0.5 M Ala plus 3% (w/v) spent catalyst were prepared ($pH_{initial}$ 11 with NaOH). Ala-free control flasks ($pH_{initial}$ 11) were also set up in parallel. All flasks were incubated and shaken at 150 rpm and 45°C. Liquid samples were taken periodically to monitor pH and metal concentrations (Mo, Co, and Al) by ICP-OES.

2.3.2 Step-2: Hot water leaching

In Step-1, the dissolution of Co was found to be accompanied by its simultaneous precipitation (regardless of the presence of Ala). Therefore, Step-2 attempted the selective re-solubilization of Co. The Step-1 solid residues (deriving from either Ala system or Ala-free control) were individually collected by centrifugation (10,000 G for 10 min; Suprema 21, TOMY), washed with deionized water four to five times until the pH dropped to 9.0, filtered and finally freeze-dried (EYELA, FDU-1200, Tokyo, Japan) before being applied for Step-2. In Step-2, 500 ml Erlenmeyer flasks containing 150 ml of deionized water plus 3% (w/v) of the Step-1 residue were prepared and incubated, shaken at 150 rpm and 70°C for 48 h.

2.3.3 Step-3: Second alkaline L-alanine leaching

The Step-2 solid residues (deriving from either Ala system or Ala-free control in Step-1) were individually collected by centrifugation (10,000 G for 10 min), washed with deionized water and freeze-dried for later analyses. Only the solid residue derived from the Ala system was further processed in Step-3. In Step-3, two types of Ala solutions were compared; 1) pregnant Ala solution reused from Step-1 ($pH_{initial}$ re-adjusted to 11 with NaOH) or 2) fresh 0.5 M Ala solution ($pH_{initial}$ 11). One-hundred milliliters of Ala solution (either 1 or 2) and 3% (w/v) of the Step-2 solid residue were transferred into 300 ml Erlenmeyer flasks and incubated, shaken at 150 rpm and 45°C for 96 h.

At the end of Step-1, 2, and 3, washed and freeze-dried solid residues were subjected to XRD and SEM analyses. The final Step-3 residues were subjected to complete acid digestion to confirm their elemental compositions as follows; 0.1 g of the residue was digested in 10 ml aqua regia (HCl: HNO_3 = 2:1 v/v) in the microwave (heated at 1,000 W for 30 min to reach 210°C, kept at 210°C for 15 min, then allowed to cool to room temperature). The leachate was then filtered and diluted with deionized water for ICP-OES analysis. The three-step leaching tests and final acid digestion was done in duplicate.

2.4 Chemical synthesis of Co-Ala complex as reference compounds

During Step-1 (Section 2.3.1), apparent Co-precipitates were formed. In order to identify this precipitate, the following three separate tests were conducted to synthesize Co-Ala complexes as reference compounds;

(i) The ethanol reflux method (Alam et al., 2019; modified): Fifty milliliters of 0.4 M Ala (natural pH) and 40 ml of hot

TABLE 1 Elemental composition of the as-received spent catalyst determined by XRF or acid digestion followed by ICP-OES analysis.

Element	XRF (wt. %)	Acid digestion followed by ICP-OES (wt. %)
Al	26.8	24.8 ± 0.27
Mo	13.1	10.1 ± 0.80
Co	3.4	2.4 ± 0.08
As	0.3	0.3 ± 0.02
Fe	0.2	0.2 ± 0.01
S	10.4	9.3 ± 1.13
Ni	0.1	0.04 ± 0

ethanol containing 250 mM Co^{2+} (added as $CoCl_2 \cdot 6H_2O$) were separately prepared. The former was added drop by drop into the latter under vigorous stirring, followed by pH adjustment to 7.5 with Na_2CO_3. The reaction mixture was refluxed (in a beaker closed with aluminum foil) at 80°C under vigorous stirring for 3 h. The resulting purple precipitate was recovered by filtration (0.45 μm).

(ii) 500 ml Erlenmeyer flasks containing 200 ml of 0.5 M Ala ($pH_{initial}$ 11) plus 50 mM Co^{2+} (added as $CoSO_4 \cdot 7H_2O$) were incubated shaken at 45°C and 150 rpm. After 48 h, the resultant pink precipitate was recovered by filtration (0.45 μm).

(iii) 500 ml Erlenmeyer flasks containing 200 ml of 0.5 M Ala ($pH_{initial}$ 11) plus 6% (w/v) ground spent catalyst were incubated and shaken at 45°C and 150 rpm. After 3 h-incubation (before the initiation of extensive Co-precipitation), spent catalyst particles were separated from the leachate by filtration (0.45 μm). The solid-free leachate was then transferred into a new 500 ml Erlenmeyer flask and further incubated, shaken at 45°C and 150 rpm. After 48 h, the resultant pink precipitate was recovered by filtration (0.45 μm).

The resultant three types of Co-precipitates were compared by XRD and SEM. For qualitative elemental composition analysis, elemental mapping was done using EDS software (Aztec EDS, Oxford Instruments, United Kingdom).

3 Results and discussion

3.1 Characterization of spent catalyst

As-received spent catalyst sample was quadlobe in shape with particle length varying from 1.5 to 5 mm (Figure 4A). The elemental compositions of the spent catalyst analyzed by XRF and acid digestion (followed by ICP-OES measurement) are compared in Table 1: According to the latter, critical metals such as Mo and Co were present at approximately 10% and 2.4%, respectively. The average particle size (P_{50}) of the ground spent catalyst was 38.3 ± 1 μm. The XRD analysis confirmed that the spent catalyst comprises MoS_2 and Co_3S_4 supported on Al_2O_3 (Figure 1A). Other contaminant metals such as As, Fe, S, and Ni (Table 1) were likely derived from the crude oil through the desulfurization process, leading to catalyst deactivation (Angelidis et al., 1995; Park et al., 2006; Ilhan, 2020). Similar values were also obtained from the XRF analysis (Table 1).

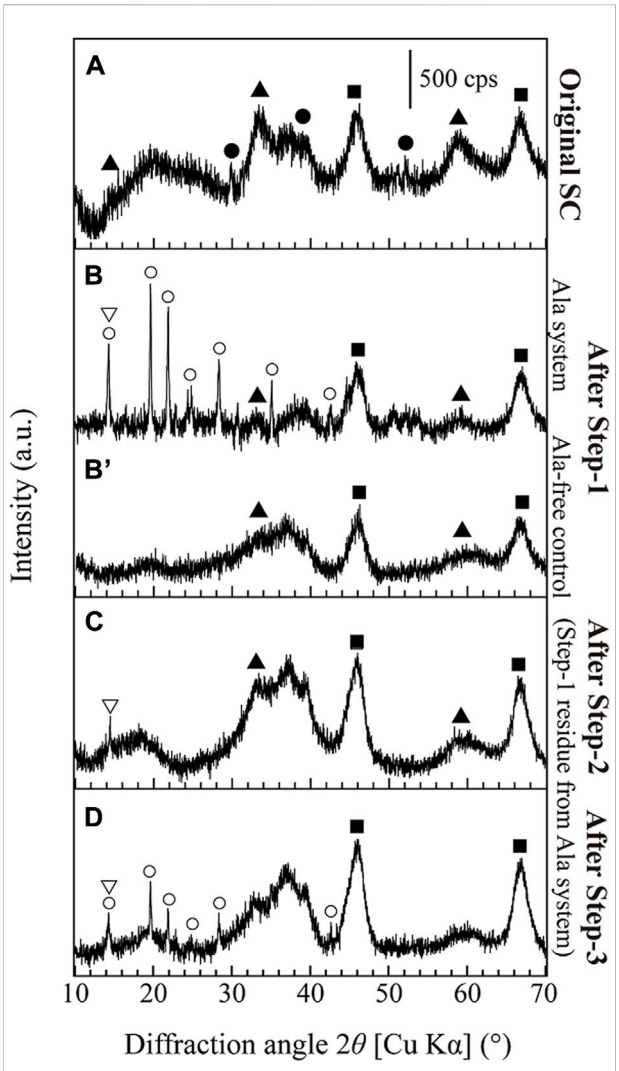

FIGURE 1
XRD patterns of; **(A)** the original spent catalyst, **(B,B')** the leaching residue after Step-1 (comparison of with or without Ala, respectively), **(C)** the leaching residue after Step-2 and **(D)** the leaching residue after Step-3. Symbols: ▲ (MoS_2; JCPDS No. 37-1492), ● (Co_3S_4; JCPDS No. 42-1448), ■ (Al_2O_3; JCPDS No. 75-0921), ▽ (AlO(OH); PDF No. 01-073-9093), ○ (Co-Ala complex; Figure 5).

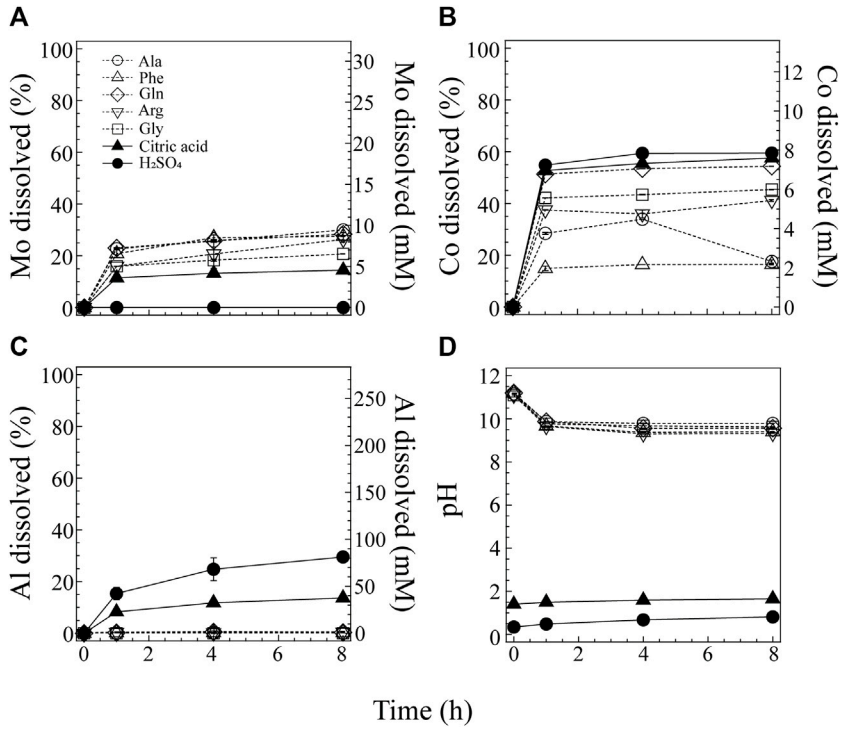

FIGURE 2
Comparison of 0.5 M sulfuric acid (●), 0.5 M citric acid (▲) and a variety of alkaline-amino acids (0.5 M; Ala ○, Phe △, Gln ◇, Arg ▽, Gly □) as a lixiviant for spent catalyst. Changes in the Mo dissolution **(A)**, Co dissolution **(B)**, Al dissolution **(C)** and pH **(D)** are shown.

3.2 Effect of different acids on the spent catalyst leaching

Figure 2 compares different lixiviant: 0.5 M H_2SO_4, 0.5 M citric acid and several amino acids (0.5 M Ala, Gly, Phe, Gln or Arg; pH_{ini} 11). The use of H_2SO_4 as a conventional inorganic acid lixiviant was ineffective in the Mo leaching, while the dissolution of Co (70% at 48 h; Figure 2B) and Al (48%; Figure 2C) was the greatest of all. Citric acid showed the second lowest pH range (1.4~1.9) after H_2SO_4 (pH 0.3~1.8; Figure 2D), where the Mo dissolution was improved to ~19% and Co and Al leached at 64% and 20%, respectively (Figures 2A–C). In contrast to these two acidic lixiviants, alkaline amino acids suppressed the Al dissolution to <1% (7.5 mM; Figure 2C). The pH trend was similar with all amino acids; i.e., pH_{ini} 11 quickly dropped to ~9.5 but stabilized (Figure 2D). However, the metal dissolution behavior varied between the different amino acids. Gln showed the greatest dissolution of both Mo (38%) and Co (61%). Ala and Phe also leached an equivalent amount of Mo (~34%) but seemingly dissolved and precipitated Co simultaneously. Gly and Arg leached a lesser amount of Mo than other amino acids (29% and 22%, respectively) and also a lesser amount of Co (49% and 39%, respectively) than Gln (Figures 2A,B).

Based on the pourbaix diagram for Mo (Supplementary Figure S1; Lyon, 2010), Co (Supplementary Figure S2; Chivot et al., 2008), and Al (Supplementary Figure S3; Pourbaix, 1974; Sukiman et al., 2012), Mo tends to ionize at neutral to alkaline pH. The use of H_2SO_4 was therefore ineffective for the acidolysis of Mo. However, despite its acidity (pH ~1.8), citric acid solubilized Mo to some extent (Figure 2D), suggesting the possible involvement of complexolysis. When amino acids were used under the alkaline condition (pH_{ini} 11), the Mo dissolution likely depended on alkalosis according to the pourbaix diagram (Supplementary Figure S1). Still, the Mo dissolution trend was not identical between different amino acids, suggesting that there may be an additional effect caused by certain types of amino acids other than alkalosis, possibly complexolysis.

On the other hand, Co^{2+} is soluble in the wide pH range from strongly acidic to neutral pHs, while at alkaline pH Co tends to precipitate as Co hydroxides, according to the pourbaix diagram (Supplementary Figure S2). Despite the nearly identical pH value maintained throughout the leaching period (pH ~10; Figure 2D), the Co dissolution profile varied largely between different amino acids. Some amino acids (such as Gln) seemed to even aid the dissolution of Co at this high pH, like other acidic lixiviants

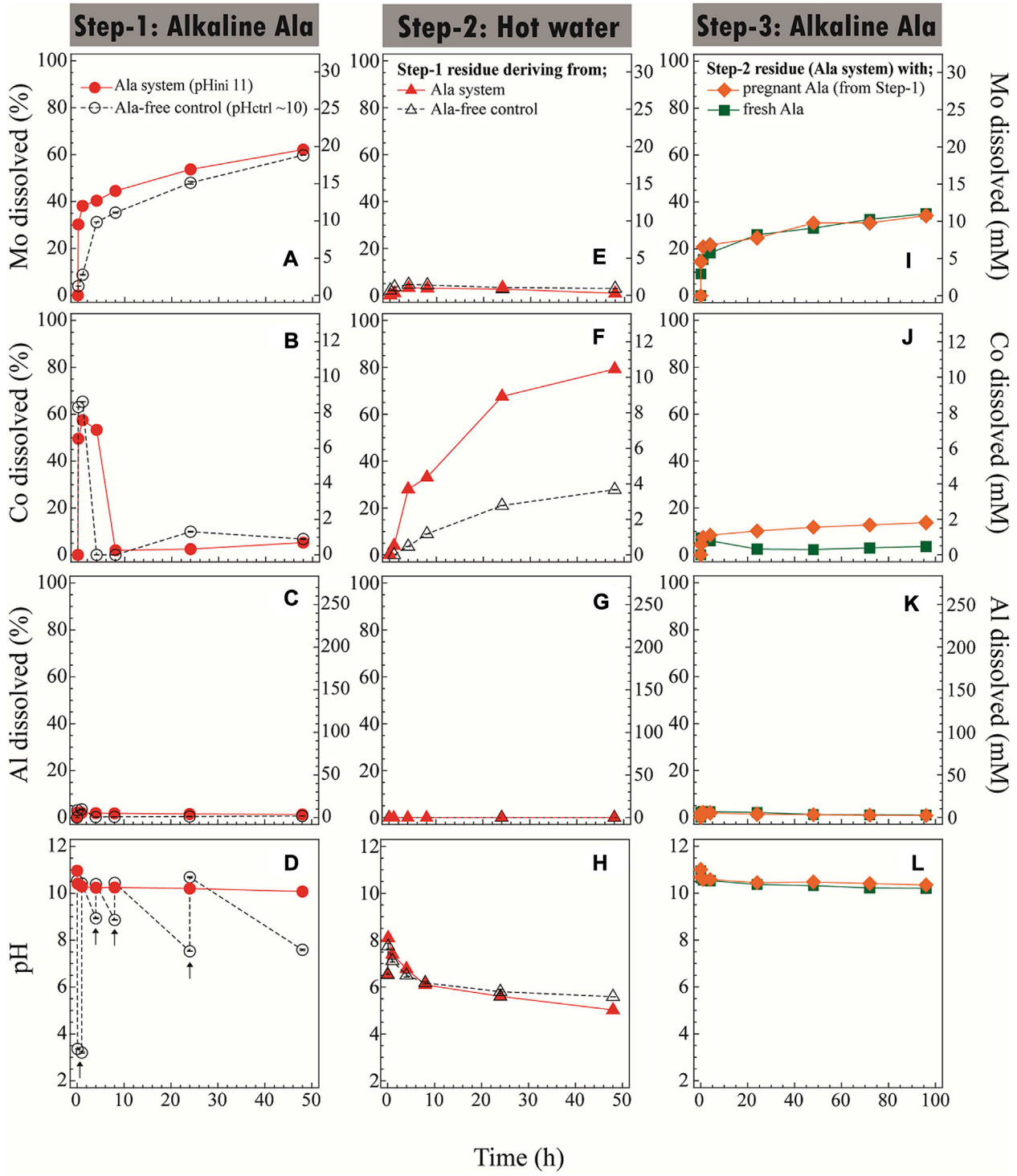

FIGURE 3
Sequential 3-step leaching of spent catalyst. Step-1 **(A–D)**: Alkaline Ala leaching (pHini 11; ●) or Ala-free control [pH adjusted to ~10 with NaOH, as indicated by arrows **(D)**; ○] at 45°C. Step-2 **(E–H)**: Hot water leaching of the Step-1 solid residue [deriving from Ala system (▲) or Ala-free control (△)] at 70°C, pHnatutal. Step-3 **(I–L)**: Second alkaline Ala leaching of the Step-2 solid residue (deriving from Ala system in Step-1), either by reusing pregnant Ala solution from Step-1 (re-adjusted to pHini 11; ◆) or by using fresh Ala solution (pHini 11; ■) at 45°C. The dissolution profile of Mo **(A,E,I)**, Co **(B,F,J)**, and Al **(C,G,K)** as well as the pH profile **(D,H,L)** are shown.

(Figure 2B). In contrast, Co was dissolved but precipitated simultaneously in the presence of Ala and Phe (Figure 2B). The dissolution trend of Al was highly pH dependent: Al dissolution was mostly suppressed under the alkaline amino acid conditions while H_2SO_4 greatly leached Al to 48% (Figure 2C), as expected from the pourbaix diagram (Supplementary Figure S3).

The contrasting leaching trend between Mo and Co was most evident when Ala and Phe were used, while unwanted Al leaching was effectively prevented (Figures 2A–C). Therefore, the following tests employed Ala as a simpler representative to attempt selective leaching of the two critical metals.

3.3 Selective leaching of Mo and Co in the alkaline L-alanine system

3.3.1 Sequential 3-step leaching

3.3.1.1 Step-1: Alkaline L-alanine leaching

As described in the previous section, Ala was found to be a possible candidate to selectively leach and recover Mo and Co while suppressing the Al dissolution. To clarify the role of Ala, the control test using Ala-free alkaline water (pH_{ini} 11) was run in parallel. In the Ala-free system, pH_{ini} 11 rapidly dropped to acidic, so it was necessary to add alkaline manually (at 1, 4, 8, and 24 h) to keep the equivalent pH level to the Ala system (Figure 3D). It was reported that Mo dissolves from MoS_2 in alkaline solution following the Eqs 3, 4 as below (Mirvaliev and Inoue, 2001), thus acidifying the leachate. However, after pH_{ini} 11 dropped slightly to ~10, no further pH adjustment was necessary for the Ala system (Figure 3D) since the pH level was stabilized after that due to the buffering effect of amino acid molecules.

$$MoS_2 + 3H_2O + 4.5O_2 = HMoO_4^- + 2SO_4^{2-} + 5H^+ \quad (3)$$

$$HMoO_4^- + 5H^+ + 6OH^- = MoO_4^{2-} + 6H_2O \quad (4)$$

Although the final Mo dissolution was nearly equal (~60% at 48 h), the initial leaching effect was quicker and continued to be more stable in the presence of Ala compared to the Ala-free control (Figure 3A). This may be due to the stable pH level maintained by Ala, as well as a possible complexolysis effect of Ala with Mo. The leaching mechanism involving the complexation of metals with the simplest amino acid, Gly, was reported (Eksteen et al., 2017; Li et al., 2020). Djordjevic et al. (1997) chemically synthesized the Mo(IV) complex with various amino acids, including Mo-Ala. However, whether or not the formation of the Mo-Ala complex occurs during the leaching reaction (such as in this study) remains to be clarified in further investigations.

In both conditions (with or without Ala), about 60% of Co was found to solubilize during the first few hours and then continued to precipitate thereafter. At 48 h, only 5% of Co was soluble under both conditions (Figure 3B). From the acidic and weak alkaline solution, Co tends to exist as Co^{2+} but precipitate as Co-hydroxides at elevated pHs (Huang et al., 2004). Without Ala, therefore, Co was likely precipitated as Co-hydroxides of blackish brown color (Figure 4B′), which was not easily distinguishable from the spent catalyst particles. On the other hand, the presence of Ala altered the nature of precipitate to exhibit the distinctive pink color and characteristic fiber-like structure (Figure 4B). The formation of secondary Co-precipitate was also evidenced by the emergence of new, unknown crystalline XRD peaks after Step-1 (Figure 1B). Since the acidity constant of Ala is $pKa_2 = 9.69$, its carboxylic functional group tended to deprotonate at the reaction pH of ~10 in this test, leading to the complexation of Co^{2+} with two negatively charged Ala molecules and precipitate (Alam et al., 2019).

The overall dissolution of Al was low throughout the leaching period in Step-1; only 1.3% or 0.7% Al was found to be soluble with or without Ala, respectively, at 48 h (Figure 3C). The pH level seemed to play a major role in the Al dissolution as the presence of Ala only had a marginal effect. In an alkaline solution, Al_2O_3 was reported to dissolve at pH 10.5 as $Al(OH)_4^-$ (Pinto and Soares, 2012). A small portion of Al (~3%) was dissolved at the starting point in Step-1 but then seemingly precipitated as AlO(OH), as was confirmed by XRD (Figures 1B–D). Overall, in Step-1, the dissolution trends of Mo, Co and Al were seemingly similar regardless of the presence of Ala. However, the buffering capacity of Ala effectively maintained the alkalinity in the leachate without necessitating a continuous pH re-adjustment.

Applying different temperatures (25, 45 or 70°C) to Step-1 affected the Mo dissolution and, more significantly, the Co-precipitation behavior (Supplementary Figures S4A,B). Lower temperature (25°C) seemed to stabilize Co-precipitate while higher temperature (70°C) inhibited Co-Ala complexation. O'Connor et al. (2018) and Li et al. (2020) also reported the decomposition of aqueous Gly, the simplest amino acid, at temperatures such as 55 and 60°C. In this case, applying a moderate temperature (45°C) was shown to be most effective in terms of Mo dissolution and Co-precipitation (Supplementary Figure S4).

3.3.1.2 Step-2: Hot water leaching

This step attempted to compare the leachability of Co from the Step-1 residue (mixture of spent catalyst plus Co-precipitate formed with or without Ala) by hot water treatment (pH natural; 70°C). The leachability of Co from Ala-free Co-precipitate was significantly lower (28%) than that from Co-Ala precipitate (79%) (Figure 3F). The greater Co leachability from the latter may have resulted from the decomposition of Ala (through deamination and decarboxylation to produce mainly lactic acid and ethylamine; Klingler et al., 2007) in hot water, leading to the release of free Co^{2+} in the leachate. The dissolution of Mo and Al from the spent catalyst was

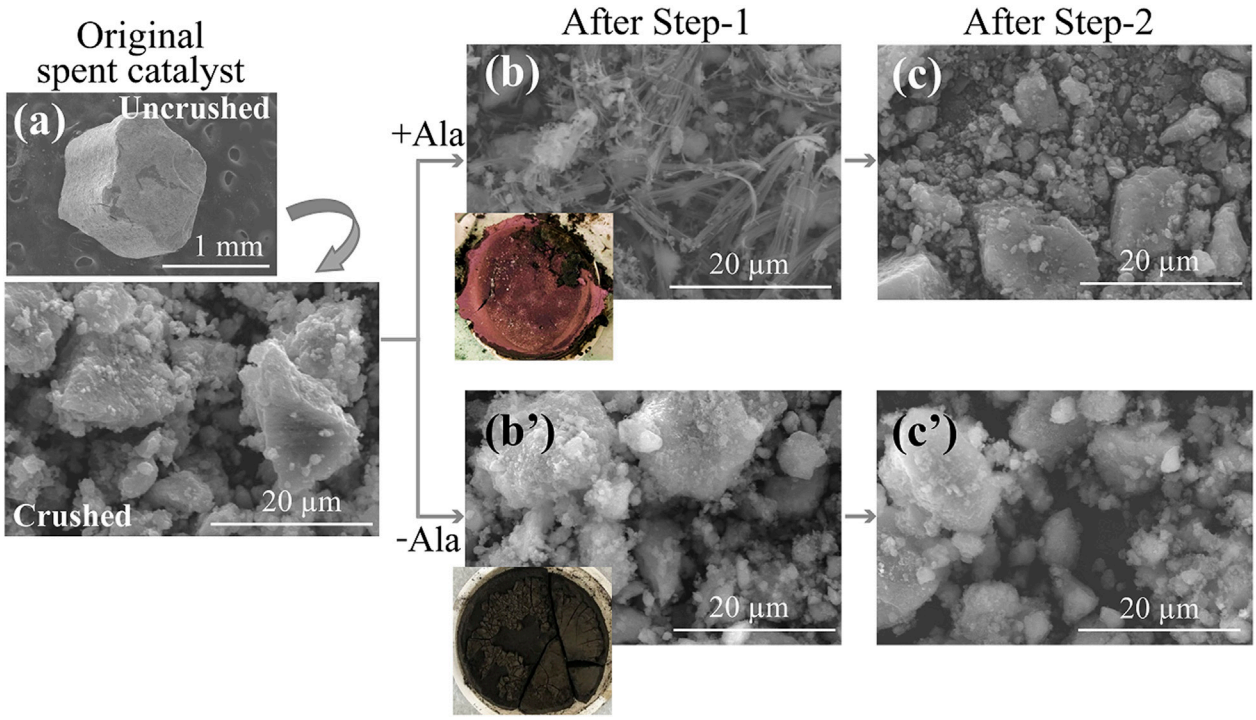

FIGURE 4
SEM images showing morphological and colorimetric differences of Co-precipitates formed during the Step-1 and their transition during Step-2. **(A)** Original spent catalyst (before and after crushing). **(B,B′)** The leaching residue after Step-1 **(B)**; Ala system, **(B′)**; Ala-free control. **(C,C′)** The leaching residue after Step-2 **(C)**; Ala system applied in Step-1, **(C′)**; Ala-free control system applied in Step-1.

negligible in Step-2 (Figures 3E,G). In fact, applying lower temperatures (25 or 45°C) resulted in increasingly lower Co^{2+} release (Supplementary Figure S5B), suggesting that higher temperature is favorable to resolubilize Co-Ala precipitates. A decrease in pH was seen during Step-2 regardless of the presence of Ala (Figure 3H). This was possibly caused by the slight dissolution of spent catalyst particles.

The decomposition of Co-Ala precipitates was also suggested by XRD (Figure 1C) and SEM (Figure 4C): XRD peaks emerged during Step-1 (deriving from Co-Ala precipitates; Figure 1B) disappeared during Step-2 (Figure 1C), accompanied by the disappearance of distinctive fiber-like structures (Figure 4C). In contrast, most of the amorphous Co-precipitates formed in the Ala-free control (Figure 1B'; Figure 4B') persisted the hot water treatment in Step-2 (Figure 4C'). This was consistent with the lower Co dissolution in the Ala-free system as shown in Figure 3F. Overall, the advantage of using the Ala system in Step-1 was emphasized in Step-2 in that Co^{2+} can be selectively released by a simple water treatment through the resolubilization of Co-Ala precipitates.

3.3.1.3 Step-3: Second alkaline L-alanine leaching

This final step attempted to leach out remaining Mo (~37%) from the Step-2 residue by applying the alkaline Ala solution for the second time. Two types of Ala solution (one reusing pregnant Ala solution from Step-1, the other using fresh Ala solution) were compared. The Mo dissolution progressed nearly to completion in 96 h, while the Al dissolution was largely suppressed in both reused and fresh Ala solutions (Figures 3I,K). However, the Co dissolution trend was different between the two; i.e., the remaining Co in the spent catalyst dissolved and precipitated in the fresh Ala solution (as was seen in Step-1), but Co did not precipitate in the pregnant Ala solution (Figure 3J). This may have been caused by the less availability of free Ala molecules (to be precipitated with Co) in the pregnant Ala solution because Ala could have been consumed in Step-1 not only by Co but also by Al and/or Mo through complexation. It can be speculated that the number of free Ala molecules was stoichiometrically enough for the chelation with Co, but not enough to thermodynamically stabilize the complex for precipitation. Another factor could be the effect of temperature (45°C, in this case) after a certain period of incubation on the stability of Ala molecules. To clarify this,

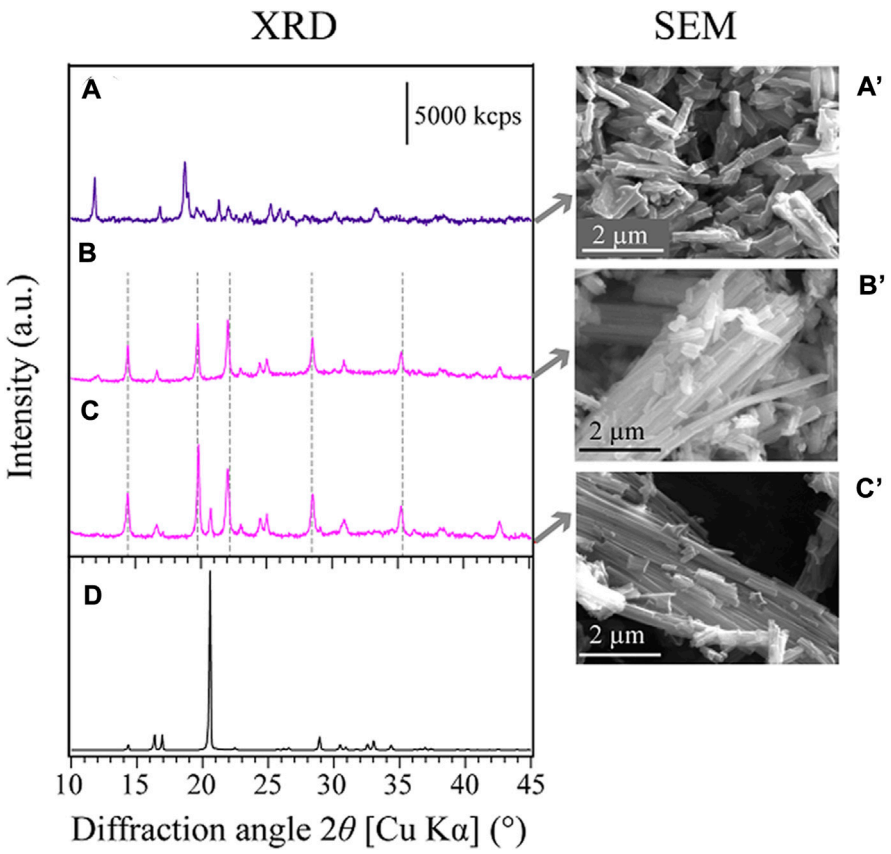

FIGURE 5
Comparison of XRD patterns **(A–D)** and SEM images **(A′–C′)** of synthesized Co-Ala precipitates: **(A,A′)** Co-Ala complex produced by the ethanol reflux method at 80°C. **(B,B′)** Co-Ala complex produced from pure Ala and Co^{2+} reagents at 45°C. **(C,C′)** Co-Ala complex formed in the actual spent catalyst leachate (spent catalyst particles separated prior to Co-Ala precipitation) at 45°C. **(D)** Pure Ala reagent. **(A–C)** All XRD peaks derived from the synthesized Co-Ala complexes under each condition and did not match the database.

further studies are ongoing to investigate the stability and reusability of amino acid lixiviant.

3.3.2 Chemical synthesis and comparison of Co-Ala complexes

As described in Section 3.3.1.1, the XRD peaks of the Co-precipitate formed in Step-1 did not match the XRD database (Figure 1B). Hence, a separate test was done to obtain chemically-synthesized Co-Ala complexes as reference materials to confirm its identity. XRD peaks (Figures 5A–C) and SEM images (Figures 5A′–C′) of three different Co-Ala preparations are shown together with XRD peaks of pure Ala reagent (Figure 5D).

The Co-Ala sample obtained from the ethanol reflux method at 80°C (Alam et al., 2019; modified) exhibited a purple color with shorter needles (Figure 5A′). Its XRD peak positions (Figure 5A) differed from those obtained under milder conditions (45°C; Figures 5B,C). The Co-precipitate formed in the particle-free spent catalyst leachate (Figures 5C,C′) displayed nearly identical color (pink), morphology (long needle-like crystals), and XRD peaks to that formed from pure Co and Ala reagents (Figures 5B,B′) under similar physicochemical conditions (temperature, concentrations). This suggests that the Co-precipitate formed during Step-1 (Section 3.3.1.1) indeed consisted of Co and Ala. Additionally, Figure 6 reveals the elemental composition of the Co-precipitate formed in the spent catalyst leachate: Co, as well as N and O (originating from amino acid molecules), were shown to be the component of this precipitate. The presence of other metals such as Mo and Al was negligible.

3.3.3 Effect of different sequential order

Before selecting the above 3-step order (Section 3.3.1), preliminary tests were conducted to compare different sequential orders. Supplementary Figure S6 shows the results from a different 3-step order (Step-1: Alkaline Ala leaching, Step-2: Second alkaline Ala leaching, Step-3: Hot water leaching). The leaching trend of Mo in alkaline Ala solutions was relatively similar between the two different sequential orders (Supplementary Figures S6A,E; Figures 3A,I). However, applying the hot water treatment as Step-3 (Supplementary Figure S6J) instead of Step-2 (Figure 3F) significantly lowered the solubilization of Co^{2+} from Co-Ala

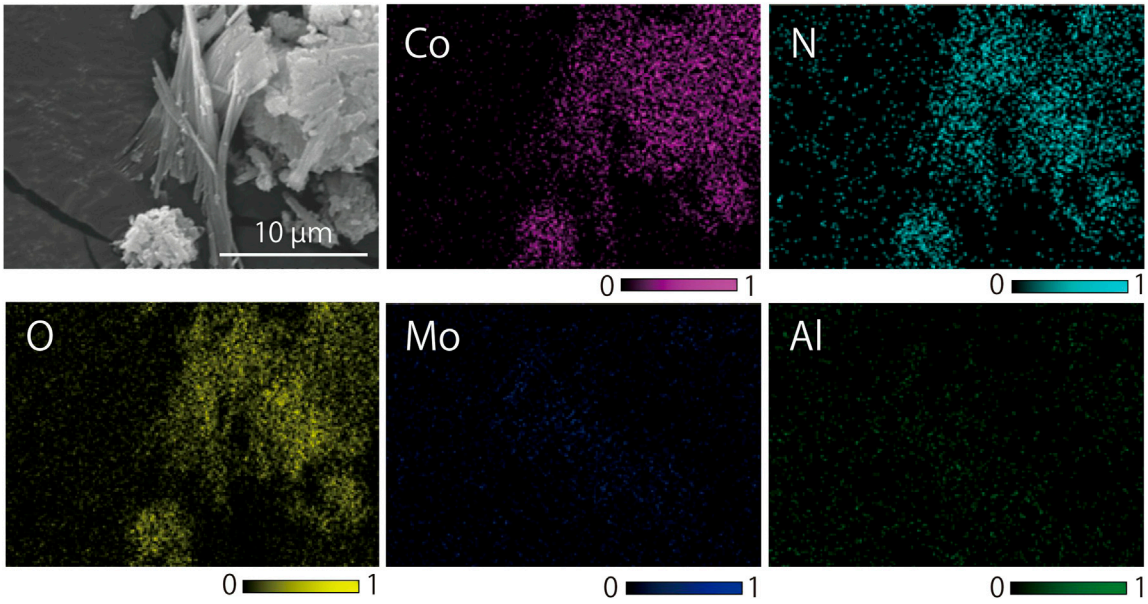

FIGURE 6
SEM-EDS elemental mapping of Co-Ala complex formed in the actual spent catalyst leachate (spent catalyst particles separated prior to Co-Ala precipitation) at 45°C (corresponding to Figures 5C,C′): The secondary electron image was mapped for Co, N, O, Mo and Al.

precipitates. This was likely caused by a pH spike during the hot water leaching in Step-3 (Supplementary Figure S3L), owing to an excessive alkalization of spent catalyst particles in Step-1 and Step-2. Setting the hot water Co leaching at Step-1 was also found to be unfavorable since Co dissolution was accompanied by co-dissolution of a certain level of Mo and Al (data not shown). Overall, the sequential leaching order described in Section 3.3.1 was found to be most effective in terms of the total metal dissolution as well as metal selectivity.

3.3.4 Process overview and comparison with previous studies

Figure 7 summarizes the process flow overview of the sequential 3-step leaching described in Section 3.3.1. Two separate leachates, "Co-rich leachate" and "Total Mo-rich leachate" were eventually obtained with highly selective metal dissolutions (Figure 7). Reusing the pregnant Ala solution in Step-3 was favorable in terms of more concentrated Mo content and cost-effectiveness, although the metal selectivity between Mo and Co became slightly lowered (Figure 7).

When calculated on the liquid analysis basis (Figures 3, 7), the whole 3-step leaching process solubilized a total of ~97% Mo, 98% Co and ~2.1% Al from the original spent catalyst (E_l; Table 2). In order to verify these values, the final Al-rich Step-3 residue was acid digested, followed by ICP-OES analyzed to calculate its metal mass (Table 2). This solid-based calculation led to the total metal dissolution of 90% Mo, 93% Co and 1.5% (Table 2). Although a slight overestimation was found when calculated solely on the liquid analysis basis, the overall tendency was consistent.

Overall, the role of alkaline Ala solution in the process was three-fold; 1) maintaining alkalinity in Step-1 and Step-3 by amino acid's buffering capacity to assist Mo leaching, 2) selectively precipitating Co by forming Co-Ala complex, which can readily re-dissolve in hot water to be separated from spent catalyst particles. 3) suppressing dissolution of Al throughout the reaction without needing pH control. In addition, the possibility of the Mo-Ala complexation effect cannot be exempted at this stage. Further studies are necessary to clarify this.

So far, several literatures have reported the use of inorganic and organic lixiviant for the dissolution of critical metals (Mo, Co, Ni) from spent hydrodesulfurization catalysts (Table 3). Angelidis et al. (1995) attempted to selectively recover Mo, Co, and Ni using a two-step alkali-acid leaching. Mo and Co were selectively dissolved (96% and 91%, respectively), but the Al dissolution was not well controlled (Table 3). Barik et al. (2012) attempted to leach Mo and Co from spent catalyst using H_2SO_4 by adding various oxidants. When using H_2O_2 as an oxidant, Mo and Co were nearly completely but non-selectively leached (99.8% and 96.2%, respectively), accompanied by 11% Al dissolution (Table 3). Pinto and Soares (2012) applied NaOH-based microwave treatment for four cycles, resulting in the dissolution of 91% Mo and 8.8% Al. Pinto and Soares (2013) then used organic chelating agents (Ethylenediaminetetraacetic acid, EDTA; Nitrilotriacetic acid,

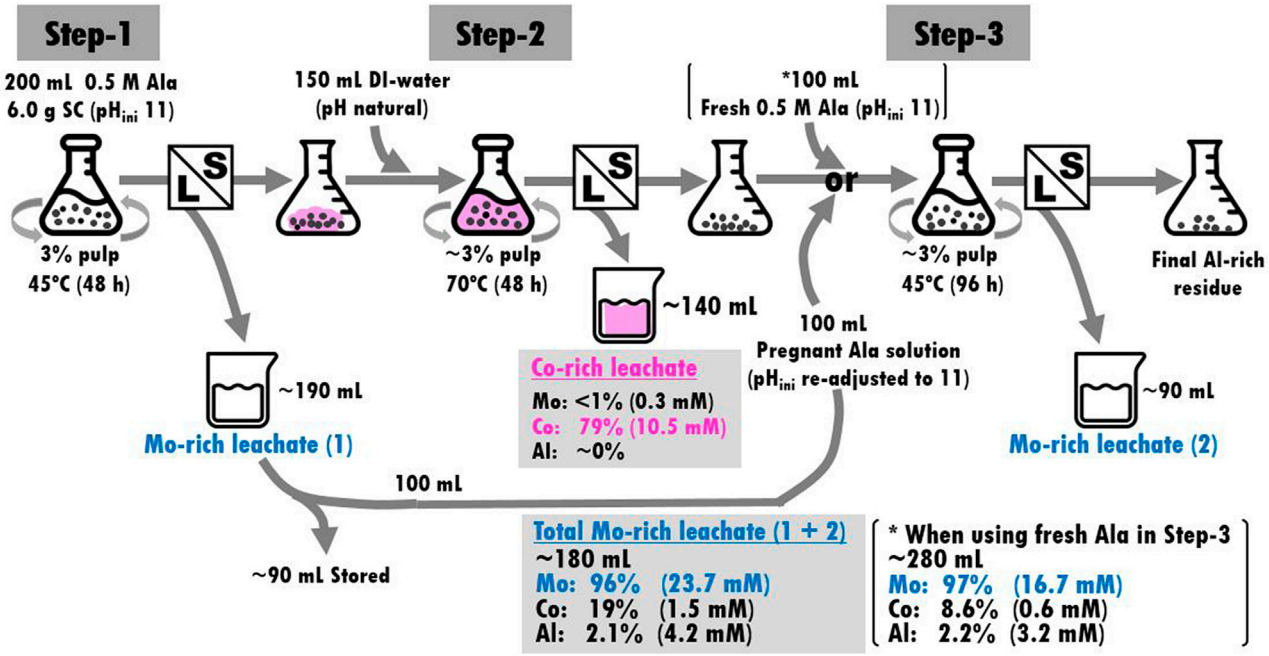

FIGURE 7
The overview of 3-step leaching flow and the resultant metal contents of Co-rich and Mo-rich leachates.

TABLE 2 Total metal dissolution calculated based solely on the liquid analysis or the combination of liquid and solid analyses.

	Original spent catalyst	Final Al-rich residue (after Step-3 reusing pregnant Ala solution)		
	Metal mass[a] (m_o, mg/g)	Metal mass[a] (m_r, mg/g)	Total metal dissolution (Sum of Step-1, 2, and 3);	
			Caluculated from liquid analysis (Figure 7) (E_l, %)	Calculated from liquid + solid analysis (E_m, %)
Mo	101 ± 8	10.8 ± 0.02	97	90
Co	24 ± 0.8	1.7 ± 0.03	98	93
Al	248 ± 2.7	359 ± 0.6	2.1	1.5

$E_m = m_f/(m_f + m_r) \times 100\%$ Li et al. (2020). $m_f = E_l\% m_o$ (the mass of dissolved metal, calculated based on the liquid analysis).
[a]Solid analysis data (acid digestion followed by ICP-OES analysis).

NTA) under the microwave condition to selectively leach Ni from Ni-Mo spent catalyst. EDTA gave a better Ni dissolution (80%) than NTA (64%), with some co-solubilization of Mo and Al (Table 3). Arslanoğlu and Yaraş (2019) applied formic acid for the roasted spent Mo-Co-Ni/Al_2O_3 catalyst, wherein 76% Mo, 97% Co, and 94% Ni were leached with relatively high co-solubilization of Al (19%) (Table 3). Compared to the previous reports summarized in Table 3, the results obtained in this study achieved highly selective leaching of critical metals from spent desulfurization catalyst.

4 Conclusion

The spent hydrodesulfurization catalyst sample used in this study consisted of MoS_2 and Co_3S_4 supported on Al_2O_3, at the Mo and Co grade of 10% and 2.4%, respectively. In contrast to the case of H_2SO_4 and citric acid, alkaline amino acids generally suppressed the dissolution of unwanted Al. Still, the leaching trend of Mo and Co differed largely depending on the type of amino acids.

TABLE 3 Comparison of the spent hydrodesulfurization catalyst leaching studies.

Spent catalyst	Lixiviant		Condition		Metal dissolution, %			References
	Type	Conc.			Mo	Co/Ni	Al	
Mo-Co/Al_2O_3	NaOH, H_2SO_4	10 g/L	Two-step alkali and acid leaching	Alkali leachate	96*	0.09/-	14	Angelidis et al. (1995)
				Acidic leachate	0.03	91[a]/-	54	
Mo-Co/Al_2O_3	H_2SO_4	0.5 mol/L	Leaching reactor		99[a]	96[a]/-	11	Barik et al. (2012)
Mo-Co/Al_2O_3	NaOH	10 g/L	Microwave assisted		91[a]	N.D.	8.8	Pinto and Soares (2012)
Mo-Ni/Al_2O_3	EDTA	0.1 mol/L	Microwave assisted		10	-/80[a]	2.8	Pinto and Soares (2013)
Mo-Ni/Al_2O_3	NTA	0.2 mol/L	Microwave assisted		8	-/64[a]	1.8	Pinto and Soares (2013)
Mo-Co-Ni/Al_2O_3	Formic acid	0.6 mol/L	Roasting and leaching		76[a]	97/94[a]	19	Arslanoğlu and Yaraş (2019)
Mo-Co/Al_2O_3	Alanine, H_2O	0.5 mol/L	Sequential leaching	Co-rich leachate	<1	79[a]/-	0	This study
				Total Mo-rich leachate	96[a, P] (97[F])	19[P] (8.6[F])/-	2.1[P] (2.2[F])	

[a]Target metal. P, Pregnant Ala solution reused in Step-3. F, Fresh Ala solution used in Step-3. N.D., No data available. -,.Not applicable.

Alanine was the most effective, simple amino acid in supporting the Mo alkalosis by its buffering effect while simultaneously precipitating Co as Co-Ala complex of distinctive color and morphology, enabling selective recovery of Mo-rich leachate (96% Mo, 19% Co, and 2.1% Al dissolved). The formation of the Co-Ala complex was favorable in terms of its solubility in hot water (supposedly due to the decomposition of amino acids), enabling selective recovery of Co-rich leachate (<1% Mo and 79% Co dissolved, Al not detected). Consequently, the sequential 3-step process (Step-1: Alkaline Ala leaching at 45°C, Step-2: Hot water leaching at 70°C, Step-3: Alkaline Ala leaching at 45°C) achieved highly selective leaching of critical metals (Mo and Co) compared to previous studies.

Data availability statement

The original contributions presented in the study are included in the article/Supplementary Material, further inquiries can be directed to the corresponding author.

Author contributions

Funding acquisition, conceptualization, methodology and supervision, NO; experimental work, IP, YT, and SY; draft manuscript preparation, IP; manuscript revision and editing, NO.

Funding

This work was supported by the JSPS KAKENHI Grant Number 20H00647 and 16H04616.

Acknowledgments

The spent hydrodesulfurization catalyst sample was kindly provided by Dr. Himawan T. B. M. Petrus from Universitas Gadjah Mada, Indonesia. IP is thankful to the MEXT (Ministry of Education, Culture, Sports, Science and Technology, Japan) for providing the scholarship.

Conflict of interest

The authors declare that the research was conducted in the absence of any commercial or financial relationships that could be construed as a potential conflict of interest.

Publisher's note

All claims expressed in this article are solely those of the authors and do not necessarily represent those of their affiliated organizations, or those of the publisher, the editors and the reviewers. Any product that may be evaluated in this article, or claim that may be made by its manufacturer, is not guaranteed or endorsed by the publisher.

Supplementary material

The Supplementary Material for this article can be found online at: https://www.frontiersin.org/articles/10.3389/fchem.2022.1011518/full#supplementary-material

SUPPLEMENTARY FIGURE S1
Pourbaix diagram for Molybdenum—H_2O system. ∑ Mo = 10^{-5} M at 25°C (Lyon, 2010).

SUPPLEMENTARY FIGURE S2
Pourbaix diagram for Cobalt—H_2O system. ∑ Co = 10^{-6} M at 25°C (Chivot et al., 2008).

SUPPLEMENTARY FIGURE S3
Pourbaix diagram for Aluminum—H_2O system. ∑ Al = 3 × 10^{-6} M at 25°C (Pourbaix, 1974; Sukiman et al., 2012).

SUPPLEMENTARY FIGURE S4
The effect of different temperatures (25, 45, and 70°C) on Step-1.

SUPPLEMENTARY FIGURE S5
The effect of different temperatures (25, 45, and 70°C) on Step-2.

SUPPLEMENTARY FIGURE S6
Sequential 3-step leaching of spent catalyst (Step-2 and Step-3 reversed from Figure 3). Step-1 **(A-D)**: Alkaline Ala leaching (pH_{ini} 11) at 45°C. Step-2 **(E–H)**: Second alkaline Ala leaching of the Step-1 solid residue in fresh Ala solution (pH_{ini} 11) at 45°C. Step-3 **(I–L)**: Hot water leaching of the Step-2 solid residue at 70°C. The dissolution profile of Mo **(A,E,I)**, Co **(B,F,J)**, and Al **(C,G,K)** as well as the pH profile **(D,H,L)** are shown.

References

Akcil, A., Vegliò, F., Ferella, F., Okudan, M., and Tuncuk, A. (2015). A review of metal recovery from spent petroleum catalysts and ash. *Waste Manag.* 45, 420–433. doi:10.1016/j.wasman.2015.07.007

Alam, M. M., Mubarak, A. T., Assiri, M. A., Ahmed, S. M., and Fouda, A. M. (2019). A facile and efficient synthesis of 1, 8-dioxodecahydroacridines derivatives catalyzed by cobalt–alanine metal complex under aqueous ethanol media. *BMC Chem.* 13, 40. doi:10.1186/s13065-019-0545-3

Alonso, S., Rendueles, M., and Díaz, M. (2015). Microbial production of specialty organic acids from renewable and waste materials. *Crit. Rev. Biotechnol.* 35, 497–513. doi:10.3109/07388551.2014.904269

Angelidis, T., Tourasanidis, E., Marinou, E., and Stalidis, G. (1995). Selective dissolution of critical metals from diesel and naptha spent hydrodesulphurization catalysts. *Resour. Conservation Recycl.* 13, 269–282. doi:10.1016/0921-3449(94)00049-b

Arslanoğlu, H., and Yaraş, A. (2019). Recovery of precious metals from spent Mo–Co–Ni/Al2O3 catalyst in organic acid medium: Process optimization and kinetic studies. *Petroleum Sci. Technol.* 37, 2081–2093. doi:10.1080/10916466.2019.1618867

Asghari, I., Mousavi, S. M., Amiri, F., and Tavassoli, S. (2013). Bioleaching of spent refinery catalysts: A review. *J. Industrial Eng. Chem.* 19, 1069–1081. doi:10.1016/j.jiec.2012.12.005

Astuti, W., Hirajima, T., Sasaki, K., and Okibe, N. (2016). Comparison of effectiveness of citric acid and other acids in leaching of low-grade Indonesian saprolitic ores. *Miner. Eng.* 85, 1–16. doi:10.1016/j.mineng.2015.10.001

Barik, S. P., Park, K. H., Parhi, P. K., and Park, J. T. (2012). Direct leaching of molybdenum and cobalt from spent hydrodesulphurization catalyst with sulphuric acid. *Hydrometallurgy* 111–112, 46–51. doi:10.1016/j.hydromet.2011.10.001

Chivot, J., Mendoza, L., Mansour, C., Pauporté, T., and Cassir, M. (2008). New insight in the behaviour of Co–H2O system at 25–150 °C, based on revised Pourbaix diagrams. *Corros. Sci.* 50, 62–69. doi:10.1016/j.corsci.2007.07.002

Dewi, M. P., Petrus, H. T. B. M., and Okibe, N. (2020). Recovering secondary REE value from spent oil refinery catalysts using biogenic organic acids. *Catalysts* 10, 1090–1115. doi:10.3390/catal10091090

Djordjevic, C., Vuletic, N., Jacobs, B. A., Lee-Renslo, M., and Sinn, E. (1997). Molybdenum(VI) peroxo α-amino acid Complexes: synthesis, spectra, and properties of $MoO(O_2)_2$(α-aa)(H_2O) for α-aa = Glycine, alanine, proline, valine, leucine, serine, asparagine, glutamine, and glutamic acid. X-Ray crystal structures of the Glycine, alanine, and proline compounds. *Inorg. Chem.* 36, 1798–1805. doi:10.1021/ic9610997

Eksteen, J. J., Oraby, E. A., and Tanda, B. C. (2017). A conceptual process for copper extraction from chalcopyrite in alkaline glycinate solutions. *Min. Eng.* 108, 53–66. doi:10.1016/j.mineng.2017.02.001

Feng, D., and van Deventer, J. S. J. (2011). The role of amino acids in the thiosulphate leaching of gold. *Miner. Eng.* 24, 1022–1024. doi:10.1016/j.mineng.2011.04.017

Hamza, M. F., Roux, J-C., and Guibal, E. (2018). Metal valorization from the waste produced in the manufacturing of Co/Mo catalysts: Leaching and selective precipitation. *J. Mat. Cycles Waste Manag.* 21, 525–538. doi:10.1007/s10163-018-0811-9

Han, J., and Chi, Y. S. (2010). Vibrational and electronic spectroscopic characterizations of amino acid-metal complexes. *J. Korean Soc. Appl. Biol. Chem.* 53, 821–825. doi:10.3839/jksabc.2010.124

Huang, J. H., Kargl-Simard, C., Oliazadeh, M., and Alfantazi, A. M. (2004). pH-Controlled precipitation of Cobalt and Molybdenum from industrial waste effluents of a cobalt electrodeposition process. *Hydrometallurgy* 75, 77–90. doi:10.1016/j.hydromet.2004.06.008

Ilhan, S. (2020). Extraction of molybdenum, nickel and aluminium from spent Ni–Mo hydrodesulphurization (HDS) catalyst in oxalic acid solutions. *Can. Metall. Q.* 59, 26–35. doi:10.1080/00084433.2020.1715691

Klingler, D., Berg, J., and Vogel, H. (2007). Hydrothermal reactions of alanine and glycine in sub- and supercritical water. *J. Supercrit. Fluids* 43, 112–119. doi:10.1016/j.supflu.2007.04.008

Li, H., Oraby, E. A., and Eksteen, J. J. (2020). Extraction of copper and the co-leaching behaviour of other metals from waste printed circuit boards using alkaline glycine solutions. *Resour. Conserv. Recycl.* 154, 104624. doi:10.1016/j.resconrec.2019.104624

Li, X., Qiao, K., Subhan, F., Xing, W., Liu, X., and Yan, Z. (2015). Preparation and hydrodesulfurization properties of cobalt–molybdenum–phosphorous catalysts for removal of dibenzothiophene. *Appl. Petrochem. Res.* 5, 405–411. doi:10.1007/s13203-015-0124-z

Liu, P., Xu, H., and Zhang, X. (2022). Metabolic engineering of microorganisms for L-alanine production. *J. Ind. Microbiol. Biotechnol.* 49, kuab057. doi:10.1093/jimb/kuab057

Lyon, S. B. (2010). Corrosion of molybdenum and its alloys. *Shreir's Corros.* 3, 2157–2167. doi:10.1016/B978-044452787-5.00106-2

Marafi, M., and Stanislaus, A. (2007). Studies on recycling and utilization of spent catalysts: Preparation of active hydrodemetallization catalyst compositions from spent residue hydroprocessing catalysts. *Appl. Catal. B Environ.* 71, 199–206. doi:10.1016/j.apcatb.2006.09.005

Mirvaliev, R., and Inoue, K. (2001). Pressure oxidative leaching of molybdenite in alkaline media; Autoclave processing of low-grade molybdenite concentrates (2nd report). *Shigen-to-Sozai* 117, 72–76. doi:10.2473/shigentosozai.117.72

O'Connor, G. M., Lepkova, K., Eksteen, J. J., and Oraby, E. A. (2018). Electrochemical behaviour of copper in alkaline glycine solutions. *Hydrometallurgy* 181, 221–229. doi:10.1016/j.hydromet.2018.10.001

Okafor, N. (2007). *Production of amino acid by fermentation" in modern industrial microbiology and biotechnology.* 1st ed. Boca Raton: CRC Press, 380–396. doi:10.1201/b21298

Oraby, E. A., and Eksteen, J. J. (2013). *Australian provisional patent Application No. 2013903380, A process of precious metals recovery*. Available at: https://patents.google.com/patent/WO2015031943A1.

Oraby, E. A., Li, H., and Eksteen, J. J. (2019). An alkaline glycine-based leach process of base and precious metals from powdered waste printed circuit boards. *Waste Biomass Valorization* 11, 3897–3909. doi:10.1007/s12649-019-00780-0

Park, K. H., Mohapatra, D., and Reddy, B. R. (2006). Selective recovery of molybdenum from spent HDS catalyst using oxidative soda ash leach/carbon adsorption method. *J. Hazard. Mater.* 138, 311–316. doi:10.1016/j.jhazmat.2006.05.115

Pinto, I. S. S., and Soares, H. M. V. M. (2013). Microwave-assisted selective leaching of nickel from spent hydrodesulphurization catalyst: A comparative study between sulphuric and organic acids. *Hydrometallurgy* 140, 20–27. doi:10.1016/j.hydromet.2013.08.009

Pinto, I. S. S., and Soares, H. M. V. M. (2012). Selective leaching of molybdenum from spent hydrodesulphurisation catalysts using ultrasound and microwave methods. *Hydrometallurgy* 129-130, 19–25. doi:10.1016/j.hydromet.2012.08.008

Pourbaix, M. (1974). *Atlas of electrochemical equilibria in aqueous solutions*. Houston, TX, USA: National Association of Corrosion Engineers.

Sodhi, R. K., and Paul, S. (2019). Metal complexes in medicine: An overview and update from drug design perspective. *Cancer Ther. Oncol. Int. J.* 14, 25–32. doi:10.19080/CTOIJ.2019.14.555883

Sukiman, N. L., Zhou, X., Birbilis, N., Hughes, A. E., Mol, J. M. C., Garcia, S. J., et al. (2012). Durability and corrosion of aluminium and its alloys: Overview, property space, technique and developments. *Alum. Alloy. New Trend Fabr. Applic.* 5, 47–97. doi:10.5772/53752

Zeng, L., and Cheng, C. Y. (2009). A literature review of the recovery of molybdenum and vanadium from spent hydrodesulphurisation catalysts part I: Metallurgical processes. *Hydrometallurgy* 98, 1–9. doi:10.1016/j.hydromet.2009.03.010

frontiers | Frontiers in Chemistry

TYPE Original Research
PUBLISHED 24 October 2022
DOI 10.3389/fchem.2022.1036726

Check for updates

OPEN ACCESS

EDITED BY
Xiangning Bu,
China University of Mining and Technology, China

REVIEWED BY
Tatiana Plisko,
Institute of Physical and Organic Chemistry (NASB), Belarus
Zongli Xie,
Commonwealth Scientific and Industrial Research Organisation (CSIRO), Australia

*CORRESPONDENCE
Xiaozhuan Zhang,
zhangxiaozhuan0103@126.com

†These authors have contributed equally to this work and share first authorship

SPECIALTY SECTION
This article was submitted to Green and Sustainable Chemistry, a section of the journal Frontiers in Chemistry

RECEIVED 05 September 2022
ACCEPTED 10 October 2022
PUBLISHED 24 October 2022

CITATION
Zhang X, Zhao K, Shi X, Tian Z, Huang Z and Zhao L (2022), Novel strategy for reusing agricultural mulch film residual by iron modification for arsenic removal in gold-smelting wastewater. *Front. Chem.* 10:1036726. doi: 10.3389/fchem.2022.1036726

COPYRIGHT
© 2022 Zhang, Zhao, Shi, Tian, Huang and Zhao. This is an open-access article distributed under the terms of the Creative Commons Attribution License (CC BY). The use, distribution or reproduction in other forums is permitted, provided the original author(s) and the copyright owner(s) are credited and that the original publication in this journal is cited, in accordance with accepted academic practice. No use, distribution or reproduction is permitted which does not comply with these terms.

Novel strategy for reusing agricultural mulch film residual by iron modification for arsenic removal in gold-smelting wastewater

Xiaozhuan Zhang[1*†], Kejiang Zhao[1,2†], Xibao Shi[3†], Zhenbang Tian[2], Zuohua Huang[2] and Liang Zhao[2]

[1]Henan International Joint Lab of Key Technology in Water Treatment, Key Laboratory of Yellow River and Huai River Water Environmental and Pollution Control, Ministry of Education, School of Environments, Henan Normal University, Xinxiang, Henan, China, [2]Henan Institute of Chemistry, Henan Academy of Sciences, Zhengzhou, Henan, China, [3]College of Life Sciences, Henan Normal University, Xinxiang, Henan, China

In gold-smelting wastewater after the original treatment process of flocculation and precipitation using mainly lime, a mixture of As, Cu, Pb, Mn, Zn, Al, Ni, and Fe existed with an arsenic concentration of 813.07 mg/L and other ions' concentration at ug/L levels. In this work, a new clean process of mainly adsorption with self-made adsorbent Fe-PE, which was synthesized by loading ferric lignin on agricultural mulch film residual, was investigated to purify and remove arsenic from gold-smelting wastewater. A batch of column experiments was investigated to explore the reaction behavior between wastewater and adsorbent Fe-PE. The results showed while operating the adsorption columns at a pilot scale for 68 days, the arsenic concentration in the effluent was below 0.5 mg/L, and there was no significant change in the concentration of co-existing metal ions, indicating that Fe-PE had a good selective adsorption performance for arsenic in wastewater. Furthermore, Fe-PE did not dissolve and release Fe ions in wastewater, and the whole process could not produce sludge. This work first suggested an efficient and potential application for the purification and removal of arsenic from gold-smelting wastewater with agricultural mulch film residual after chemical modification, which will provide a novel strategy for reusing the agricultural mulch film residual.

KEYWORDS

arsenic, purification and removal, gold-smelting wastewater, adsorption, iron-modified agricultural mulch film residual

Introduction

Arsenic at higher concentrations in water or land poses a great threat to human health and ecological safety (Lamm and Kruse, 2005; Rodriguez-Lado et al., 2013; Celebi et al., 2014). It is very important that arsenic residues must be strictly restrained to be directly disposed of into the environment. In metallurgical and mining wastewaters (Sekula, 2008; Nazari et al., 2017), arsenic, usually with an extremely high concentration, is one of the main contaminants among other arsenic-associated minerals such as Cu, Fe, Pb, Zn, and Ni (Anderson and Twidwell, 2008; Oishi et al., 2008; Cheng et al., 2009). It is necessary to investigate an efficient process to remove arsenic from metallurgical wastewater in order to meet the environmental legislation.

Iron oxides or oxyhydroxides have a high affinity to arsenic, and the mobility of As is closely correlated with Fe in natural environments (Cances et al., 2005; Jia and Demopoulos, 2005; Jia et al., 2007; Jia and Demopoulos, 2008). Researchers have concluded an adsorption mechanism where As would be bound as a bidentate inner sphere complex with Fe (Ford, 2002; Jia et al., 2006; Gomez et al., 2011; De Klerk et al., 2015). Otherwise, the precipitation as crystalline scorodite (Langmuir et al., 2006; Bluteau and Demopoulos, 2007; Caetano et al., 2009) was reported to offer the advantages of combining a relatively high arsenic content and low release of arsenic in aqueous solutions, but large amounts of neutralizing agents were necessary because of the high alkalinity in the final leaching solution. Therefore, the process of arsenic removal by precipitation is commonly used by the metallurgical and mining industry (De Klerk et al., 2012; Cui et al., 2014; Coudert et al., 2020), mainly due to its lower cost. However, the concentration of residual arsenic is always at the level of mg/L, which is the limit to the technology of precipitation, and most seriously, much sludge with arsenic contamination will be generated, resulting in serious secondary pollution during transportation, storage, and disposal (Lin, 2004; Feng et al., 2017a; Coudert et al., 2020). Focusing on the possible leakage and secondary pollution of arsenic, this work aims to find a new process for arsenic removal in gold-smelting wastewater by adsorption technology using a new adsorbent, expected with no sludge and hazardous solid waste.

Though different adsorbents such as granular activated carbon, activated alumina, biochar, magnetite nanoparticles, and polymeric adsorbents have been proved to be effective in water for arsenic removal, there have been few studies involving the use of agricultural mulch film residual (AMFR) after chem-modification as adsorbents to remove arsenic in wastewater. Because polyethylene film is widely used for the exchange of heat and moisture in agriculture (Liu et al., 2017), AMFR in large amounts is known as one of the agricultural wastes of hard degradation in a short time and could release hazardous substances such as polyethylene particles, plasticizers, or additives into soils and waters during the process of degradation, and it also has the possibility to become microplastics (Zhang et al., 2021). Because of the low-rate recycling (a recycling rate of less than 2/3 each year in China), potentially severe pollution, and plastic-restriction orders by governmental management (MOA, 2017), it is meaningful to investigate a new strategy to reuse AMFR. In our previous work (Zhang et al., 2022), ferric lignin has been loaded on the polyethylene film, and AMFR will also be promisingly modified by ferric lignin because of the same composition as the original polyethylene film. But before modification, AMFR must be pretreated, for example, cleaning to move the pollutants adhered to the surface of AMFR.

In this work, we monitored a kind of gold-smelting wastewater, after the original treatment of flocculation and precipitation using mainly lime; a mixture of arsenic, copper, lead, manganese, zinc, aluminum, nickel, cadmium, and iron existed with an arsenic concentration of 813.07 mg/L and other ions' concentration was at the level of ug/L. AMFR would be loaded with ferric lignin after chemical modification and used in the process of arsenic removal in this wastewater. A batch of column experiments was investigated to explore the reaction behavior between wastewater and the adsorbent, and the objective of this work was to investigate an integrated process for arsenic purification from gold-smelting wastewater, which may have potential application for arsenic removal in all gold-smelting wastewaters after the precipitation process using mainly lime as pretreatment.

Experimental

Materials and reagents

Sodium lignosulphonate, ferrous sulfate heptahydrate, sodium sulfite anhydrous, sodium hydroxide, and ethanol absolute were all in reagent grade and purchased from Shanghai Macklin Biochemical Co., Ltd., China.

Different specifications of plexiglass ion-exchange columns were ordered from Zhengzhou Glass Factory, China. The column with a diameter of 50 mm and a length of 500 mm was used for a lab-scale experiment, and the column with a diameter of 300 mm and a length of 1500 mm was used for a pilot-scale experiment. The centrifugal pump, peristaltic pump, and flowmeter were purchased from Jiangsu Pump Industry, Co., Ltd. Taizhou, China. The normal window gauze, bought from a local grocery store, was applied as the supporting material. The de-ionized water was used for dilution, and 1 M of HCl or NaOH was used for adjusting the pH of the solution.

The gold-smelting wastewater after the original treatment process of flocculation and precipitation using mainly lime, was

TABLE 1 Composition of the gold-smelting wastewater after the original treatment process of flocculation and precipitation using mainly lime (mg/L).

Element	As	Mn	K	Ni	Zn	Fe	Ba	Al	Cu	Pb	SO_4^{2-}	NO_3^-	CO_3^{2-}
Concentration	813.07	0.428	0.332	0.205	0.271	0.167	0.065	0.044	0.039	0.011	1.013	0.586	3.261

from a local company smelting precious metals such as gold and copper. Table 1 shows the chemical composition of the wastewater during the period of observation. In view of the potentially toxic substances, during the process of handling the wastewater, CAUTION in the Supplementary Materials must be obeyed.

Method for preparing arsenic-removal adsorbent

The adsorbent named Fe-PE used by us in this work was prepared by loading ferric lignin on AMFR. The synthesis route of Fe-PE is shown in Figure S1. AMFR exposed for 6 months in the farmland with growing romaine lettuce plants was manually fetched without pulling too much, and the thickness of AMFR was 0.012 mm with a tensile resistance strength of 1.77 N. After being cleaned by watersteam with pressure and HCl or NaOH solution to remove the surface pollutants, cleaned AMFR was dried at a room temperature of 25°C–30°C and immersed into 1 M NaOH solution in an ultrasonic reactor for 12 h at 70°C. Solutions of sodium lignosulphonate, ferrous sulfate heptahydrate, and sodium sulfite anhydrous were allowed to react to get ferric lignin by adjusting the pH using 0.1 M of NaOH. Then, AMFR and ferric lignin solution were put into a water-bath kettle at 80°C for 6–8 h. After that, AMFR was dried in an air oven at 100°C–140°C. In addition to the soil, mud, and plant residues, especially in the process of cleaning the AMFR, 1.007 mg/L of chlorantraniliprole and 0.001 mg/L of phoxim were detected and measured by GC-MS/MS in the wastewater after the cleaning process, due to the insecticides used in the growth of romaine lettuce plants, so the wastewater after the cleaning process must be collected.

Adsorption experiments using Fe-PE for arsenic removal on the lab scale

The arsenic-bearing wastewater was collected from the outlet after the process of precipitation, and the pH was 8.62~8.89. The total arsenic concentration was 813.07 mg/L with 68.7% of As (V) and 31.3% of As (III). The size of the column with a volume of 0.981 L was 50 mm diameter and 500 mm length. A peristaltic pump was used to supply impetus. The load density (LD) was calculated according to the following equation: LD = the amount of Fe-PE (g)/the volume of the column (L).

Static adsorption experiments were used to determine the adsorption capacity of the Fe-PE. The arsenic-bearing wastewater was diluted into different concentrations of 8.03, 16.23, 32.35, 81.60, 161.9, 405.2, and 813.07 mg/L. Different mass of 5 g, 10 g, and 20 g of Fe-PE were, respectively, immersed in the wastewater of 1 L in a plastic bucket for 12 h. The Fe-PE was wrapped in a window gauze before to be used.

Methods used to set up the column experiment

A batch of column experiments was conducted to investigate the performance of Fe-PE to remove arsenic from the wastewater. Fe-PE was wrapped in the window gauze and filled into the plexiglass ion-exchange column. The wastewater was pumped into the column from the bottom to the top. The basic flow chart of the adsorption process is shown in Figure S2.

Characterizations and testing

FT-IR spectra were collected on a spectrometer in the range of 400–4,000 cm^{-1} (jx20112184, PerkinElmer, United States). The pH value of liquid samples was measured using a PHS-3E pH meter (Shanghai, LeiCi, China). Element concentrations of liquid samples were measured using an ICP-OES spectrometer (PQ-900, Analytik Jena, Germany) or ICP-MS (jx20110281, PE, United States). An FESEM (Quanta FEG250, Thermo Fisher Scientific, United States) was used to scan the surface of the adsorbent and further confirm the distribution of elements.

Results and discussion

FT-IR and SEM analyses of the prepared adsorbent Fe-PE

An FT-IR spectrum was used to predict and confirm the reaction behavior between cleaned AMFR and ferric lignin. Figure 1 shows the spectra of cleaned AMFR (Figure 1A), ferric lignin prepared by us (Figure 1B), and Fe-PE

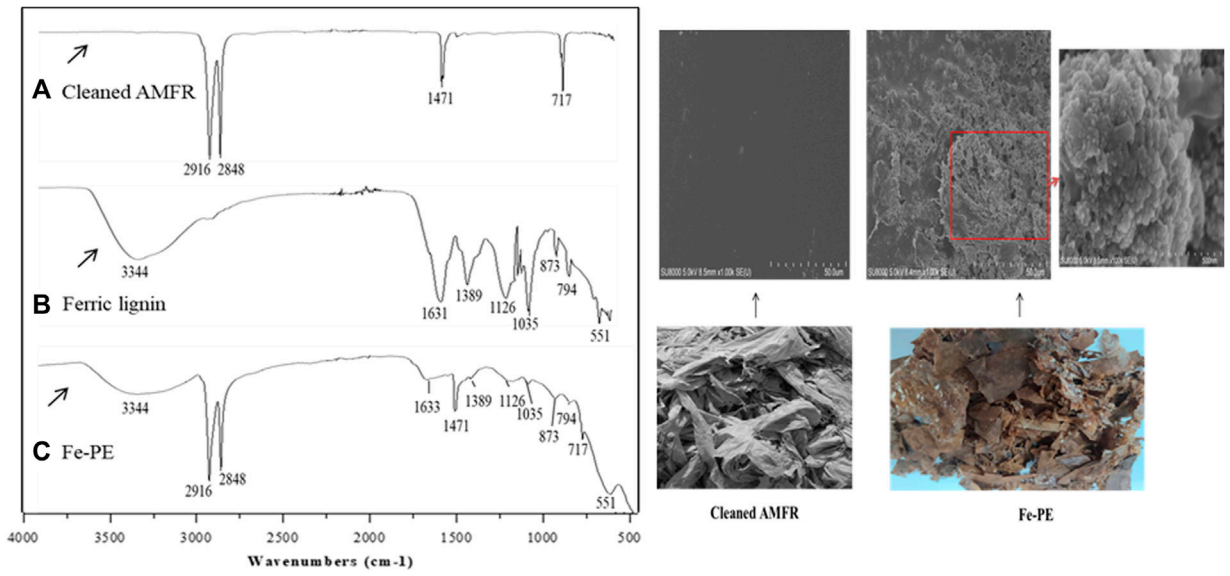

FIGURE 1
FTIR spectra of **(A)** cleaned AMFR, **(B)** ferric lignin, and **(C)** Fe-PE and SEM images and photographs of cleaned AMFR and Fe-PE.

(Figure 1C). As shown in Figure 1A, adsorption peaks at 2,916 cm^{-1}, 2848 cm^{-1}, 1471 cm^{-1}, and 717 cm^{-1} represent the antisymmetric stretching, symmetrical stretching, bending, and rocking vibration of $-CH_2$, respectively, which are the four characteristic adsorption peaks of polyethylene (Weng, 2010). The IR spectra of cleaned AMFR showed that there was no other obvious characteristic adsorption peaks except that of polyethylene, indicating that there was no other substance on the cleaned AMFR. As shown in Figure 1B, there were adsorption peaks at 3,344, 1,631, 1,389, 1,126, 1,035, 873, 794, and 551 cm^{-1} of ferric lignin. As shown in Figure 1C, compared with Figure 1A, the spectra showed that the absorption peaks at 2916 cm^{-1}, 2848 cm^{-1}, 1471 cm^{-1}, and 717 cm^{-1} were obviously weakened, and new adsorption peaks at 3,344, 1,633, 1,389, 1,126, 1,035, 873, 794, and 551 cm^{-1} appeared. Compared with Figure 1B, except for the characteristic adsorption peaks of polyethylene, there were same adsorption peaks on Fe-PE as those on ferric lignin, indicating that ferric lignin has been loaded on AMFR. Furthermore, the total content of the Fe element on Fe-PE was determined using an ICP-OES spectrometer after Fe-PE was digested with the mixed acid of HNO_3–$HClO_4$–HF, and 263.68 mg (on average) of Fe element on 1 g of Fe-PE could be examined.

Figure 1 also shows the SEM images and photographs of Fe-PE and cleaned AMFR. It showed that there were many flower-like particles on Fe-PE, compared to that of AMFR. The images also showed that the distribution of the particle size was about 500 nm and the morphology was uniform, indicating that the reaction was sufficient and moderate.

Adsorption behaviors of arsenic removal from gold-smelting wastewater by Fe-PE on the lab scale

Figure S3 shows the arsenic adsorption capacity of Fe-PE. There is a trend that higher solution concentration results in increasing adsorption capacity, but there is no expected increasing trend when using more Fe-PE, probably due to the effect of the As/Fe ratio and effective adsorption sites on the surface of Fe-PE during the process of adsorption. From Figure S3, the higher adsorption capacity of 44.73 mg/g for arsenic could be calculated, while using 10 g of Fe-PE in 1 L of wastewater with arsenic concentration of 813.07 mg/L.

Based on the arsenic adsorption capacity of Fe-PE and the volume of the column, while the adsorption column was full of Fe-PE and window gauze, the load density (LD) should be 360~400 g/L except for the weight of the window gauze. Also, the lower operating pressure must be taken into consideration. Figure 2 shows the adsorption performance of Fe-PE in column experiments in the laboratory. Figure 2A shows the curve of the breakthrough, Figure 2A1 shows the curve of the bed volume, and Figure 2A2 shows the curve of arsenic removal efficiency, when the velocity of the flow was 1 ml/s. Figure 2B shows the curve of the breakthrough, Figure 2B1 shows the curve of the bed volume, and Figure 2B2 shows the curve of arsenic removal efficiency, when the velocity of the flow was 5 ml/s. Figure 2C shows the curve of the breakthrough, Figure 2C1 shows the curve of the bed volume, and Figure 2C2 shows the curve of arsenic removal efficiency, when the velocity of the flow was 10 ml/s.

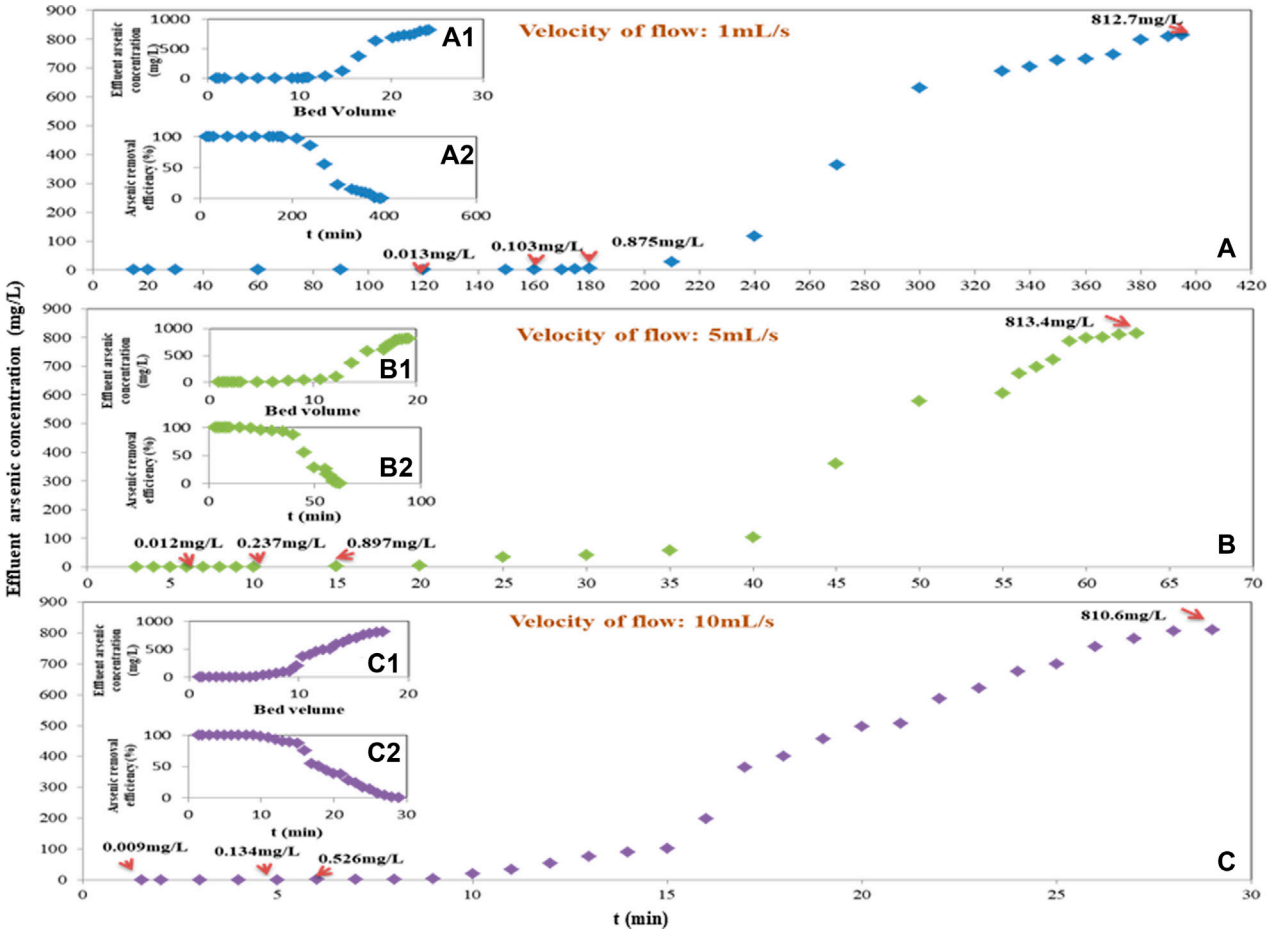

FIGURE 2
Adsorption column experiments on the lab scale [A, B, and C curve of breakthrough. **(A1)**, **(B1)**, and **(C1)** curve of bed volume. **(A2)**, **(B2)**, and **(C2)** curve of arsenic-removal efficiency. The velocity of flow was 1.0, 5.0, and 10.0 ml/s].

The empty bed contact time (EBCT) of the column was investigated and analyzed by different values of the flow velocity. When the velocity of the flow was 1, 5, and 10 ml/s, the EBCT was 981, 196.2, and 98 s, respectively. With the longer EBCT, as shown in Figure 2A, the arsenic concentration in the effluent was kept below 0.013 mg/L within 120 min, and 99% of arsenic could be removed when the column was operated for 180 min. With the shorter EBCT, as shown in Figure 2C, the arsenic concentration in the effluent was kept below 0.013 mg/L within 1 min, and 99% of arsenic was removed when the column was operated for 9 min. The adsorption efficiency decreased as the velocity increased with a correspondingly shorter EBCT. Within the scope of experimental investigation, the optimum velocity was 1 ml/s with an EBCT of 981 s, and the bed volume was 24.15 after the effluent arsenic concentration exceeded 813.07 mg/L. Also, when the flow velocity was 5 or 10 ml/s, the bed volume was 19.27 or 17.73, respectively. Figure 2 shows that the breakthrough time and arsenic removal efficiency increased with the increasing EBCT. Furthermore, based on the measured arsenic concentration (on average) of all effluent water during the time period at different flow velocities, the loading mass of Fe-PE in the column, and the column volume, the arsenic adsorption capacity for every column experiment could be 65.63, 53.46, and 49.87 mg/g at the velocity of 1, 5, and 10 ml/s, respectively, indicating a higher arsenic adsorption capacity with an increasing EBCT. The arsenic adsorption capacity calculated from the column experiment was a little higher than that calculated in the static experiment in this work and also a little higher than that calculated in other's work (Feng et al., 2017a; Feng et al., 2017b) using nano Fe_3O_4@SiO_2@TiO_2 or γ-Fe_2O_3@ZrO_2 with the total arsenic adsorption capacity of 21.3 or 42.3 mg/g during the process of removing arsenic from simulated process water of a cyanide gold leach plant, probably due to the faster mass transfer and larger contact area between arsenic and Fe-PE in the column

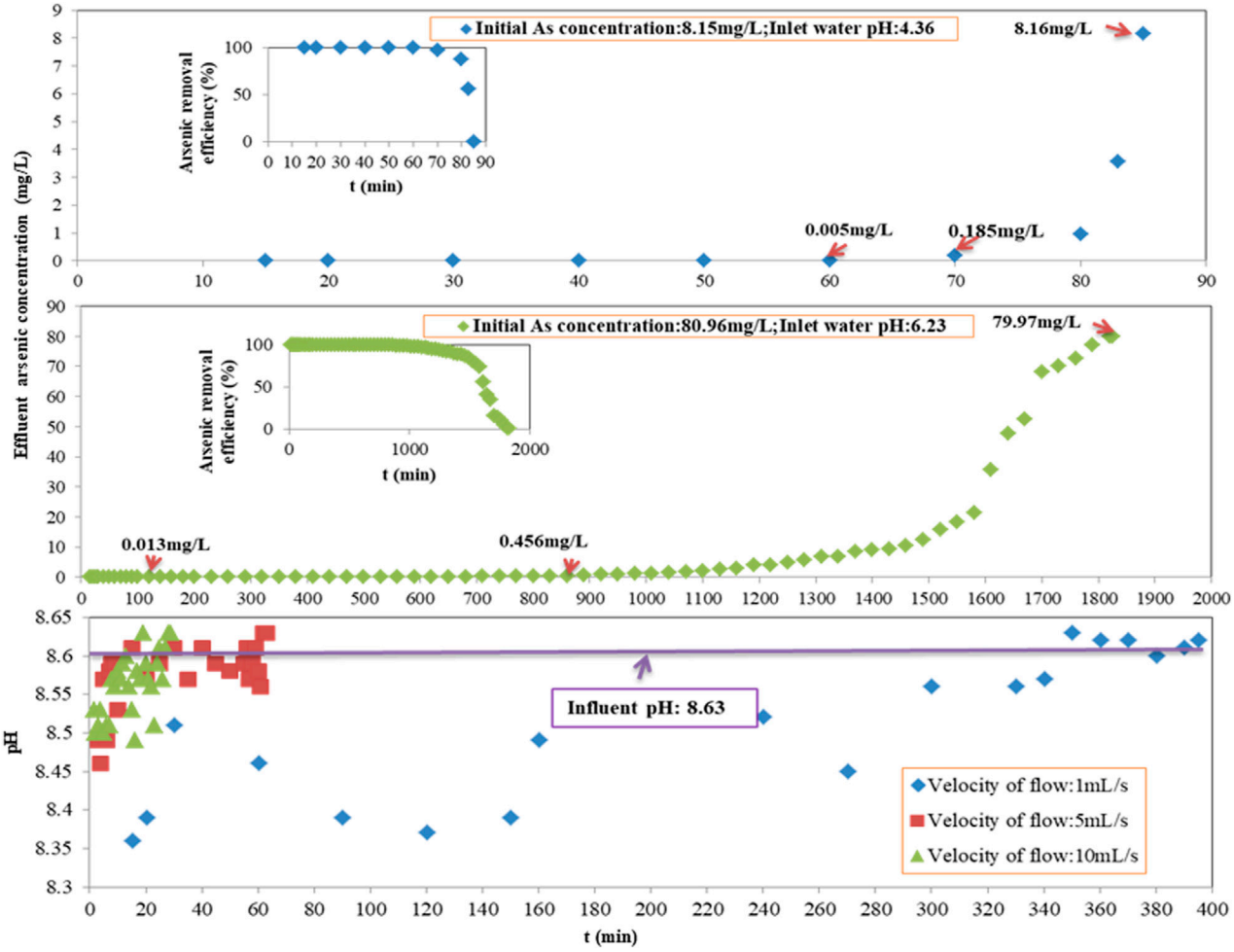

FIGURE 3
Performance evaluation of Fe-PE for arsenic removal at an initial arsenic concentration of 8.15 mg/L with pH = 4.36 and 80.96 mg/L with pH = 6.23; and the effluent pH of the adsorption column with time at different velocities of the flow.

process with a proper EBCT. The results showed again that effective and sufficient contact between the adsorbents and contaminants was essential in the process of adsorption (Neumann et al., 2013; Shakya and Ghosh, 2018).

The aforementioned experiments showed that arsenic could be promisingly removed by Fe-PE to meet drinking-water standards (below 0.01 mg/L) or discharging standards for arsenic in industrial wastewater (below 0.5 mg/L) with a proper velocity flow and EBCT.

Performance of Fe-PE for arsenic removal at varying initial arsenic concentrations with different pH values

In the process of column adsorption, varying initial arsenic concentrations of 8.15 mg/L (with a pH of 4.36 adjusted by HCl), 80.96 mg/L (with a pH of 6.23 adjusted by HCl), and 813.07 mg/L (with a pH of 8.63, the original wastewater) were applied after the wastewater was diluted. The arsenic removal performance of Fe-PE is shown in Figure 3. The operating conditions were as follows: the EBCT was 981 s at a flow velocity of 1 ml/s, and the LD of Fe-PE was 370 g/L except for the weight of the window gauze.

Figures 2, 3 show that under the same operating conditions, inlet wastewater with a lower initial arsenic concentration resulted in a better adsorption performance of Fe-PE than that with a higher initial arsenic concentration, due to the adsorption capacity of the adsorbents. More interestingly, there occurred an exception when the concentration of inlet wastewater was 8.15 mg/L. Researchers (Antelo et al., 2005; Capobianco et al., 2020; Fan et al., 2020) have revealed that the solution pH has an important effect on adsorption performance because of different arsenic species under different

pH conditions as well as the effects of H^+ or OH^-. But in this work, Fe-PE was prepared under alkaline conditions, so acidic solutions with more H^+ may have an effect on the dissolution of Fe ions from Fe-PE and then on the performance of Fe-PE for arsenic removal. To verify this, 1 g of Fe-PE was immersed into the deionized water with HCl or NaOH, the pH was adjusted to 2.13, 4.01, 6.15, 8.07, and 10.05, and the concentration of total Fe ions was measured using an ICP-OES spectrometer. Simultaneously, another 1 g of Fe-PE was put into 5 mg/L of arsenic solutions with HCl or NaOH, the pH was adjusted to 2.05, 4.17, 6.36, 8.17, and 10.19, and the concentration of total arsenic was measured using an ICP-OES or ICP-MS spectrometer. The results are shown in Figure S4. Under acidic conditions, Fe ions were detected in deionized water. The lower the pH values, the more the Fe ions, and it showed Fe ions were in the solution from Fe-PE because of the reaction between Fe oxides and H^+. Correspondingly, the arsenic concentration in the solution was higher during the process of arsenic removal by Fe-PE at pH = 2.05 or 4.17, resulting in a lower arsenic removal efficiency. On the contrary, under neutral and alkaline conditions, almost no iron ions were examined, resulting in a higher arsenic removal efficiency correspondingly during the process of arsenic removal by Fe-PE at pH = 6.36 or 8.17 or 10.19. However, it was not that the higher the alkalinity was, the more favorable the adsorption was because a large amount of OH^- under strong alkaline conditions will compete with arsenic ions to occupy the effective adsorption sites on Fe-PE. As shown in Figure S4, during the process of arsenic removal by Fe-PE, the optimum pH value of the inlet should be approximately 8.00.

Also, this work investigated the pH of the effluent of the adsorption column. The result is shown in Figure 3. At a flow rate of 1 ml/s, the pH of the effluent decreased slightly with time. When the flow rate increased, the pH of the effluent did not change significantly with time, especially when the flow rate reached 10 ml/s. Iron-based adsorbents may decrease the pH of water because of H^+ releasing from the reaction between Fe and As during the process of the adsorption. The experimental results of detecting the pH value of the effluent of the adsorption column in this work were consistent with these conclusions, but applying Fe-PE for arsenic removal will not significantly change the pH value of the raw water. In order to further verify this result, we reduced the flow rate to 0.1 ml/s to ensure full contact and reaction of Fe and As and observed the change in the effluent pH value with time. When the experiment reached the point of breakthrough, the lowest pH value of the effluent from the adsorption column was 8.36, which was still within the optimal range of the pH value in the process of arsenic adsorption by Fe-PE (data not shown). Furthermore, Figures 2, 3 reveal that the pH value of the effluent of the adsorption column was correlated with the arsenic-removal performance of Fe-PE at the same time period, in which the pH of the effluent would decrease slightly during the period of high adsorption efficiency and was almost the same as that of the inlet at the point of breakthrough.

Effect of backflushing with NaOH on the performance of Fe-PE for arsenic removal

The arsenic concentration to meet the discharging standards for arsenic in industrial wastewater was below 0.5 mg/L. Backflushing began while the arsenic concentration in the outlet of the adsorption column was greater than 0.5 mg/L. The velocity of flow for adsorption was 1 ml/s, the concentration of inlet wastewater was 813.07 mg/L, the diameter of the column was 50 mm and the length was 500 mm, and the LD of Fe-PE was 371 g/L. The direction of the water inlet and outlet during backflushing is opposite to that of the adsorption process. The end of the backflushing process using NaOH was determined by detecting the concentration of arsenic in the backflushing water. The effect of 0.1 M, 0.5 M, 1 M, 5 M, and 10 M of NaOH has been studied, and the results (data not shown) showed that 1 M of NaOH could have a better backflushing performance. So 1 M of NaOH was applied in the process of backflushing. Figure 4 shows the backflushing performance at different velocities of the flow. The results showed that applying NaOH for backflushing could desorb arsenic from Fe-PE because OH^- could compete with arsenate or arsenite ions to occupy the effective adsorption sites on Fe-PE, so that arsenic ions could enter into the solution. Usually, in the backflushing process, we hope that the flushing speed is not too slow, the efficiency of arsenic desorption is higher, and a small amount of desorption solution with a higher concentration of arsenic can be gathered. Figure 4 shows that the flow rate of NaOH had significant effects on backflushing. When the flow rate of NaOH was 0.1 ml/s, the arsenic concentration in the desorption solution could reach 698,231 mg/L. When the flow rate of NaOH was 0.5 ml/s, the arsenic concentration in the desorption solution could reach 783652 mg/L. When the flow rate of NaOH was 1 ml/s, a higher arsenic concentration in the desorption solution could reach 964,562 mg/L. Furthermore, when the arsenic concentration in the outlet was at the ppb level and the backflushing ended, the arsenic desorption solutions gathered in three groups were 1.2 L, 1.7 L, and 1.1 L with average arsenic concentrations of 6681.4, 4337.1, and 5469.0 mg/L, respectively, and the backflushing lasted for 200 min, 56 min, and 19 min, respectively. The total arsenic (in mass) eluted from the columns in three groups was 8017.7, 7373.1, and 6015.9 g, respectively. Compared with the total arsenic (in mass) adsorbed on Fe-PE in columns in three groups, which was 8049.4, 8046.1, and 7997.3 g, 99.6%, 91.6%, and 75.2% of arsenic could be eluted, respectively, from the

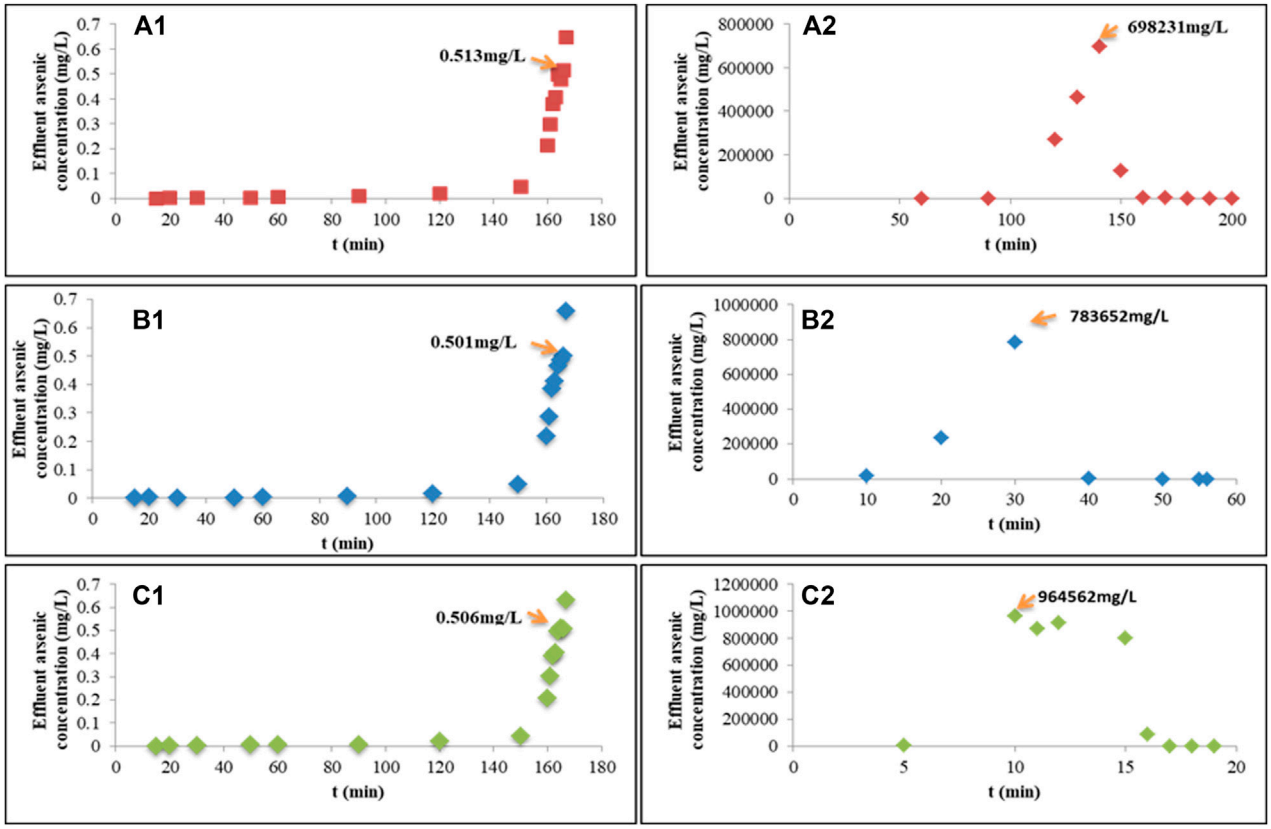

FIGURE 4
Adsorption breakthrough curves at the breakthrough point of 0.5 mg/L and backflushing curves using 1 M of NaOH with different velocities of the flow. **(A1)** Adsorption curves and **(A2)** the corresponding backflushing curve with an inlet velocity of flow = 0.1 ml/s; **(B1)** adsorption curves and **(B2)** the corresponding backflushing curve with an inlet velocity of flow = 0.5 ml/s; **(C1)** adsorption curves and **(C2)** the corresponding backflushing curve with an inlet velocity of flow = 1 ml/s.

columns in three groups. In order to judge which experimental conditions were more suitable for the backflushing, a further experiment was conducted to evaluate the adsorption performance for arsenic removal after backflushing the adsorption column. The operation process was as follows: the adsorption column after backflushing was used for the next adsorption experiment. Figure S5 shows the results of the adsorption performance before and after backflushing. Columns 1, 2, and 3 represented the experiments in three adsorption columns operated simultaneously. Under the same operating conditions, before backflushing, three columns reached the breakthrough point (0.5 mg/L) after 166 min. Then, after columns 1, 2, and 3 were backflushed using 1 M of NaOH at 0.1, 0.5, and 1 ml/s, respectively, the second adsorption began. Compared with the first adsorption, although the time taken to reach the adsorption breakthrough was earlier, the adsorption columns after backflushing were still effective for arsenic removal, indicating that backflushing with 1 M of NaOH could regenerate Fe-PE. Figure S5 also shows that with the lower flow rate, the time taken to reach the adsorption breakthrough in the column after backflushing was closer to the time in the first adsorption, which indicated that the lower flow rate of NaOH solution resulted in efficient desorption of arsenic from Fe-PE.

Treatment of gold-smelting wastewater by Fe-PE in the company on the pilot scale

Based on the overall consideration of the performance of Fe-PE for arsenic removal on the lab scale, a group of three adsorption columns in series controlled by valves was used for pilot experiments. Figure 5 shows the pilot scale schematic diagram of the adsorption and backflushing system. When pilot equipment started, columns 1 and 2 were used for adsorption, and column 3 was on standby. When column 1 was saturated, the adsorption was switched to columns 2 and 3, and column 1 was backflushed. Part of the treated water was used to flush the adsorption column after backflushing, in order to discharge the residual NaOH to avoid the effect of OH^- on the adsorption. Therefore, while switching the processes of adsorption and backflushing,

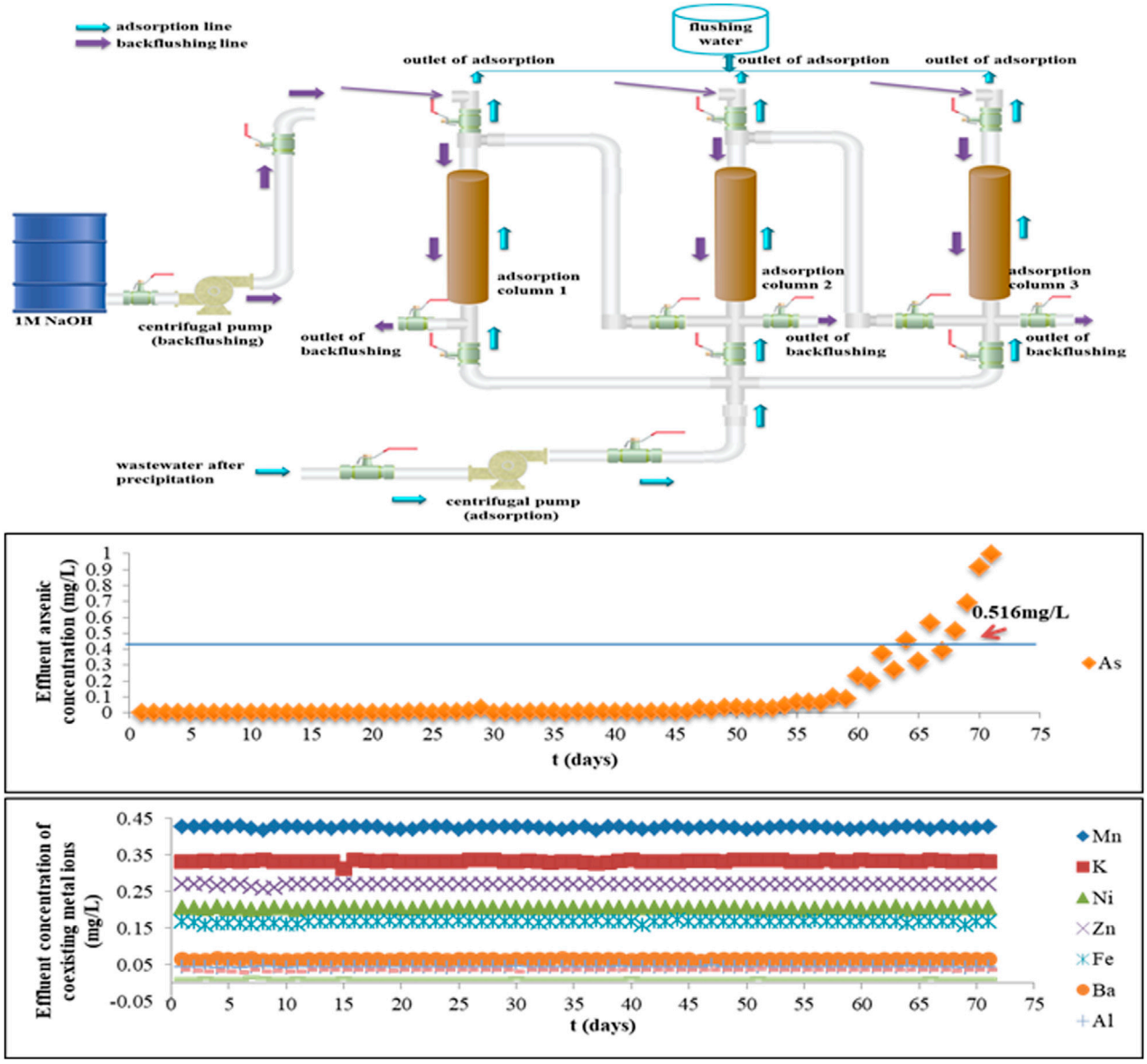

FIGURE 5
Pilot-scale schematic diagram and the performance evaluation of the adsorption and backflushing system for arsenic removal by Fe-PE.

continuous operation started. Samples were taken every 30 min, and samples taken during the day were tested at night, and samples taken at night were tested the next day.

After precipitation with lime, the temperature of wastewater was 36°C–38°C, pH was 8.62–8.89, and arsenic concentration was 813.07 mg/L. According to the adsorption capacity of Fe-PE for arsenic and the influence of flow rate and EBCT on the adsorption process, as well as the point of breakthrough (0.5 mg/L), the experimental parameters selected for the pilot-scale experiment were as follows: the diameter of the column was 300 mm and the length was 1500 mm, the LD of Fe-PE was 373 g/L, and the velocity of the flow for adsorption was 10 L/min to ensure that the EBCT was not lower than 10 min.

The performance of arsenic removal by Fe-PE from gold-smelting wastewater in the company on the pilot scale is shown in Figure 5. Simultaneously, the performance of pilot equipment to arsenic and other coexisting metal ions was evaluated. There was no significant change in the concentration of coexisting metal ions in the effluent, indicating that the adsorption column did not work with the removal of coexisting metal ions, and the adsorbent had good selective adsorption performance for arsenic in wastewater and also indicating that Fe-PE did not dissolve and release Fe ions in wastewater. Within 68 days of the operation of

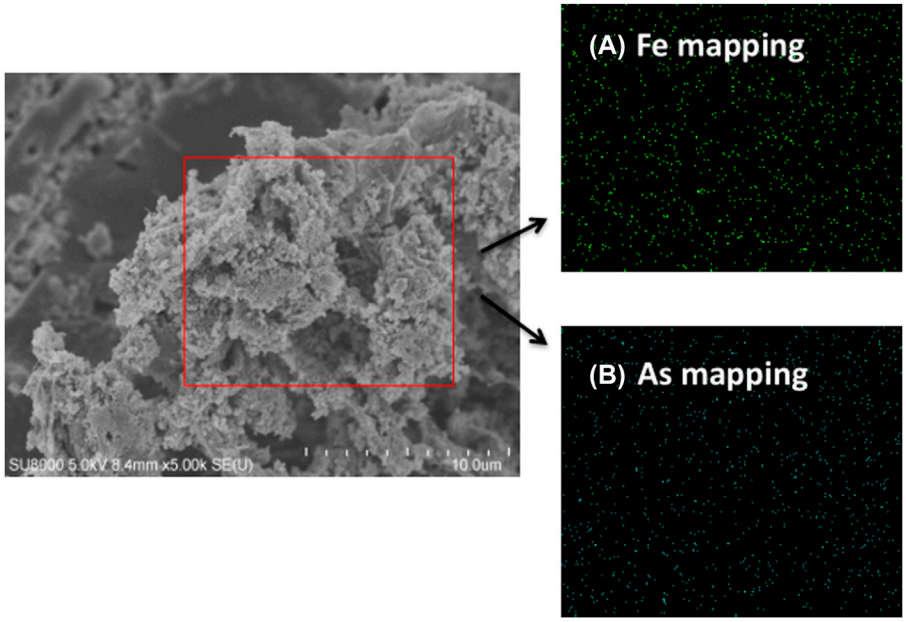

FIGURE 6
FESEM micrograph and elemental mapping of Fe-PE after adsorption. **(A)** Mapping of iron element and **(B)** mapping of arsenic element.

the adsorption column, the concentration of arsenic in the effluent was below 0.5 mg/L. The pH of effluent water was between 8.36 and 8.65 during the entire period of operation (data not shown). After the column adsorption, the concentration of SO_4^{2-}, NO_3^-, and CO_3^{2-} in effluent water was kept almost the same as before. Thus, it could be concluded that the adsorption column with Fe-PE could remove arsenic efficiently with an adequate EBCT of not less than 10 min in this experiment.

Characterizing the adsorbent Fe-PE after adsorption saturation

Figure 6 shows FESEM images of the surface of Fe-PE after arsenic adsorption in the wastewater, and the presence of small and uniform granular structures could be clearly seen. The elemental distribution on the surface of Fe-PE was further confirmed by elemental mapping. Figure 6 shows the mapping of the encircled portion, which showed the uniform distribution and presence of a substantial amount of iron and arsenic on the surface of Fe-PE. Elemental mapping of individual elements clearly indicated the higher content of iron and arsenic.

Conclusion

In this study, the process of purification and removal of arsenic in gold-smelting wastewater was conducted by column experiments with Fe-PE. Whether it was a laboratory test or a pilot test, Fe-PE had good purification performance for arsenic. Within 68 days of operating the adsorption column on the pilot scale, the concentration of arsenic in the effluent was below 0.5 mg/L, and there was no significant change in the concentration of coexisting metal ions in the effluent, indicating that the adsorbent had good selective adsorption performance for arsenic in wastewater. There was a high content of iron and arsenic on the surface of the saturated Fe-PE tested using an FESEM by elemental mapping of individual elements. Furthermore, compared with the conventional process, the promising environmental advantages of this work are the following: the higher concentration of arsenic in backwashed water obtained in this work deserves the refinement of arsenic compounds by precipitating or recrystallization. Fe-PE with arsenic adsorption could be pyrolyzed in which the ash could be leached by acid or alkali to refine the arsenic compound, and the exhaust gas with higher temperature could be used for the heater and could be purified using a biological filter or a functional fibrous filter. Therefore, it could be concluded from the present findings that arsenic could be removed from gold-smelting wastewater by using agricultural exhausted polyethylene film loaded with ferric lignin at an optimal empty bed contact time, and the adsorption and backflushing system on the pilot scale could make arsenic concentration possible to meet the discharge standards for arsenic (below 0.5 mg/L) in industrial wastewater, with no sludge being produced.

However, the pretreatment of cleaning the AMFR before modification and loading the Fe-PE into columns was a laborious and time-consuming job by manual operation, so the machinery promotion by automatic or semi-automatic operation may be suitable in the future.

Data availability statement

The original contributions presented in the study are included in the article/Supplementary Material; further inquiries can be directed to the corresponding author.

Author contributions

XZ: investigation, funding acquisition, conceptualization, formal analysis, and writing—original draft. KZ: conceptualization, formal analysis, and methodology. XS: conceptualization, formal analysis, and methodology. ZT: methodology and software. ZH: methodology and software. LZ: writing—review and editing, funding acquisition, and supervision.

Funding

This work was supported by the National Natural Science Foundation of China (grant number: 41907121).

Acknowledgments

All authors acknowledge the experimental site provided by the local gold-smelting company for conducting the pilot experiment.

Conflict of interest

The authors declare that the research was conducted in the absence of any commercial or financial relationships that could be construed as a potential conflict of interest.

Publisher's note

All claims expressed in this article are solely those of the authors and do not necessarily represent those of their affiliated organizations, or those of the publisher, the editors, and the reviewers. Any product that may be evaluated in this article, or claim that may be made by its manufacturer, is not guaranteed or endorsed by the publisher.

Supplementary material

The Supplementary Material for this article can be found online at: https://www.frontiersin.org/articles/10.3389/fchem.2022.1036726/full#supplementary-material

References

Anderson, C. G., and Twidwell, L. G. (2008). Hydrometallurgical processing of gold-bearing copper enargite concentrates. *Can. Metall. Q.* 47 (3), 337–346. doi:10.1179/cmq.2008.47.3.337

Antelo, J., Avena, M., Fiol, S., Lopez, R., and Arce, F. (2005). Effects of pH and ionic strength on the adsorption of phosphate and arsenate at the goethite-water interface. *J. Colloid Interface Sci.* 285 (2), 476–486. doi:10.1016/j.jcis.2004.12.032

Bluteau, M. C., and Demopoulos, G. P. (2007). The incongruent dissolution of scorodite - solubility, kinetics and mechanism. *Hydrometallurgy* 87 (3-4), 163–177. doi:10.1016/j.hydromet.2007.03.003

Caetano, M. L., Ciminelli, V. S. T., Rocha, S. D. F., Spitale, M. C., and Caldeira, C. L. (2009). Batch and continuous precipitation of scorodite from dilute industrial solutions. *Hydrometallurgy* 95 (1-2), 44–52. doi:10.1016/j.hydromet.2008.04.010

Cances, B., Juillot, F., Morin, G., Laperche, V., Alvarez, L., Proux, O., et al. (2005). XAS evidence of As(V) association with iron oxyhydroxides in a contaminated soil at a former arsenical pesticide processing plant. *Environ. Sci. Technol.* 39 (24), 9398–9405. doi:10.1021/es050920n

Capobianco, L., Di Caprio, F., Altimari, P., Astolfi, M. L., and Pagnanelli, F. (2020). Production of an iron-coated adsorbent for arsenic removal by hydrothermal carbonization of olive pomace: Effect of the feedwater pH. *J. Environ. Manage.* 273, 111164. doi:10.1016/j.jenvman.2020.111164

Celebi, A., Sengorur, B., and Klove, B. (2014). Human health risk assessment of dissolved metals in groundwater and surface waters in the Melen watershed, Turkey. *J. Environ. Sci. Health Part A* 49 (2), 153–161. doi:10.1080/10934529.2013.838842

Cheng, H. F., Hu, Y. N., Luo, J., Xu, B., and Zhao, J. F. (2009). Geochemical processes controlling fate and transport of arsenic in acid mine drainage (AMD) and natural systems. *J. Hazard. Mater.* 165 (1-3), 13–26. doi:10.1016/j.jhazmat.2008.10.070

Coudert, L., Bondu, R., Rakotonimaro, T. V., Rosa, E., Guittonny, M., and Neculita, C. M. (2020). Treatment of As-rich mine effluents and produced residues stability: Current knowledge and research priorities for gold mining. *J. Hazard. Mater.* 386, 121920. doi:10.1016/j.jhazmat.2019.121920

Cui, J., Du, Y. G., Xiao, H. X., Yi, Q. S., and Du, D. Y. (2014). A new process of continuous three-stage co-precipitation of arsenic with ferrous iron and lime. *Hydrometallurgy* 146, 169–174. doi:10.1016/j.hydromet.2014.03.012

De Klerk, R. J., Jia, Y. F., Daenzer, R., Gomez, M. A., and Demopoulos, G. P. (2012). Continuous circuit coprecipitation of arsenic(V) with ferric iron by lime neutralization: Process parameter effects on arsenic removal and precipitate quality. *Hydrometallurgy* 111, 65–72. doi:10.1016/j.hydromet.2011.10.004

De Klerk, R. J., Feldmann, T., Daenzer, R., and Demopoulos, G. P. (2015). Continuous circuit coprecipitation of arsenic(V) with ferric iron by lime neutralization: The effect of circuit staging, co-ions and equilibration pH on long-term arsenic retention. *Hydrometallurgy* 151, 42–50. doi:10.1016/j.hydromet.2014.11.003

Fan, Y. R., Zheng, C. L., Liv, H. X., He, C., Shen, Z. X., and Zhang, T. C. (2020). Effect of pH on the adsorption of arsenic(V) and antimony(V) by the black Checksoil in three systems: Performance and mechanism. *Ecotox Environ. Safe* 191, 110145. doi:10.1016/j.ecoenv.2019.110145

Feng, C., Aldrich, C., Eksteen, J. J., and Arrigan, D. W. M. (2017). Removal of arsenic from alkaline process waters of gold cyanidation by use of gamma-Fe2O3@ZrO2 nanosorbents. *Hydrometallurgy* 174, 71–77. doi:10.1016/j.hydromet.2017.09.007

Feng, C., Aldrich, C., Eksteen, J. J., and Arrigan, D. W. M. (2017). Removal of arsenic from alkaline process waters of gold cyanidation by use of Fe3O4@SiO2@TiO2 nanosorbents. *Miner. Eng.* 110, 40–46. doi:10.1016/j.mineng.2017.04.007

Ford, R. G. (2002). Rates of hydrous ferric oxide crystallization and the influence on coprecipitated arsenate. *Environ. Sci. Technol.* 36, 2459–2463. doi:10.1021/es015768d

Gomez, M. A., Becze, L., Cutler, J. N., and Demopoulos, G. P. (2011). Hydrothermal reaction chemistry and characterization of ferric arsenate phases precipitated from Fe-2(SO4)(3)-As2O5-H2SO4 solutions. *Hydrometallurgy* 107 (3-4), 74–90. doi:10.1016/j.hydromet.2011.01.007

Jia, Y. F., and Demopoulos, G. P. (2005). Adsorption of arsenate onto ferrihydrite from aqueous solution: Influence of media (sulfate vs nitrate), added gypsum, and pH alteration. *Environ. Sci. Technol.* 39 (24), 9523–9527. doi:10.1021/es051432i

Jia, Y. F., and Demopoulos, G. P. (2008). Coprecipitation of arsenate with iron(III) in aqueous sulfate media: Effect of time, lime as base and co-ions on arsenic retention. *Water Res.* 42 (3), 661–668. doi:10.1016/j.watres.2007.08.017

Jia, Y. F., Xu, L. Y., Fang, Z., and Demopoulos, G. P. (2006). Observation of surface precipitation of arsenate on ferrihydrite. *Environ. Sci. Technol.* 40 (10), 3248–3253. doi:10.1021/es051872+

Jia, Y. F., Xu, L. Y., Wang, X., and Demopoulos, G. P. (2007). Infrared spectroscopic and X-ray diffraction characterization of the nature of adsorbed arsenate on ferrihydrite. *Geochim. Cosmochim. Acta* 71 (7), 1643–1654. doi:10.1016/j.gca.2006.12.021

Lamm, S. H., and Kruse, M. B. (2005). Arsenic ingestion and bladder cancer mortality - what do the dose-response relationships suggest about. *Hum. Ecol. Risk Assess. Int. J.* 11 (2), 433–450. doi:10.1080/10807030590925678

Langmuir, D., Mahoney, J., and Rowson, J. (2006). Solubility products of amorphous ferric arsenate and crystalline scorodite (FeAsO4·2H2O) and their application to arsenic behavior in buried mine tailings. *Geochim. Cosmochim. Acta* 70 (12), 2942–2956. doi:10.1016/j.gca.2006.03.006

Lin, H. (2004). Treatment of arsenic-contaning acidic wastewater from gold metallurgical process. *ShiFaYeJin* 33 (06), 493–496.

Liu, Y., Yang, H. S., Li, Y. F., Yan, H. J., and Li, J. S. (2017). Modeling the effects of plastic film mulching on irrigated maize yield and water use efficiency in sub-humid Northeast China. *Int. J. Agric. Biol. Eng.* 10 (5), 69–84. doi:10.25165/j.ijabe.20171005.2799

MOA (2017). *The issuance of the action plan for recycling agricultural film*. China: Ministry of Agriculture of the People's Republic of China.

Nazari, A. M., Radzinski, R., and Ghahreman, A. (2017). Review of arsenic metallurgy: treatment of arsenical minerals and the immobilization of arsenic. *Hydrometallurgy* 174, 258–281. doi:10.1016/j.hydromet.2016.10.011

Neumann, A., Kaegi, R., Voegelin, A., Hussam, A., Munir, A. K. M., and Hug, S. J. (2013). Arsenic removal with composite iron matrix filters in Bangladesh: A field and laboratory study. *Environ. Sci. Technol.* 47 (9), 4544–4554. doi:10.1021/es305176x

Oishi, T., Yaguchi, M., Koyama, K., Tanaka, M., and Lee, J. C. (2008). Hydrometallurgical process for the recycling of copper using anodic oxidation of cuprous ammine complexes and flow-through electrolysis. *Electrochim. Acta* 53 (5), 2585–2592. doi:10.1016/j.electacta.2007.10.046

Rodriguez-Lado, L., Sun, G. F., Berg, M., Zhang, Q., Xue, H. B., Zheng, Q. M., et al. (2013). Groundwater arsenic contamination throughout China. *Science* 341 (6148), 866–868. doi:10.1126/science.1237484

Sekula, F. (2008). Hydrometallurgical method of processing the tetrahedrite concentrate from Maria Mine in Roznava, Slovakia. *Acta Montan Slovaca* 13 (1), 50–57.

Shakya, A. K., and Ghosh, P. K. (2018). Simultaneous removal of arsenic, iron and nitrate in an attached growth bioreactor to meet drinking water standards: Importance of sulphate and empty bed contact time. *J. Clean. Prod.* 186, 1011–1020. doi:10.1016/j.jclepro.2018.03.176

Weng, S. F. (2010). *Fourier transform infrared spectroscopy and Analysis*. China: Chemical Industry Press. Chapter 6-8.

Zhang, Q. Q., Ma, Z. R., Cai, Y. Y., Li, H. R., and Ying, G. G. (2021). Agricultural plastic pollution in China: Generation of plastic debris and emission of phthalic acid esters from agricultural films. *Environ. Sci. Technol.* 55 (18), 12459–12470. doi:10.1021/acs.est.1c04369

Zhang, X. Z., Zhao, G. H., Shi, X. B., Yuan, B. B., Zhao, K. J., Tian, Z. B., et al. (2022). Loading ferric lignin on polyethylene film and its influence on arsenic-polluted soil and growth of romaine lettuce plant. *Environ. Sci. Pollut. R.* 29 (30), 50362–50375. doi:10.1007/s11356-022-19490-7

frontiers | Frontiers in Chemistry

TYPE Original Research
PUBLISHED 01 November 2022
DOI 10.3389/fchem.2022.1050827

Check for updates

OPEN ACCESS

EDITED BY
Xiangning Bu,
China University of Mining and Technology, China

REVIEWED BY
Biswajit Debnath,
Jadavpur University, India
Wei Fan,
Xi'an Polytechnic University, China

*CORRESPONDENCE
Mingfei Xing,
mingfeixing@163.com

SPECIALTY SECTION
This article was submitted to Green and Sustainable Chemistry, a section of the journal Frontiers in Chemistry

RECEIVED 22 September 2022
ACCEPTED 20 October 2022
PUBLISHED 01 November 2022

CITATION
Li Z, Xing M, Zhao L, Li Z and Wang Y (2022), Recovery of carbon fiber-reinforced polymer waste using dimethylacetamide base on the resin swelling principle.
Front. Chem. 10:1050827.
doi: 10.3389/fchem.2022.1050827

COPYRIGHT
© 2022 Li, Xing, Zhao, Li and Wang. This is an open-access article distributed under the terms of the Creative Commons Attribution License (CC BY). The use, distribution or reproduction in other forums is permitted, provided the original author(s) and the copyright owner(s) are credited and that the original publication in this journal is cited, in accordance with accepted academic practice. No use, distribution or reproduction is permitted which does not comply with these terms.

Recovery of carbon fiber-reinforced polymer waste using dimethylacetamide base on the resin swelling principle

Zixin Li[1], Mingfei Xing[1]*, Li Zhao[1], Zhan Li[1] and Yaping Wang[2]

[1]Institute of Resource and Environment, Henan Polytechnic University, Jiaozuo, China, [2]School of Surveying and Land Information Engineering, Henan Polytechnic University, Jiaozuo, China

The mechanical recycling method of the carbon fiber-reinforced polymer (CFRP) has the advantages of simple process, less pollution and low cost, but only low utilization value of carbon fibers in powder or short fibers form can be obtained. To reduce the length and strength loss of the recycled carbon fibers, a novel and cost-effective dimethylacetamide (DMAC) swelling technique was developed to achieve rapid delamination of the CFRP laminates under mild conditions (120°C–160°C, 1 h). The corresponding swelling ratios and mass-loss rates of cured epoxy resin (CEP) were about 121.39%–157.39% and 0–0.69%, respectively. Excessive swelling of CEP in DMAC resulted in the cracking of the resin matrix between the adjacent carbon fiber layers. Thus the CFRP laminates were delaminated into soft single carbon fiber layers, which showed excellent cutting performance and reinforcing properties. The delamination products were cut into thin strips of different sizes and vacuum bag molded into new CFRP laminates. The flexural strength and tensile strength of the newly produced CFRP laminates were about 76.38%–90.98% and 94.61%–98.54% of the original CFRP laminates, respectively. More importantly, the chemical compositions of DMAC and CEP were unchanged during the physical swelling process. No organic pollutants (caused by resin degradation) were generated. And the used DMAC can be easily recycled by filtration. Therefore, this study provides a strategy for low-cost and high-valued recycling of CFRP waste.

KEYWORDS

waste carbon fiber-reinforced polymer, dimethylacetamide, resin swelling, delamination, recovery

1 Introduction

Advanced carbon fiber-reinforced polymer (CFRP) composites can be widely applied to new energy equipment (e.g., high-pressure vessel and wind turbine), lightweight transport facilities (aircraft and vehicle), and sporting tools (fishing rod and tennis racket) because of their low specific gravity, high strength, corrosion resistance, and good thermal stability (Lee et al., 2020; Zhang et al., 2020; Sun et al., 2022). However, numerous waste CFRP composites may be produced during the production and utilization processes. The

generation of CFRP wastes reached 62000 tons in 2020 (Wei and Hadigheh, 2022). And the global waste CFRP composite output is estimated to be around nearly 500000 tons by 2050 (Lefeuvre et al., 2017). Improper disposal of CFRP waste may take up a substantial portion of land and contaminate the environment. Carbon fiber manufacturing is an example of a high-consumption industry (Dér et al., 2021). Approximately 198–595 MJ energy is consumed in the production of 1 kg of raw carbon fibers, while the greenhouse gas emissions are 31 kg carbon dioxide equivalent (Li et al., 2016; Meng et al., 2018). Recycling waste CFRP can effectively reduce energy consumption and carbon emission, lower the CFRP preparation cost, and promote the application in people's daily lives.

Cured epoxy resins (CEP), which are typical thermosetting resins, are commonly used as CFRP structure matrices because they provide exceptional mechanical properties and corrosion-resistance to CFRP (Mustata and Tudorachi, 2017; Hanaoka et al., 2021; Wei et al., 2022). However, the excellent thermal and chemical stability of CEP makes the recycling of long and high-modulus carbon fibers from waste CFRP difficult (Hao et al., 2020). CFRP has been recycled *via* thermal processing (Oliveux et al., 2015; Hadigheh et al., 2021; Guo et al., 2022), chemical recycling (Kim et al., 2017; Kim et al., 2019; La Rosa et al., 2021; Hanaoka et al., 2022), and mechanical recycling (Li et al., 2016; Giorgini et al., 2020). The thermal recycling process is simple, but the high pyrolysis temperature (400°C–1000°C) results in high energy consumption and tensile strength loss of the recycled carbon fibers (about 15%–50%) (Zhu et al., 2019; Lu et al., 2022). Accordingly, some catalysts (Wu et al., 2019; Wu et al., 2022) (such as $ZnCl_2$ and KCl) have been applied to reduce the pyrolysis temperature to ≤ 400°C and the tensile strength loss to ≤ 5%. Several solvents (strong acid, base and oxidant) with unique properties and catalysis have been used to degrade the resin matrix of CFRP by chemical recycling (Jiang et al., 2017; Liu et al., 2021; Huang et al., 2022). The reaction conditions of chemical recycling are relatively moderate, which aids in reducing the tensile strength loss of the recovered carbon fibers (Yu et al., 2016; Zhao et al., 2022). However, chemical methods also have disadvantages that must be addressed, such as large reagent consumption, harsh reaction conditions, and high equipment cost. Mechanical recovery methods can achieve the dissociation of resin matrix and carbon fiber by comminution or grinding process (Palmer et al., 2009). The processing cost and environmental impact of mechanical methods are lower than the traditional thermal processing and chemical recycling (Shuaib and Mativenga, 2016; Meng et al., 2017). However, soft carbon fibers are tightly bonded together by brittle CEP of glassy state in CFRP (Moosburger-Will et al., 2013; Tam et al., 2019). During the mechanical dissociation process of CFRP, long carbon fibers covered with a sheet of brittle CEP are easily broken into powder or staple fibers (Fonseca et al., 2020; Butenegro et al., 2021). The significant loss of carbon fiber length and strength (Gopalraj and Kärki, 2020) greatly limits the industrial application of mechanical recycling (Meng et al., 2018). Thus, the loss of carbon fiber strength and length must be mitigated to improve the reinforcing properties and recovery value of mechanical recovery products.

CEP is insoluble in common solvents because of its cross-linking structure. Nonetheless, CEP could swell in some organic solvents. The resin swelling phenomenon could benefit the penetration of catalysts so as to accelerate the reaction of degradation (Wang et al., 2015; Xing et al., 2021). In our previous study (Xing et al., 2021), an acetic acid swelling technology was developed as a pretreatment process of mechanical methods based on the theory of resin swelling. When CEP is fully swollen, its mechanical properties are significantly changed, transitioning from a glass state (brittle solid) to a highly elastic state (similar to rubber). Carbon fiber layers that contained in the CFRP laminates were delaminated from each other in acetic acid medium (160°C–220°C, 1 h). The soft delamination products were cut into various required shapes and hot pressed into new CFRP laminates. However, the acetic acid swelling technology also had some disadvantages: 1) the swelling temperature was higher which need to be further reduced to save energy. 2) Beside swelling effect, acetic acid also has a certain catalytic degradation effect on the resin. About 13.11%–23.33% of resin was degraded during the acetic acid swelling process result in the generation of many harmful organic pollutants (phenol and isopropyl-phenol, etc.). The new generated organic pollutants contained in the used acetic acid solution was also not conducive to the reuse of acetic acid solution.

In order to solve above problems, the swelling agent of acetic acid was replaced by DMAC which exhibited a better swelling effect on CEP. The delaminated temperature of CFRP could be obviously reduced from 160°C–220°C to 120°C–160°C in the DMAC swelling medium, and the resin was hardly degraded with less pollution in the recovery process (resin mass-loss rates were less than 0.70%). The flexural strength of the newly produced laminates (prepared by vacuum bag molding method) was 76.38%–90.98% of the original CFRP laminates. Accordingly, the energy consumption and environmental impact caused by resin degradation could be further reduced by the mild DMAC swelling method. In addition, DMAC has the characteristics of high thermal stability, and low corrosivity (Verma et al., 2017; Zhu et al., 2020). These features are conducive to recycling DMAC and reducing the corrosion of reaction equipment. Therefore, DMAC swelling technology was used in this study for low-cost and high-valued recycling of CFRP waste. The primary goals of this research are to 1) analyze the delamination properties of CFRP laminates in DMAC swelling media, 2) reveal the delamination process and mechanism of CFRP laminates in DMAC, 3) investigate the chemical composition changes of CEP and DMAC during the swelling process, and 4) examine the mechanical properties of the swelling CFRP laminates and the newly produced CFRP laminates.

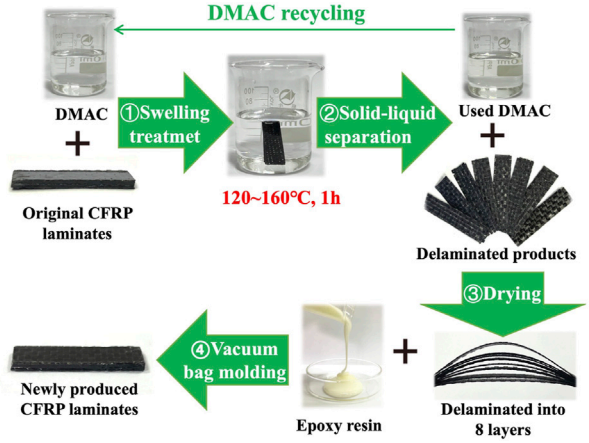

FIGURE 1
Delamination and recycling of the CFRP laminates by DMAC swelling technique.

2 Experimental section

2.1 Materials

The prepreg was WP-3011 (Weihai Guangwei Co., Ltd. China), a fabric composed of 60 wt% carbon fiber impregnated with 40 wt% uncured 6,508 epoxy resin as the matrix resin. The curing agent of 6,508 epoxy resin was dicyandiamide. The organic solvents used in this study were all analytically pure: DMAC (SCRC, ≥99.5%), DMSO (SCRC, ≥99.5%), DMF (SCRC, ≥99.5%), acetic acid (SCRC, ≥99.5%), ethyl alcohol (SCRC, ≥99.5%), dichloromethane (Kermel, ≥99.5%). KBr (Kermel, ≥99.9%).

2.2 Preparation of a carbon fiber-reinforced polymer laminate

An original CFRP laminate (8 cm × 10 cm×0.2 cm) was prepared from eight pieces of prepregs (8 cm × 10 cm×0.02 cm) by vacuum bag molding process. The curing temperature, curing time, and system pressure of the vacuum bag molding process were 120°C, 3 h, and 100 Pa, respectively.

2.3 Preparation of cured epoxy resin cube

CEP cube (1 cm × 1 cm×1 cm) was prepared for the better reveal the swelling effect on the resin volume expansion degree and resin cracking process. The liquid 6,508 epoxy resin was poured into a 1 cm cube silica gel mold. The silica gel mold was then placed into the curing oven for 3 h at 120°C. After the curing treatment, the solid CEP cube was removed from the silica gel mold.

2.4 Swelling recovery procedure of the carbon fiber-reinforced polymer laminates in dimethylacetamide

Figure 1 displays the main swelling recovery process of the CFRP laminates in DMAC media. First, a CFRP laminate (2 g) or a *CEP cube* (0.5 g) was placed in a Teflon bottle (100 ml). Then, 45 ml of DMAC was placed into the Teflon bottle to ensure that the CFRP laminate or CEP cube was immersed in the DMAC solution. Subsequently, the Teflon bottle was heated in a high temperature oven at 80°C–160°C (with an interval temperature of 20°C) and held for 0.5, 1, 2, 3, 4, and 6 h. The boiling point of DMAC at atmospheric pressure is 166.1°C, and the maximum swelling temperature was limited to 160°C. Finally, the Teflon bottle removed from the oven and allowed to cool to room temperature. The solid products (CFRP laminate or *CEP cube*) were collected by using a filtering method and dried at 105°C for further use.

The CFRP laminates were delaminated into eight pieces of soft carbon fiber layers in DMAC at 120–160°C within 1 h. Approximately 1 g of uncured epoxy resin was brushed on the surface of the delaminated products. Then, the delaminated products were vacuum bag molded into new CFRP laminates (the same curing condition as the original CFRP laminates). A part of the redundant liquid epoxy resin was expelled from the delaminated products during the vacuum bag molding process.

2.5 Dimethylacetamide recycling process

After the swelling treatment, the used DMAC obtained after solid–liquid separation was filtered with a filter pump (with a pumping speed of 30 L/min and a membrane diameter of 0.45 μm). The filtered DMAC could be recycled for CFRP swelling treatment.

2.6 Analysis

The resin swelling ratio was calculated using Eq. 1, while the resin mass-loss rate was computed using Eq. 2.

$$S(\%) = \frac{M_1 - M_2}{M_0{}^{*}M_r - (M_0 - M_2)} \times 100\% \quad (1)$$

$$D(\%) = \frac{M_0 - M_2}{M_0{}^{*}M_r} \times 100\% \quad (2)$$

where M_0 denotes the original CFRP laminate weight, M_1 denotes the weight of the swelling CFRP laminate (contains a certain amount of DMAC), M_2 represents the weight of the swelling CFRP laminate after drying treatment, and M_r represents the epoxy resin mass fraction of the original CFRP.

A three-point bending test was carried out for the measurement of the sample flexural strength at a loading speed of 0.2 cm/min, as shown in Eq. 3.

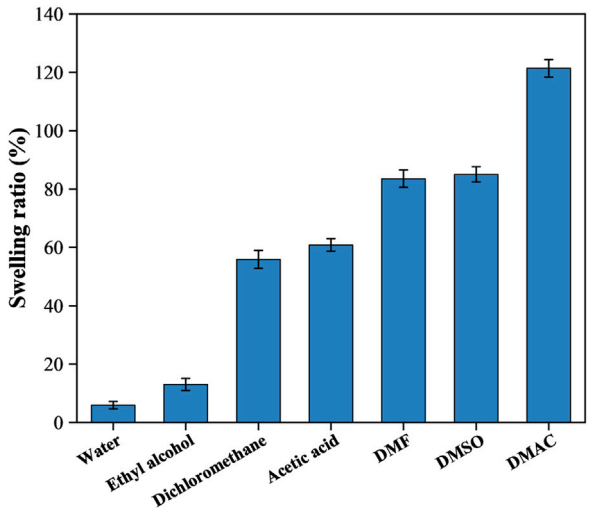

FIGURE 2
Swelling behavior of CFRP in various solvents at 120°C for 1 h.

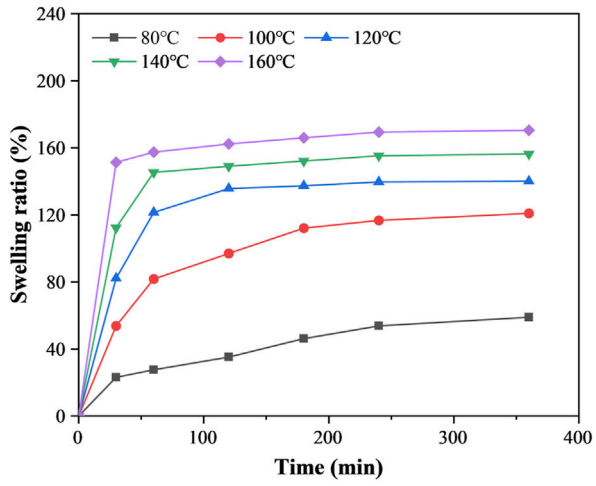

FIGURE 3
Swelling curves of CFRP in DMAC at different temperatures.

$$\sigma = \frac{3PL}{2bh^2} \tag{3}$$

where P denotes the load (N) measured; L denotes the span (mm); and h and b represent the thickness and width (mm), respectively.

A universal testing machine was used for the measurement of sample tensile strength at a loading speed of 1 cm/min, as shown in Eq. 4.

$$\sigma = \frac{F_b}{S_o} \tag{4}$$

where F_b is the maximum force sustained when the swelling product is broken (N), while S_o is the original cross-sectional area of the CFRP laminate (mm^2).

A scanning electron microscope (SEM, Zeiss Supra 40, Germany) was utilized to observe the surface microstructure of the sample. Fourier transform infrared spectroscopy (FTIR, Shimadzu AIM-9000, Japan) was adopted to study the main chemical functional groups of the resin.

3 Results and discussion

3.1 Swelling properties of the carbon fiber-reinforced polymer in various solvents

The swelling properties of the CFRP in diverse solvents (120°C, 1 h) are shown in Figure 2. The swelling ability of water and ethyl alcohol is relatively low, and the swelling ratios were only about 5.96% and 13.08%, respectively. CFRP swelled the most in DMAC, with a swelling ratio of 121.39%. The swelling ratios of dichloromethane, acetic acid, DMF, and DMSO were 55.89%, 60.85%, 83.57%, and 85.02%, respectively. The selection of polymer swelling media was primarily based on the principle of similar polarity and solubility parameters (Zhu et al., 2018). Epoxy resin is a polar substance that contains several polar groups. DMF, DMSO, and DMAC are strongly aprotic polar solvents with an excellent swelling effect on epoxy resin (Verma et al., 2016; Tatariants et al., 2018; Han et al., 2019). Meanwhile, the solubility parameters of epoxy resin, DMF, DMSO, and DMAC are 19.85–20.46, 24.86, 26.68, and 22.77 $MPa^{1/2}$, respectively (Hansen, 2007). The solubility parameters of DMAC and epoxy resin were close in value among the three solvents. Thus, DMAC was selected as the sweller in this study because it shows an excellent swelling effect on CEP. In addition, DMAC is an important solvent which is widely used in pharmaceutical, chemical applications and organic synthesis for its excellent thermal stability and low corrosivity. (Le Bras and Muzart, 2017; Gao et al., 2021).

Figure 3 shows the swelling curves of CFRP in DMAC at different temperatures. The swelling ratio of CFRP increased along with the temperature enhancement and the time extension. A substantial amount of time was required to reach the swelling equilibrium at a low temperature (≤100°C). The swelling ratio at 100°C was only 120.93% when the swelling time was 6 h. However, the swelling ratio rapidly increased in the first hour and gradually reached the swelling equilibrium above 120°C. The swelling ratios were about 121.39%–157.39% at 120°C–160°C within 1 h. Meanwhile, the mass-loss rates of resin at 120°C, 140°C, and 160°C within 1 h were only 0%, 0.03% and 0.69%, respectively. This phenomenon indicated that CEP was stable in mild DMAC swelling media.

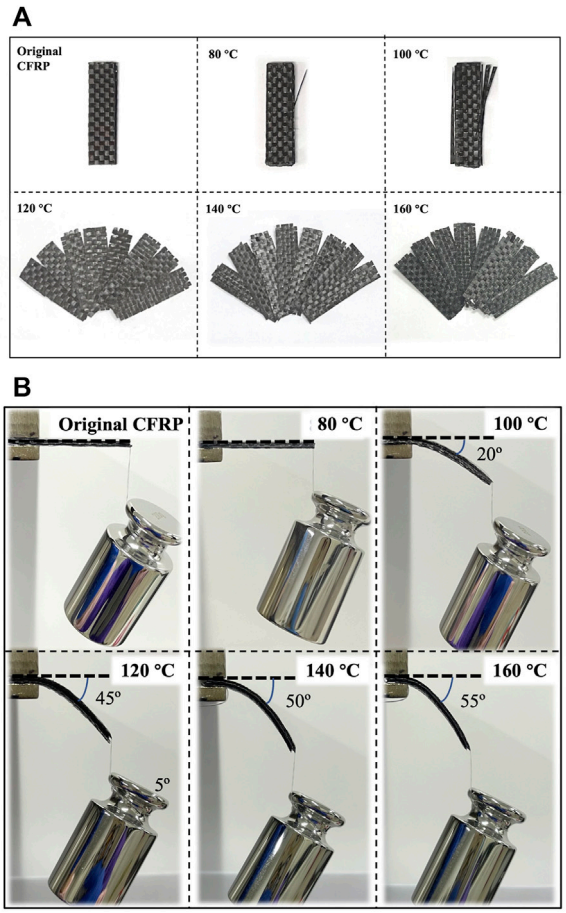

FIGURE 4
(A) CFRP laminates treated in DMAC at 80°C–160°C for 1 h and **(B)** corresponding load deformation comparison.

3.2 Delaminating characteristic of carbon fiber-reinforced polymer in dimethylacetamide

Figure 4A presents the images of the CFRP laminates treated in DMAC at 80°C–160°C for 1 h. Figure 4B shows the corresponding load–deformation comparison. Eight layers of carbon fibers were closely bonded together in the untreated CFRP laminates, and the stiff CFRP had no bending deformation under the load action. Part of the CFRP layers located on the CFRP surface began to peel off at 100°C, and the CFRP laminate was slightly bent under the load action. Above 120°C, the CFRP laminate began to delaminate into multiple single carbon fiber layers. Meanwhile, the CFRP laminate was bent under the load action. The experimental results indicated that the glassy state (brittle solid) of CEP could be changed into a highly elastic form (like rubber) by the CEP swelling phenomenon, which is helpful in improving the mechanical cutting performance of the CFRP laminates. The cross-linked segment movement of the glassy state CEP is frozen at low temperature, and only small-sized vibration and short-range rotational motion with low energy exist (Mijović and Zhang, 2004). The CEP obtained enough thermal energy and absorbed substantial DMAC as the swelling temperature increased, which gradually strengthened the interchain motion (Adamson, 1980). Therefore, the soft single carbon fiber layer could be cut into various required shapes.

The surface morphology of the CFRP laminates treated at different temperatures is shown in Figure 5. Figure 5A represents the micrographs of the original CFRP laminates. The surface of the untreated CFRP laminates was smooth and devoid of cracks. When the temperature was increased to 80°C–100°C, the volume of resin gradually expanded, resulting in the formation of many cracks at the intersection of longitude and latitude of the carbon fiber fabric, as shown in Figures 5B,C. These cracks might reduce the bonding effect between carbon fibers and influence the mechanical properties of the CFRP laminates. At 140°C, considerable CEP fell off the CFRP surface, and the carbon fiber layer was exposed, as shown in Figure 5D. The delamination phenomenon of CFRP was mainly attributable to the volume expansion and fragmentation of resin that distributed on the surface of the adjacent carbon fiber layers. Thus, sandwich model was used to approximate simulation of the swelling and delamination process of CFRP in DMAC (as shown in Figure 6).

3.3 Potential rapid swelling process and mechanism of cured epoxy resin in dimethylacetamide

Figure 7 shows the swelling products of the CEP cube obtained at different temperatures (80°C–160°C) when the swelling time and solid–liquid mass ratio of CEP/DMAC were fixed at 1 h and 1:25, respectively. The original CEP was a light yellow cube with a length of 10 mm. After the swelling treatment in DMAC at 80°C, only the CEP located on the cube surface cracked into small pieces and peeled off from the cube surface. This phenomenon confirmed that CEP could be fully swelled in DMAC under mild conditions. The volume expansion of resin was increased at a higher temperature, and the resin matrix eventually cracked into small pieces at 160°C. In addition, DMAC could quickly penetrate the inner part of the CEP cube along the cracks to further accelerate the resin swelling process.

Figure 8 shows the FTIR spectra of the CEP cube treated under different temperatures (80–160°C, 1 h). The peak intensity of the C–H stretch (830 cm^{-1}), C–O–C stretch (1031 and 1246 cm^{-1}), C–N stretch (1420 cm^{-1}), C–C stretch (1508 cm^{-1}), and C=C stretch (1607 cm^{-1}) had no noticeable change with the increment of the swelling temperature (Guelachvili and Rao, 1986). This phenomenon indicated that the fragmentation of the resin matrix in DMAC was mainly

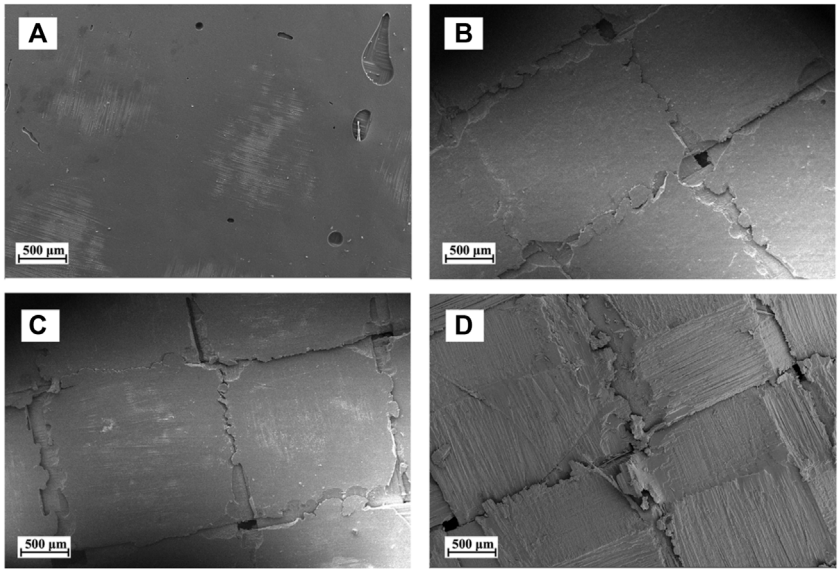

FIGURE 5
Surface morphology of the CFRP laminates treated under different temperatures: **(A)** original CFRP laminates, **(B)** 80°C, **(C)** 100°C, and **(D)** 140°C.

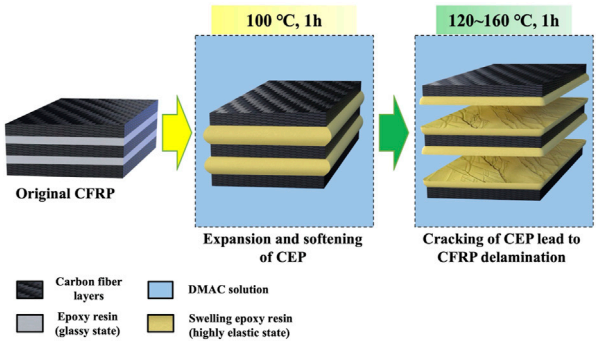

FIGURE 6
Possible delamination process of CFRP in DMAC.

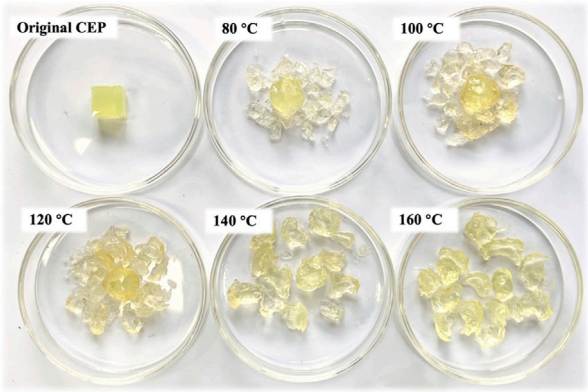

FIGURE 7
Images of the swelling products of the CEP cube treated at different temperatures.

attributed to the excessive expansion of the resin volume rather than the chemical degradation of CEP.

DMAC is a strongly nonprotonic polar solvent with an amide bond (–CO–NH–) in its molecular structure that can form hydrogen bonding interactions with numerous polar molecules (Verma et al., 2017; Pei et al., 2021). Meanwhile, epoxy resin as a polar material also contains many polar groups. The hydrogen bond acceptors of the resin segment include the unreacted epoxy group in the network structure, the O atom in the ether bond, the N atom on the tertiary amine, and the OH group. Specifically, the molecular structures of DMAC and epoxy resin (dicyandiamide cured bisphenol A epoxy resin) that can be used as hydrogen donors include the unreacted OH group of the resin network structure and the H atom of–CH_3 contained in DMAC. The H acceptors include the O atom of C=O contained in DMAC, the N atom of DMAC, the On atom in the ether bond of the resin, and the N atom on tertiary amine atoms. The possible forms of hydrogen bond between CEP and DMAC are shown in Figure 9 (Zhu et al., 2013; Verma et al., 2017). The swelling mechanism can be explained by the hydrogen bonds present in the swelling system. However, the specific mechanism needs further study.

10.3389/fchem.2022.1050827

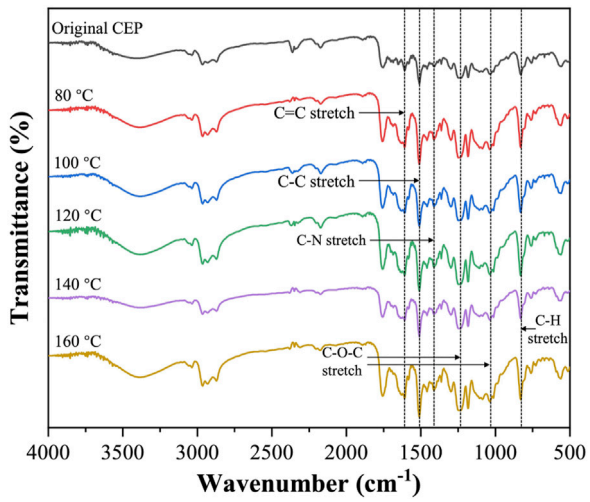

FIGURE 8
FTIR spectra of original CEP and swelling CEP treated at 80°C, 100°C, 120°C, 140°C, and 160°C.

3.4 Mechanical properties of the carbon fiber-reinforced polymer swelling products

Figure 10A displays the flexural strength of the swelled CFRP laminates after drying treatment. The original CFRP laminates had a high flexural strength (about 604.61 MPa). After the swelling treatment, the flexural strength quickly reduced from 513.07 MPa to 306.99 MPa as the swelling temperature rose from 80°C to 100°C. Above 120°C, eight layer of carbon fiber fabrics that contained in the CFRP laminates were delaminated from each other, and the flexural strength was significantly reduced to less than 22 MPa. The reduction of flexural strength was mainly attributed to the fragmentation phenomenon of CEP, which could reduce the adhesion degree between the adjacent carbon fiber fabric. Figure 10B shows the tensile strength of the single-layer CFRP treated at different temperature. The tensile strength of the single-layer CFRP was slightly decreased from 752.91 MPa MPa to 739.59 MPa as the swelling temperature rose from 80°C to 160°C. And the tensile strength was 97.44%–99.19% of the original single-layer CFRP (759.05 MPa). Accordingly, the mild swelling system has a minimal influence on the mechanical properties of the carbon fibers.

3.5 Mechanical properties of the newly produced carbon fiber-reinforced polymer laminates

The dried delamination products were vacuum bag molded again to create new CFRP laminates. The flexural strength and tensile strength of the newly produced CFRP laminates were shown in Figure 11. The newly produced CFRP laminates' flexural strength was approximately 76.38%–90.98% that of the untreated CFRP laminates as shown in Figure 11A. Then the flexural strength increased

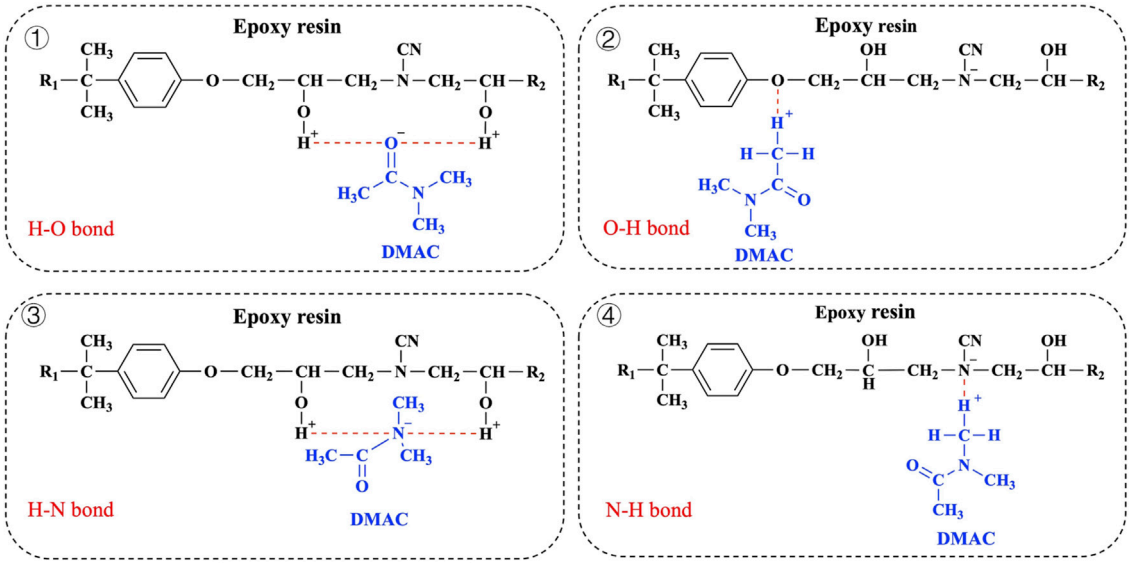

FIGURE 9
Possible swelling mechanism of CEP in DMAC media.

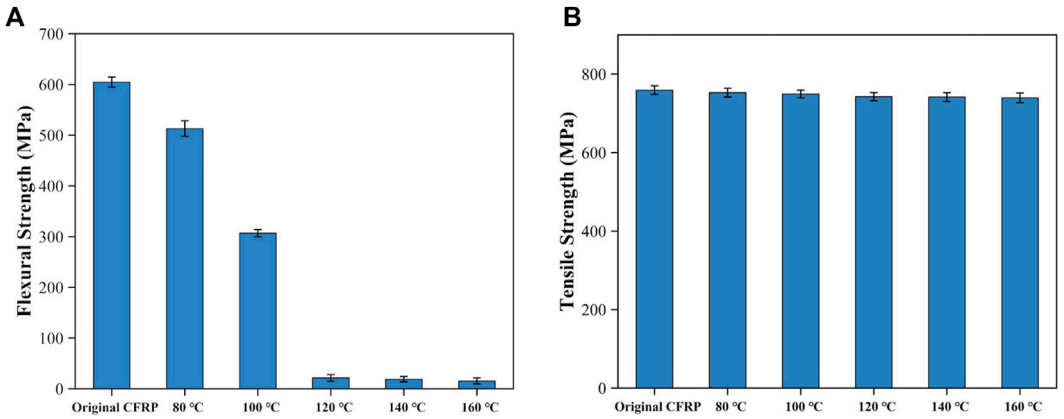

FIGURE 10
Mechanical properties of the swelling products: **(A)** flexural strength and **(B)** tensile strength.

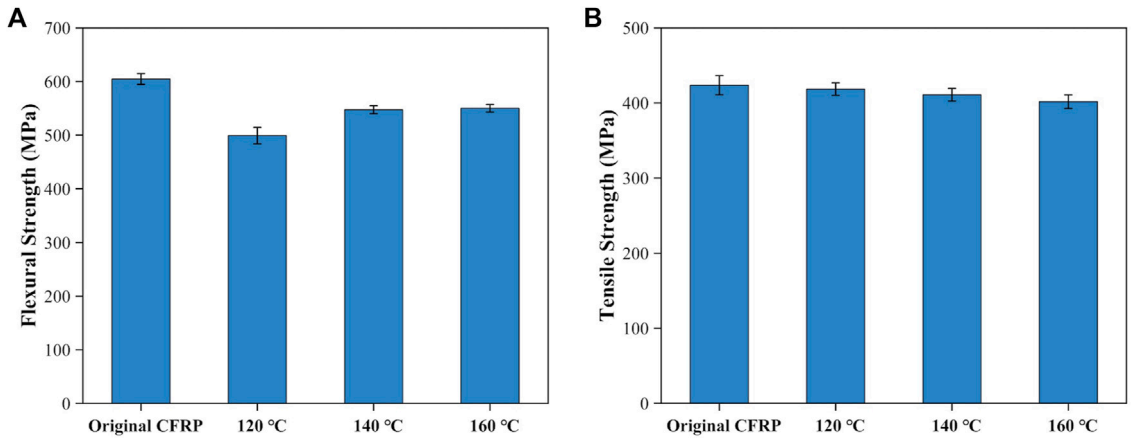

FIGURE 11
Mechanical properties of the newly produced CFRP laminates: **(A)** flexural strength and **(B)** tensile strength.

from 499.21 MPa to 547.41 MPa as swelling temperatures increased from 120°C to 140°C. Finally, the flexural strength reached the maximum value of 550.07 MPa at 160°C. The possible reason was that the degree of resin swelling increased under elevated swelling temperature leading to the increment of cracks' size and number and more resin was fell off from the carbon fiber layer's surface. Under the vacuum condition, the infusion of the liquid epoxy resins could fill these large cracks and tightly bonded to the surface of the carbon fiber layer to revive the CFRP laminates' flexural strength (Xing et al., 2021). Figure 11B shows the tensile strength of the new produced CFRP laminates. The tensile strength of the newly produced CFRP laminates was 401.78 MPa–418.49 MPa, which was 94.61%–98.54% of the untreated CFRP laminates (424.68 MPa). This phenomenon suggested that the effect of DMAC swelling treatment on the mechanical properties of carbon fiber was insignificant.

The soft delaminated products could be easily cut into thin slices of various shapes in the practical application, as shown in Figure 12. Furthermore, the shear products could be prepared into different CFRP products *via* a vacuum bag molding process. The newly produced CFRP products could be used for general load-bearing components, such as carbon fiber seats, bicycle wheels, and fishing platforms. However, the mechanical properties of the newly produced products were also related to the size of the shear product, the kind and amount of the resin matrix, and the molding type. In addition, CEP contained in CFRP was not degraded during the swelling process and was transferred into the newly produced CFRP products. Thus, the DMAC

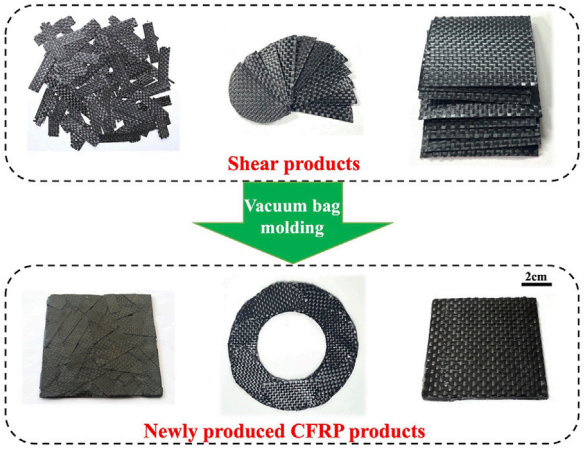

FIGURE 12
Different utilization methods for the CFRP delamination products.

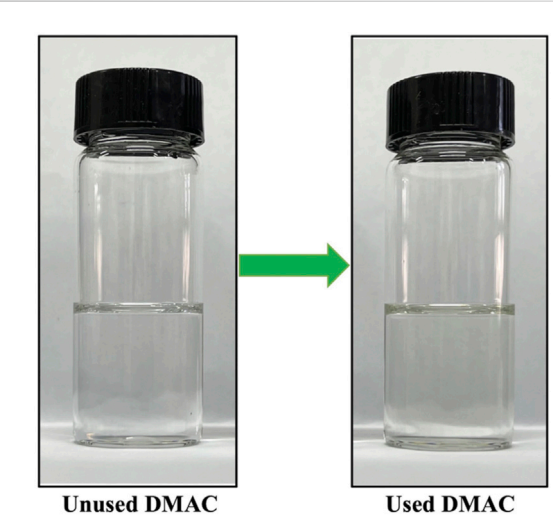

FIGURE 13
Images of the unused and used DMAC (filtrated).

swelling technique could realize the overall utilization of waste CFRP.

3.6 Dimethylacetamide recycling

Figures 13, 14 show the corresponding FTIR spectra of the unused and used DMAC (filtrated). No significant change can be observed in the DMAC color before and after swelling treatment in Figure 13. DMAC contains several chemical bonds, such as C–H bond (3000–2850 cm^{-1}), C–N bond

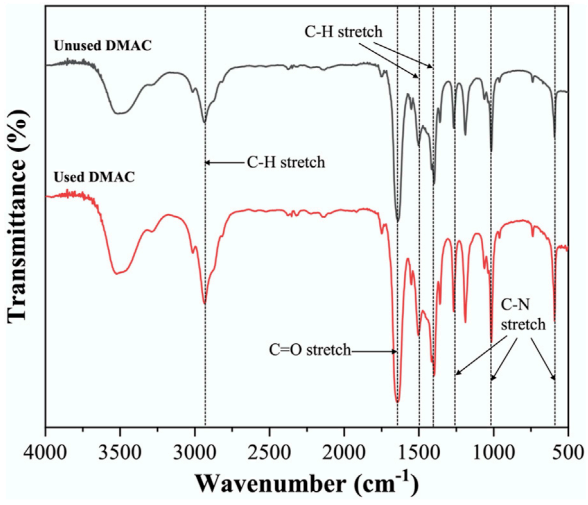

FIGURE 14
FTIR spectra of the unused DMAC and used DMAC (filtrated).

(1250, 1020, and 657 cm^{-1}), and C=O bond (1670 cm^{-1}) (Guelachvili and Rao, 1986; Verma et al., 2017). No significant change was observed between the FTIR spectra of the unused and used DMAC. The FTIR result validated that DMAC has good thermal and chemical stability under mild swelling conditions. The recycling of DMAC can be achieved by simple filtration using the Millipore filter (Nylon 66, 0.22 μm), which is conducive to reducing the treatment cost and environmental pollution. In addition, DMAC is flammable liquid and toxic gases may be generated when burning. Thus, temperature control (<160°C) is required in the actual production process to prevent combustion or thermal decomposition of DMAC. And other environmentally-friendly swelling solvent should be explored in future research.

4 Conclusion

The DMAC swelling technology could realize rapid softening and delamination of the CFRP laminates under mild conditions (120°C–160°C, 1 h) due to the excellent swelling effect of DMAC on CEP. The corresponding swelling ratios and mass-loss rates of CEP were about 121.39%–157.39% and 0–0.69%, respectively. The overexpansion of the CEP volume resulted in the fragmentation of CEP between the adjacent carbon fiber layers of CFRP, and CFRP was delaminated into soft single layers. The delaminated product's flexural strength was only about 2.55%–3.55% of the original CFRP laminates, while the tensile strength minimally decreased (≥97.44%). The obtained soft carbon fiber layer could be easily cut into various required shapes. Then, the shear products were dried and mixed with a small amount of

liquid epoxy resin to obtain a new CFRP laminate by using a vacuum bag molding process. The cracks in the shear products can be filled with epoxy resin under the vacuum environment. Thus, the flexural strength and tensile strength of the newly produced CFRP laminates were about 76.38%–90.98% and 94.61%–98.54% of the original CFRP laminates, respectively. After the swelling process, the chemical composition of DMAC was unchanged, which was conducive to realizing the recycling of DMAC. Therefore, this study may provide a novel and cost-effective approach for CFRP recycling.

Data availability statement

The original contributions presented in the study are included in the article/supplementary material, further inquiries can be directed to the corresponding author.

Author contributions

ZL: Writing- Original draft, Methodology, Software. MX: Writing- Reviewing and Editing, Formal analysis, Funding acquisition. LZ: Resources, Validation. ZL: Investigation, Visualization. YW: Conceptualization.

Funding

This research was financed by China's National Natural Science Funds (51508165). The Science and Technology Research Key Project for development and promotion (212102310061, 212102310502). Outstanding Youth Fund Project of Henan Polytechnic University (J2022-2). Foundation of Key Scientific Research Projects of Henan Colleges and Universities in 2022(22B610002).

Conflict of interest

The authors declare that the research was conducted in the absence of any commercial or financial relationships that could be construed as a potential conflict of interest.

Publisher's note

All claims expressed in this article are solely those of the authors and do not necessarily represent those of their affiliated organizations, or those of the publisher, the editors and the reviewers. Any product that may be evaluated in this article, or claim that may be made by its manufacturer, is not guaranteed or endorsed by the publisher.

References

Adamson, M. J. (1980). Thermal expansion and swelling of cured epoxy resin used in graphite/epoxy composite materials. *J. Mat. Sci.* 15, 1736–1745. doi:10.1007/BF00550593

Butenegro, J. A., Bahrami, M., Abenojar, J., and Martínez, M. Á. (2021). Recent progress in carbon fiber reinforced polymers recycling: A review of recycling methods and reuse of carbon fibers. *Materials* 14, 6401. doi:10.3390/ma14216401

Dér, A., Dilger, N., Kaluza, A., Creighton, C., Kara, S., Varley, R., et al. (2021). Modelling and analysis of the energy intensity in polyacrylonitrile (PAN) precursor and carbon fibre manufacturing. *J. Clean. Prod.* 303, 127105. doi:10.1016/j.jclepro.2021.127105

Fonseca, E., Demétrio da Silva, V., Klitzke, J. S., Schrekker, H. S., and Amico, S. C. (2020). Imidazolium ionic liquids as fracture toughening agents in DGEBA-TETA epoxy resin. *Polym. Test.* 87, 106556. doi:10.1016/j.polymertesting.2020.106556

Gao, X., Li, M., Zhang, H., Tang, X., and Chen, K. (2021). Fabrication of regenerated cellulose films by DMAc dissolution using parenchyma cells via low-temperature pulping from Yunnan-endemic bamboos. *Ind. Crops Prod.* 160, 113116. doi:10.1016/j.indcrop.2020.113116

Giorgini, L., Benelli, T., Brancolini, G., and Mazzocchetti, L. (2020). Recycling of carbon fiber reinforced composite waste to close their life cycle in a cradle-to-cradle approach. *Curr. Opin. Green Sustain. Chem.* 26, 100368. doi:10.1016/j.cogsc.2020.100368

Gopalraj, S. K., and Kärki, T. (2020). A review on the recycling of waste carbon fibre/glass fibre-reinforced composites: Fibre recovery, properties and life-cycle analysis. *SN Appl. Sci.* 2, 433. doi:10.1007/s42452-020-2195-4

Guelachvili, G., and Rao, K. N. (1986). *Handbook of infrared spectra*. New York: Academic Press.

Guo, L., Xu, L., Ren, Y., Shen, Z., Fu, R., Xiao, H., et al. (2022). Research on a two-step pyrolysis-oxidation process of carbon fiber-reinforced epoxy resin-based composites and analysis of product properties. *J. Environ. Chem. Eng.* 10, 107510. doi:10.1016/j.jece.2022.107510

Hadigheh, S. A., Wei, Y., and Kashi, S. (2021). Optimisation of CFRP composite recycling process based on energy consumption, kinetic behaviour and thermal degradation mechanism of recycled carbon fibre. *J. Clean. Prod.* 292, 125994. doi:10.1016/j.jclepro.2021.125994

Han, J., Duan, C., Lu, Q., Jiang, H., Fan, X., Wen, P., et al. (2019). Improvement of the crushing effect of waste printed circuit boards by co-heating swelling with organic solvent. *J. Clean. Prod.* 214, 70–78. doi:10.1016/j.jclepro.2018.12.288

Hanaoka, T., Arao, Y., Kayaki, Y., Kuwata, S., and Kubouchi, M. (2021). New approach to recycling of epoxy resins using nitric acid: Regeneration of decomposed products through hydrogenation. *ACS Sustain. Chem. Eng.* 9, 12520–12529. doi:10.1021/acssuschemeng.1c01737

Hanaoka, T., Ikematsu, H., Takahashi, S., Ito, N., Ijuin, N., Kawada, H., et al. (2022). Recovery of carbon fiber from prepreg using nitric acid and evaluation of recycled CFRP. *Compos. Part B Eng.* 231, 109560. doi:10.1016/j.compositesb.2021.109560

Hansen, C. M. (2007). *Hansen solubility parameters: A user's handbook*. Boca Raton, FL: CRC Press.

Hao, S., Kuah, A. T. H., Rudd, C. D., Wong, K. H., Lai, N. Y. G., Mao, J., et al. (2020). A circular economy approach to green energy: Wind turbine, waste, and material recovery. *Sci. Total Environ.* 702, 135054. doi:10.1016/j.scitotenv.2019.135054

Huang, Z., Deng, Z., Dong, C., Fan, J., and Ren, Y. (2022). A closed-loop recycling process for carbon fiber reinforced vinyl ester resin composite. *Chem. Eng. J.* 446, 137254. doi:10.1016/j.cej.2022.137254

Jiang, J., Deng, G., Chen, X., Gao, X., Guo, Q., Xu, C., et al. (2017). On the successful chemical recycling of carbon fiber/epoxy resin composites under the mild condition. *Compos. Sci. Technol.* 151, 243–251. doi:10.1016/j.compscitech.2017.08.007

Kim, K. W., Lee, H. M., An, J. H., Chung, D. C., An, K. H., and Kim, B. J. (2017). Recycling and characterization of carbon fibers from carbon fiber reinforced epoxy matrix composites by a novel super-heated-steam method. *J. Environ. Manage.* 203, 872–879. doi:10.1016/j.jenvman.2017.05.015

Kim, Y. N., Kim, Y. O., Kim, S. Y., Park, M., Yang, B., Kim, J., et al. (2019). Application of supercritical water for green recycling of epoxy-based carbon fiber

reinforced plastic. *Compos. Sci. Technol.* 173, 66–72. doi:10.1016/j.compscitech.2019.01.026

La Rosa, A. D., Greco, S., Tosto, C., and Cicala, G. (2021). LCA and LCC of a chemical recycling process of waste CF-thermoset composites for the production of novel CF-thermoplastic composites. Open loop and closed loop scenarios. *J. Clean. Prod.* 304, 127158. doi:10.1016/j.jclepro.2021.127158

Le Bras, J., and Muzart, J. (2017). "*N,N*-dimethylformamide and *N,N*-dimethylacetamide as carbon, hydrogen, nitrogen, and/or oxygen sources," in *Solvents as reagents in organic synthesis: Reactions and applications*. Editor X. F. Wu (Weinheim: Wiley VCH), 199–314.

Lee, M., Kim, D. H., Park, J. J., You, N. H., and Goh, M. (2020). Fast chemical recycling of carbon fiber reinforced plastic at ambient pressure using an aqueous solvent accelerated by a surfactant. *Waste Manag.* 118, 190–196. doi:10.1016/j.wasman.2020.08.014

Lefeuvre, A., Garnier, S., Jacquemin, L., Pillain, B., and Sonnemann, G. (2017). Anticipating in-use stocks of carbon fiber reinforced polymers and related waste flows generated by the commercial aeronautical sector until 2050. *Resour. Conserv. Recycl.* 125, 264–272. doi:10.1016/j.resconrec.2017.06.023

Li, X., Bai, R., and McKechnie, J. (2016). Environmental and financial performance of mechanical recycling of carbon fibre reinforced polymers and comparison with conventional disposal routes. *J. Clean. Prod.* 127, 451–460. doi:10.1016/j.jclepro.2016.03.139

Liu, W., Huang, H., Zhu, L., and Liu, Z. (2021). Integrating carbon fiber reclamation and additive manufacturing for recycling CFRP waste. *Compos. Part B Eng.* 215, 108808. doi:10.1016/j.compositesb.2021.108808

Lu, Y., Liu, T., Wang, S., Sun, Y., Zhang, Y., Kang, J., et al. (2022). A mild, environmental, and low-destructive recycling strategy for the 3D multiaxial braided composites cured by the vacuum-assisted resin transformed molding process. *Compos. Commun.* 35, 101354. doi:10.1016/j.coco.2022.101354

Meng, F., McKechnie, J., Turner, T. A., and Pickering, S. J. (2017). Energy and environmental assessment and reuse of fluidised bed recycled carbon fibres. *Compos. Part A Appl. Sci. Manuf.* 100, 206–214. doi:10.1016/j.compositesa.2017.05.008

Meng, F., Olivetti, E. A., Zhao, Y., Chang, J. C., Pickering, S. J., and McKechnie, J. (2018). Comparing life cycle energy and global warming potential of carbon fiber composite recycling technologies and waste management options. *ACS Sustain. Chem. Eng.* 6, 9854–9865. doi:10.1021/acssuschemeng.8b01026

Mijović, J., and Zhang, H. (2004). Molecular dynamics simulation study of motions and interactions of water in a polymer network. *J. Phys. Chem. B* 108, 2557–2563. doi:10.1021/jp036181j

Moosburger-Will, J., Greisel, M., Sause, M. G. R., Horny, R., and Horn, S. (2013). Influence of partial cross-linking degree on basic physical properties of RTM6 epoxy resin. *J. Appl. Polym. Sci.* 130, 4338–4346. doi:10.1002/app.39722

Mustata, F., and Tudorachi, N. (2017). Curing kinetics and thermal characterization of epoxy resin cured with amidodicarboxylic acids. *Appl. Therm. Eng.* 125, 285–296. doi:10.1016/j.applthermaleng.2017.07.037

Oliveux, G., Dandy, L. O., and Leeke, G. A. (2015). Current status of recycling of fibre reinforced polymers: Review of technologies, reuse and resulting properties. *Prog. Mat. Sci.* 72, 61–99. doi:10.1016/j.pmatsci.2015.01.004

Palmer, J., Ghita, O. R., Savage, L., and Evans, K. E. (2009). Successful closed-loop recycling of thermoset composites. *Compos. Part A Appl. Sci. Manuf.* 40, 490–498. doi:10.1016/j.compositesa.2009.02.002

Pei, C., Chen, P. Y., Kong, S. C., Wu, J., Zhu, J. H., and Xing, F. (2021). Recyclable separation and recovery of carbon fibers from CFRP composites: Optimization and mechanism. *Sep. Purif. Technol.* 278, 119591. doi:10.1016/j.seppur.2021.119591

Shuaib, N. A., and Mativenga, P. T. (2016). Energy demand in mechanical recycling of glass fibre reinforced thermoset plastic composites. *J. Clean. Prod.* 120, 198–206. doi:10.1016/j.jclepro.2016.01.070

Sun, Y., Fan, W., Song, C., Gao, X., Liu, T., Song, W., et al. (2022). Effects of stitch yarns on interlaminar shear behavior of three-dimensional stitched carbon fiber epoxy composites at room temperature and high temperature. *Adv. Compos. Hybrid. Mat.* 5, 1951–1965. doi:10.1007/s42114-022-00526-y

Tam, L. H., He, L., and Wu, C. (2019). Molecular dynamics study on the effect of salt environment on interfacial structure, stress, and adhesion of carbon fiber/epoxy interface. *Compos. Interfaces* 26, 431–447. doi:10.1080/09276440.2018.1506901

Tatariants, M., Yousef, S., Denafas, G., and Bendikiene, R. (2018). Separation and purification of metal and fiberglass extracted from waste printed circuit boards using milling and dissolution techniques. *Environ. Prog. Sustain. Energy* 37, 2082–2092. doi:10.1002/ep.12899

Verma, H. R., Singh, K. K., and Mankhand, T. R. (2017). Comparative study of printed circuit board recycling by cracking of internal layers using organic solvents-dimethylformamide and dimethylacetamide. *J. Clean. Prod.* 142, 1721–1727. doi:10.1016/j.jclepro.2016.11.118

Verma, H. R., Singh, K. K., and Mankhand, T. R. (2016). Dissolution and separation of brominated epoxy resin of waste printed circuit boards by using di-methyl formamide. *J. Clean. Prod.* 139, 586–596. doi:10.1016/j.jclepro.2016.08.084

Wang, Y., Cui, X., Ge, H., Yang, Y., Wang, Y., Zhang, C., et al. (2015). Chemical recycling of carbon fiber reinforced epoxy resin composites via selective cleavage of the carbon–nitrogen bond. *ACS Sustain. Chem. Eng.* 3, 3332–3337. doi:10.1021/acssuschemeng.5b00949

Wei, X., Liu, F., Guo, X., Gao, F., Li, Y., Zhu, D., et al. (2022). Exploring of the property of epoxy resins based on diselenide and disulfide dynamic linkers. *Front. Chem.* 10, 991010. doi:10.3389/fchem.2022.991010

Wei, Y., and Hadigheh, S. A. (2022). Cost benefit and life cycle analysis of CFRP and GFRP waste treatment methods. *Constr. Build. Mat.* 348, 128654. doi:10.1016/j.conbuildmat.2022.128654

Wu, T., Zhan, W., Jia, X., Li, H., Sui, G., and Yang, X. (2022). Solvent-free rapid degradation of epoxy composites and recycling application of high performance carbon fibers through the synergic catalysis effect of molten salts and titanium dioxide. *Polym. Degrad. Stab.* 196, 109849. doi:10.1016/j.polymdegradstab.2022.109849

Wu, T., Zhang, W., Jin, X., Liang, X., Sui, G., and Yang, X. (2019). Efficient reclamation of carbon fibers from epoxy composite waste through catalytic pyrolysis in molten $ZnCl_2$. *RSC Adv.* 9, 377–388. doi:10.1039/C8RA08958B

Xing, M., Li, Z., Zheng, G., Du, Y., Chen, C., and Wang, Y. (2021). Recycling of carbon fiber-reinforced epoxy resin composite via a novel acetic acid swelling technology. *Compos. Part B Eng.* 224, 109230. doi:10.1016/j.compositesb.2021.109230

Yu, K., Shi, Q., Dunn, M. L., Wang, T., and Qi, H. J. (2016). Carbon fiber reinforced thermoset composite with near 100% recyclability. *Adv. Funct. Mat.* 26, 6098–6106. doi:10.1002/adfm.201602056

Zhang, J., Chevali, V. S., Wang, H., and Wang, C. H. (2020). Current status of carbon fibre and carbon fibre composites recycling. *Compos. Part B Eng.* 193, 108053. doi:10.1016/j.compositesb.2020.108053

Zhao, Q., An, L., Li, C., Zhang, L., Jiang, J., and Li, Y. (2022). Environment-friendly recycling of CFRP composites via gentle solvent system at atmospheric pressure. *Compos. Sci. Technol.* 224, 109461. doi:10.1016/j.compscitech.2022.109461

Zhu, C., Zhou, Y., Zhao, H., and Farajtabar, A. (2020). Thiamethoxam in aqueous co-solvent mixtures of 1, 4-dioxane, *N, N*-dimethylacetamide, dimethyl sulfoxide and acetonitrile: Solubility solute-solvent and solvent-solvent interactions, and preferential solvation analysis. *J. Chem. Thermodyn.* 150, 106229. doi:10.1016/j.jct.2020.106229

Zhu, J. H., Chen, P. Y., Su, M. N., Pei, C., and Xing, F. (2019). Recycling of carbon fibre reinforced plastics by electrically driven heterogeneous catalytic degradation of epoxy resin. *Green Chem.* 21, 1635–1647. doi:10.1039/C8GC03672A

Zhu, P., Chen, Y., Wang, L. Y., Zhou, M., and Zhou, J. (2013). The separation of waste printed circuit board by dissolving bromine epoxy resin using organic solvent. *Waste Manag.* 33, 484–488. doi:10.1016/j.wasman.2012.10.003

Zhu, P., Yang, Y. Z., Chen, Y., Qian, G. R., and Liu, Q. (2018). Influence factors of determining optimal organic solvents for swelling cured brominated epoxy resins to delaminate waste printed circuit boards. *J. Mat. Cycles Waste Manag.* 20, 245–253. doi:10.1007/s10163-016-0574-0

frontiers | Frontiers in Chemistry

TYPE Original Research
PUBLISHED 12 January 2023
DOI 10.3389/fchem.2022.1095500

Check for updates

OPEN ACCESS

EDITED BY
Ugur Ulusoy,
Cumhuriyet University, Türkiye

REVIEWED BY
Silvio Teixeira,
São Paulo State University, Brazil
Parjaree Thavorniti,
Thailand National Metal and Materials Technology Center, Thailand

*CORRESPONDENCE
Shucai Zhang,
zhangsc.qday@sinopec.com

SPECIALTY SECTION
This article was submitted to Green and Sustainable Chemistry, a section of the journal Frontiers in Chemistry

RECEIVED 11 November 2022
ACCEPTED 28 December 2022
PUBLISHED 12 January 2023

CITATION
Hao Z, Zhang H, Tang X, Sui L, Li Y and Zhang S (2023), Utilization of gasification slag and petrochemical incineration fly ash for glass ceramic production.
Front. Chem. 10:1095500.
doi: 10.3389/fchem.2022.1095500

COPYRIGHT
© 2023 Hao, Zhang, Tang, Sui, Li and Zhang. This is an open-access article distributed under the terms of the Creative Commons Attribution License (CC BY). The use, distribution or reproduction in other forums is permitted, provided the original author(s) and the copyright owner(s) are credited and that the original publication in this journal is cited, in accordance with accepted academic practice. No use, distribution or reproduction is permitted which does not comply with these terms.

Utilization of gasification slag and petrochemical incineration fly ash for glass ceramic production

Zhenyu Hao, Hai Zhang, Xiaoli Tang, Lihua Sui, Yanan Li and Shucai Zhang*

State Key Laboratory of Safety and Control for Chemicals, SINOPEC Research Institute of Safety Engineering Co, Ltd., Qingdao, China

This study investigated glass ceramics produced using coal gasification slag (CGS) and petrochemical incineration fly ash (PIFA) to immobilize hazardous heavy metals such as Cr and As. However, the crystallization kinetics and stabilization behavior mechanism of different heavy metals in the petrochemical incineration fly ash-derived glass-ceramics remains unclear. And X-ray diffraction, differential scanning calorimetry, scanning electron microscopy, and inductively coupled plasma mass spectrometry were used to characterize glass and crystalline products. In this paper, we reported the crystallization kinetics and chemical leaching characteristics of the glass ceramic. A low crystallization activation energy of 121.49 kJ/mol was achieved from crystallization peak of several different heating rates around 850°C, implying that it is easier to produce the glass ceramics at that temperature. The Avrami parameter of the former crystallization was determined to be 1.23 ± .12, which indicated two-dimensional crystal growth with heterogeneous nucleation. The toxicity characteristic leaching procedure results indicated that the heavy metals were well solidified, and that the leaching concentration was significantly lower than the limit specified by governmental agencies. The potentially toxic element index of the parent glass and the two glass ceramics were 11.7, 5.8, and 3.6, respectively. Therefore, the conversion of hazardous petrochemical incineration fly ash and other solid waste into environmentally friendly glass ceramics shows considerable potential and reliability.

KEYWORDS

glass ceramics, Fe_2O_3, crystallization kinetics, PIFA, TCLP

1 Introduction

Oil accounts for one third of the global energy consumption and is the largest share of all the energy categories (Dutta et al., 2019; Melichar and Atems 2019; Dong et al., 2020). The rapidly developing petrochemical industry in China is expected to make China the largest producer of refined oil and ethylene by 2022 (Fang et al., 2021). The disposal of solid residues from various industrial thermal processes, such as petrochemical incineration fly ash (PIFA), has increasingly become a concern. PIFA, which contains multiple and large amounts of potentially risky heavy metals, is regarded as hazardous waste in the National Hazardous Waste List (2021 edition).

Abbreviations: XRF, X-ray fluorescence; XRD, X-ray diffraction; SEM, scanning electron microscopy; PIFA, petrochemical incineration fly ash; TCLP, toxicity characteristic leaching procedure; PTE, potentially toxic element; STIM, synthesis toxicity index model; STI, synthesis toxicity index; DSC, differential scanning calorimetry; ICDD, the International Centre for Diffraction Data; PEI, potential ecological risk.

Therefore, the treatment and disposal of PIFA and bottom slag has recently become an important social and environmental issue (Nikravan et al., 2018). Therefore, the effective recycling of hazardous wastes from the petrochemical industry has become an urgent requirement to realize the waste-free city goal in China (Fu et al., 2014).

While crude oil extraction and natural gas production have modernized our society, the environmental pollution cost has been more severe than expected (Blumer and Sass 1972; Almeda et al., 2014; Beyer et al., 2016; Ghorbani and Behzadan 2021). Incineration is one of the most common, effective and high-performance technologies for the disposal of municipal solid waste (Liu et al., 2019; Zhao et al., 2019), oil sludge (Gong et al., 2018), oil shale ash (Konist et al., 2020), and medical wastes (Thind et al., 2021). However, the disposal of fly and bottom ash produced by the incineration of various types of waste results in the occupation of large amounts of land resources (Allegrini et al., 2014), which is accompanied by secondary pollution problems, such as the transfer of heavy metals to the gas phase (Li et al., 2003; Tian et al., 2012). Although coal gasification technology as an environmentally friendly method has become an important part of the energy strategy in China (Wei et al., 2018), it creates large amounts of by-products.

Glass ceramics have the dual advantages of glasses and ceramics, such as environmental friendliness and excellent mechanical properties. Glass ceramics are polycrystalline materials produced by the melting/quenching of raw materials. The current mostly used common technology for treating hazardous solid waste is the heavy metal stabilization mechanism, which is realized by bonding the hazardous solid waste into the glass matrix, substituting the elements in the crystal phase with the hazardous solid waste, and forming a new crystal compound (Guo et al., 2017).

Thus, effectively recycling waste materials into a variety of ceramic products could be a promising strategy to solve this problem (Karpukhina et al., 2014). Previous studies reported that various solid wastes, such as coal fly ash (Albertini et al., 2013), metallurgical slags (Deng et al., 2020; Ceylan et al., 2021; Shang et al., 2021), and oil shale fly ash (Luan et al., 2010), have been used as part of the raw materials to produce glass ceramics. To the best of our knowledge, studies on the use of coal gasification slag and PIFA in glass ceramic matrices are limited. However, the use of pure chemical reagents and nucleating agents increases the cost of waste-based glass ceramics. Therefore, this study uses solid waste to realize all-waste-based fly ash glass ceramics, which is of great significance for sustainable social and economic development.

The main purpose of our research is to use PIFA and gasification slag as the main raw materials for the preparation of glass ceramics, and to prepare samples based on all-waste-based fly ash glass ceramics. The transformation and characteristics of the raw materials and glass-ceramics were analyzed using X-ray fluorescence (XRF) spectroscopy, X-ray diffraction (XRD), and scanning electron microscopy (SEM). The main goals of this study are 1) to investigate the crystallization kinetics, such as thermal stability, crystallization activation energy, and crystallization index, of these materials; 2) to establish a theoretical and technical foundation for developing an environmentally friendly glass ceramic by combining hazardous waste; and 3) to demonstrate the leaching behavior and potential environmental risks of the glass ceramics using different heat-treatment processes.

2 Materials and methods

2.1 Materials and reagents

The PIFA used in this study was acquired from a hazardous waste incinerator in southern China. The gasification slags used in this study were acquired from a refinery in Shandong Province, China. The PIFA and gasification slag samples were crushed and sieved to a size <.125 mm using a ball grinding mill (FRITSCH, Pulverisette 7, Germany). The collected samples were dried in an oven at 105°C for 24 h before the analyses. The chemical compositions of the samples were determined using XRF (ZSX Priums, RIGAKU, Japan), and the results are presented in Table 1. Acetic acid, hydroxylammonium chloride, ammonium acetate and hydrochloric acid used in this study were purchased from Sigma-Aldrich (Shanghai, China) and were used as received.

2.2 Characterization analyses

The thermal behavior of the basic glass sample was analyzed from room temperature to 1,200°C using differential scanning calorimetry (DSC; STA 449F3, NETZSCH, Germany) at the heating rates of 5, 10, 15, and 20°C/min in a N_2 atmosphere. To study the crystallization kinetics of the parent glass, DSC curve analysis are performed, and the details can be found in Figure 1. The temperature of the exothermic peak in the DSC curves is defined as the crystallization temperature, T_p, which is often selected as the optimum nucleation temperature. The crystalline phases of the samples were investigated using XRD (Miniflex 600, Rigaku, Japan). The 2θ degree range was 5°-80° and the step angle was 2°/min under Cu Kα radiation at 40 kV and 30 mA. The crystalline phases were determined by comparing the peak intensities and positions with those of the International Centre for Diffraction Data (ICDD PDF-2 Release 2004). And using the Rietveld refinement method to assess the validity of the XRD data. The morphology of the glass ceramics was characterized using a high-resolution SEM (MIRA LMS, TESCAN, Czech Republic).

2.3 Preparation of glass-ceramics

Glass samples were prepared from PIFA and gasification slag with a mass ratio of PIFA:gasification slag of 20:80. In each batch, the mixed samples were melted in a platinum crucible for 2 h in an electrically heated furnace at 1,300°C to ensure complete melting. The melt was then immediately quenched into water to obtain glass frit. The water-quenched glass was then dried in an oven at 105°C for 4 h, followed by grinding and screening (200 mesh) for use. The treated powder was placed in a cylindrical mold (Φ 19.05 mm) and pressed at 40 MPa using a powder compressing machine (YLJ-40TA, Hefei Kejing Materials Technology Co., Ltd., China). The mold containing the sample was then placed in a muffle furnace and heated to the nucleation temperature at 5°C/min and maintained at this temperature for 1h, followed by further heating to the crystallization temperature (850°C and 1,050°C) for 1 h or 2 h and the details can be found in Figure 1. The glass ceramics were obtained after naturally cooling to room temperature.

TABLE 1 Chemical composition of the coal gasification slag and petrochemical incineration fly ash (wt%).

	SiO_2	K_2O	Na_2O	CaO	MgO	Al_2O_3	Fe_2O_3	MnO	P_2O_5	TiO_2	LOI
PIFA	.36	.48	55.40	.31	.10	.03	1.43	.02	.27	.07	41.53
Slag	41.39	2.05	1.05	12.59	.72	12.86	11.28	.14	.12	.55	17.25

TABLE 2 Detailed parameters of the Modified Sequential Extraction Method for based on GB/T 25282-2010.

Step	Concentration	Agent	Time (h)	Speciation
F1	40 mL, 1 mol/L	CH_3COOH	16	Mild acid-soluble
F2	40 mL, 1 mol/L	$NH_2OH{\cdot}HCl$	16	Reducible
F3	10 mL, 30%	H_2O_2	1	Oxidizable
	50 mL, 1 mol/L	CH_3COONH_4	16	
F4	15 mL	$HCl{\cdot}HNO_3{\cdot}HF{\cdot}HClO_4$	3	Residual

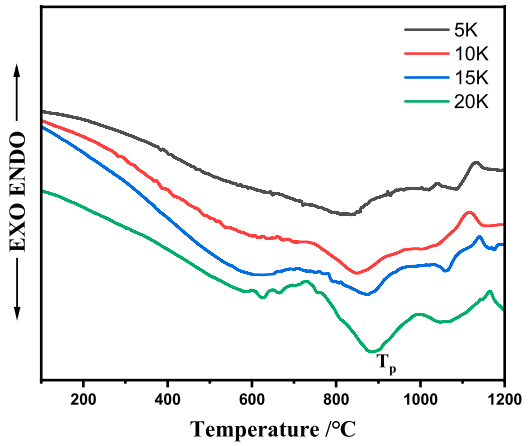

FIGURE 1
The DSC curves of the fly ash-slag-based parent-glass samples with different heating rate ranging from 100°C to 1,000°C/min: 5°C/min, 10°C/min, 15°C/min, and 20°C/min.

2.4 Heavy metal determination and leaching test

The total and leaching concentrations of heavy metals in the PIFA and glass ceramic samples were analyzed using inductively coupled plasma mass spectrometry (ICP-MS; Agilent 7800, United States). The safety and stability of the samples were estimated through leaching experiments using the toxicity characteristic leaching procedure (TCLP). The leaching fluid used was an acetic acid solution with pH 2.9. Then, 1.0 g of crushed sample and 20 mL of extraction fluid were mixed in a leaching vial and adequately rotated for 16 h. The state of the heavy metals in the glass samples were analyzed using a modified four-step sequential extraction procedure based on a method reported in the literature (Rauret et al., 1999). Table 2 shows the detailed processes.

2.5 Environmental risk assessment

The synthesis toxicity index model (STIM) was established to explore the changes in the environmental toxicity of targeted heavy metals (Luan et al., 2009). The potentially toxic elements (PTEs) index used for the environmental risk assessment was calculated using Eq. 1 (Devi and Saroha 2014).

$$PTEs = \sum_{i=1}^{m} T_i \left(\frac{\sum_{j=1}^{m} \left(E_j Q_i^j \right)}{C_N^i} \right) \quad (1)$$

where n is the number of heavy metal species; m is the number of chemical speciation (m = 4); T_i is the toxicity response coefficient of heavy metal i; E_j is the bioavailability of chemical speciation j of heavy metal i; Q_j^i is the content of chemical speciation j and C_n^i is the background value of i in the natural environment (Hakanson, 1980). For a more comprehensive and reliable assessment, the background values refer to the secondary living standard of GB-15618-2008 (Luan et al., 2018).

3 Results and discussion

3.1 Characterization of the raw materials

Table 1 lists the chemical compositions of the PIFA and gasification slag. SiO_2, CaO, Na_2O, Al_2O_3, and Fe_2O_3, which are essential for glass-ceramic preparation, accounted for more than 80% of the raw material. Additionally, the Fe_2O_3 content in the gasification slag was approximately 12.86%. To the best of our knowledge, Fe_2O_3 is a commonly used nucleating agent in the glass industry (Alizadeh et al., 2004; Kang et al., 2019; Chen et al., 2021). The chemical composition of PIFA contained 40% Na_2O and gasification slag contained SiO_2, CaO, Al_2O_3, and Fe_2O_3 was suitable for implementation in the precursor glass raw material. Consequently, the SiO_2-CaO-Al_2O_3-Na_2O-Fe_2O_3 (fly ash: gasification slag = 20:80%) glass-ceramics were designed for the experiments. The sintering method was used to prepare solid waste glass ceramics with a higher crystallinity.

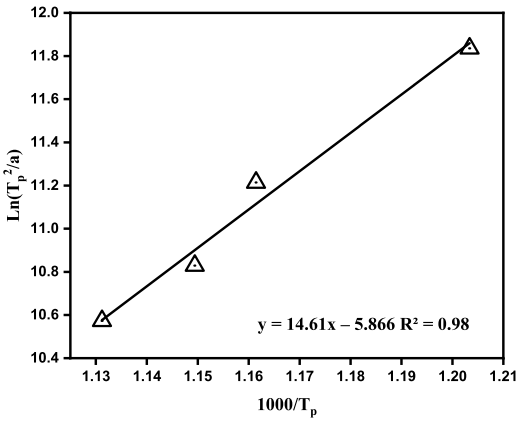

FIGURE 2
Linear fitting results of ln (T_p^2/α) ~1,000/T_p, R^2 is the Pearson correlation coefficient.

3.2 Crystallization kinetics

Thermal analysis has been used to study the crystallization kinetics of various glass systems. Figure 1 shows that the DSC curves of the prepared base glasses, which were analyzed at different heating rates (α = 5, 10, 15, and 20°C/min) to determine the crystallization activation energy. The DSC curves of the base glass exhibited two peaks at approximately 850°C and 1,050°C. The crystallization peak temperatures (T_P), with respect to the increasing heating rate (β °C/min), were 827.6, 854.8, 878.4, and 886.6°C, respectively. The second crystallization peak for the different heating rates was at approximately 1,050°C. The crystallization exothermic peak temperatures of the base glass at the heating rates of 20°C and 5°C/min were 886°C and 827°C, respectively. The T_p of the base glasses with the same chemical composition gradually increased and the crystallization peaks at different temperatures increased and broadened with a continuously increasing heating rate. The base glass did not have sufficient nucleation time with an increasing heating rate, and crystallization became relatively delayed. When the heating rate increased, the hysteresis was more severe and the crystallization temperature was further increased.

The crystallization kinetics can be determined using the Kissinger (Kissinger 1956) and Augis-Bennett equations (Augis and Bennett 1978), which are defined in Eqs 2, 3, respectively. Therefore, Eqs 2, 3 were adopted in this study to investigate the crystallization activation energy (E_c) and the crystallization index (n) of the gasification slag-based parent glass.

$$\ln\left(\frac{T_p^2}{\alpha}\right) = \frac{E_c}{RT_p} + \ln\left(\frac{E_c}{R}\right) - ln\,\vartheta \tag{2}$$

where E_c (kJ/mol) is the crystallization activation energy; α (°C/min) is the DSC heating rate; T_p (°C) is the temperature of the exothermic peak in the DSC curve as shown in Figure 1; R is the gas constant per mole [8.314 J/(K mol)]; and ν is the frequency factor. After calculating E_c, the crystal growth index (n) can be obtained using the Augis-Bennett equation, as defined in Eq. 3.

$$n = \frac{2.5T_p^2}{\Delta T_f E_c/R} \tag{3}$$

where ΔT_f (°C) is the full width at half maximum of the exothermic crystallization peak shown in Figure 1; 'E_c/R' is the slope in Figure 2 and T_p (°C) is the temperature of the exothermic peak in the DSC curve.

Figure 2 shows the relationship between ln(T_P^2/α) and 1,000/T_P. As previously mentioned, the *Ec* must be obtained before calculating *n*. The *Ec* of the gasification slag-based glass ceramic was calculated from the slope in Figure 2 as 121.49 kJ/mol. A glass melt requires a certain activation energy to overcome the energy barrier when it transforms from a high-energy glassy state to a crystalline state. For example, the E_c of blast furnace slag-based glass ceramics, fused-cast basalt crystallization, HCFS-based glass ceramics, and pickling sludge are 300–400, 238, approximately 200, and 187 kJ/mol (Bai et al., 2016a; Bai et al., 2016b; Zhao et al., 2020). The low E_c of the gasification slag and PIFA indicated that the parent glass crystallized more easily. To our best knowledge, the addition of Fe_2O_3 greatly reduces the precipitation temperature of the relevant crystals, resulting in a decreased E_c (Wang 2010). In this study, an E_c of only 121.49 kJ/mol was required to form the glass ceramics for the base glass. However, it is worth noting that although the E_c was lower than that of other waste-based samples, the glass ceramics prepared in this study could result in a decrease in the mechanical properties of the final product. Relevant studies have shown that Fe_2O_3 has little effect on the crystal phase type but has a greater effect on its crystallinity and precipitation temperature (Kang et al., 2019). Therefore, both the Fe_2O_3 content and the heat treatment temperature and time greatly influence crystal precipitation, which in turn affects the properties of the obtained glass ceramics. Therefore, the improvement of the mechanical properties of glass ceramics should be studied further.

n represents the number of growth directions as well as the nucleation and crystal growth mechanism. When *n* is greater than 3, the parent crystal is a bulk crystal, which is a three-dimensional volume-dominated crystal, and when n is 0–3, the crystal is a surface crystal, which is a two-dimensional surface-dominated crystal (Hosono and Abe, 1992; Hosono and Abe, 1994). In this study, the mean value of n was 1.23 ± .12, and the obtained *n* was not an integer, indicating that crystallization occurred through more than one mechanism. Because the gasification slag contained 16.17% carbon residue, the formation of the base glass and the crystallization kinetics were studied in an oxidizing atmosphere, in which iron will be oxidized to Fe^{3+}. Karamonov *et al.* found that an oxidizing atmosphere could lead to a decrease in *n* (Karamanov et al., 2000). As previously mentioned, due to the presence of Fe^{3+} as the main form of iron in this system, the content of Fe_2O_3 in the formulation system was 9.3% and acted as the main nucleating agent, resulting in two-dimensional surface-dominated crystallization, which resulted in a lower Avrami parameter (Kim and Park 2020).

3.3 Crystalline phase analysis

XRD analysis was performed on the thermally treated glass ceramics at 850°C and 1,050°C to identify the crystalline phase. The NaO-CaO-Al_2O_3-SiO_2-Fe_2O_3-based glass is the basic silicate system that is widely used in many industrial fields and solid waste recycling,

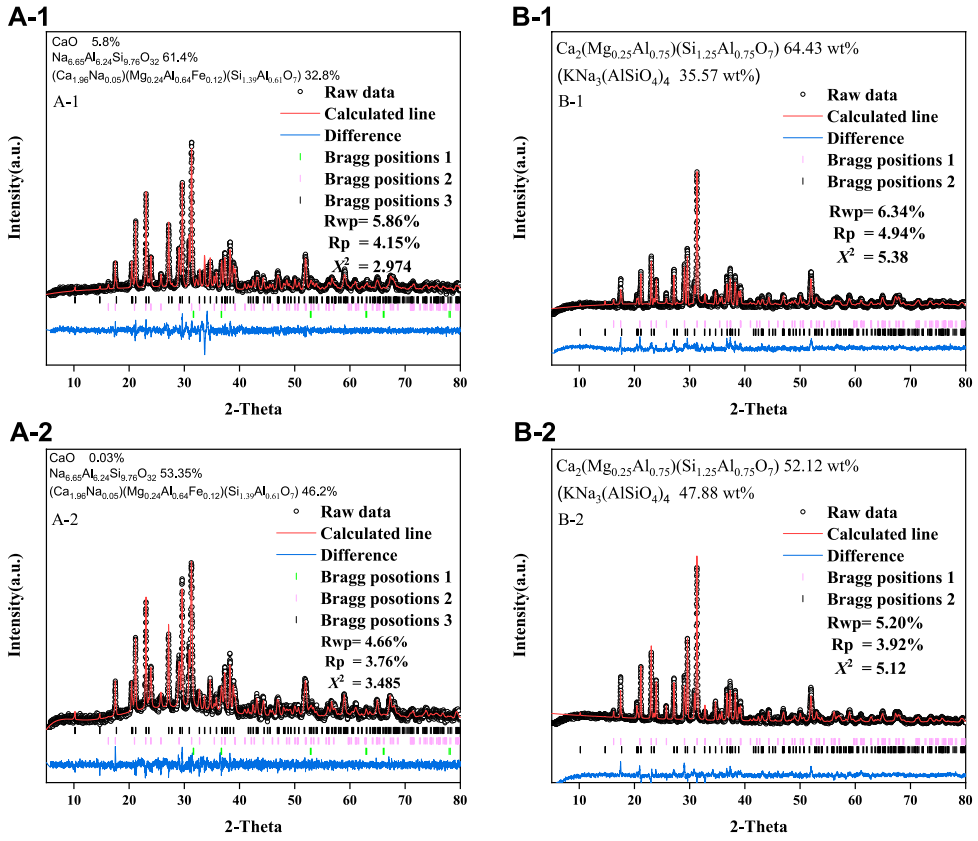

FIGURE 3
Rietveld refinement analysis of the XRD patterns for A-1 and B-1 at 850°C, and A-2 and B-2 at 1,050°C. For A-1 and A-2: Bragg position 1 is CaO; Bragg position 2 is $KNa_3(AlSiO_4)_4$; Bragg position 3 is $Ca_2(Mg_{0.25}Al_{0.75})$ $(Si_{1.25}Al_{0.75}O_7)$. For B-1 and B-2: Bragg position 1 is $Na_{6.65}Al_{6.24}Si_{9.76}O_{32}$; Bragg position 2 is $(Ca_{1.9}6Na_{0.05})$ $(Mg_{0.24}Al_{0.64}Fe_{0.12})$ $(Si_{1.39}Al_{0.61}O_7)$.

in which Fe_2O_3 can effectively promote the nucleation rate as a nucleating agent (Erol et al., 2007).

Figure 3 shows the XRD patterns of the base glass after heat treatment. After crystallization at 850°C for 1 and 2 h, the main crystalline phases were $(Ca_{1.96}Na_{0.05})$ $(Mg_{0.24}Al_{0.64}Fe_{0.12})$ $(Si_{1.39}Al_{0.61}O_7)$ (PDF No. 72-2128), nepheline $(Na_{6.65}Al_{6.24}Si_{9.76}O_{32})$ (PDF No. 83-2372) and calcium oxide (CaO) (PDF No. 99-0070). When the crystallization temperature was raised to 1,050°C, the main crystalline phases were forsterite $Ca_2(Mg_{0.25}AI_{0.75})$ $(Si_{1.25}AI_{0.75}O_7)$ (PDF No. 79-2422) and nepheline $KNa_3(AlSiO_4)_4$, (PDF No. 74-0387). Clearly, the crystallization time had no significant effect on the formation of the phases in this study, and the XRD peak of the 2 h treatment was slightly higher than that of the 1 h treatment. In summary, toxic elements may be incorporated in the crystalline phase or fixed within the glassy matrix during this process.

Figure 4 shows the surface morphology of the glass ceramic microstructure of the particles. The particle size of the prepared glass ceramic samples was approximately 1 μm and the arrangement was relatively uniform. Figures 4A, B depicts the microstructure of the glass ceramics crystallized at 850°C, which shows some oriented disordered platelets and a large number of crystals distributed in the glass matrix. With an increasing crystallization time, thinner and larger multi-layer flaky crystals with a disordered orientation were observed in the glass ceramics treated for 2 h. Figures 4C, D shows that in the glass samples continually sintered at 1,050°C for 1 and 2 h, the flaky crystals disappeared and some short columnar crystals were formed. When the heating time increased to 2 h, the boundary of the crystallized grains was clearer. Additionally, the glass ceramic crystals, which exhibited a higher degree of crystallization and a more uniform grain distribution, became larger and denser at higher crystallization temperatures. Furthermore, the crystals exhibited a particle stacking arrangement. However, the base glass was not only precipitated as a single material crystal during the heat treatment process, but also had a variety of secondary crystal phases, mainly because there were many impurities in the slag and PIFA, which influence the crystal precipitation process.

3.4 Leaching tests

The total heavy metal concentrations in all the gasification slag and PIFA glass ceramics were determined using ICP-MS, which are listed in Table 3. The leaching concentrations of chromium and arsenic in the PIFA were significantly higher than the limits specified in GB5083.3-2007 and GB16889-2008. The leaching concentrations of chromium, arsenic, and zinc were 269.8, 158, and 43.5 mg/L, respectively. The leaching concentrations of heavy metals in the slag did not exceed the limits specified in GB5083.3-2007 and GB16889-2008. Thus, the PIFA used in this study cannot be

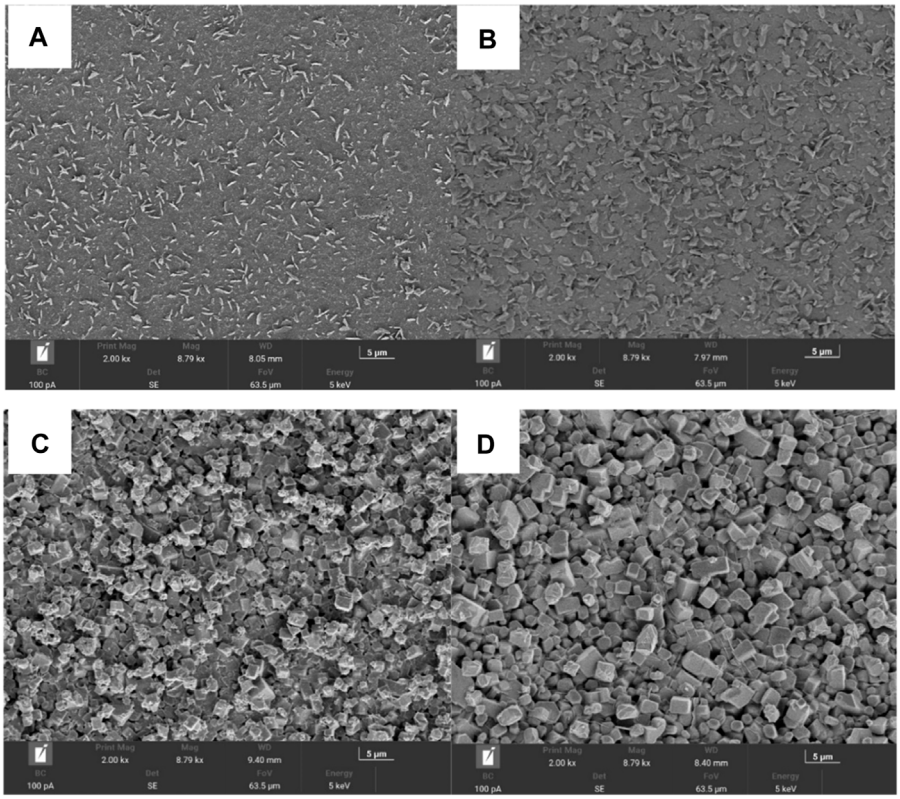

FIGURE 4
The SEM images of gasification slag-based glass ceramics prepared by **(A)** at 850°C for 1 h, **(B)** at 850°C for 2 h, **(C)** at 1,050°C for 1 h, and **(D)** at 1,050°C for 2 h.

TABLE 3 Total concentration and leaching concentration of heavy metal contents of the PIFA and gasification slag.

		V	Cr	Ni	Cu	Zn	Cd	Ba	Pb	Mn	As
Total concentration (ppm)	PIFA	2244	2811	108	37.5	672	.063	8.14	3.13	260	683.4
	Slag	82.3	53.4	29.6	35.0	43.8	ND	4152	27.6	1210	43.8
Leaching concentration (ppm)	PIFA	ND	269.8	.08	1.4	43.5	.04	.24	.12	ND	158
	Slag	ND	.01	.01	.012	.016	ND	.184	.05	ND	.019
	Limit level[a]	—	5	5	100	100	1	100	5	—	5

[a]GB 5085.3 Identification standard for hazardous waste-identification for extraction toxicity.
ND, not detected.

disposed in a landfill without further treatment. Previous studies have shown that waste PIFA easily reacts with heavy metals at high temperatures to form low-boiling heavy metal chlorides (Zhang et al., 2020). In this study, the volatilization of heavy metals during heat treatment were negligible, as chloride was not detected.

3.5 The solidification of the parent glass and glass ceramic

Figure 5 shows the TCLP leaching concentrations of the existing heavy metals in the different glass ceramics of gasification slag co-processed with PIFA. The leaching concentrations of chromium, nickel, copper, zinc, and arsenic of the glass and glass ceramic samples complied with the requirements of the United States EPA and the Chinese national standards.

After the first and second heat treatment, the leaching heavy metal concentrations in both samples (A-1, A-2, B-1, and B-2) showed a significant decreasing trend, where the decreasing trend of chromium was the most significant, decreasing from 116.3 to below 30 ng/g^{-1}. However, the leaching concentration of arsenic remained in the steady state level for the different crystallization times or heat treatments. This is because acetic acid was used as the buffer solution in the TCLP leaching experiments, which hardly reacts with the crystallite phase but can react with the glass phase. Increasing the sintering temperature is beneficial for reducing the leaching concentration of heavy metals in

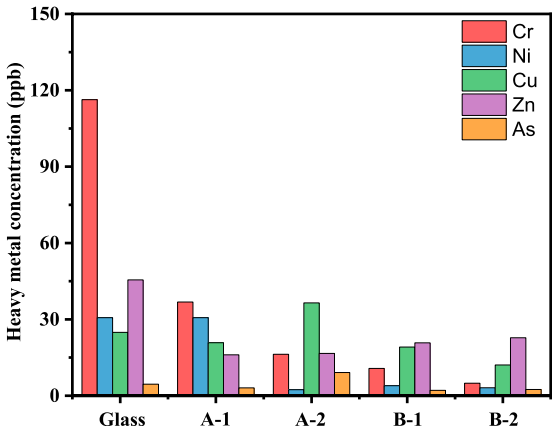

FIGURE 5
Leaching concentration of Cr, Ni, Cu, Zn and As in different sample. A-1: sintered at 850°C for 1 h, A-1: sintered at 850°C for 2 h, B-1: sintered at 1,050°C for 1 h, B-2 is sintered at 1,050°C for 2 h.

the samples, mainly because metal ions participate in the phase transition and intercalate into the crystal structure of the glass ceramics at high temperature. In conclusion, the preparation of glass ceramics can be used as an effective method for PIFA solidification and stabilization.

3.6 Potential ecological risk assessment of heavy metals

Heavy metals can exist in glass ceramics in the acid-soluble, reduction, oxidation, and residual states. The distribution of the four forms of heavy metals in different solids strongly affects their leaching behavior and potential toxicity risk to the environment. Figure 6 shows the distribution of the different heavy metal chemical forms in the eutectic solidified body.

Nickel, copper, and zinc exist in PIFA as the residual state; therefore, the leaching concentration is low, as shown in Figure 6. However, the residual state of chromium accounts for 9.6% of the total existent states. It is worth noting that the acid-soluble state of arsenic is up to 40% in the chemical speciation distributions. This indicates that the toxicity of PIFA mainly originates from chromium and arsenic. The oxidizable and reducible states of chromium and arsenic in the glass matrix was <4% and 6%, respectively. The main form of the five heavy metals in the glass ceramic samples A-1 and A-2 was the residual state, all of which were >75%. The predominant form of chromium and arsenic after secondary crystallization at 1,050°C was the residual state, which increased significantly to 99% and 95%, respectively. There was no discernible difference in the nickel and zinc forms between the parent glass and glass ceramic. Measurement of the weight of the solid matter before and after the reaction indicated that the vitrification process resulted in a lower mass loss rate of 5%–10%, which was mainly due to the decomposition of carbonate in the system. The organic fly ash was measured using ion chromatography, and no chloride ions were detected. Therefore, at high temperature, zinc will not react to generate heavy metal chlorides. Additionally, heavy metals form more stable and insoluble species (such as metal and mineral salts), resulting in poor leaching capacity (Guo et al., 2017), which can indicate that the glass ceramic has a high heavy metal fixation efficiency. The contribution of the different heavy metals was similar at different temperatures, and the slight difference is likely due to experimental errors.

The STIM assessment method can comprehensively reflect the potential impact of heavy metals on the ecological environment. According to STIM, the synthesis toxicity index (STI) value of each sample can be calculated using Eq. 1, which is equal to the PTEs index, as shown in Figure 7. The base glass had a toxicity value of 11.7.

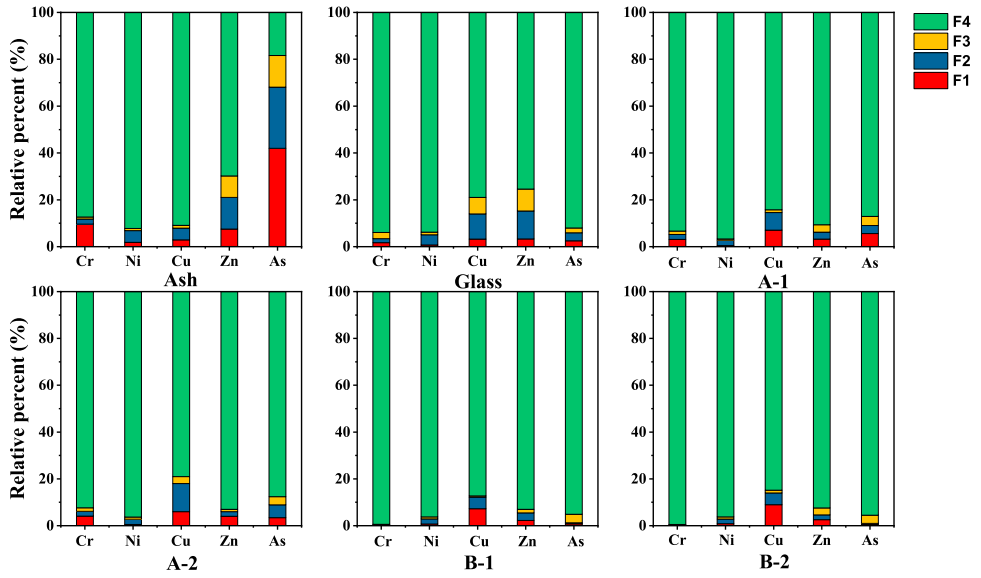

FIGURE 6
Chemical speciation distributions of heavy metals in glass and ceramics-glass. A-1: sintered at 850°C for 1 h, A-2: sintered at 850°C for 2 h, B-1: sintered at 1,050°C for 1 h, B-2 is sintered at 1,050°C for 2 h.

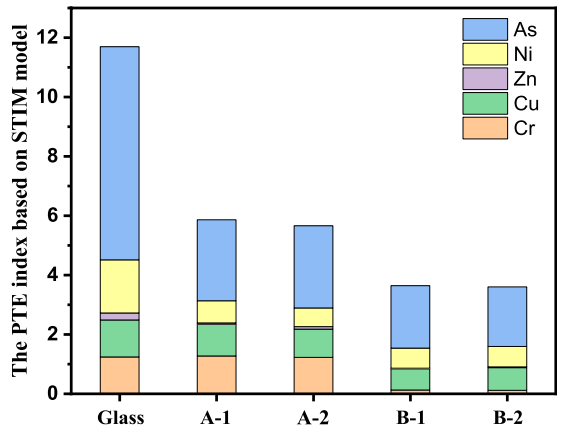

FIGURE 7
PTEs index of heavy metals. A-1: sintered at 850°C for 1 h, A-1: sintered at 850°C for 2 h, B-1: sintered at 1,050°C for 1 h, B-2 is sintered at 1,050°C for 2 h.

Arsenic is the main elements responsible for toxicity, which of PTEs index is 7.2. The PTEs indices of the glass ceramics sintered at A: 850 and B: 1,050°C was <5.8 and 3.6, respectively. The PTEs index of the glass ceramic was lower than that of the parent glass. Glass ceramic, as compared to glass, reduces the potential risk of heavy metals polluting the ecological environment. Based on PTEs calculations and residential land soil background values, a PTEs of 0–132 indicates a mild level (Luan et al., 2018), which means that the glass ceramics obtained in this study can be used as building materials for their high value utilization.

4 Conclusion

The crystallization kinetics of the glass ceramics prepared from coal gasification slag and PIFA were studied. The thermal stability of the PIFA-based parent glass was reported first. The samples were prepared with a fly ash: slag ratio of 2:8 and were treated with four heating rates (α = 5, 10, 15, and 20°C/min). The low crystallization activation energy (121.49 kJ/mol) implied that it is easier to make glass ceramics. The Avrami parameter of the former was determined to be 1.23 ± .12, indicating the formation of two-dimensional crystal growth with heterogeneous nucleation at 850°C. These results indicated that using gasification slag and PIFA to produce glass ceramics both facilitated their recyclability and saved energy. At 850°C, the main crystalline phases were $(Ca_{1.96}Na_{0.05})$ $(Mg_{0.24}Al_{0.64}Fe_{0.12})$ $(Si_{1.39}Al_{0.61}O_7)$, $Na_{6.65}Al_{6.24}Si_{9.76}O_{32}$, and CaO. When the crystallization temperature increased to 1,050°C, the main crystalline phases were $Ca_2(Mg_{0.25}AI_{0.75})$ $(Si_{1.25}AI_{0.75}O_7)$ and $KNa_3(AlSiO_4)_4$. The glass ceramics, as compared to the parent glass, enhanced the solidification efficiency of heavy metals. The distribution of the four forms of heavy metals, their leaching behavior, and potential toxicity risk to the environment were investigated. The base glass exhibited a PTEs value of 11.7 and the glass ceramic sintered at 850°C and 1,050°C exhibited PTEs values of 5.8 and 3.6, respectively, indicating that the risk of environmental pollution was greatly reduced. This reduced risk was mainly due to the heavy metals existing in the glass ceramics in the form of residues. From the sustainable development and low environmental risk perspectives, using PIFA and other silicate solid waste to produce glass ceramics is a potential and promising technique for the solidification/stabilization of heavy metals. However, further studies on improving the mechanical and physical properties of the mixed materials are required for the practicability and environmental benefits of slag and ash recycling.

Data availability statement

The original contributions presented in the study are included in the article/supplementary material, further inquiries can be directed to the corresponding author.

Author contributions

ZH: Conceptualization, methodology, software, investigation, formal analysis, writing—original draft; HZ, XT, LS, YL, and SZ: Conceptualization, funding acquisition, writing—review and editing.

Funding

This study was supported by the Technology Development Program of SINOPEC, China.

Conflict of interest

Authors ZH, HZ, XT, LS, YL, and SZ were employed by SINOPEC Research Institute of Safety Engineering Co, Ltd.

Publisher's note

All claims expressed in this article are solely those of the authors and do not necessarily represent those of their affiliated organizations, or those of the publisher, the editors and the reviewers. Any product that may be evaluated in this article, or claim that may be made by its manufacturer, is not guaranteed or endorsed by the publisher.

References

Albertini, A. V. P., Silva, J. L., Freire, V. N., Santos, R. P., Martins, J. L., Cavada, B. S., et al. (2013). Immobilized invertase studies on glass–ceramic support from coal fly ashes. *Chem. Eng. J.* 214, 91–96. doi:10.1016/j.cej.2012.10.029

Alizadeh, P., Yekta, B. E., and Gervei, A. (2004). Effect of Fe2O3 addition on the sinterability and machinability of glass-ceramics in the system MgO–CaO–SiO2–P2O5. *J. Eur. Ceram. Soc.* 24 (13), 3529–3533. doi:10.1016/j.jeurceramsoc.2003.11.028

Allegrini, E., Maresca, A., Olsson, M. E., Holtze, M. S., Boldrin, A., and Astrup, T. F. (2014). Quantification of the resource recovery potential of municipal solid waste incineration bottom ashes. *Waste. Manag.* 34 (9), 1627–1636. doi:10.1016/j.wasman.2014.05.003

Almeda, R., Baca, S., Hyatt, C., and Buskey, E. J. (2014). Ingestion and sublethal effects of physically and chemically dispersed crude oil on marine planktonic copepods. *Ecotoxicology* 23 (6), 988–1003. doi:10.1007/s10646-014-1242-6

Augis, J., and Bennett, J. (1978). Calculation of the Avrami parameters for heterogeneous solid state reactions using a modification of the Kissinger method. *J. Therm. analysis* 13 (2), 283–292. doi:10.1007/BF01912301

Bai, Z., Qiu, G., Peng, B., Guo, M., and Zhang, M. (2016a). Synthesis and characterization of glass-ceramics prepared from high-carbon ferrochromium slag. *RSC Adv.* 6 (58), 52715–52723. doi:10.1039/c6ra06245h

Bai, Z., Qiu, G., Yue, C., Guo, M., and Zhang, M. (2016b). Crystallization kinetics of glass–ceramics prepared from high-carbon ferrochromium slag. *Ceram. Int.* 42 (16), 19329–19335. doi:10.1016/j.ceramint.2016.09.102

Beyer, J., Trannum, H. C., Bakke, T., Hodson, P. V., and Collier, T. K. (2016). Environmental effects of the deepwater horizon oil spill: A review. *Mar. Pollut. Bull.* 110 (1), 28–51. doi:10.1016/j.marpolbul.2016.06.027

Blumer, M., and Sass, J. (1972). Oil pollution: Persistence and degradation of spilled fuel oil. *Science* 176 (4039), 1120–1122. doi:10.1126/science.176.4039.1120

Ceylan, İ., Gökdemir, H., Cengiz, T., and Çiçek, B. (2021). Development of CaO-rich blast furnace slag containing fluorine mica-based glass ceramic coatings. *Ceram. Int.* 47 (21), 29988–29994. doi:10.1016/j.ceramint.2021.07.173

Chen, H., Lin, H., Zhang, P., Yu, L., Chen, L., Huang, X., et al. (2021). Immobilisation of heavy metals in hazardous waste incineration residue using SiO2–Al2O3–Fe2O3–CaO glass-ceramic. *Ceram. Int.* 47 (6), 8468–8477. doi:10.1016/j.ceramint.2020.11.213

Deng, L., Wang, S., Zhang, Z., Li, Z., Jia, R., Yun, F., et al. (2020). The viscosity and conductivity of the molten glass and crystallization behavior of the glass ceramics derived from stainless steel slag. *Mat. Chem. Phys.* 251, 123159. doi:10.1016/j.matchemphys.2020.123159

Devi, P., and Saroha, A. K. (2014). Risk analysis of pyrolyzed biochar made from paper mill effluent treatment plant sludge for bioavailability and eco-toxicity of heavy metals. *Bioresour. Technol.* 162, 308–315. doi:10.1016/j.biortech.2014.03.093

Dong, G., Qing, T., Du, R., Wang, C., Li, R., Wang, M., et al. (2020). Complex network approach for the structural optimization of global crude oil trade system. *J. Clean. Prod.* 251, 119366. doi:10.1016/j.jclepro.2019.119366

Dutta, A., Bouri, E., and Roubaud, D. (2019). Nonlinear relationships amongst the implied volatilities of crude oil and precious metals. *Resour. Policy* 61, 473–478. doi:10.1016/j.resourpol.2018.04.009

Erol, M., Küçükbayrak, S., and Ersoy-Meriçboyu, A. (2007). Production of glass-ceramics obtained from industrial wastes by means of controlled nucleation and crystallization. *Chem. Eng. J.* 132 (1), 335–343. doi:10.1016/j.cej.2007.01.029

Fang, C., Ma, Y., Li, P., and Chen, G. (2021). *Annual report on China's petroleum industry development (2021)*. Beijing, China: Social Sciences Academic Press.

Fu, X.-W., Wang, D.-G., Ren, X.-H., and Cui, Z.-J. (2014). Spatial distribution patterns and potential sources of heavy metals in soils of a crude oil-polluted region in China. *Pedosphere* 24 (4), 508–515. doi:10.1016/s1002-0160(14)60037-0

Ghorbani, Z., and Behzadan, A. H. (2021). Monitoring offshore oil pollution using multi-class convolutional neural networks. *Environ. Pollut.* 289, 117884. doi:10.1016/j.envpol.2021.117884

Gong, Z., Wang, Z., and Wang, Z. (2018). Study on migration characteristics of heavy metals during oil sludge incineration. *Pet. Sci. Technol.* 36 (6), 469–474. doi:10.1080/10916466.2018.1430156

Guo, B., Liu, B., Yang, J., and Zhang, S. (2017). The mechanisms of heavy metal immobilization by cementitious material treatments and thermal treatments: A review. *J. Environ. Manage* 193, 410–422. doi:10.1016/j.jenvman.2017.02.026

Hakanson, L. (1980). An ecological risk index for aquatic pollution control.a sedimentological approach. *Water. Res.* 14 (8), 975–1001. doi:10.1016/0043-1354(80)90143-8

Hosono, H., and Abe, Y. (1992). Porous glass-ceramics with a skeleton of the fast-lithium-conducting crystal Li1+ xTi2− xAlx (PO4) 3. *J. Am. Ceram. Soc.* 75 (10), 2862–2864. doi:10.1111/j.1151-2916.1992.tb05517.x

Hosono, H., and Abe, Y. (1994). Silver ion selective porous lithium titanium phosphate glass-ceramics cation exchanger and its application to bacteriostatic materials. *Mat. Res. Bull.* 29 (11), 1157–1162. doi:10.1016/0025-5408(94)90185-6

Kang, J., Chen, Z., Zhu, X., Zhou, S., Zhou, L., Wang, Z., et al. (2019). Effect of replacement of Na2O by Fe2O3 on the crystallization behavior and acid resistance of MgO Al2O3SiO2 glass-ceramics. *J. Non. Cryst. Solids* 503-504, 1–6. doi:10.1016/j.jnoncrysol.2018.09.013

Karamanov, A., Pisciella, P., and Pelino, M. (2000). The crystallisation kinetics of iron rich glass in different atmospheres. *J. Eur. Ceram. Soc.* 20 (12), 2233–2237. doi:10.1016/S0955-2219(00)00077-7

Karpukhina, N., Hill, R. G., and Law, R. V. (2014). Crystallisation in oxide glasses - a tutorial review. *Chem. Soc. Rev.* 43 (7), 2174–2186. doi:10.1039/c3cs60305a

Kim, Y., and Park, H. (2020). A value-added synthetic process utilizing mining wastes and industrial byproducts for wear-resistant glass ceramics. *ACS Sustain. Chem. Eng.* 8 (5), 2196–2204. doi:10.1021/acssuschemeng.9b05884

Kissinger, H. E. (1956). Variation of peak temperature with heating rate in differential thermal analysis. *J. Res. Natl. Bur. Stand* 57 (4), 217–221. doi:10.6028/jres.057.026

Konist, A., Neshumayev, D., Baird, Z. S., Anthony, E. J., Maasikmets, M., and Jarvik, O. (2020). Mineral and heavy metal composition of oil shale ash from oxyfuel combustion. *ACS Omega* 5 (50), 32498–32506. doi:10.1021/acsomega.0c04466

Li, C.-T., Huang, Y.-J., Huang, K.-L., and Lee, W.-J. (2003). Characterization of slags and ingots from the vitrification of municipal solid waste incineration ashes. *Ind. Eng. Chem. Res.* 42 (11), 2306–2313. doi:10.1021/ie0208164

Liu, Y., Clavier, K. A., Spreadbury, C., and Townsend, T. G. (2019). Limitations of the TCLP fluid determination step for hazardous waste characterization of US municipal waste incineration ash. *Waste. Manag.* 87, 590–596. doi:10.1016/j.wasman.2019.02.045

Luan, J., Chai, M., Liu, Y., and Ke, X. (2018). Heavy-metal speciation redistribution in solid phase and potential environmental risk assessment during the conversion of MSW incineration fly ash into molten slag. *Environ. Sci. Pollut. Res. Int.* 25 (4), 3793–3801. doi:10.1007/s11356-017-0734-3

Luan, J., Li, A., Su, T., and Cui, X. (2010). Synthesis of nucleated glass-ceramics using oil shale fly ash. *J. Hazard. Mater* 173 (1-3), 427–432. doi:10.1016/j.jhazmat.2009.08.099

Luan, J., Li, A., Su, T., and Li, X. (2009). Translocation and toxicity assessment of heavy metals from circulated fluidized-bed combustion of oil shale in Huadian, China. *J. Hazard. Mater* 166 (2-3), 1109–1114. doi:10.1016/j.jhazmat.2008.12.023

Melichar, M., and Atems, B. (2019). Global crude oil market shocks and global commodity prices. *OPEC Energy Rev.* 43 (1), 92–105. doi:10.1111/opec.12143

Nikravan, M., Ramezanianpnour, A. A., and Maknoon, R. (2018). Technological and environmental behavior of petrochemical incineration bottom ash (PI-BA) in cement-based using nano-SiO2 and silica fume (SF). *Constr. Build. Mater* 191, 1042–1052. doi:10.1016/j.conbuildmat.2018.09.135

Rauret, G., López-Sánchez, J., Sahuquillo, A., Rubio, R., Davidson, C., Ure, A., et al. (1999). Improvement of the BCR three step sequential extraction procedure prior to the certification of new sediment and soil reference materials. *J. Environ. Monit.* 1 (1), 57–61. doi:10.1039/A807854H

Shang, W., Peng, Z., Huang, Y., Gu, F., Zhang, J., Tang, H., et al. (2021). Production of glass-ceramics from metallurgical slags. *J. Clean. Prod.* 317, 128220. doi:10.1016/j.jclepro.2021.128220

Thind, P. S., Sareen, A., Singh, D. D., Singh, S., and John, S. (2021). Compromising situation of India's bio-medical waste incineration units during pandemic outbreak of COVID-19: Associated environmental-health impacts and mitigation measures. *Environ. Pollut.* 276, 116621. doi:10.1016/j.envpol.2021.116621

Tian, S., Li, J., Liu, F., Guan, J., Dong, L., and Wang, Q. (2012). Behavior of heavy metals in the vitrification of MSWI fly ash with a pilot-scale diesel oil furnace. *Procedia Environ. Sci.* 16, 214–221. doi:10.1016/j.proenv.2012.10.030

Wang, S. (2010). Effects of Fe on crystallization and properties of a new high infrared radiance glass-ceramics. *Environ. Sci. Technol.* 44 (12), 4816–4820. doi:10.1021/es1003268

Wei, J., Gong, Y., Ding, L., Yu, J., and Yu, G. (2018). Influence of biomass ash additive on reactivity characteristics and structure evolution of coal char–CO2 gasification. *Energy Fuel* 32 (10), 10428–10436. doi:10.1021/acs.energyfuels.8b02028

Zhang, M., Guo, M., Zhang, B., Li, F., Wang, H., and Zhang, H. (2020). Stabilization of heavy metals in MSWI fly ash with a novel dithiocarboxylate-functionalized polyaminoamide dendrimer. *Waste Manag.* 105, 289–298. doi:10.1016/j.wasman.2020.02.004

Zhao, K., Hu, Y., Wang, Y., Chen, D., and Feng, Y. (2019). Speciation and risk assessment of heavy metals in municipal solid waste incineration fly ash during thermal processing. *Energy Fuel* 33 (10), 10066–10077. doi:10.1021/acs.energyfuels.9b02187

Zhao, S., Liu, B., Ding, Y., Zhang, J., Wen, Q., Ekberg, C., et al. (2020). Study on glass-ceramics made from MSWI fly ash, pickling sludge and waste glass by one-step process. *J. Clean. Prod.* 271, 122674. doi:10.1016/j.jclepro.2020.122674

Frontiers in Chemistry

Explores all fields of chemical science across the periodic table

Advances our understanding of how atoms, ions, and molecules come together and come apart. It explores the role of chemistry in our everyday lives - from electronic devices to health and wellbeing.

Discover the latest Research Topics

See more →

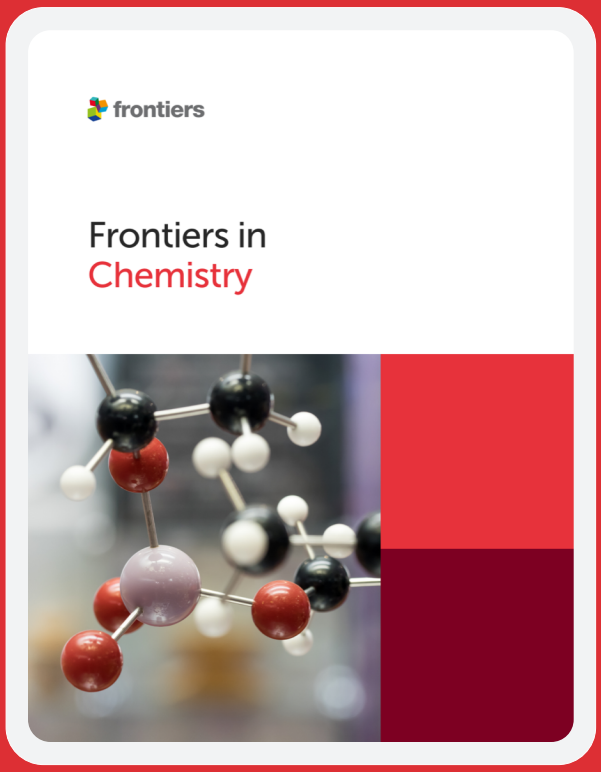

Frontiers

Avenue du Tribunal-Fédéral 34
1005 Lausanne, Switzerland
frontiersin.org

Contact us

+41 (0)21 510 17 00
frontiersin.org/about/contact